

Direct Measurements of the Damping of Alfvén Eigenmodes for an Assessment of their Stability Limits in Tokamak Plasmas

THÈSE N° 4940 (2010)

PRÉSENTÉE LE 21 DÉCEMBRE 2010

À LA FACULTÉ SCIENCES DE BASE
CRPP - INSTALLATIONS INTERNATIONALES
PROGRAMME DOCTORAL EN PHYSIQUE

ÉCOLE POLYTECHNIQUE FÉDÉRALE DE LAUSANNE

POUR L'OBTENTION DU GRADE DE DOCTEUR ÈS SCIENCES

PAR

Theodoros PANIS

acceptée sur proposition du jury:

Prof. G. Gremaud, président du jury
Prof. A. Fasoli, Dr D. Testa, directeurs de thèse
Dr S. Sharapov, rapporteur
Prof. L. Villard, rapporteur
Dr P. Woskov, rapporteur



ÉCOLE POLYTECHNIQUE
FÉDÉRALE DE LAUSANNE

Suisse
2010

A ma famille:
Maria, Stefanos, Vasilis.

Résumé

Des mesures directes du taux d'amortissement des modes propres d'Alfvén propres ("Alfvén eigenmodes, AEs") sont obtenues en utilisant le système de spectroscopie MHD active installé dans le tokamak JET. Le système a été récemment équipé de nouvelles antennes conçues pour étudier en particulier les modes de nombre toroïdal n intermédiaire, $|n| = 3 - 15$, étant donné que les modes de cette gamme sont les plus aisément déstabilisés par les particules rapides dans JET et dans les futures expériences avec des plasmas en combustion, comme ITER.

Le large spectre en n produit par les nouvelles antennes, ainsi que la structure localisée des AEs de n intermédiaire, ont des conséquences importantes sur la capacité à mesurer des taux d'amortissement de n intermédiaire. Afin d'obtenir une base de données expérimentale de mesures de haute précision des n individuels, il a été indispensable de travailler sur plusieurs aspects expérimentaux dans le domaine de l'excitation des modes, ainsi que dans le domaine de la détection.

Concernant l'excitation, le modèle électrique du système d'excitation des AEs a été construit dans le cadre de cette thèse. Le modèle est utilisé pour déterminer les capacités opérationnelles du système avec les nouvelles antennes, ainsi que pour optimiser les courants des antennes et concevoir les circuits d'adaptation d'impédance associés.

Quant à la détection, l'excitation simultanée des modes avec plusieurs n à des fréquences très proches a nécessité une méthode sophistiquée pour estimer le spectre en n de la réponse du plasma. Dans ce but, une méthode basée sur la représentation des spectres creux ("sparse") a été adaptée pour pouvoir traiter des données complexes et en temps réel. La décomposition de la réponse du plasma en n exige une calibration précise des bobines magnétiques. A cette fin, une méthode *in situ*

basée sur le couplage direct des bobines avec les nouvelles antennes AE a été développée et appliquée.

Une riche collection de mesures du taux d’amortissement des modes d’Alfvén toroïdaux (TAEs) a été obtenue durant les campagnes expérimentales de JET des années 2008 et 2009, suite à l’optimisation du système. Dans cette thèse, des mesures de modes TAE de $|n| = 3, 4$ et $|n| = 7$ ont été comparées avec les modèles de plasma incorporés dans les codes numériques LEMan et CASTOR. La robustesse des résultats des simulations a été testée contre les incertitudes expérimentales dans les profils de densité et du facteur de sécurité q . Les modes excités par les antennes sont caractérisés et les mécanismes d’amortissement sont identifiés dans plusieurs cas, confirmant le rôle stabilisant du cisaillement magnétique du bord pour une large gamme de n . Les comparaisons montrent que les effets cinétiques sont importants pour obtenir une estimation de l’amortissement proche de l’expérience.

Par ailleurs, l’étude d’une base de données expérimentale d’environ 3000 taux d’amortissement des modes TAE mesurés dans des plasmas ohmiques est présentée. Les dépendances des mesures de l’amortissement en fonction du cisaillement magnétique du bord, de l’élongation du bord et du profil de q sont examinées. Cette analyse fournit des preuves expérimentales de la variation des propriétés de l’amortissement des TAEs de $|n| = 2 - 7$ avec l’augmentation du mode toroidal n . En particulier, l’analyse montre que les modes de n élevé subissent en général moins d’amortissement que les modes de bas n . Dans des plasmas de JET, le point tournant pour que les propriétés des modes changent d’un comportement bas- n vers un comportement haut- n est situé à $|n| \approx 3 - 4$.

Mots-clés: fusion magnétique, ITER, plasma, tokamak, particules énergétiques, modes d’Alfvén, stabilité, mesure du taux d’amortissement, mécanisme d’amortissement, effect cinétique, adaptation (matching) d’impédances, analyse spectrale, représentation creuse (“sparse”).

Abstract

Direct damping rate measurements of AEs are obtained using the active MHD spectroscopy system installed on the JET tokamak. The system was recently equipped with new antennas, designed to study especially the modes of intermediate toroidal mode number n , $|n| = 3 - 15$, as the AEs of this range are most prone to destabilization by the fast particles in JET and in future burning plasma experiments such as ITER.

The broad n -spectrum that is driven by the new antennas and the more localized structure of intermediate- n AEs has important implications for the ability to measure damping rates of intermediate n . To obtain an extended database of high accuracy individual- n measurements, experimental work on technical and engineering aspects was indispensable both on the excitation side and on the detection side.

On the excitation side, the electrical model of the AE exciter has been constructed during this thesis. The model is used to determine the operational capabilities of the exciter with the new antennas, to optimize the antenna currents and to design the relevant impedance matching circuits.

On the detection side, the excitation of multiple- n , degenerate AEs at close frequencies prompted for a sophisticated method to correctly estimate the n -spectrum of the plasma response. To this end, a sparse spectrum representation method was adapted to deal with the complex and real-time data produced by the active MHD spectroscopy system. The n -decomposition of the plasma response requires an accurate relative calibration of the magnetic pick-up coils. An *in situ* method was developed and applied for the calibration of the coils using the direct coupling to the new AE antennas.

A large collection of damping rate measurements of, mainly, toroidal AEs (TAEs) was obtained during the 2008/2009 JET experimental

campaigns following the technical optimization of the antenna system. Selected measurements of $|n| = 3, 4$ and $|n| = 7$ TAEs are compared to the plasma models of the numerical codes LEMan and CASTOR. The robustness of the results of the simulations is tested against uncertainties in density and safety factor profiles. The antenna-driven modes are characterized and the dominant damping mechanisms are identified in a number of cases, and confirm in general for a wide n -range the stabilizing role played by the edge magnetic shear. These comparisons underline the importance of the kinetic effects in order to achieve a realistic estimation of the TAE damping.

A database of approximately 3000 TAE damping rate measurements in ohmic plasmas is studied. The dependence of the damping rate measurements of $|n| = 2 - 7$ TAEs on the edge magnetic shear, the edge elongation and the q profile is investigated. The analysis provides experimental evidence that the damping properties of TAEs with $|n| = 2 - 7$ change as the toroidal mode number n increases, showing that medium- n modes tend to be less damped than low- n modes. In JET plasmas, the turning point for the damping properties to change from low- n to medium- n behavior is found to be at $|n| \approx 3 - 4$.

Keywords: magnetic fusion, ITER, tokamak plasma, energetic particles, Alfvén eigenmodes, stability, damping rate measurement, damping mechanism, kinetic effect, electrical circuit, impedance matching, spectral analysis, sparse representation.

Contents

1	Introduction	1
1.1	Thermonuclear fusion and burning plasma physics	1
1.2	Motivation for this thesis	2
1.3	Outline of the thesis	3
2	Alfvén wave physics and state of research	5
2.1	Basic properties of Alfvén waves	5
2.1.1	Plasma description in the MHD limit	6
2.1.2	Shear Alfvén waves and resonant mode conversion	9
2.1.3	Gap modes	11
2.1.4	Drive mechanisms for AEs	14
2.1.5	Damping mechanisms for AEs	15
2.1.5.1	Collisionless (Landau) damping	15
2.1.5.2	Trapped electron collisional damping	15
2.1.5.3	Mode conversion to kinetic Alfvén waves	16
2.1.6	Summary	17
2.2	AEs driven by fast ion populations	17
2.3	AEs driven by external antennas	19
2.3.1	The method	19
2.3.2	Experimental results from JET and other machines	20
2.4	New AE antennas on JET	22
2.5	Conclusions	23
3	Electrical modeling of the AE exciter and matching unit design	27
3.1	Introduction	27
3.2	Layout of the AE exciter	28

3.3	Modeling	29
3.3.1	Antennas	29
3.3.1.1	Individual antennas	29
3.3.1.2	Inductive coupling between antennas	34
3.3.2	Power transmission lines	35
3.3.3	Distribution and isolation transformers	42
3.3.4	Power amplifier	46
3.3.5	Complete model of the AE exciter	49
3.3.6	Discussion	57
3.3.6.1	Interpretation of the resonances of current gain G_{lb}	57
3.3.6.2	Maximization of the antenna currents and limitations	58
3.3.6.3	Minimization of the antenna inductive coupling effects	60
3.4	Matching	61
3.4.1	Matching unit design	62
3.4.1.1	Equivalent model and optimization aspects	63
3.4.1.2	Results	66
3.4.2	Experimental results	69
3.5	Conclusions	72
4	The n-spectrum of the antenna excitation and of the plasma response	75
4.1	Introduction	75
4.2	The magnetic field of the AE antennas in vacuum	76
4.3	Calibration of the magnetic pick-up coils using their direct coupling to the AE antennas in vacuum	87
4.3.1	Direct coupling: background and formulation	87
4.3.2	Measurements and results	93
4.3.3	Comparison with the calibration from impedance measurements	98
4.4	The n -spectrum of the plasma response	100
4.5	Integration of SparSpec in the real-time mode-tracking system	102
4.6	Estimation of the damping rates from the raw data	105
4.6.1	Data processing algorithm	105

4.6.2	Automatic processing of the raw data	108
4.7	Summary and conclusions	111
5	Experimental measurements and comparisons with plasma mod-	
	els	113
5.1	Introduction	113
5.2	LEMan	114
5.3	CASTOR	115
5.4	Damping of $n = 3$ TAEs	116
5.4.1	Damping rate measurements	116
5.4.2	Input data for the simulations	118
5.4.3	Results from LEMan	119
5.4.3.1	Comparison with experiment	119
5.4.3.2	Sensitivity to q and density profiles	119
5.4.3.3	Mode structure and damping mechanisms	128
5.4.4	Results from CASTOR	135
5.4.4.1	Input data and parameters	135
5.4.4.2	Comparison with experiment	137
5.4.4.3	Mode structure and damping mechanisms	140
5.4.5	Comparison between CASTOR and LEMan	140
5.5	Damping of $n = 4$ TAEs	142
5.5.1	Damping rate measurements	142
5.5.2	Input data for the simulations	143
5.5.3	Comparison between measurements and simulations	145
5.5.4	Mode structure and damping mechanisms	145
5.6	Damping of $n = 7$ TAEs	149
5.6.1	Damping rate measurements	149
5.6.2	Input data for the simulations	151
5.6.3	Mode identification and interpretation	152
5.7	Summary and discussion	159
5.8	Conclusions	162

6	AE damping rate measurements	163
6.1	Introduction	163
6.2	AE database and statistics	165
6.2.1	Damping rate dependence on plasma shape	167
6.3	Effect of the edge shear/elongation and the role of the $q_{95} - q_0$. .	170
6.3.1	$ n = 3$ TAEs	171
6.3.2	$ n = 6 - 7$ TAEs	176
6.4	Effect of the q profile relaxation	178
6.4.1	$ n = 3$ TAEs	181
6.4.2	$ n = 5$ TAEs	181
6.4.3	$ n = 6 - 7$ TAEs	183
6.5	Comparisons between modes of different n in the same plasma conditions	187
6.6	Effect of the ICRF heating on $n = 3$ TAEs	190
6.7	Discussion	193
6.8	Summary and conclusions	195
7	Conclusions and outlook	197
7.1	Summary	197
7.2	Conclusions	201
7.3	Outlook	202
A	Circuits	203
A.1	Single-line m-antenna model of the AE exciter	203
A.2	Matching units	204
A.3	Proof of the fundamental theorem for the remote calibration of the magnetic coils using impedance measurements	205
B	Field formulas	209
C	Relation between damping rate expressions	213
D	Publications and scientific presentations	215
	References	229

List of Figures

2.1	Qualitative diagrams of Alfvén modes	13
2.2	Unstable TAEs and antenna signature	18
2.3	View of the new AE antennas (layout).	23
2.4	View of the new AE antennas.	24
3.1	Layout of the AE exciter.	30
3.2	Impedance measurements of the antennas mounted-on-frame. . . .	31
3.3	Circuit model for an individual antenna coil.	31
3.4	Comparisons between fits of the impedance measurements for the antennas 2 and 7.	32
3.5	Antenna model that includes the effect of inductive coupling. . . .	35
3.6	Geometry of the antennas used for the calculation of the inductances	36
3.7	Measured impedance of the open-circuited riser cable of the an- tenna 1.	38
3.8	Effect of small stray elements on the a transmission line.	39
3.9	Verification of the riser model for antenna 1.	39
3.10	Antenna impedance comparison at the LBs.	41
3.11	Circuit used to model the DU and IU transformers.	43
3.12	Circuit of the DU 1:2.	43
3.13	Measured admittances for the open-circuit tests	45
3.14	Impedance measurements of the short-circuit tests on the DU and IU transformers	46
3.15	Power amplifier	47
3.16	Decrease of the capacity of the power amplifier	48
3.17	PSpice model	50
3.18	Various impedance measurements of the antennas	51

LIST OF FIGURES

3.19	Effect of antenna phasing on the antenna impedance	52
3.20	Current gain #3356	53
3.21	Effect of the amplifier output impedance	54
3.22	Current gain for the pulse #3894	55
3.23	Exciter simulation for the pulse #3358	56
3.24	Reduced model of transmission line terminated by one antenna. .	57
3.25	Effect of the modification of the attenuation stage	59
3.26	Effect of the antenna 8 as passive antenna	60
3.27	Effect of ‘decoupling’ antenna 5 from antenna 6	61
3.28	Reduced model for a configuration with 4 active antennas.	63
3.29	Impedance comparison for the validity of the reduced model . . .	64
3.30	Reduced model without MU.	65
3.31	MU design at 197 kHz	66
3.32	MU design at 197 kHz	67
3.33	MU design at 107 kHz	68
3.34	View of manufactured matching unit	69
3.35	Experimental test of matching unit, pulse #3918	70
3.36	Total current gain, pulse #3918	70
3.37	Experimental test of matching unit, pulse #4016	71
3.38	Overview of the maximum LB currents measured with the MUs .	72
4.1	View of the antennas and the structure of the wall	77
4.2	Geometry of an antenna turn and coordinates	78
4.3	3-D view of the antenna magnetic field	82
4.4	Antenna field as function of different sets of active antennas (top, middle and bottom rows), n number and the distance r	84
4.5	Even- n driven spectrum for antennas 1, 4, 6 and 7	85
4.6	Effect of antenna current distribution on the driven n -spectrum .	86
4.7	View of the toroidal cross-section with AE antennas and magnetic coils.	88
4.8	Circuit model of a magnetic coil.	89
4.9	Antenna currents for magnetic coil calibration (#3929)	93
4.10	Calibration data and fits for coils T004 and H304	94
4.11	Calibration data and optimization calculation for the coil T001 . .	95
4.12	Final calibration curves with respect to the reference coil T004 . .	96

4.13	Comparison of the direct-coupling calibration with impedance measurement calibration	99
4.14	Comparison between SparSpec and phase-fitting	101
4.15	Example of comparison on the parity of the n -spectrum (#78752)	102
4.16	Illustration of the n -number filtering achieved in real-time	104
4.17	Data processing algorithm to extract measured damping rates	107
4.18	Damping rate measurements - comparison between automatic and manual processing	109
4.19	Resonance fit sensitivity	110
5.1	Damping rate measurements $n = 3$ in #77788	117
5.2	Resonance fits of $n = 3$ TAEs in the discharge #77788	118
5.3	Profiles of q in the discharge #77788 for LEMan simulations	120
5.4	Profiles of n_e and T_e in the discharge #77788 for LEMan simulations	121
5.5	Error bars on the density profile for the discharge #77788	121
5.6	#77788: LEMan versus experiment	122
5.7	Sensitivity to q profile, t_2 in the discharge #77788	123
5.8	Sensitivity to edge n_e profile, t_3 in the discharge #77788	124
5.9	Sensitivity to n_e profile, t_4 in the discharge #77788	126
5.10	Sensitivity to n_e profile for t_0 in the discharge #77788	127
5.11	LEMan results for t_1 in the discharge #77788	129
5.12	KAW features on $\Im(A_{\parallel})$, $\Im(\phi)$ for t_1 in the discharge #77788	130
5.13	LEMan results for t_4 in the discharge #77788	131
5.14	Non-ideal parameter in #77788	132
5.15	Local electron Landau damping in #77788	134
5.16	Temperature scan for plasma response at t_4 in #77788	135
5.17	Overview of the power absorption profiles in #77788	136
5.18	Comparison between EFIT and HELENA	137
5.19	Comparison between CASTOR and experiment in #77788	138
5.20	CASTOR results for $t = 6.1$ s in the discharge #77788	139
5.21	CASTOR results for $t = 4.5$ and 7.8 s in #77788	141
5.22	Damping rate measurements of n TAEs in #77783	144
5.23	Profiles of q and n_e in #77783	146
5.24	LEMan against experiment in #77783	147
5.25	Sensitivity to n_e profile, $t_3 = 15$ s in the discharge #77783	148

LIST OF FIGURES

5.26	LEMan results for $t = 10.7$ s in the discharge #77783	150
5.27	LEMan plasma response and Alfvén continuum for $t = 8.7$ s in #77783	151
5.28	LEMan ϕ and power absorption for $t = 15$ s in #77783	152
5.29	Damping rate measurements in #78740	153
5.30	Resonance fits for #78740	154
5.31	Profiles of q , n_e and T_e in #78740	155
5.32	Plasma response $n = 3$ and $n = 7$ for #78740.	156
5.33	Mode structure and power absorption for $n = 3$ and $n = 7$ for #78740.	158
6.1	Number of damping rate measurements as function of n	166
6.2	Database of damping rates as function of edge elongation	168
6.3	Database of damping rates as function of q_0	169
6.4	Database of damping rates as function of q_{95}	170
6.5	q profiles #77788	171
6.6	Damping rate measurements in #77417	173
6.7	Resonance fits #77417	174
6.8	q profiles in pulses 77417 and 77788	174
6.9	Damping rate measurements in #77962	175
6.10	Damping rate measurements in #79238	177
6.11	Resonance fits #79238	178
6.12	Damping rate measurements in #78738	179
6.13	Damping rate measurements in #77736	180
6.14	Damping rate measurements in #78754	182
6.15	q profiles in pulses 78754 and 78740	183
6.16	Damping rate measurements odd- n in #78752 and #79215	184
6.17	q profiles in the discharge #78738	185
6.18	Damping rate measurements in #78764	186
6.19	Resonance fits for #78764	187
6.20	Damping rate measurements even- n in #77432 and #77967	188
6.21	Resonances fits for the discharges #77432 and #77967	189
6.22	q profiles in pulses 77432 and 77967	189
6.23	Damping rate measurements in #77792 (ICRH)	191

LIST OF FIGURES

A.1	MU design at 143 kHz	204
A.2	MU design at 175 kHz	205
A.3	Circuit configuration of the measurement of the coil impedance . .	206
A.4	Circuit configuration during plasma operation	207

List of Tables

3.1	Estimates of the goodness of the antenna impedance fits.	33
3.2	The parameters of the antenna circuit model estimated using robust fitting.	34
3.3	The parameters of the antenna circuit model estimated using linear fitting.	34
3.4	Cable technical specifications.	37
3.5	Cable lengths in m estimated from impedance measurements. . . .	40
3.6	Circuit parameters of DU and IU transformers	44
4.1	Summary of the toroidal array of the magnetic pick-up coils used in this work, all located at $[R, Z] \simeq [3.88, 1.01]$ m with a poloidal orientation 108.9°	88
5.1	LEMan results against the experiment measurements for the discharge #78740, $t = 6.5$ s.	157
6.1	Range of ohmic plasma parameters.	165

Chapter 1

Introduction

1.1 Thermonuclear fusion and burning plasma physics

The most promising device for the production of energy from controlled nuclear fusion reactions is the tokamak [1]. Tokamaks have achieved record fusion power levels (16.1 MW in JET in 1997) under controlled conditions. In future fusion reactors based on the tokamak concept, the fuel ions, deuterium (D) and tritium (T), will be in thermodynamic equilibrium with a thermal energy of the order of 20 keV. Since the reactors will be based on the DT fusion reaction,



highly energetic alpha particles (charged nuclei of helium) will be generated at the energy of 3.5 MeV. The subsequent collisions between the fusion-born alpha particles and the electrons will play the role of alpha particle thermalization, allowing the plasma to be self-heated. When this self-heating mechanism is sufficient to maintain the plasma temperature that is required for fusion, the reaction becomes self-sustaining, i.e. no external plasma heating is required. This condition is referred to as ignition. A measure of the proximity to fusion reactor conditions is given by the ratio Q , of the produced thermonuclear power to the heating power supplied. At ignition, Q tends to infinity.

In ITER, the next large magnetic fusion experiment, the goal is to achieve for the first time $Q \geq 10$. In this regime, the heating power carried by the alphas

is dominant and exceeds the auxiliary heating: such plasmas are called burning plasmas.

A good alpha particle confinement is therefore a necessary condition for sustaining the burning plasma regime. This condition imposes an upper limit on the acceptable alpha particle transport. Fortunately, classical cross-field transport due to collisions does not lead to significant transport. Nonetheless, there exists a class of plasma collective instabilities that could increase the alpha particle transport to unacceptable levels: it is the weakly-damped Alfvén eigenmodes (AEs). For typical fusion plasma parameters (magnetic field $B \sim 5$ T, ion density $\sim 10^{20} \text{ m}^{-3}$), the phase velocity of the Alfvén wave is just lower than fusion-born alpha particle speed. During their slowing down, the alpha particles encounter the Alfvén wave-particle resonance which can lead to a very effective exchange of energy and momentum with the modes. This exchange takes place in a time scale much shorter than alpha particle relaxation time and hence, the self-heating process can be compromised. More importantly, the interaction between the AEs and the alphas can lead to damages to the first wall by the ejection of highly energetic alphas. In present experiments, fusion-born alpha particles are not produced in sufficiently high numbers to drive AEs unstable. However, the destabilization of the AEs from fast particles that are accelerated by other methods, such as ion cyclotron resonance heating and neutral beam injection, is a routine observation in present experiments.

Thus, the physics of the Alfvén waves are intrinsically connected to the burning plasma regime. Research in this area is critical for the success of the ITER experiment [2, 3] and future magnetic fusion devices.

1.2 Motivation for this thesis

This thesis addresses the linear stability properties of the AEs that are more prone to destabilization by fast particles. In the JET tokamak, these modes are typically observed to have toroidal mode number n in the intermediate- n range, $n = 3 - 11$. In ITER, it is predicted that the most unstable n -range will shift to higher mode numbers, $n \sim 5 - 15$. The linear stability of these modes is a key element because the mode damping rate determines the instability threshold and affects the saturation amplitude once the mode is destabilized. The active MHD

spectroscopy system [4, 5] that is installed in JET is used to measure directly the AE damping rates. The system was recently equipped with new antennas, designed to study especially the intermediate- n range.

As explained previously, it is important to assess the effect of the Alfvén wave-particle interaction in burning plasma regimes. Despite the progress achieved so far, AEs remain one of the most important uncertainties in predicting alpha-particle behavior in future burning plasma devices. An important milestone towards increasing the reliability of the predictions is to ensure that the existing numerical models are in good agreement with the damping measurements in the present devices. In such a context, it is important that the damping rates are measured on JET plasmas, as JET is the most ITER-relevant device in terms of size and overall plasma conditions.

The broad n -spectrum that is driven by the new antennas and the more localized structure of intermediate- n AEs has important implications for the ability to measure intermediate- n damping rates. To obtain experimental data of high quality and quantity, extensive experimental work on technical and engineering aspects was indispensable both on the excitation side and on the detection side. Thus, this work had to deal with several challenges of experimental nature. Finally, to characterize and identify the damping mechanisms of the driven AEs, the experimental data are compared with plasma models.

1.3 Outline of the thesis

The contents of this thesis are organized as follows:

Chapter 2 The basic properties of the Alfvén wave physics in tokamaks are described. Recent and past studies in the field are briefly reviewed. The method to directly measure mode damping rates using external antenna excitation is described. This chapter places the physics objective of the thesis in the context of the current state of research.

Chapter 3 The electrical model of the AE exciter is constructed. The model is used to determine the operational capabilities of the exciter with the new antennas, to optimize the antenna currents and to design the relevant impedance matching circuits.

Chapter 4 The electromagnetic field produced by the antennas in vacuum is computed. This computation is used to derive the driven n -spectrum as function of the antenna currents and the tokamak coordinates R and Z . The measurements of the magnetic pick-up coils are calibrated *in situ* using the direct coupling to the new AE antennas. The post-pulse estimation of n via the code SparSpec is compared with the phase-fitting method and the driven n -spectrum. The integration of SparSpec into the existing real-time resonance tracking software is described and the real-time results are compared to the post-pulse analysis. The algorithm for the data analysis of the damping rate measurements is described.

Chapter 5 Selected measurements of $n = 3$, 4 and $n = -7$ TAEs are compared to the plasma models of the numerical codes LEMan and CASTOR. The robustness of the results is tested against uncertainties in the density and q profiles. The antenna-driven modes are characterized and the dominant damping mechanisms are identified.

Chapter 6 Damping rate measurements of approximately 70 ohmic plasma discharges are entered into a database. Medium- n AE damping rates are studied as a function of the safety factor q , the magnetic shear and the plasma shape, and are compared with the measured damping of lower- n AEs. The drive on $|n| = 3$ TAEs produced from ICRH-accelerated fast ions is estimated from the damping rate measurements in a particular case.

Chapter 7 A summary of the work carried out in this thesis is presented. The main conclusions are highlighted and an outlook for future work in the field is given.

A number of appendices are provided in the end of the thesis. Appendix A provides circuit calculations and results from the matching unit design. Appendix B provides analytical expressions for the field produced by the antennas. In appendix C, the relation between the the quality factor of a resonance and the damping rate expressed as γ/ω is derived. Finally, a list of the peer-reviewed publications, conference contributions and selected scientific meeting presentations that the author has contributed to is given in Appendix D.

Chapter 2

Alfvén wave physics and state of research

This chapter situates the objectives of this thesis with respect to past and recent studies in the field of Alfvén waves and their interaction with fast particles in tokamaks. The chapter is organized as follows. Section 2.1 describes the basic properties of the Alfvén waves. Emphasis is given on how the tokamak geometry modifies the waves transforming them into Alfvén gap modes and how non-ideal effects modify the basic picture of the ideal magneto-hydrodynamic (MHD) theory. Section 2.2 discusses briefly the knowledge gained from the studies on unstable Alfvén eigenmodes (AEs) that are driven by fast-particle populations. The method of exciting stable AEs using external antennas is described in section 2.3, as well as the studies that were undertaken using the method before the commencement of this work. Finally, the new antennas that are used in this work to obtain the damping rate measurements are described in section 2.4.

2.1 Basic properties of Alfvén waves

Hannes Alfvén, in 1942, was investigating the properties of plasmas, treating them as highly conducting, magnetized and incompressible fluids. He predicted that electromagnetic-hydrodynamic waves could propagate in these fluids along the magnetic field lines [6]. These waves are called shear or torsional Alfvén waves. The existence of the wave, in the conducting fluid mercury, was experimentally demonstrated by Lundquist and it was found that is strongly damped due to

finite conductivity[7, 8]. Alfvén waves have been the subject of intense study in the succeeding decades in laboratory, space and astrophysical plasmas. In this work, we are interested in the Alfvén wave properties in tokamak plasmas.

2.1.1 Plasma description in the MHD limit

The existence of Alfvén waves can be shown in the ideal magnetohydrodynamics (MHD) model. In this model, the plasma is a single fluid governed by long-wavelength, low-frequency macroscopic dynamics. It is useful to describe briefly the most important properties of the plasma in the ideal MHD limit, in which resistive effects are neglected. The reader is invited to refer to the classical textbooks of Freidberg [9] and Boyd [10]. Also, an introduction to the topic can be found in the lecture notes of Fitzpatrick ¹.

The plasma is a medium composed of electrons and various species (denoted by the index α) of ions. The number of these particles is so high that it is possible to describe them statistically, by using probability density or distribution functions. These distribution functions behave like an incompressible liquid in the $6N$ -dimensional phase space (N is the total number of particles), obeying the general conservation law of the probability density described by the Liouville equation [11]. From such a general description, one can obtain a reduced, fluid description of the plasma, by taking moments of the velocity distribution function. Macroscopically observable quantities can be then defined, such as density, particle flux, velocity, current density, heat flux and pressure, pertaining to each species. Conservation laws govern these macroscopic quantities. However, this system of equations is infinite, or, practically, incomplete, because more and more equations are required to describe higher-order correlations between the fluid variables: the density evolution depends on the flow velocity, the flow velocity evolution depends on the pressure tensor, etc. The closure of this system of equations is done by invoking a set of approximations and assumptions.

As a first step, very high-frequency or short-wavelength behavior is filtered out. In the Maxwell equations, the displacement current $\epsilon_0 \partial \mathbf{E} / \partial t$ is dropped as the characteristic phase velocities (ω/k) or thermal velocities ($v_T = (2k_B T/m)^{1/2}$) are much smaller than the speed of light. The term of the net charge $\epsilon_0 \nabla \cdot \mathbf{E}$ is also neglected. Therefore, charge fluctuations that vary in time at the characteristic

¹Freely available at <http://farside.ph.utexas.edu/teaching/plasma/plasma.html>

2.1 Basic properties of Alfvén waves

electron plasma frequency $\omega_{pe} = (n_0 e^2 / m_e \epsilon_0)^{1/2}$ or that take place at a spatial scale comparable to the Debye length $\lambda_d = v_{Te} / \omega_{pe}$ are too fast or too localized to be described. The plasma is quasi-neutral in the sense that electrons are fast enough (because of negligible inertia) to cancel any low-frequency macroscopic charge separation, i.e. $n_e \approx \sum Z_a n_a$ with $\epsilon_0 \nabla \cdot \mathbf{E} / e n_e \ll 1$. The electrons are assumed to have negligible inertia ($m_e \rightarrow 0$) and all the momentum of the fluid is carried by the ions. With the above approximations, single-fluid variables (mass density ρ , fluid velocity \mathbf{u} , current density \mathbf{J} , pressure p (isotropic part) and temperature T) can be defined as a function of the multi-fluid variables. Finally, this single fluid is assumed to follow the ideal gas law, $p = n k_B T$.

However, the single-fluid model contains still terms of unresolved higher moments. These terms arise from the anisotropy between the parallel and perpendicular to the magnetic field directions and they are different for ions and electrons. This anisotropy, combined with the difference in mass, leads to different energy transport properties for the ions and the electrons and gives rise to gyro-effects such as the Hall drift and the electron diamagnetic drift. To further simplify by neglecting the description of these effects and close the equations consistently, two approaches are proposed.

In the first approach, sufficiently high collisionality for both ions and electrons is invoked so that the particles find approximately the same difficulty in moving perpendicular to the field as in moving parallel to it. This condition is imposed on ions because electrons collide faster by a factor of $(m_i/m_e)^{1/2}$ and is

$$\tau_i \ll \sqrt{\frac{m_e}{m_i}} \tau, \quad (2.1)$$

where the τ_i is the collision (in terms of momentum exchange) time between ions and τ is the minimum MHD time scale of interest. This leads to the simplification of having single temperature $T_e \approx T_i$ and pressure $p_e \approx p_i$, since temperature equilibration takes place in time less than τ . Additionally, by requiring high ion-electron friction

$$\tau_{ei} \ll 1/|\Omega_e|, \quad (2.2)$$

where Ω_e is the electron cyclotron frequency, and that the scale of the gyro motion is small with respect to the MHD spatial scale L ($r_{Li} \ll L$) and fast with respect to the MHD time scale τ ($1/\Omega_i \ll \tau$), the Ohm's law is obtained in the form,

$$\mathbf{E} + \mathbf{u} \times \mathbf{B} = \eta \mathbf{J} \quad (2.3)$$

2.1 Basic properties of Alfvén waves

where η is a small scalar resistivity coming from friction between electrons and ions. The small but finite η is the only dissipative mechanism in this MHD model called resistive MHD. By taking the limit $\eta \rightarrow 0$ and imposing an even stronger upper limit on the ion Larmor radius,

$$\frac{r_{Li}}{L} \ll \sqrt{\beta} \ll 1, \quad (2.4)$$

where β is the ratio of thermal pressure p over magnetic pressure $B^2/2\mu_0$, the ideal MHD limit is obtained.

While the conditions of small ion gyro radius and high ion cyclotron frequency are easily satisfied in fusion plasmas, the high collisionality conditions are not satisfied at all, as the fusion plasmas of interest are practically collisionless, i.e the particles travel a relatively long way along the field line before they are scattered by a collision. Thus, collisionless and strongly magnetized plasmas are considered in the second approach for the closure the fluid equations [9]. This approach starts from the guiding-center equations of drift motion of a single particle and adopts the heuristic assumption that the motions of interest are incompressible, i.e. $\nabla \cdot \mathbf{u} = 0$. This leads to a very similar set of ideal MHD equations, as that of the collisional model.

Both models of collisional and collisionless ideal MHD make the same and successful predictions for the cross-field fluid-like behavior. However, the parallel dynamics are too fast for the ideal MHD model and they are treated inaccurately. It turns out that in both varieties of MHD the motion of the plasma parallel to magnetic field-lines is associated with the dynamics of sound waves, whereas the motion perpendicular to field-lines is associated with the dynamics of a pure MHD wave, the shear Alfvén wave. It is only the sound wave dynamics which are significantly modified when we move from a collisional to a collisionless plasma. It follows, therefore, that the ideal MHD equations remain a reasonable approximation in a collisionless plasma in situations where the dynamics of sound waves, parallel to the magnetic field, are unimportant compared to the dynamics of Alfvén waves, perpendicular to the field. This situation arises when $\beta \ll 1$, which is the case in a typical tokamak equilibrium, and in this regime, it is expected that the ideal MHD is able to capture at least part of the plasma Alfvénic dynamics.

2.1.2 Shear Alfvén waves and resonant mode conversion

The basic properties of the Alfvén waves can be recovered from the ideal MHD equations. A normal-mode approach is considered. The equations are linearized by considering a small perturbation onto a static equilibrium, as shown here for a component of the magnetic field

$$B(\mathbf{r}, t) = B_0(\mathbf{r}) + B_1(\mathbf{r})e^{i\omega t} , \quad (2.5)$$

where $B_1 \ll B_0$, and the fluid is assumed to be at rest in the equilibrium, i.e. $u_0 = 0$. A linear system of equations is then obtained in the form

$$-\omega^2 \boldsymbol{\xi} = \frac{1}{\rho_0} \mathbf{F}(\boldsymbol{\xi}) , \quad (2.6)$$

where the operator $\mathbf{F}(\boldsymbol{\xi})$ is a self-adjoint, Hermitian operator [12]. It follows that the eigenvalues ω^2 must be real, so either purely exponentially growing modes $-\omega^2 > 0$, or oscillatory waves, $-\omega^2 < 0$ are obtained.

For the simplest plasma geometry, i.e. when an infinite, homogeneous and stationary plasma slab is considered, two classes of waves arise

- the incompressible shear Alfvén wave (SAW), with the dispersion relation

$$\omega^2 = k_{\parallel}^2 v_A^2 , \quad (2.7)$$

where

$$v_A = \frac{B_0}{\sqrt{\mu_0 \rho_0}} \quad (2.8)$$

is the Alfvén speed.

- and the compressible Alfvén waves (CAWs), with the dispersion relation

$$\omega^2 = \frac{1}{2} k^2 (v_s^2 + v_A^2) \left[1 \pm \sqrt{1 - 4 \frac{k_{\parallel}^2}{k^2} \frac{v_A^2 v_s^2}{(v_A^2 + v_s^2)^2}} \right] , \quad (2.9)$$

where the sign $+$ corresponds to the fast wave and the sign $-$ to the slow wave and

$$v_s = \sqrt{\gamma p_0 / \rho_0} \quad (2.10)$$

is the adiabatic sound speed.

2.1 Basic properties of Alfvén waves

Both classes of waves are purely oscillatory with $\Im(\omega) = 0$ and stable. No instability is found because there is not a free energy source to drive one. However, in more physically interesting inhomogeneous magnetic geometries, the SAW branch is inherently a better candidate for instability than the CAW branch because it is incompressible. It can be formally shown [9] that, from the general stability point of view, the most unstable perturbations (such as the pressure-driven and current-driven modes) are incompressible (compressing the plasma requires relatively more energy) and as such, they are coupled to the SAW branch. In this thesis, only the effects that are associated to the SAW class are considered.

The dispersion relation (2.7) shows that no restriction is imposed on the spatial variation perpendicular to the field. However, in an inhomogeneous plasma, this is not the case. Specifically, if one considers inhomogeneity along the dimension that is perpendicular to the magnetic field, a singularity appears in the ideal MHD equations at the position x , where the equation (2.7) is satisfied locally, i.e. where $\omega = k_{\parallel} v_A(x)$. The relation (2.7) is now called the Alfvén resonance. Because of this singularity, the scale length of the solution, which is qualitatively similar to $2\pi/k_{\perp}$, tends to zero and thus becomes comparable to the ion gyroradius. At this point, the ideal MHD description breaks down and only with the help of a kinetic refinement to the model, can the physical mechanism hidden behind the singularity be clarified. It has been shown indeed that when the effects of finite ion gyroradius and finite electron inertia are taken into account, a mode conversion process takes place to the kinetic Alfvén wave (KAW) [13, 14] or to the surface quasi-electrostatic wave (SQEW) [15]. The KAW is a short-wavelength electrostatic wave that obeys the dispersion relation

$$\omega^2 = k_{\parallel}^2 v_A^2 \left(1 + k_{\perp}^2 \rho_i^2 \left(\frac{3}{4} + \frac{T_e}{T_i} \right) \right), \quad (2.11)$$

where ρ_i is the ion gyroradius, T_e and T_i are the temperatures of electrons and ions. Note that the KAW carries energy perpendicularly to magnetic field, since $\partial\omega/\partial k_{\perp} \neq 0$. At this point, we will not describe in more detail the kinetic processes and final damping mechanism of the KAW, as we want to restrict ourselves to the ideal MHD picture. More information is provided in the later Section 2.1.5.

When the expression (2.7) is drawn as a function of x , a bounded continuous spectrum is formed, referred to as Alfvén continuum. If the frequency of an

excited wave intersects the Alfvén continuum, the plasma absorbs energy from the wave and this is called resonant absorption or continuum damping. The continuum spectrum and the continuum mode structure in the context of the ideal MHD are shown schematically for a nonuniform cylinder plasma in figure 2.1a.

2.1.3 Gap modes

The SAW is modified significantly in the magnetic geometry of a tokamak because of the toroidal current, the $\sim 1/R$ dependence of the toroidal magnetic field and the shape of the nested flux surfaces, which is characterized by ellipticity and triangularity. The plasma beta can also modify the SAW spectrum.

Before considering the effect of the toroidal geometry on the SAW, it is useful to start from the cylindrical geometry, as it is the unfolded analog of a torus. In a nonuniform cylindrical plasma with an axial magnetic field, the ideal MHD spectrum is composed of continuum modes with $\omega = k_{\parallel} v_A(r)$, where r is the radial coordinate and k_{\parallel} is independent of r . In the absence of plasma current, this spectrum has no extrema away from the plasma axis (figure 2.1a). When an axial current flows along the cylinder, an azimuthal component with a radial dependence is added to the magnetic field and k_{\parallel} becomes a function of r . Then, the Alfvén continuum branch can have a minimum off axis. Below this minimum, weakly-damped radially-extended solutions exist [16, 17], as shown in figure 2.1b. These modes are called global Alfvén eigenmodes (GAEs).

When toroidicity is present, more extrema emerge in the Alfvén continuum structure. Specifically, frequency gaps are created in the Alfvén spectrum by the coupling of the poloidal harmonics [18]. This can be simply shown by considering the expression (2.7). The wavenumber k_{\parallel} is approximately given by

$$k_{\parallel} = \frac{1}{R} \left(n - \frac{m}{q(r)} \right), \quad (2.12)$$

where n and m are the toroidal and poloidal mode number from the Fourier decomposition

$$\xi(r, \theta, \phi) = \sum_{m,n} \xi_{m,n}(r) e^{i(n\phi - m\theta - \omega t)}, \quad (2.13)$$

and $q(r)$ is radially-dependent safety factor that is a measure of the magnetic field torsion[1]. At the points $r = r_0$ where counter-propagating poloidal harmonics m

2.1 Basic properties of Alfvén waves

and $m + 1$ have the same frequency,

$$-k_{\parallel,m}(r_0)v_A(r_0) = +k_{\parallel,m+1}(r_0)v_A(r_0) , \quad (2.14)$$

a frequency gap in the Alfvén continuum is created by the coupling of the m and $m + 1$ harmonics. The condition 2.14 requires that, for a given n , the position r_0 is uniquely determined by q and m and it is a rational- q surface with

$$q(r_0) = \frac{2m + 1}{2n} , \quad (2.15)$$

and the center of the gap frequency is

$$\omega_0 = \frac{v_A}{2qR} . \quad (2.16)$$

Note that ω_0 does not depend on n . The number of these gaps is approximately $n(q_a - q_0)$. It was found [19, 20] that discrete solutions exist in these gaps. These solutions have the form of standing waves with a finite radial extent. They were called shear toroidal Alfvén eigenmodes (TAEs). There are usually multiple gaps at all $q = (2m + 1)/(2n)$ and this creates modes that are composed of several pairs of coupled harmonics, e.g. $(m, m + 1)$, $(m + 1, m + 2)$, $(m + 2, m + 3)$ etc. The gaps may be aligned in their frequency $\omega_0(r)$, so that the modes do not experience continuum damping. In this case, ideal MHD suggests a zero damping, since no other dissipative mechanism acts on these modes. If the gaps are misaligned in their frequency $\omega_0(r)$, continuum damping can occur because of possible intersection of the mode frequency with the continuum.

Gaps and discrete modes that can exist therein can be created by other mechanisms and a list is available in reference [22]. To name a few examples, the coupling of the harmonics m and $m + 2$ leads to ellipticity Alfvén eigenmodes (EAEs) and negative shear s ($s = (r/q)(dq/dr)$) leads to the reverse-shear AEs (RSAEs) [23]. It is worth to note the prediction of kinetic TAEs (KTAEs) [24] which are formed by the coupling of counterpropagating KAWs at a frequency just above the TAE gap. The KTAEs were discovered experimentally in JET [25].

The breaking of the continuum and the existence of discrete weakly-damped modes is analogous to the gaps which appear in the energy spectrum of a single electron in a periodic potential lattice [18]. This is because the phenomenon is generic: the periodic variation of the quantity $k_{\parallel}v_A$ along a magnetic field line acts as an effective periodic mirror configuration that reflects backwards and forwards Alfvén waves [22].

2.1 Basic properties of Alfvén waves

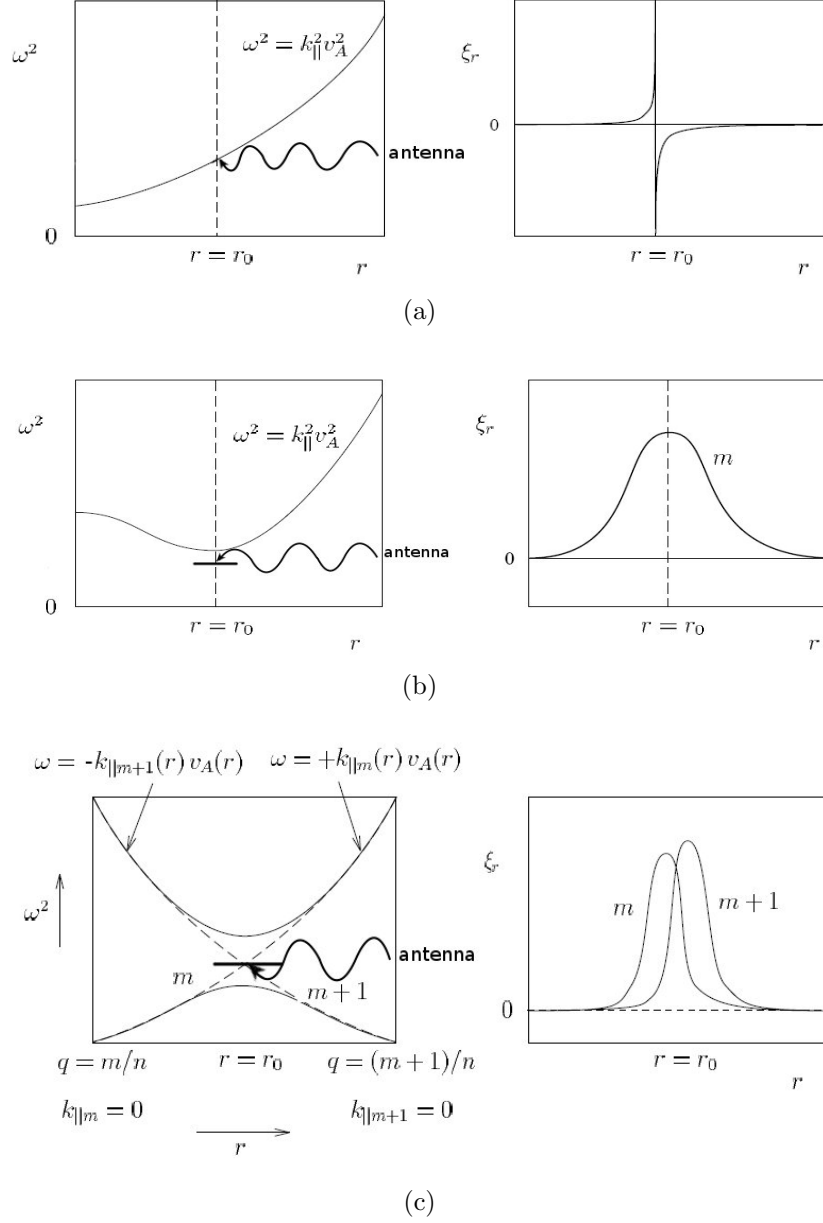


Figure 2.1: Qualitative diagrams of the frequency spectrum (left) and the mode structure (right) of ideal MHD Alfvén modes as function of the minor radius r . A localized antenna excites the wave at a frequency ω_0 . (a) Cylinder model without axial current and with a density profile that decreases monotonically towards the edge. Continuum mode with singularity at r_0 . (b) Cylinder model with an axial current. Discrete mode with one dominant poloidal harmonic with frequency just below the continuum extremum. (c) Toroidal model. Discrete mode with two dominant poloidal harmonics with a frequency in the gap created by the toroidal coupling. Adapted from ref. [21].

2.1.4 Drive mechanisms for AEs

The AEs can be destabilized by fast (or energetic) particles via resonant wave-particle interaction. The effect was predicted in the seventies [26] and it was observed experimentally for the first time in the early nineties [27].

The AE instability emerges as soon as the total linear drive of the fast particles γ_f exceeds the total damping of the mode γ_b that is due to the background plasma, i.e. when $\gamma_f > \gamma_b$. The drive can be cast in the general form [3]

$$\gamma_f = (\omega_{*f} - \omega_{AE}) F \left(\frac{v_f}{v_A} \right) G \left(\frac{\Delta_f}{\Delta_m} \right), \quad (2.17)$$

where ω_{*f} is the fast-particle diamagnetic drift frequency, ω_{AE} is the AE frequency, v_f is the fast-particle velocity, Δ_f is the orbit width of the fast particle and Δ_m is the radial width of the poloidal harmonic m of the resonant AE. F is a function that depends on the shape of the fast-ion distribution function. G is a function that depends on the ratio Δ_f/Δ_m . As seen in equation 2.17, the drive comes from the drift term ω_{*f} that represents the radial fast-ion pressure gradient, while the second term represents the Landau damping associated to the negative slope of the fast-particle distribution function with respect to energy, $\partial f/\partial \mathcal{E} < 0$.

The scaling of the fast-particle drive γ_f with n is of importance because it helps us to understand the n -range of the most unstable modes. The drive increases in the low- n range as the radial scale length of the mode Δ_m decreases and becomes comparable to the fast-particle pressure gradient. In this regime, ω_{*f} is proportional to k_\perp . As n increases further, the effects from the finite orbit width (FOW) and the finite Larmor radius (FLR) counterbalance the $\omega_{*f} \propto k_\perp$ tendency. Thus, the drive is maximized in the region where the radial scale length of the eigenmode is similar to the particle Larmor radius, i.e. $k_\perp \rho_f \sim 1$ [28]. At higher n , the orbit width becomes larger than Δ_m and the drive decreases as m^{-2} for $\Delta_f > r/m$ [29, 30]. In the previous description, a single-gap TAE is assumed so that n is directly proportional to m via the equation (2.15). This description agrees well with the experimental observations, which show that the modes that are most prone to destabilization tend to be those with intermediate n [31]. However, the observed n is slightly less than the expected n that comes from the scaling $k_\perp \rho_f \sim 1$ [31].

2.1.5 Damping mechanisms for AEs

Various mechanisms for the background plasma damping have been proposed. Their basic properties are described in the following.

2.1.5.1 Collisionless (Landau) damping

The available portion of the thermal ion tail that could damp an AE through the $v_{\parallel} = v_A$ resonance is negligibly small in typical tokamak plasmas. However, due to the magnetic field curvature, the resonance condition becomes $\omega - k_{\parallel}v_{\parallel} - \mathbf{k}_{\perp} \cdot \mathbf{v}_d = 0$, where \mathbf{v}_d is the magnetic drift velocity, and this allows the wave to resonate through the $v_{\parallel} = v_A/3$ resonance. Then, the damping rate from the ions γ_{iL} becomes proportional to $\exp(-\frac{1}{9\beta_i})$ [32, 33], where $\beta_i = 2T_i/m_i v_A^2$, and for high β_i , γ_{iL} can become important. Indeed, stability studies show that the ion Landau damping is strongly stabilizing in burning plasmas for low frequency AEs [34].

The direct electron Landau damping, i.e. when it is not the result of mode conversion to KAWs, depends on the relation between v_{Te} and v_A . This damping was considered in [35, 36] and it was concluded that it is small for typical tokamak parameters because $v_A \ll v_{Te}$. However, in reference [37], it was suggested that electron Landau damping can make an important contribution to the total damping of global AEs. The following expression was given for the local damping rate

$$\frac{\gamma_L}{\omega} = \frac{\sqrt{\pi}}{2} (k_{\perp} \hat{\rho}_i)^2 \frac{v_A}{v_{Te}} \exp\left(-\frac{v_A^2}{v_{Te}^2}\right), \quad (2.18)$$

where k_{\perp} is the projection of the wave vector onto the plane perpendicular to \mathbf{B}_0 , $\hat{\rho}_i$ is the ion Larmor radius evaluated with the electron temperature and $v_{Te} = \sqrt{2k_B T_e / m_e}$. As seen in the expression, the electron Landau damping can be important in the edge of the plasma where $v_A \approx v_{Te}$. In addition, it is enhanced by high k_{\perp} , i.e. by strong radial gradients of the electrical wavefield. Nonetheless, equation (2.18) does not take into account trapped particle effects and thus probably overestimates the damping rate in the collisionless limit [37].

2.1.5.2 Trapped electron collisional damping

In the plasma region where the condition $v_A \ll v_{Te}$ holds, the electrons that can interact with the mode via the resonance condition $v_{\parallel,e} \approx v_A$, satisfy necessarily

the condition $v_{\parallel,e} \ll v_{\perp,e}$. This means that these electrons are trapped. Electron Landau damping is not very effective for the trapped electrons. However, collisions between trapped electrons with passing electrons and ions can ‘detrap’ the trapped electrons into passing orbits leading to the damping of the mode. The damping is favored especially in the edge region due to the combination of relatively high density with low temperature. A first estimation of the effect on TAEs was reported in [36] and the effect of the parallel electric field, which is more important, was added in [28].

2.1.5.3 Mode conversion to kinetic Alfvén waves

Two mechanisms are intrinsically related to the mode conversion to localized Alfvén waves: the resonant absorption or continuum damping and the radiative damping.

Continuum damping occurs when the AE eigenfrequency intersects the Alfvén continuum and the radial AE eigenfunction has finite amplitude at the point of the intersection. As seen in section 2.1.2, non-ideal effects resolve the ideal MHD singularity and mode conversion to the KAW occurs. After their emergence, the KAWs can be damped very effectively due to their small wavelength by collisionless and collisional mechanisms on electrons and ions [14]. The Landau damping may be reduced in toroidal plasmas due to the trapped particles in the local mirror field.

The continuum damping depends critically on the mode structure and localization. Thus, in reference [38], it is found that it can make the most important contribution to the total damping for low and moderate n , as compared to electron Landau damping. In reference [39], it is found that it is significant for high n unless the shear is small or the gaps are radially aligned. Furthermore, it decreases with n , roughly as $n^{-3/2}$. The misalignment of the gaps is found to be important also in reference [37] for $n = 1 - 3$. Finite pressure effects enhance significantly the TAE continuum damping according to [40].

Radiative damping is a kinetic effect that was discovered theoretically in [24]. It is the result of the coupling between the TAE and the KAW in the gap region and depends on the proximity of the mode frequency to the continuum, as opposed to the direct intersection of the mode frequency with the continuum which is the case of the continuum damping. It is not linearly proportional to the dissipative

effect and for that reason it was called non-perturbative [41]. It was also called tunneling [41]. The radiative damping is controlled by the kinetic parameter λ

$$\lambda = 4 \frac{\rho_i}{r} \frac{ms}{\epsilon^{3/2}} \sqrt{\frac{3}{4} + \frac{T_e}{T_i}}, \quad (2.19)$$

where ρ_i is the ion Larmor radius, r is radial position of the gap, m is the poloidal harmonic, $\epsilon = 5r/2R$, T_e and T_i are the electron and ion temperatures. Radiative damping was reported to be one of the most important stabilizing mechanisms in a TAE stability study for DT TFTR experiments [42].

2.1.6 Summary

To summarize, ideal MHD predicts the existence of waves that propagate parallel to the magnetic field without compressing the plasma, called the shear Alfvén waves. In a tokamak configuration, these waves can form radially-extended standing-wave structures, called the Alfvén eigenmodes (AEs). Non-ideal effects change the picture of purely magnetohydrodynamic modes in two different aspects: the frequency of the AEs is affected only marginally, whereas the effect on the damping rate can be significant. Extensive theoretical calculations that take into account the non-ideal effects in large aspect ratio, low- β circular plasmas were presented in [41, 43].

2.2 AEs driven by fast ion populations

Typically, most of the experimental observations are made on unstable AEs, which, in present tokamak devices, can be routinely excited by fast ions created with ion-cyclotron resonance heating and neutral beam injection. Figure 2.2 shows the spectral signature of several TAEs driven unstable by ion cyclotron resonance heating (ICRH) recorded on a magnetic pick-up coil in a JET discharge. Unstable AE observations can provide the mode frequency in the laboratory frame, the toroidal mode number n and information on instability thresholds. Furthermore, in principle, one may also measure the spatial structure of the modes and estimations of growth and damping rates can be obtained by fitting the exponentially growing or decaying amplitude in the beginning or ending phase of the AE activity [44].

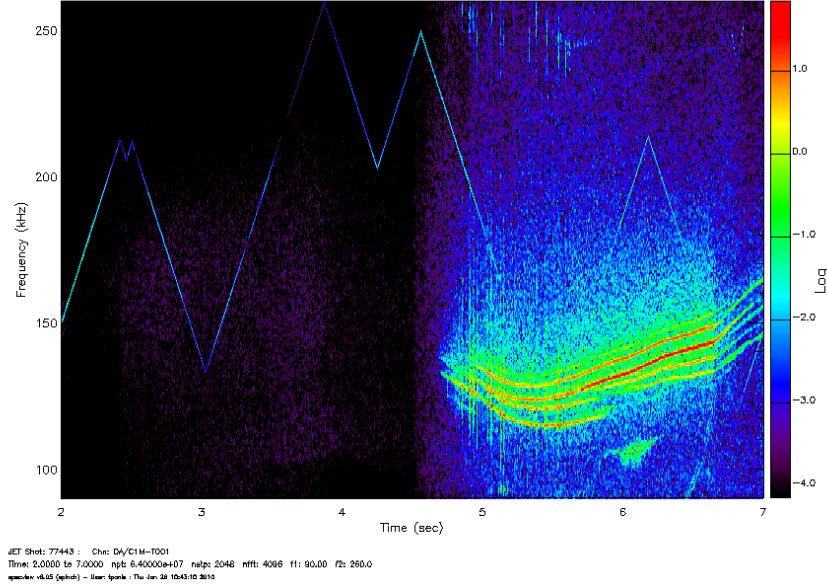


Figure 2.2: Unstable TAEs (appearing at $t = 4.8$ s) and the AE antenna signature as it scans in the TAE frequency range (triangular waveform).

These measurements and their comparison to the theory have helped to clarify several aspects of the most unstable AEs. For example, the observed frequencies depend as expected on the magnetic field, density and q . The most unstable modes tend to have intermediate n , $n \sim 3 - 10$ [31]. Their spatial structures have been found to be in good agreement with theory predictions [45, 46]. Weak central magnetic shear and elevated central q are favorable conditions for the AE excitation. In such conditions, TAEs were driven solely by alpha particles [47], as it had been predicted by the theory [42]. It has been a challenge for the theory to explain the observed instability thresholds in the early AE experiments, as these thresholds were higher by an order of magnitude than the initial predictions [48]. These initial observations led to extensive theoretical and experimental research on the mechanisms of the AE damping and drive.

In experiments with unstable AEs, studies are undertaken in order to investigate the fast ion transport due to the presence of AEs. Observations of fast-ion redistribution or losses that are coherent with AE activity have been reported in the largest tokamaks. For example, the reduction of γ -ray emission observed in JET plasmas indicated redistribution of ICRH-accelerated, highly energetic (> 5 MeV) hydrogen ions, induced by core TAEs [49]. In the DIII-D tokamak,

anomalous flattening of the fast-ion profile was observed in NBI-heated plasmas with Alfvén activity [50]. Thus, AEs can have a large effect on the fast-ion confinement, depending on the tokamak parameters and the plasma configuration.

AE observations up to 1997 are reviewed in [27]. More recent results on the AE physics, presented in the context of energetic particle physics, are presented in the review articles [2, 3]. Finally, the review article [51] reports on burning plasma studies on JET.

2.3 AEs driven by external antennas

As mentioned in the previous section, the initial experiments showed higher instability thresholds than those that were initially predicted, an observation that prompted for a separate investigation of the drive and damping terms. Exciting AEs with external antennas is a method that can address specifically these issues, as it allows to directly measure the total damping rate of a mode in the linear regime. If no drive is present from fast ions, the damping comes purely from the bulk plasma.

2.3.1 The method

The plasma in a vacuum vessel can be treated as a dielectric in a microwave cavity, and AEs as normal modes of the cavity. An external antenna can couple to the AEs. By sweeping the driving frequency on the antenna, the damping rate can be determined from the resonant mode width. The triangular waveform that is shown in figure 2.2 shows the spectral signature of the AE antenna at JET, scanning in the TAE frequency range. This is akin to the technique used to measure the quality factor Q of microwave cavities [52].

The method is based on considering the plasma as a linear time-invariant (LTI) system. The linearity is satisfied as the antenna perturbation is very small, $\delta B/B < 10^{-5}$, and it does not change the plasma equilibrium or produces any significant fast-ion transport. The time invariance is satisfied as the antenna perturbation varies much faster than the plasma conditions, which can be therefore considered stationary with respect to the perturbation.

The plasma response to the antenna frequency-sweeping perturbation can be measured at several positions, either inside the plasma with internal fluctuation

diagnostics, or at the plasma edge with magnetic sensors. By dividing the signal of the plasma response measured at the spatial coordinate x over the signal of the antenna excitation, e.g. an antenna current, the experimental transfer function $H_{\text{exp}}(\omega, x)$ is obtained as a function of frequency. Since the plasma is an LTI system, the experimental H_{exp} can be approximated by a rational function of two polynomials with real coefficients H_{fit} . After a partial fraction decomposition, the function (for a single-input single-output system) can be brought to the form

$$H_{\text{fit}}(\omega, x) = \frac{\sum_{m=0}^M b_m(x) s^m}{\sum_{k=0}^K a_k s^k} = \frac{1}{2} \sum_{k=1}^{K/2} \left(\frac{r_k(x)}{s - p_k} + \frac{r_k^*(x)}{s - p_k^*} \right) + \sum_{m=0}^{M-K} d_m(x) s^m, \quad (2.20)$$

where $s = i\omega$ and the perturbation is proportional to e^{st} . The pairs of conjugate poles p_k and p_k^* correspond to the plasma resonances and they do not depend on the spatial coordinate x . The number $K/2$ denotes the total number of resonances in the considered frequency scan. The coordinate x enters in the residues $r_k(x)$. The terms $d_m(x)$ corresponds to the direct, non-resonant part of the coupling between the antenna and the response measured at x . In the case where a single resonance with resonant frequency ω_0 and damping rate γ , with $\gamma^2 \ll \omega_0^2$, the transfer function can be written as follows

$$\frac{1}{2} \left(\frac{r}{s - p} + \frac{r}{s - p^*} \right) = \frac{1}{\omega_0} \frac{C \frac{s}{\omega_0} + D}{\left(\frac{s}{\omega_0} \right)^2 + \frac{2\gamma}{\omega_0} \frac{s}{\omega_0} + 1}, \quad (2.21)$$

where $p = -\gamma + i\omega_0$, $C = \Re(r)$ and $D = -\frac{\Re(rp^*)}{\omega_0}$. System identification methods [53, 54] can be used to fit the experimental data H_{exp} into H_{fit} .

If a plasma resonance of a single mode with toroidal number n is identified for a toroidal array of N magnetic pick-up coils, then the complex residues are solely a function of the toroidal angle of the coils, i.e. $r_\nu = r_\nu(\phi)$, $\nu = 1 \dots N$. From the vector r_ν , the toroidal mode number n is determined.

This method was used for the first AE damping measurements on JET [55]. Previously, external antennas had been used to measure the discrete Alfvén wave spectrum on the tokamak TCA [56].

2.3.2 Experimental results from JET and other machines

The external antennas that were used on JET initially (they were dismantled in the 2004/5 shutdown) were the saddle coils: these coils were extended along the

toroidal and poloidal directions and they could excite modes up to $|n| = 2$. The coils were receiving power from a 3 kW broadband power amplifier through coaxial cables, distribution and isolation transformers and an impedance matching circuit. Analog synchronous detection was employed for extracting the amplitude and the phase of the frequency component that is oscillating with the same frequency as the antenna signal (synchronous). This type of detection allowed very precise detection of the antenna frequency because of the narrow output bandwidth (< 200 Hz). The signals were digitized at a sampling rate of 1 kHz. A real-time algorithm and software was developed in order to track the plasma resonances, once they were detected. This allowed to perform in a repetitive manner small frequency sweeps around the central frequency of a plasma mode resonance, and thus track the mode frequency and its damping rate as function of the slowly evolving plasma parameters. More details about the experimental arrangement can be found in [4, 57].

With the saddle coils, the stability properties of the AEs of $|n| = 0 - 2$ were explored in detail. The measurements showed that the AE dampings span a large range of magnitude, $\gamma/\omega = 0.01 - 10\%$ and they are also sensitive to the plasma equilibrium profiles [55, 57]. Big radial variation of the factor $q(r)\sqrt{\rho(r)} \propto 1/f_{TAE}$ indicates gap misalignment and increased continuum damping [55]. The damping of low- n GAEs and TAEs were found to increase with increasing edge magnetic shear, elongation and triangularity [58]. The $n = 1$ TAEs were found to be more unstable for high values of the central safety factor q_0 [59]. A summary of the low- n linear AE stability studies can be found in [60]. Apart from investigating the AE stability, the excitation with external antennas can be used for obtaining local information of the bulk plasma parameters, the so-called active MHD spectroscopy [61, 62].

The low- n experimental results have been compared to the theory predictions. Good agreement was found with the gyrokinetic model of the code PENN [63, 64]. However, the specific damping mechanism that was found by PENN (mode conversion in the core) could not be confirmed by the gyrokinetic code LIGKA [65] or by the global reduced kinetic model developed in [66]. The model of NOVA-K yielded damping rates that were too small to account for the measured damping rates of $n = 1$ TAEs [67]. In another comparison, fluid models predicted damping rates 25 time less than those measured and a different scaling the effective

plasma mass $A_{\text{eff}} = \sum_i n_i A_i / \sum_i n_i$ from the one that was measured. Conversely, consistency in both scaling and magnitude was found with the gyrokinetic model PENN [64].

The apparent lack of agreement between different theory models, as well as between the theory and experiment raised concerns about the ability of the existing theory models to predict the AE stability in ITER and future reactors. Apart from benchmarking the codes between themselves and understand the implications of their approximations, more experimental data was needed for the higher n , ITER-relevant AEs. To address these issues, new antennas were installed on JET with a different geometry that is able to drive a high- n excitation spectrum [68].

Furthermore, AE antennas were installed on Alcator C-Mod [69] and MAST [60]. The results of Alcator C-Mod for $n = 4 - 14$ do not show a clear dependence on the edge magnetic shear, as that found for $n \leq 2$ on JET [70]. However, the results from C-Mod could be due to a changing n during the scan [70]. The damping rates measured on C-Mod were also compared to the predictions of the code NOVA-K and it was found that the damping rates were very sensitive on the q profile [71]. The initial results from the MAST show big damping rates in the range $\gamma/\omega \sim 4 - 20\%$. More results, especially as function of the plasma β , are expected in the future.

2.4 New AE antennas on JET

To overcome the low toroidal mode number limitation of the saddle coil, a new antenna system was designed and installed on JET, to replace the saddle coils and excite modes in the same Alfvén frequency range (20 – 500 kHz). The new antennas were connected to the existing excitation system.

Eight compact antennas are installed on the low-field-side wall below the $z = 0$ midplane at JET. They are divided into two groups of four antennas located at toroidally opposite positions Figures 2.3 shows a view of the designed antenna layout and figure 2.4a shows the one group of four antennas as installed in-vessel. Each antenna is a rectangular coil with 18 turns of 4mm diameter inconel 718 wire and measures 23 cm toroidally, 21 cm poloidally and 14 cm radially (figure 2.4b). Adjacent antennas are separated by 7.2 cm. The first turn

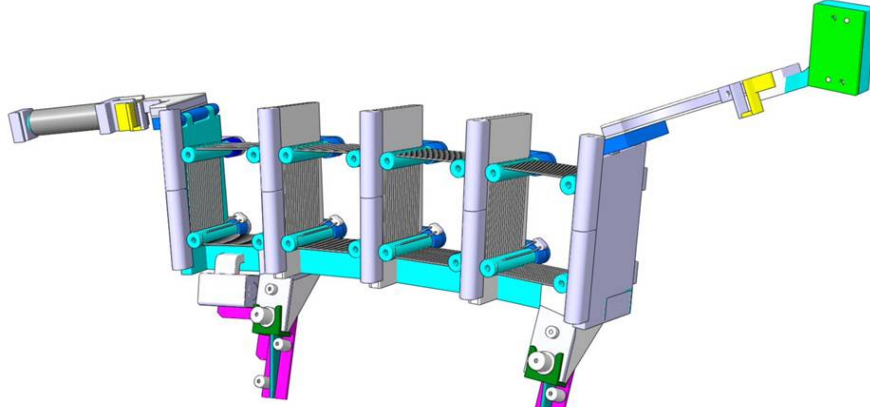


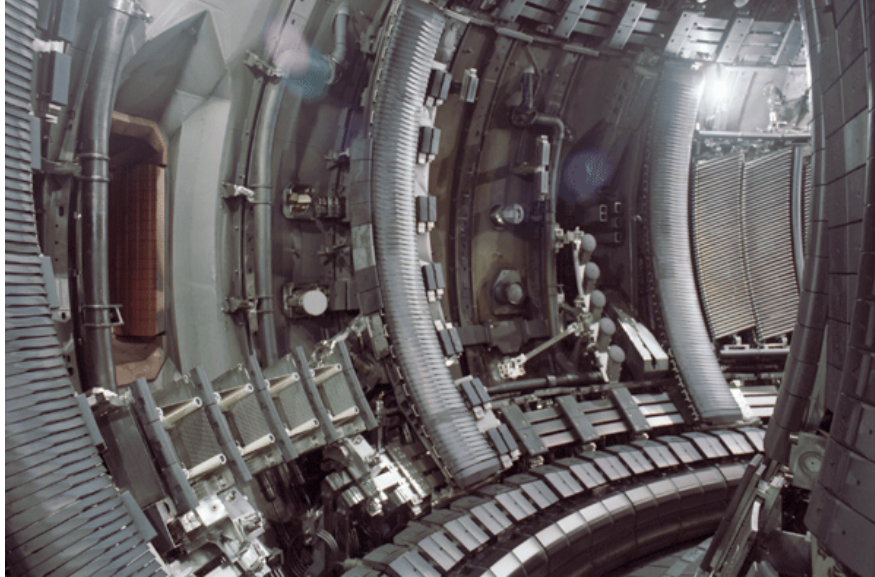
Figure 2.3: New JET AE antennas: engineering layout of one group of four coils.

that faces the plasma is approximately 4.5 cm behind the poloidal limiters. Each 4-antenna array is mounted on an inconel open frame in order to avoid a closed path for disruption-induced currents. The antenna mechanical design was shown to perform adequately for all identified disruption loading [72]. Initial calculations with the code LION[37] indicated that the antenna-plasma coupling for $n = 5$ TAEs is of the same order as that achieved with the saddle coils for $n = 2$ TAEs for the same JET equilibrium [60].

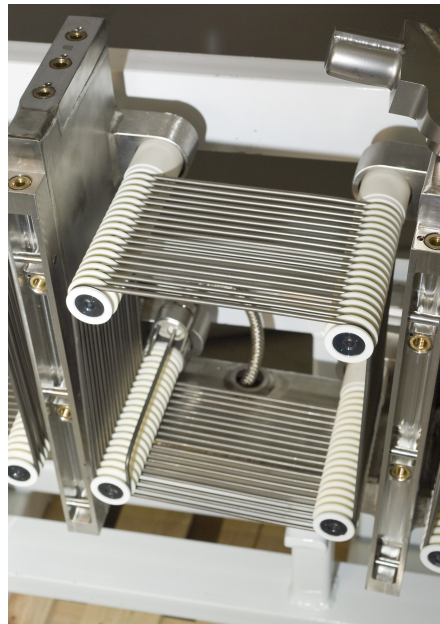
The new antennas have different electrical and electromagnetic-field characteristics from the saddle coils and this has an impact on the excitation and the adequate detection of the plasma response for the determination of the damping rate. Therefore, these characteristics are investigated in detail in this thesis. The electrical characteristics were measured and they are analyzed in Chapter 3 (Section 3.3.1). The field produced by the antennas in vacuum, as well as the associated driven n -spectrum, is calculated and analyzed in Chapter 4 (section 4.2).

2.5 Conclusions

The basic linear theory of the Alfvén eigenmodes is well developed. The drive and damping mechanisms that have been proposed by the theory are consistent with several aspects of the observations of unstable AEs, such as the most unstable n numbers. However, the lack of agreement in comparisons with the experimentally measured damping rates in specific plasma conditions suggests a gap in the



(a)



(b)

Figure 2.4: (a) View of one assembly of 4 antennas (left-bottom quadrant), as installed on the low-field-side wall of the JET vessel. (b) View of one antenna coil as mounted on its metallic frame.

understanding of the background plasma damping and raises concerns about predictions and extrapolations with respect to ITER and future reactors [3, 22, 60]. The studies with the new AE antennas on JET are expected to clarify these questions. The antennas should extend the experimental data that are obtained so far for low- n modes to the intermediate- n range, $n \sim 3 - 12$. This n range is excited by fast ions in JET and is expected to be more prone for destabilization in ITER.

Chapter 3

Electrical modeling of the AE exciter and matching unit design

3.1 Introduction

This chapter describes the technical aspects of the excitation side of the AE active diagnostic (AEAD), the so-called AE exciter. This study is motivated by the need to improve the antenna-plasma coupling by maximizing the antenna currents. To achieve this maximization in various frequency ranges, the design of matching units (MUs) was considered. Such a study necessitated the construction of an electrical model that would provide accurate predictions of the frequency response of the engineering quantities, i.e. the currents and the voltages measured at several points along the power transmission path.

Furthermore, the model helps to understand and solve the problems that were observed during the early operation of the diagnostic using 4 active antennas on the same octant. One problem was the amplifier failures when the system was configured to operate at a higher antenna current. Another issue was that the antenna currents were having big differences and strong variations in a specific frequency range around 200 kHz, were distorting the driven n -spectrum and misleading the real-time mode tracking into confusing the current variations with plasma modes.

This chapter is organized as follows. Section 3.2 provides a description of the exciter layout. In Section 3.3, the modeling of the building blocks of the exciter is described: these are the antennas, the transmission lines, the transformers

and the power amplifier. The Section finishes with the results obtained from the full model of the system and a discussion on their implications. Section 3.4 reports on the matching study and is divided in two parts: the first part describes the design while the second reports on the experimental results that have been obtained with the MUs that have been built. Finally, Section 3.5 summarizes the work presented in this chapter and its implications.

3.2 Layout of the AE exciter

The general layout of the AE excitation system (AE exciter), used to be during the saddle-coil experiments, has remained essentially the same for the new AE antennas. This is shown in detail in figure 3.1. In the following, the electrical path of the antenna signal from the function generator to the antennas is described.

A low-voltage sinusoidal signal is produced at the output of the function generator (figure 3.1, top). A stage of electronics is then used for protection (interlock trip module) and control (automatic gain control). The signal is amplified by a power amplifier at voltage and current levels of the order of 500 V and 10 A rms respectively. Following a coaxial cable of 19 m and the impedance matching unit (MU), the amplifier output signal can be split into 2, 4 or 8 antenna branches in the distribution unit (DU) (figure 3.1, middle). At the output of the DU, 8 isolation transformers are installed to provide galvanic isolation for the individual antenna circuits. The isolation unit (IU) is followed by safety isolator relays and then a series of transmission lines lead finally to the in-vessel antennas (figure 3.1, bottom). Measurement setups that are called link boxes (LBs), are installed just outside the torus vessel, next to the plasma transformer limb. These provide measurements of the antenna currents, the antenna voltages and the earth leakage currents. In the LBs, there are connections that allow the antennas to be grounded to the JET main earth ring. The part from the power amplifier to the IU primary side is grounded separately, to the earth of the J1H building.

The 8 antennas are divided physically in 2 assemblies of 4 antennas at toroidally opposite locations. The antennas are numbered proportionally to the toroidal angle, with antennas 1-4 being in octant 4 and antennas 5-8 being in octant 8.

Typical operation of the AE exciter involves current control of one of the antenna currents or the DU input current I_{tot} . This is implemented in the automatic

gain control (AGC) unit in a closed-loop scheme, where the difference between the feedback current and the reference value that is set by the operator is used to increase or decrease the amplifier input signal. This mechanism is necessary in order to keep the antenna currents as constant as possible during the frequency sweeping despite the amplitude variation of the circuit transfer functions.

3.3 Modeling

3.3.1 Antennas

Antenna modeling is divided in two parts: first, we deal with the modeling of individual antennas and then, we add the effects of inductive coupling due the proximity of antennas that are installed on the same frame.

3.3.1.1 Individual antennas

The electrical characteristics of the antennas were determined from impedance measurements, performed after mounting them on their metallic frame. These measurements (Fig. 3.2) show that the antennas have very similar electrical properties and they all follow basically the typical response of a simple parallel resonant circuit. For frequencies around the 2.4 MHz resonance, all the measured impedances exhibit a ‘wiggle’ which does not match the model accurately; the observed pattern suggests that this ‘wiggle’ should be attributed to the inductive coupling between the antennas installed on the same metallic frame. The same effect is observed in the antenna impedance measurements taken at the LBs.

The simplified electrical circuit used to model the antennas is shown in Fig. 3.3. The series resistance R_L of the antennas has a DC component, R_{DC} , and an AC component that is due to the skin effect. The following expression is used to estimate R_L [73]

$$R_L = R_{DC}(1 + C_s\sqrt{f}) , \quad (3.1)$$

where the coefficient is given by the formula $C_s = 0.1585\sqrt{\frac{\mu}{R_d}}$, f is the frequency in MHz, μ is the magnetic permeability of the conductor and R_d is the resistance to direct current for 1 cm of conductor in Ω . The R_{DC} is estimated by measuring the DC resistance at the LB and then subtracting the DC resistance due to the cables. The resulting value is of approximately 1.7 Ω is consistent with the value

3.3 Modeling

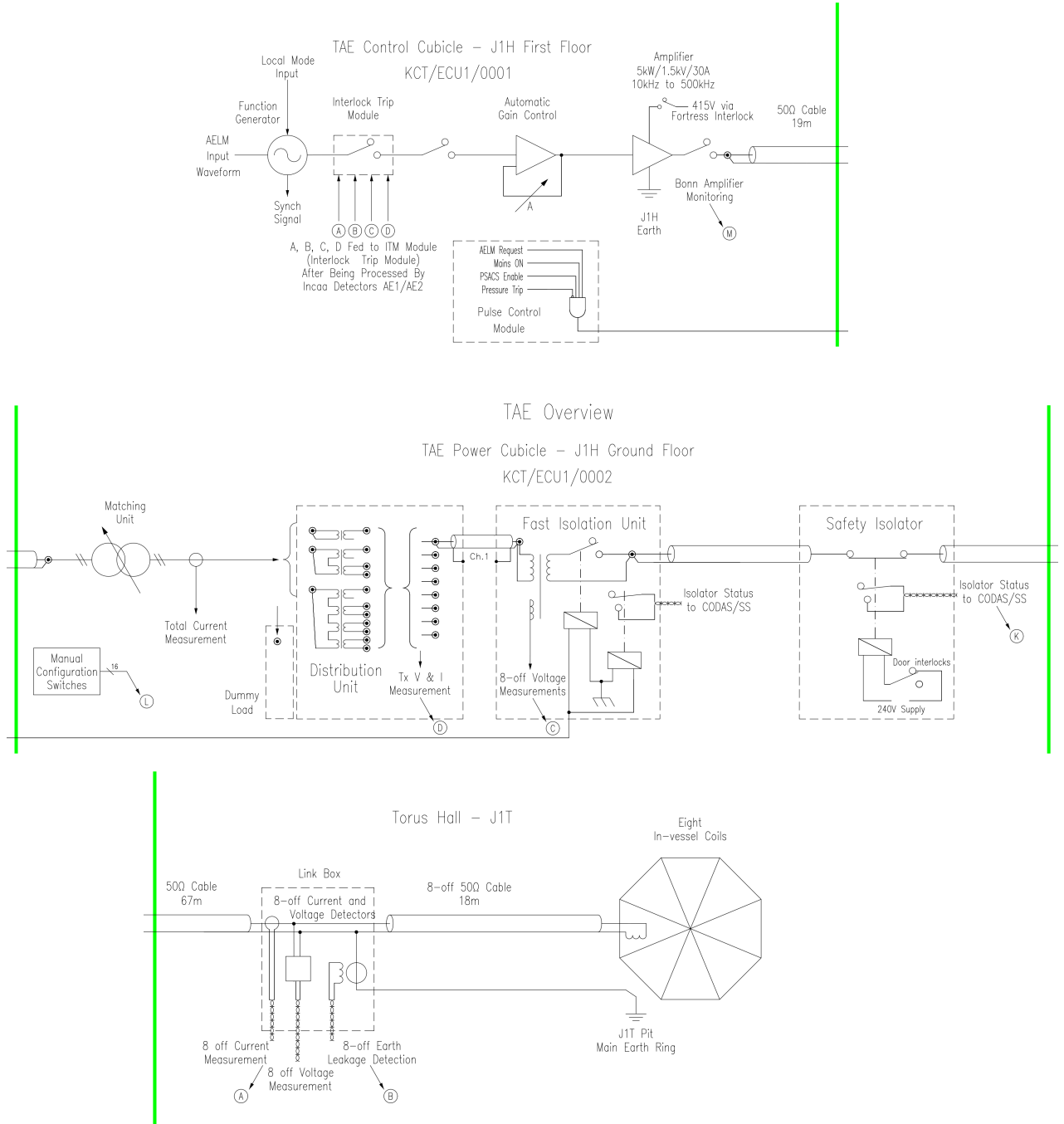


Figure 3.1: Layout of the AE exciter. *Top*– Function generator, electronics, power amplifier and coaxial cable. *Middle*– Matching unit, distribution and isolation transformers, safety isolator relays and coaxial cables. *Bottom*– Measurement point of antenna currents and voltages (link box) and transmission lines leading to the in-vessel antennas. (JET drawing office, CODAS: Y2/PCD1/4180.)

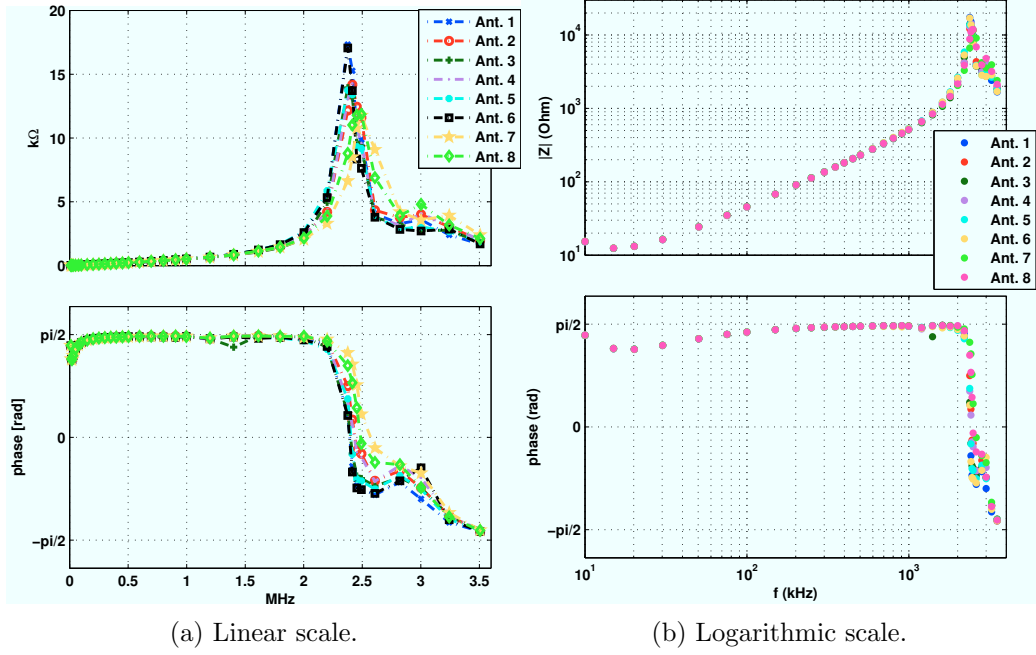


Figure 3.2: Impedance measurements of the antennas mounted-on-frame. A parallel resonance appears at $f \approx 2.4$ MHz.

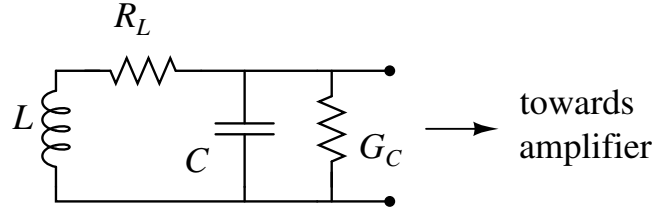


Figure 3.3: Antenna circuit model with series resistance R_L , series inductance L , shunt conductance G_C and shunt capacitance C .

obtained by the extrapolation of the antenna impedance to the zero frequency. A resistivity of the antenna wire (made from Inconel alloy 718, nickel chromium material) of $\rho = 1.245 \mu\Omega \cdot \text{m}$ leads to a value for C_s of $5.67 \text{ MHz}^{-1/2}$, resulting in $R = 7.37 \Omega$ at 1 MHz. Thus, the series resistance R_L of the antennas is very small compared to the total antenna impedance in the frequency range of interest ($20 < f < 500 \text{ kHz}$).

In order to estimate the rest of the model parameters, namely the inductance L , the capacitance C and shunt conductance G_C , least-square curve fitting was

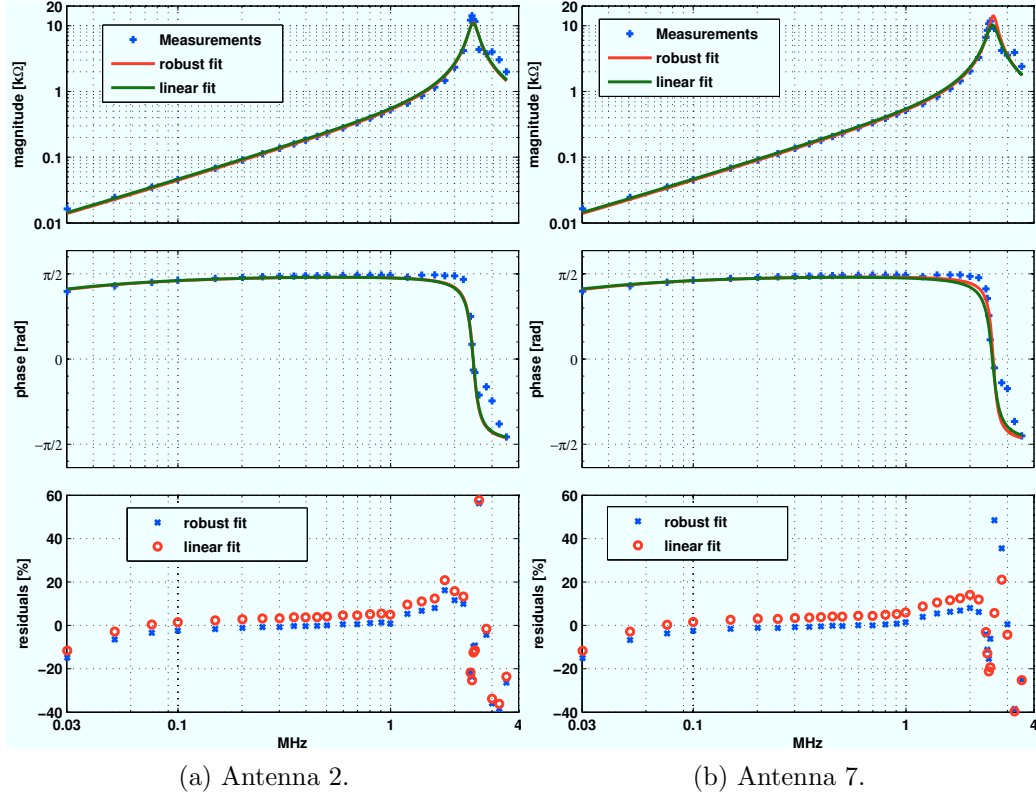


Figure 3.4: Comparisons between fits of the impedance measurements using the linear non-weighted method and the robust, weighted method for the antennas 2 and 7 (representative examples). Note that the robust method leads to less residual in the frequency range from 0.1 to 1 MHz, where the measured impedance is dominated by the inductance contribution, i.e. $Z \approx \omega L$.

applied on the impedance measurements. Typical examples of the impedance fits for antennas 2 and 7 are shown in the figure 3.4. Because of the particular pattern of the impedance measurements around the 2.4 MHz resonance, a linear non-weighted fit, i.e. a fit that considers all measurements of equal importance, results in a biased estimation, as observed from the pattern of positive residuals in the frequency range from 0.1 to 2 MHz in figure 3.4. This is because the non-weighted least-square fitting is sensitive to the outliers occurring around 2.4 MHz resonance. The fitting tends to overestimate the value of the inductance L , which is the most important parameter of the antenna model as it determines the antenna impedance in the frequency range of interest, 20-500 kHz.

In order to obtain a less biased estimation for the model parameters, a ro-

Antenna	δL (%)		δC (%)		δG (%)		RMSE	
	robust	linear	robust	linear	robust	linear	robust	linear
1	3.3	6.1	3.5	6.3	9.6	22	0.0361	0.0678
2	4.7	7.2	4.9	7.6	14.	22	0.0521	0.0794
3	4.9	7.0	5.4	7.5	14	23	0.0541	0.0778
4	5.0	8.0	5.3	8.6	16	24	0.0558	0.0886
5	3.4	6.0	3.6	6.4	13	21	0.0381	0.0668
6	3.5	6.6	3.9	6.9	9.3	28	0.0375	0.0737
7	3.4	6.0	3.7	6.5	17	23	0.0383	0.0655
8	3.6	6.3	3.9	6.8	12	22	0.0403	0.0695

Table 3.1: Results from fitting: uncertainty for fitted coefficients L , C and G based on 95% confidence bounds and root mean squared error.

bust least-square fitting method is considered, in which the measurements are weighted so that the outliers count less than the bulk of the measurements that fits well the model [74]. Better estimates of the model parameters, i.e. estimates with less uncertainty, are obtained with the robust fitting. This can be inferred by the smaller residuals in the range of 0.1-1 MHz (figure 3.4) and by the comparison between the measures of uncertainty for 95% confidence and the root mean squared error RMSE (or fit standard error) shown in the table 3.1. The RMSE is given by

$$\text{RMSE} = \sqrt{\frac{\sum_i^n w_i |y_i - \hat{y}_i|^2}{n - m}}, \quad (3.2)$$

where y_i are the measurements, \hat{y}_i is the model, n is the number of the measurements and m is the number of the model parameters (fitted coefficients). The tables 3.2 and 3.3 show the values of the fitted coefficients obtained for the two kinds of fitting.

The capacity of the model to fit reasonably well the input impedance measurements of the antennas agrees with the expectations: antennas are basically coils with a small stray capacitance. The stray capacitance is due to the distributed capacitance-to-frame and the inter-winding capacitance appearing between the turns.

Antenna	R (Ω)	L (μH)	C (pF)	G (μS)	f_0 (MHz)	Q
1	2.5	70.5	61.0	88.7	2.43	9.50
2	2.4	70.5	60.0	72.2	2.45	11.3
3	2.6	69.5	59.3	103	2.48	8.23
4	3.6	68.4	63.7	74.7	2.41	11.3
5	2.9	70.1	63.4	71.1	2.38	11.7
6	2.6	71.6	57.5	122	2.48	6.84
7	1.7	70.6	54.2	55.1	2.57	13.7
8	2.9	69.7	58.9	80	2.48	10.3

Table 3.2: Results from the robust fitting of the antenna impedance measurements: the parameters of the antenna circuit model.

Antenna	R (Ω)	L (μH)	C (pF)	G (μS)	f_0 (MHz)	Q
1	2.5	72.9	60.7	64.4	2.39	12.4
2	2.4	73.4	57.7	76.1	2.45	10.5
3	2.6	70.6	61.9	80.6	2.41	10.4
4	3.6	72.3	59.5	81.3	2.43	10.0
5	2.9	73.4	60.5	77.2	2.39	10.5
6	2.6	72.3	62.3	69.7	2.37	11.7
7	1.7	73.6	52.9	83.0	2.55	9.32
8	2.9	74.0	54.4	81.6	2.51	9.55

Table 3.3: Results from the linear fitting of the antenna impedance measurements: the parameters of the antenna circuit model.

3.3.1.2 Inductive coupling between antennas

The model introduced in the previous paragraph for individual antennas needs to be modified in case they are coupled to other antennas at small distance. This is the case for the antennas mounted together on the same frame.

In order to model the effect of inductive coupling, a current-controlled voltage source is added in series to the inductive branch of the model for individual antennas, as shown in figure 3.5. This voltage source represents the electromotive force (emf) produced by the flux linked through the antenna due to the currents flowing in nearby antennas. Assuming that neighboring antennas are linked through mutual inductances M_{nk} , the emf E_n produced on antenna n because of all the

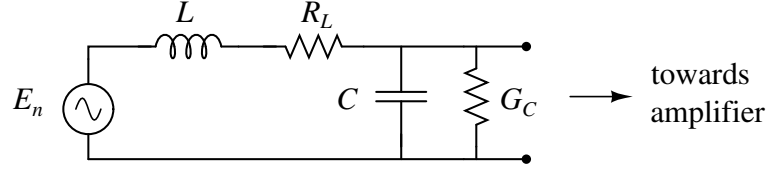


Figure 3.5: Antenna model that includes the effect of inductive coupling.

other neighboring antennas k is given by the expression

$$E_n = - \sum_{k \neq n} M_{nk} \frac{dI_k}{dt} \quad (3.3)$$

In the above expression, the minus sign is due to the relative position between the antenna windings: given the same convention for the current flow in the antenna windings, it is observed that an increasing current that flows in antenna k tends to create a current in the antenna n in the opposite direction (Lenz's law).

The self and mutual inductances have been estimated with a three-dimensional magnetostatics code [75] using a realistic geometry of the antennas (figure 3.6). The following values have been obtained:

$$L = 72.99 \mu\text{H} \quad (3.4)$$

$$M_{12} = 4.714 \mu\text{H} \quad (3.5)$$

$$M_{13} = 0.512 \mu\text{H} \quad (3.6)$$

$$M_{14} = 0.149 \mu\text{H} \quad (3.7)$$

We notice that the value of L falls well within the experimental uncertainty that is shown in the table 3.1. The coupling coefficients, defined as $k_{ij} = M_{ij} / \sqrt{L_i L_j}$, are 6.5% for the adjacent antennas and they drop at 0.7% and 0.2% for the antennas which are separated by a bigger gap.

3.3.2 Power transmission lines

The exciter implementation in JET is such that the system is divided physically in two parts. The first part, shown in the top and middle diagram of figure 3.1, is located in the area J1H. This part is connected via transmission lines to the antenna load located in the torus hall area, the so-called J1T. These transmission lines connect the safety isolator to the LBs and they are called the

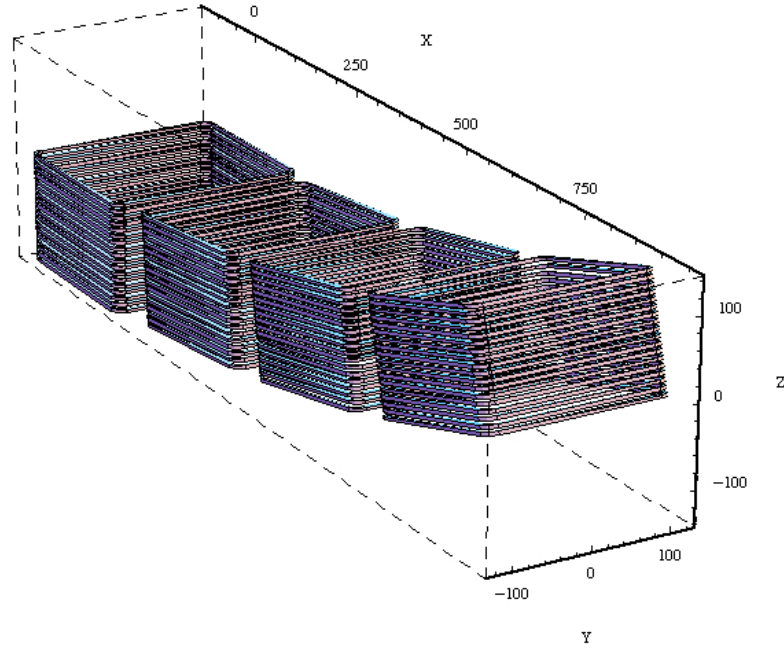


Figure 3.6: Geometry of the AE antennas mounted on the same frame used for the calculation of the self and mutual inductances. Each antenna winding has 18 turns separated by a 8 mm gap. The turns have dimensions 210x231 mm. The tilt between adjacent antennas (difference between toroidal angle) is taken to be 2.5° .

J1H-J1T transmission lines. The cables going from the LB output to the vessel feedthroughs are called the riser cables, followed by the in-vessel cables leading up to the antennas (figure 3.1, bottom). The ground cables connect the LBs to the main earth ring. Finally, the AMP-MU line connects the amplifier output to the matching unit input.

The power transmission cables of the AE exciter can be categorized in three classes with respect to their electrical specifications, as shown in the table 3.4. The lengths of the cables had not been measured precisely during installation. A first estimation was made from the installation drawings with an estimated $\pm 10\%$ accuracy. These lengths were initially used as free parameters in order to match the impedance measurements. However, the impedance measurements could be matched with different combinations of the cable lengths and therefore, a more

Cable type	R (mΩ/m)	L (μH/m)	C (pF/m)	location
LCF12-50J	1.75	0.19	76	AMP-MU, riser, ground
RG218/U	7.50	0.20	80	J1H-J1T
JET special in-vessel	12.3	0.35	120	in-vessel

Table 3.4: Technical specifications of the RF power transmission cables. R is the series resistance, L is the self-inductance and C is the shunt capacitance. All quantities are given in values per unit length.

accurate estimation of the cable length was needed.

The difficulties were overcome by estimating directly the cable lengths from impedance measurements on open-circuited cables. From the transmission-line theory (e.g., see reference [76]), one has that the input impedance of a lossless open-circuited transmission line is

$$Z_{in,oc} = -iZ_0 \cot(\omega\sqrt{LC}\ell), \quad (3.8)$$

where L is the self-inductance per unit length, C the shunt capacitance per unit length, ℓ is the length of the line, ω is the circular frequency and $Z_0 = \sqrt{L/C}$ is the characteristic impedance of the line. From this formula, it can be seen that one can determine the length of the line by measurement of the frequencies that correspond to the extrema of $Z_{in,oc}$. The impedance becomes infinite at frequencies

$$f_n^\infty = \frac{n}{2\sqrt{LC}\ell}, \quad n \in \mathbb{Z}, \quad (3.9)$$

while it goes to zero at frequencies

$$f_n^0 = \frac{n + \frac{1}{2}}{2\sqrt{LC}\ell}, \quad n \in \mathbb{Z} \quad (3.10)$$

These frequencies are equivalent to the $\lambda/2$ and $\lambda/4$ resonances, as they occur when the wavelength in the transmission line takes values of $n\lambda/2$ and $(2n+1)\lambda/4$ respectively. Thus, the length ℓ can be directly estimated by the measurement of these frequencies.

Figure 3.7 shows a typical impedance measurement of an open-circuited cable. The expected pattern of the $\lambda/2$ and $\lambda/4$ resonances is clear. However, it is noticed that the resonances are not equally-spaced as one would expect from the previous formulas. In particular, the frequency difference between the $\lambda/2$ and the

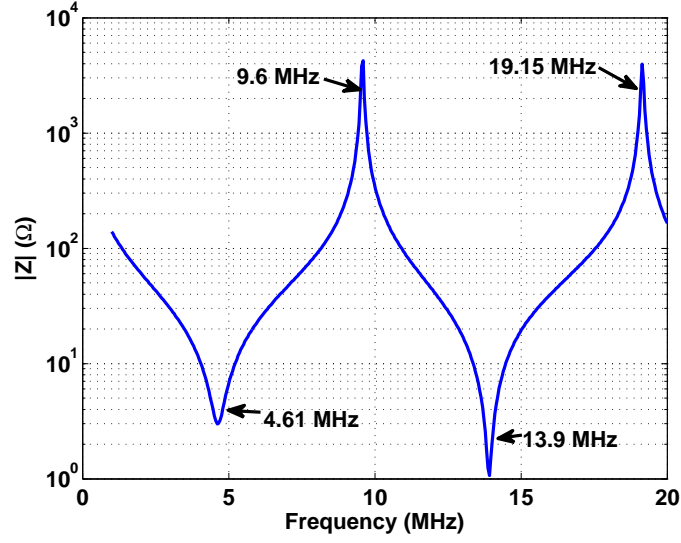


Figure 3.7: Measured impedance of the open-circuited riser cable of the antenna 1.

$\lambda/4$ resonances is 4.79 MHz, while the one between the $3\lambda/4$ and $\lambda/2$ resonances is 4.22 MHz. This difference is due to the fact that the measurement is not perfect. For an open-circuited cable and for the range of frequencies that is considered, the addition of an inductance in series results in downshifting the $(2n + 1)\frac{\lambda}{4}$ resonances (zero impedance) and leaving intact the $\frac{n\lambda}{2}$ resonances (figure 3.8). On the other hand, the addition of a shunt capacitance results in downshifting the $(2n + 1)\frac{\lambda}{4}$ resonances (zero impedance) and leaving intact the $\frac{n\lambda}{2}$ resonances. The downshifting of the resonances increases with frequency. Thus, by taking into account a very small stray inductance which can be due to an imperfect calibration of the measurement, one finds a perfect agreement between model and measurement for a unique value of cable length, as shown in figure 3.9.

For the in-vessel cables, it was not possible to have direct impedance measurements, as done for the J1H-J1T and riser cables. An estimation of the in-vessel cable lengths has been made indirectly. A model for the sub-system LB-antennas is constructed using the antenna representation and the measured riser cable length. The length of the in-vessel cable length is a free parameter that is used to match the antenna impedance measured at the LB. This comparison is shown in figure 3.10. The double or multiple humps that appear in the measured impedance at the resonant frequency are due to the inductive coupling between the antennas

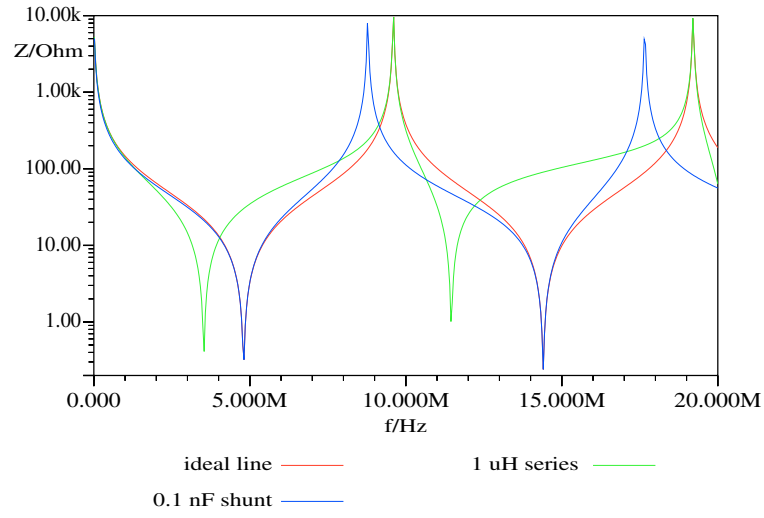


Figure 3.8: Effect of stray elements on the measured impedance of an unterminated riser cable. When a series inductance of $1\ \mu\text{H}$ is added, the series resonances f_n^0 downshift in frequency. When a shunt capacitance of $1\ \text{nF}$ is added, the parallel resonances f_n^∞ downshift in frequency.

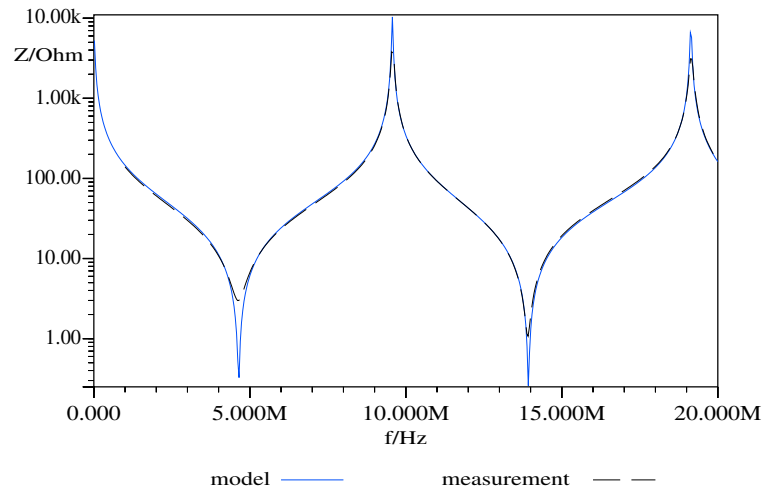


Figure 3.9: Comparison between the measured impedance of antenna 1 and the input impedance of an open-circuited, 13.74 m riser cable model with the addition of a series inductance of $80\ \text{nH}$.

Antenna	J1H-J1T	Riser	In-vessel
1	67.8	13.7	6.2
2	68.5	13.8	6.2
3	66.3	13.4	6.7
4	68.3	13.7	6.7
5	68.3	-	-
6	67.4	-	-
7	67.8	-	-
8	67.5	-	-

Table 3.5: Cable lengths in m estimated from impedance measurements. For the antennas 5-8 (octant 8), there are no available impedance measurements of the riser cables. They are therefore assumed to be similar to the ones of antennas 1-4.

and are sensitive to the change of the parasitic capacitance of the cables and the feedthrough connection. Furthermore, the humps and the resonance width depend on the magnitude of the mutual inductance between antennas. These factors result in a typical uncertainty of the estimated in-vessel cable lengths of about 5%.

The shunt conductance G of the cables (that represents the dielectric loss in the material between the two conductors) can be estimated from the extrema of the measured impedance, as the values of these extrema are controlled by G . It is found that a value around 10^{-5} S is consistent with the impedance measurements.

Table 3.5 summarizes the cable length estimations that were derived from the impedance measurements. It is observed that for the J1H-J1T and riser cables, the maximum difference between the cable lengths of the different antennas is less than 2% of the average total length, which is consistent with prior knowledge that the cables have similar lengths and with the impedance and voltage-current measurements. The length of the cable AMP-MU has been estimated from the difference in the measured antenna impedance between the amplifier output and the matching unit input. This line was found to be 19 m long.

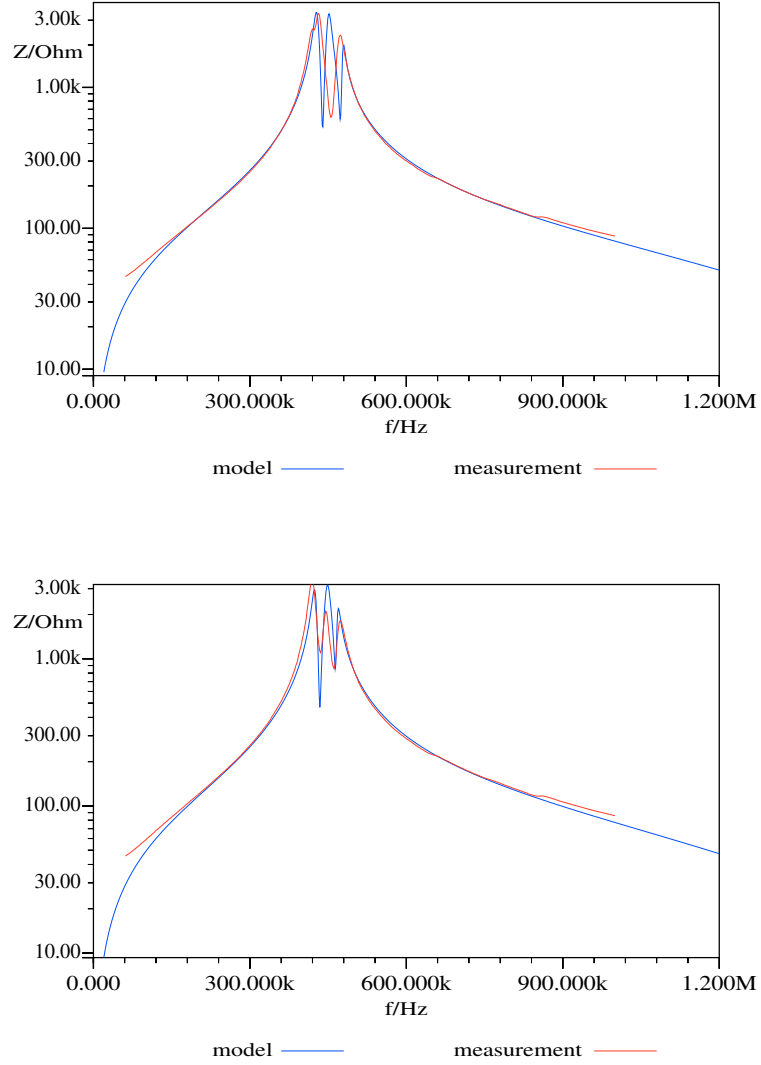


Figure 3.10: Antenna impedance measured at the LBs and modeling for antennas 1 (top) and 4 (bottom). The model predicts correctly 3 humps for antenna 4. However, in the measured impedance of antenna 1 in which the geometry is identical because of symmetry, only 2 humps appear. This is an indication of the big sensitivity of the resonance features to the exact circuit parameters.

3.3.3 Distribution and isolation transformers

The transformers that are installed in the distribution and isolation units of the system have been constructed with the same materials and have very similar configuration. The isolation unit (IU) has 8 separate isolation transformers with a winding turn ratio 10:10. The distribution unit (DU) has 3 sub-units with a circuit topology that is shown in figure 3.1. The sub-unit 1:1 consists of a transformer identical to those of the IU. The sub-unit 1:2 consists of 2 transformers with a winding turn ratio of 10:20. The 2 transformers have their primary windings connected in series and their secondary windings unconnected so that the sub-unit has in total 1 input and 2 outputs. The sub-unit 1:4 consists of 4 transformers with a winding turn ratio of 10:40 and has the same topology as the sub-unit 1:2 but with 4 outputs.

The differences in the measured antenna impedance between the IU output and the DU input prompted the construction of equivalent circuits for the distribution and isolation transformers in the frequency range of interest. The circuit shown in figure 3.11 was considered in order to capture the effects that are expected to make the transformer response deviate from the ideal one. The copper losses on the primary and secondary winding are represented by the resistances R_p and R_s . The inductances L_p and L_s account for the voltage drop that is due to flux leakage. Losses due to hysteresis and eddy current effects in the iron core are represented by the shunt conductance G_c . The magnetizing inductance L_m represents the excitation current that is needed to maintain the magnetic flux in the core due to its finite permeability. The shunt capacitance C represents a total equivalent capacitance that assembles the distributed capacitances of the two windings and the capacitance between them. The elements of this transformer model can be determined by specific measurements of the transformer frequency response. Such measurements were made with a network analyzer that is capable of measuring frequencies above 9 kHz.

The shunt elements G_c , L_m and C can be determined by measuring the impedance on one side of the transformer when the other side is open-circuit, the so-called open-circuit or no-load test. In this situation, the measured impedance is determined by the excitation branch because the winding impedance is comparatively negligible. In practice, because the admittance Y is a simpler function

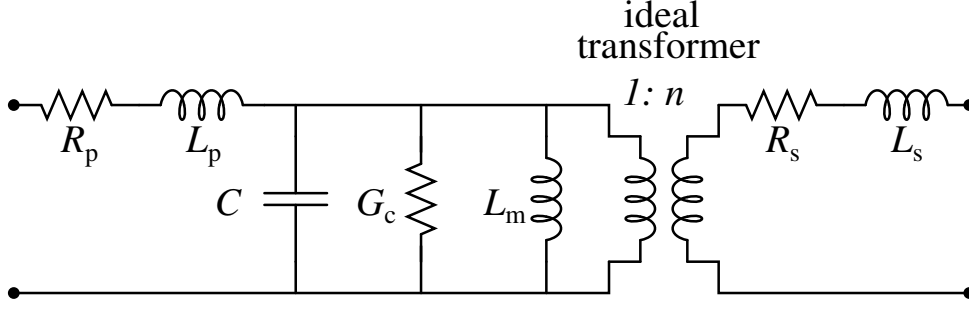


Figure 3.11: Circuit used to model the DU and IU transformers.

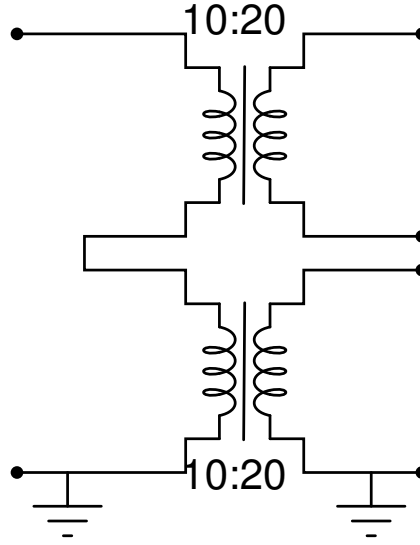


Figure 3.12: Circuit of the DU 1:2 showing the series connections of the primary windings.

of the model parameters in the frequency range of interest, the data are fitted to the following expression for Y

$$Y_{oc}(\omega) = G_c + i \frac{C}{\omega} (\omega^2 - \omega_0^2) , \quad (3.11)$$

where $\omega_0^2 L_m C = 1$. The imaginary part in the frequency range for which $\omega > 3\omega_0$ gives an estimation of C . Then, L_m is determined from the resonance frequency ω_0 , which is found from the fitting. It should be noted that, for the DUs 1:2 and 1:4, the measurements are taken on the primary side of the whole circuit (shown in figure 3.12 for the DU 1:2) and not on each transformer separately. With this configuration, the excitation branches are effectively connected in series, so the

Transformer	C (nF)	L_m (mH)	G_c (μ S)	R_p (Ω)	L_p (μ H)	R_s (Ω)	L_s (μ H)
IU7 10:10	0.367	5.789	$\lesssim 200$	1.543	6.405	1.543	6.405
IU8 10:10	0.381	5.643	$\lesssim 200$	1.625	6.775	1.625	6.775
DU 10:10	0.420	5.891	$\lesssim 200$	1.625	6.585	1.625	6.585
DU 10:20	1.253	6.041	$\lesssim 200$	1.625	6.585	4.922	23.66
DU 10:40	6.110	6.636	$\lesssim 200$	1.625	6.585	14.9	94.64

Table 3.6: Estimations of the transformer circuit parameters based on the impedance measurements of the open and short-circuit tests.

above expression for Y_{oc} has to be divided by a factor of 2 and 4, respectively.

The series elements can be determined by measuring the impedance of short-circuited transformer, the so-called short-circuit test. Here, the measured impedance is determined by the series elements. One finds the following expression

$$Z_{sc}(\omega) = R_p + \frac{R_s}{n^2} + i\omega(L_p + \frac{L_s}{n^2}) , \quad (3.12)$$

for the impedance measured on the primary side. From the slope of the imaginary part as a function of frequency, estimations of the leakage inductances are obtained. The leakage inductances of the primary and secondary windings of the transformer 10:10 of the DU 1:1 and the IU are assumed to be equal, since the windings have the same number of turns. The same argument should hold for the leakage inductances of the 10:20 and the 10:40 primaries. This allows us to estimate the unknown leakage inductances of the 10:20 secondaries by performing a short-circuit test on the primary side of the DU 1:2 and subtracting the contribution from the primary side. It should be noted that the measured impedance on the primary side of the DU 1:2 (1:4) is twice (four times) the impedance of the individual transformer Z_{sc} .

The final estimations of the parameters of the 3 transformers according to the circuit 3.11 are shown in table 3.6. Figure 3.13 shows examples of the impedance measurements for the open-circuit tests and the fits according to the assumed model. The resonance ω_0 that is due to the magnetizing inductance and the shunt capacitance, is at 101 kHz for the 10:10 transformer and decreases at 25 kHz for the 10:40, mainly because of the increase in C . The capacitance increases as a result of the increase of the number of turns in the secondary winding,

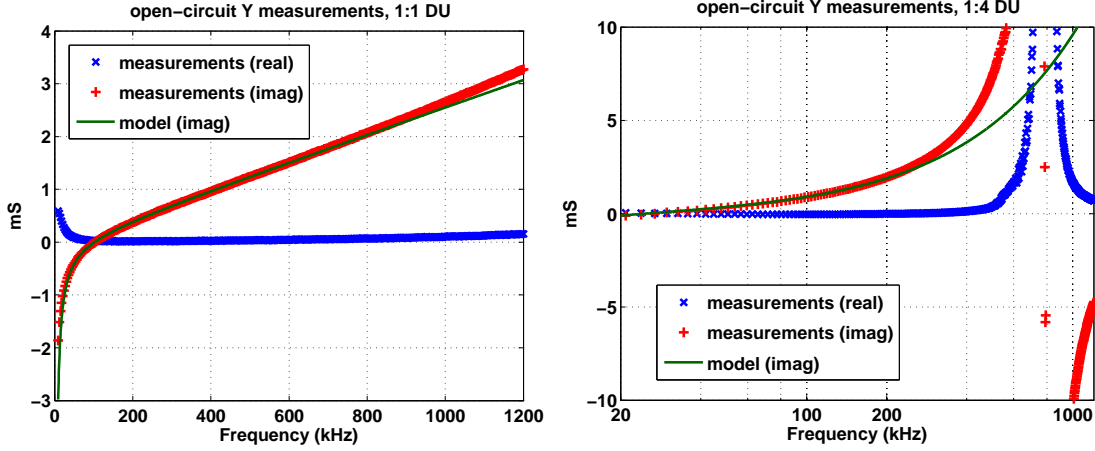


Figure 3.13: Measured admittances for the open-circuit tests on the 1:1 (left) and 1:4 (right) DU modules. The measurement is taken on the primary side. In the case of the 1:4 DU (right), the equation (3.11) applies only for frequencies below 200 kHz, which does not account for high order resonances such as the one appearing at ~ 790 kHz.

while the magnetizing inductance that depends on the iron core changes a little from one transformer to the other (table 3.6). The conductance G_c is so small that it is within the error of the measurement. From comparisons with current measurements, it is estimated that its value is similar to or less than $200 \mu S$. The increase of G_c as function of frequency is due to the increase of the hysteresis losses with frequency.

Figure 3.14 shows examples of the impedance measurements for the short-circuit tests and the fits according to the previously described model. The leakage inductance is found to increase, approximately in accordance with the n^2 increase of the number of turns in the secondary winding of the DU transformers. It was not possible to perform the short-circuit test of the DU 1:4 so the corresponding parameters were extracted by extrapolation based on the measured relation between DU 1:1 and DU 1:2 transformers. The resistance of the windings R_p and R_s increase with frequency because of the proximity effect which is not captured by the model. Estimates of these parameters are obtained by extrapolating a 2nd-order polynomial fit to the zero frequency.

It is interesting to note the appearance of the high-frequency resonances in the measured impedances, which further confirm the validity of the transformer

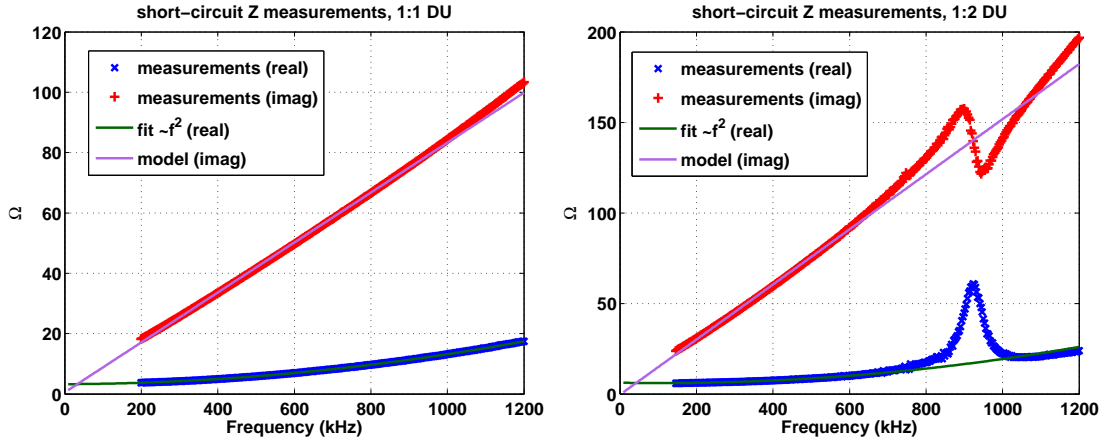


Figure 3.14: Impedance measurements of the short-circuit tests on the 1:1 (left) and 1:2 (right) DU modules. The measurement is taken on the primary side. In the case of the 1:2 DU (right), the equation (3.12) applies only for frequencies below 200 kHz, which does not account for high order resonances such as the one appearing at ~ 920 kHz.

models. The series resonance in the measured admittance of the DU 1:4 (figure 3.13, right) comes from the combination of L_p and C . The quantitative agreement with the model is noteworthy since the model predicts the resonance at $\frac{1}{2\pi\sqrt{L_p C}} = 793$ kHz. Another example of a high-frequency resonance is the parallel resonance in the measured impedance of the DU 1:2 (figure 3.14, right) which comes from the combination of L_s and C . Again, there is very good agreement with the model, which predicts the resonance at $\frac{1}{2\pi\sqrt{L_s C}} = 924$ kHz.

3.3.4 Power amplifier

The power amplifier was manufactured by BONN (Germany) and was later (1996) modified from class A to class AB. It consists of a solid state preamplifier, followed by 2 identical end-stage units of 30 vacuum tubes (tetrodes). The configuration is shown in figure 3.15a. The incoming signal is split in 2 with a 180 degree phase shift, and fed into each end stage. Thus, one end stage amplifies the positive (related to GND potential) part of the signal, while the other end stage amplifies the negative part. The two amplified parts are then recombined at the output. The splitting of the input signal and the recombination of the output signal are achieved by transformers.

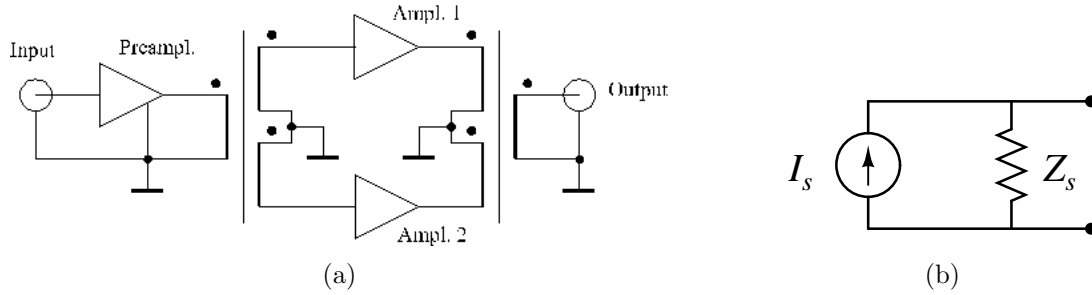


Figure 3.15: (a) Schematic diagram of the power amplifier showing the AB configuration. (b) Power amplifier model.

A simple model is used for the amplifier consisting of a controlled AC current source I_s and an output impedance Z_s in parallel (figure 3.15b). The current source is controlled in order to simulate the AGC operation. Thus, when the LB current is controlled, which is the typical setting of the plant configuration, the current I_s varies so that the LB current remains constant.

The parameter Z_s was initially estimated in accordance to the original specifications of the amplifier. The amplifier should be able to deliver a maximum power of 5 kW on a $Z_L = 50 \Omega$ load. Since maximum power is delivered when $Z_L = Z_s^*$, it is inferred that $Z_s = 50 \Omega$. The current that is delivered onto the load is $\sqrt{P/\text{Re}(Z_L)} = 10$ A rms and $I_s = 20$ A rms. This value is also assumed to be the maximum deliverable current, i.e. $I_{s,max} = 20$ A rms. The amplifier is subject also to a voltage constraint. Since the tubes are biased at an anode (or plate) voltage of 700 V, it was assumed that I_s is limited by a maximum peak voltage of ~ 700 V. In the following, the above set of values will be referred to as the nominal values of the amplifier model.

Nevertheless, detailed comparisons that combine the measurements of current and voltage across the power transmission line and the antenna load model which is benchmarked against the impedance measurements, suggest that the nominal model of the amplifier was not representative of the device during the recent experiments. In particular, the comparisons indicate that the output impedance Z_s is approximately 200Ω , instead of 50Ω . One relevant example of such an analysis is presented in the next subsection (3.3.5, figure 3.21) and further ones are provided in 3.4.2. It is shown that the 200Ω estimate leads to a very good agreement between model and measurements, while the 50Ω would result

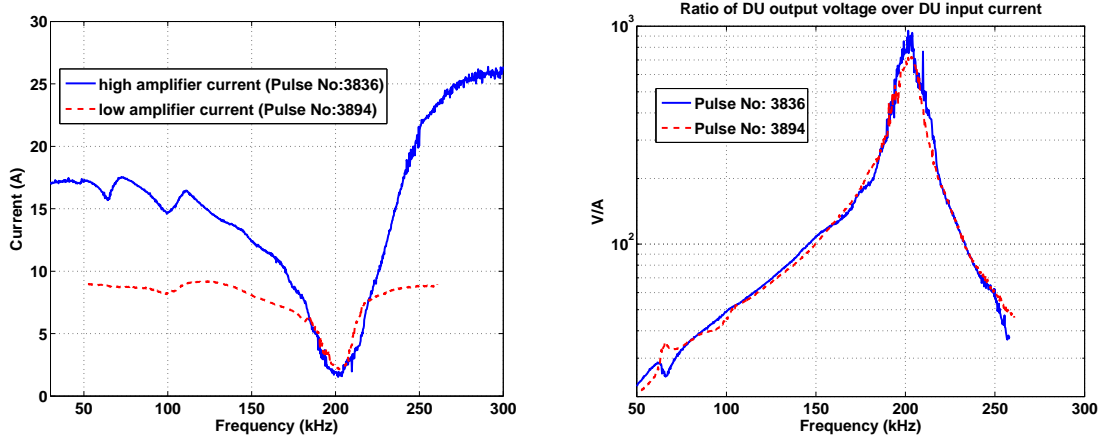


Figure 3.16: Comparison between 2 vacuum pulses with the same exciter configuration: active antennas 1, 4, 6 and 7, phasing + - -+ and DU 1:2. *Left:* Current I_{tot} measurements at the DU input. *Right:* Voltage measured at the DU output normalized on I_{tot} (note that there is no available voltage measurement at the DU input).

in a significant discrepancy.

Moreover, there is strong evidence that the maximum zero-load current I_s changed significantly during the experimental campaign. Consider, for example, the case shown in figure 3.16 which shows the current measured at the DU input I_{tot} in 2 pulses that have the same exciter configuration. A direct measurement of I_s is not available, but one can find evidence from the current I_{tot} . In the frequency range where the amplifier is pushed to deliver maximum current, i.e. all the frequencies apart from those around 200 kHz, there is a big difference between the two measurements of I_{tot} . In the high amplifier current case (pulse 3836), I_{tot} saturates at 25 A (peak), while in the low amplifier current case (pulse 3894), I_{tot} saturates at about 9 A, which represents a decrease of 64%. This behavior is not due to a change of the load impedance since the latter remains the same, as this can be deduced from the voltage measurement at the DU output (figure 3.16, left).

The change of the amplifier characteristics, verified for both Z_s and $I_{s,max}$, can be possible as a result of a change of the operating point of a subset of the tubes. This change can be due either to the fact that the tubes do not receive the nominal bias grid voltages or to the presence of several faulty tubes. It was

difficult to identify the exact reason for the change in the amplifier characteristics because the possibility of performing high-voltage tests on the amplifier in JET is very limited due to safety restrictions.

3.3.5 Complete model of the AE exciter

Using the components described in the previous subsections, a full electrical model of the exciter system has been constructed. It has been implemented in a evaluation version of the software PSpice. One particular instance of the model, for 4 active antennas located in the same octant and using the DU 1:4, is shown in figure 3.17.

The impedance measurements that are shown in figure 3.18 (left) have been taken at various points along the power transmission path and for various exciter configurations. These measurements show the typical downshifting of the resonances as the impedance is measured further away from the antennas and closer to the amplifier. They also show the difference between the one-antenna impedance (i.e. when only one antenna is connected) and the four-antenna impedance (i.e. when only four antennas are connected), as well as the effect from the inductive coupling between the closely-spaced antennas, (figure 3.18, right). These measurements were used to fix certain parameters, such as the in-vessel cable lengths (described in subsection 3.3.2), and to benchmark the electrical model.

A very good agreement between the model and all the impedance measurements has been obtained. An illustrative example for the impedance measured at the DU input is shown in figure 3.19. All 4 resonances in the frequency range until 1.2 MHz are reproduced within 1% of the measured value. The impedance amplitude is also in very good agreement. It is observed that the impedance varies from 10 to 700 Ω in the frequency range 30-500 kHz, being thus very different from the nominal value of 50 Ω . Finally, the model captures the effect of the inductive coupling between the antennas, which manifests itself with a small frequency shift of 14 kHz of the resonances at 200 and 250 kHz when the antenna phasing changes.

The amplitude deviation between model and measurement that is observed at the series resonance at 1.1 MHz is due to the fact that the parallel resistive components in the model have their low-frequency values, whereas, in reality, they change with the square of frequency because of the proximity effect, as seen in

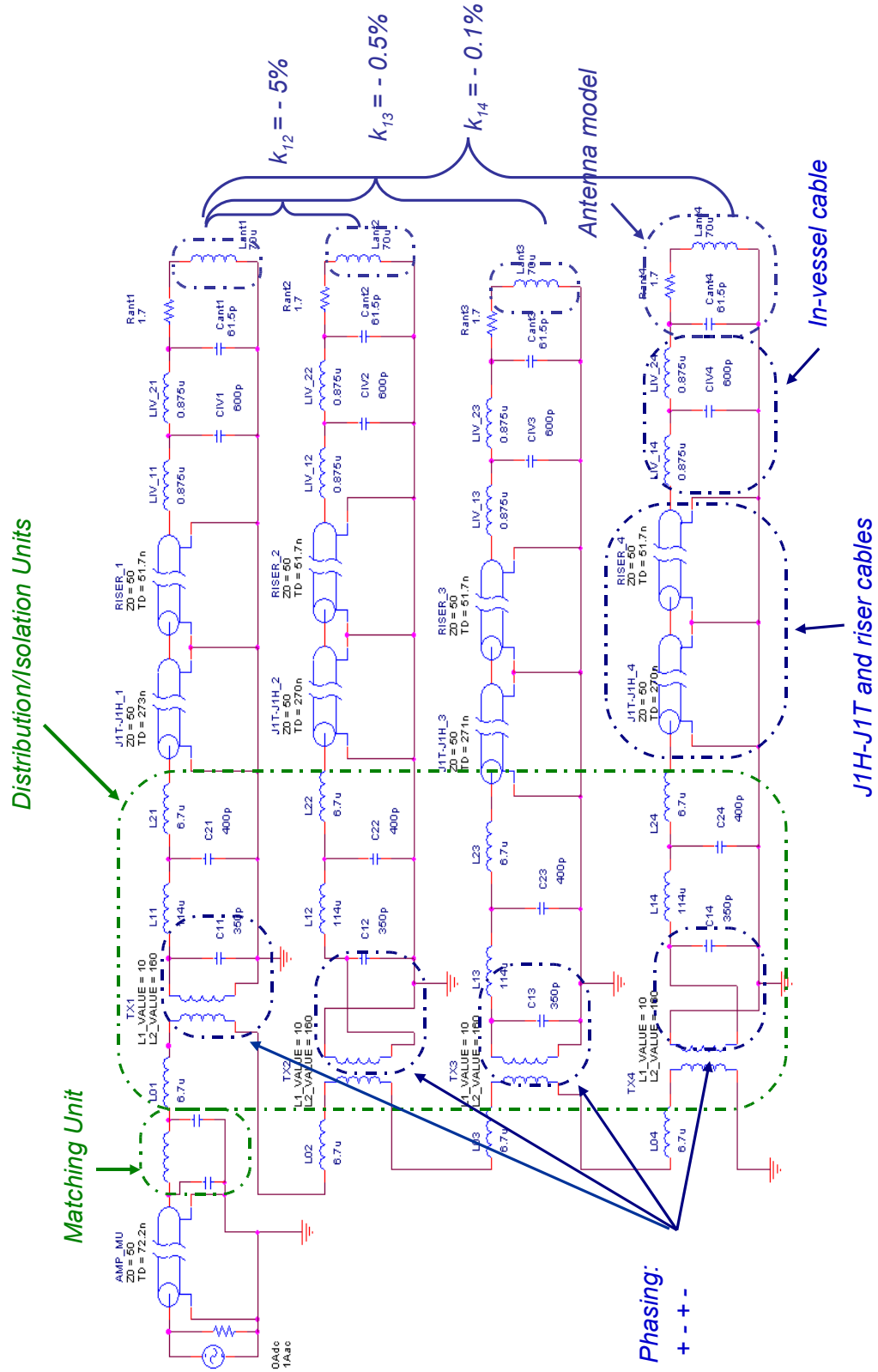


Figure 3.17: Model implementation in PSpice for 4 antennas in one octant using the DU 1:4.

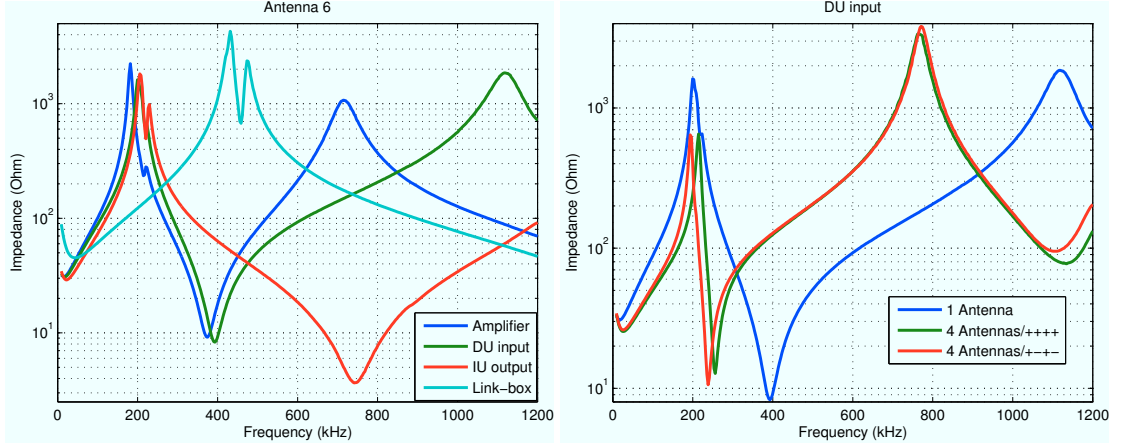


Figure 3.18: Various impedance measurements. Left– Comparison of one-antenna impedance as function of the distance from the antenna. Right– Difference between one antenna and four antennas and between different antenna phasings (four antennas in octant 8).

the transformer measurements in subsection 3.3.3. In order to model this effect, one would need to add several components in the PSpice model exceeding the maximum number of elements that is allowed by the software (it is an evaluation version). Furthermore, this effect is not important in the frequency range of interest.

An important transfer function of the exciter is the current gain

$$G_{lb} = \frac{I_{lb}}{I_{tot}} , \quad (3.13)$$

which defines how much of the current is measured at the LB, I_{lb} , for a given current measured at the DU input, I_{tot} . For a configuration of 4 active antennas and using the DU 1:4 module, and in the absence of resonances, this ratio is 1/4 for each antenna. Because of the impedance characteristics of the exciter, G_{lb} becomes strongly dependent on frequency, as shown in the figure 3.20. The current gain has a maximum at ~ 200 kHz, which corresponds to a pole in $G(\omega)$ and a minimum at ~ 450 kHz, which corresponds to a zero in $G(\omega)$. It tends to 1/4 at low frequencies. The current gain spans a range of values that vary by almost 3 orders of magnitude, from ~ 0.01 to 8.

The frequency characteristics of the currents and voltages during operation in a real pulse are reproduced by using the exciter model that is constructed so far

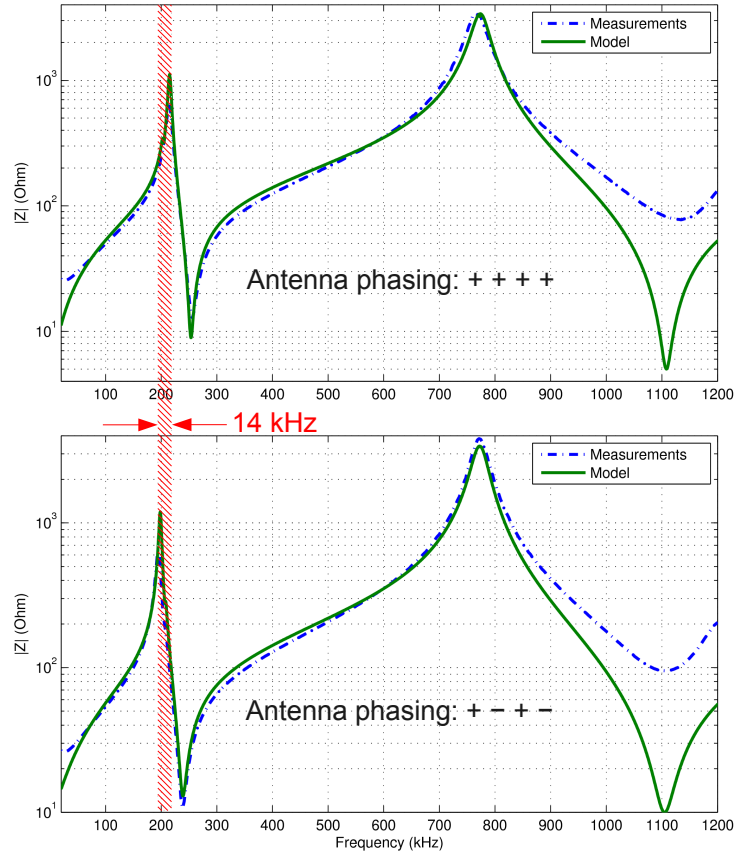


Figure 3.19: Effect of the antenna phasing on the antenna impedance. The antenna impedance is measured at DU input for a configuration with four active antennas located in octant 8 and the use of the DU 1:4. Comparison between model and measurements for 2 different antenna phasings.

and adding to it the current control loop AGC (automatic gain control) and the voltage and current limits of the amplifier. This is done by modifying the current source of the amplifier model shown in 3.15b, so that it depends on the desired value of the controlled current (e.g. I_{lb} of antenna 7) and on the amplifier limits. The results for a typical exciter configuration are shown in figure 3.21. Figure 3.21a shows a very good agreement between modeling and measurements when the amplifier output impedance Z_s is 200 Ω . Conversely, if it is assumed that Z_s is 50 Ω , the disagreement is significant, as shown in 3.21b. Note that a very good agreement between model and measurements on the system transfer functions that *do not* depend on the amplifier characteristics is obtained, and this is shown

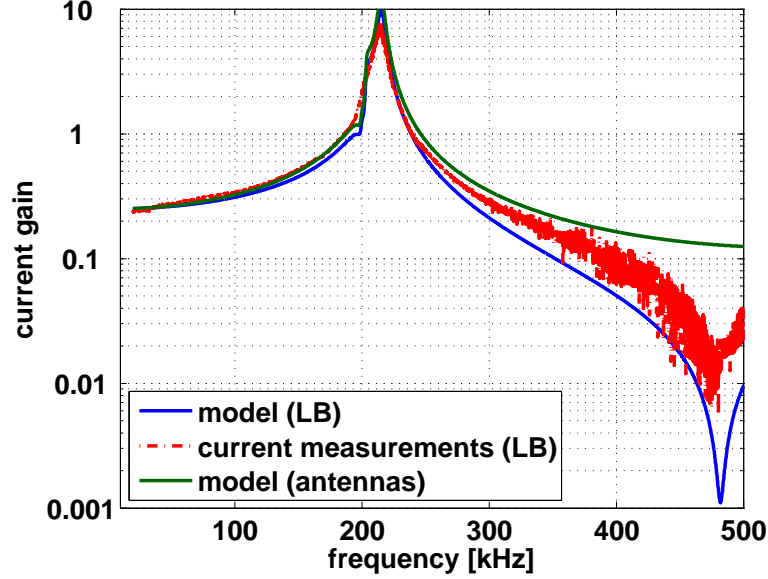


Figure 3.20: Amplitude of the current gain at the LB and at the antennas (model), defined in equation (3.13). The quality factor of the resonance at 470 kHz is slightly higher in the model than in the measurement. This is due to the inability to add more series resistive parts in the PSpice model because of the limitations of the demo version. Exciter configuration: the active antennas are the 5, 6, 7 and 8 and their phasing is + + + + (pulse No: 3356).

in figure 3.22 for the current gains I_{lb}/I_{tot} of the four active antennas.

The inductive coupling between the closely-spaced antennas can have an important effect on the antenna current gains $G(\omega)$. This is shown in figure 3.23a for a specific exciter configuration: it is observed that the antenna currents vary with respect to each other in a frequency range of about 20 kHz around the 200 kHz resonance. The deviation that comes from the spatial arrangement of the antennas can be readily observed between the inner (6, 7) and the outer (5, 8) antennas and it is especially clear in the phases of G_{lb} . This effect is captured by the model. Additionally, one can observe a deviation in the amplitude of G_{lb} between antennas 6 and 7, i.e. on antennas with the same spatial position relative to the others. This deviation is due to the fact that a few parameters of the antenna transmission line such as the in-vessel lengths, the parasitic shunt capacitances (e.g. in the feedthrough) and the shunt conductances of the antennas are not exactly the same for all the antennas. Because of the uncertainty in

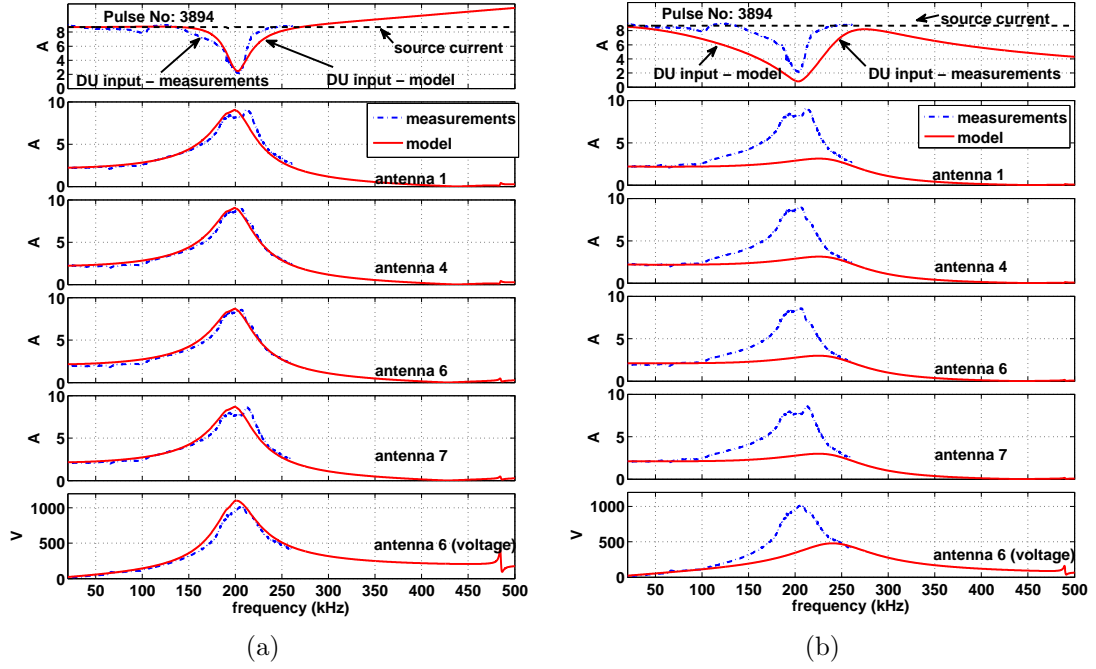


Figure 3.21: Exciter configuration: active antennas 1, 4, 6 and 7, phasing $+- - +$ and DU 1:2. Comparison between modeling and measurements. (a) Modeling with amplifier output impedance $Z_s = 200 \Omega$. (b) Modeling with amplifier output impedance $Z_s = 50 \Omega$.

these parameters, the model cannot capture sufficiently well this behavior. The extreme sensitivity of the transfer functions to these parameters in the resonance region amplifies the effect observed in the amplitude of G_{lb} , while in the rest of the frequency range the uncertainty on these parameters is negligible.

The effect of the perturbed system transfer functions can be directly observed in the current measurements obtained in the actual experimental conditions. An example is shown in figure 3.23b. In this pulse the AGC is set to control, i.e. to keep constant, the antenna 7 current (measured at the LB). Indeed, in the range from 100 to 240 kHz, the amplifier current is varying in such a way that the current of antenna 7 is approximately constant. The antenna coupling effect on the currents stands out in the frequencies around 200 kHz. Following the symmetry of the antenna spatial arrangement, the currents of the outer antennas 5 and 8 manifest a strong variation and a peaking at 210 kHz. This behavior is captured by the model reasonably well. As explained in the previous paragraph,

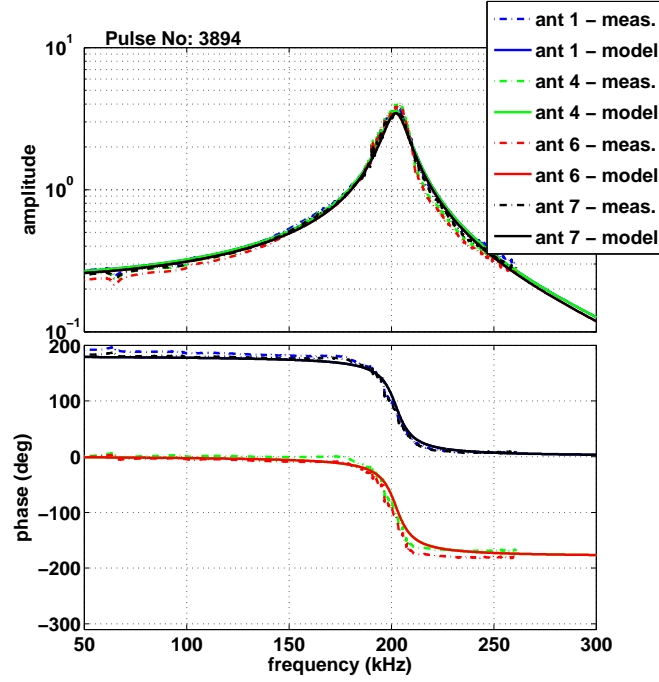


Figure 3.22: Exciter configuration: active antennas 1, 4, 6 and 7, phasing $+- -+$ and DU 1:2. Comparison between modeling and measurements. Ratio I_{lb}/I_{tot} for the four active antennas.

the smaller peaks of the antennas 6 and 7 cannot be easily reproduced. For frequencies higher than 240 kHz, the model reproduces the rapid decrease in the antenna currents. This decrease is due to the rapid decrease of the current gain and the source current saturation at $I_{s,max}$. The source current is limited by the maximum AGC gain and the fixed attenuation level at the amplifier input. The voltage and current on the amplifier remain below its limits.

Generally, good agreement between model and measurements is found for a unique set $I_{s,max}$ and $V_{s,max}$. Thus, the model becomes a good tool for providing important information on the amplifier, of which the current and voltage are not measured on the main data acquisition system. As an example, the main limiting factor for the antenna currents in the configuration shown in figure 3.21a is the source current $I_{s,max}$, which is most of the time saturated. In pulses where a higher $I_{s,max}$ has been recorded, the maximum voltage $V_{s,max}$ comes into play and limits the possible antenna currents.

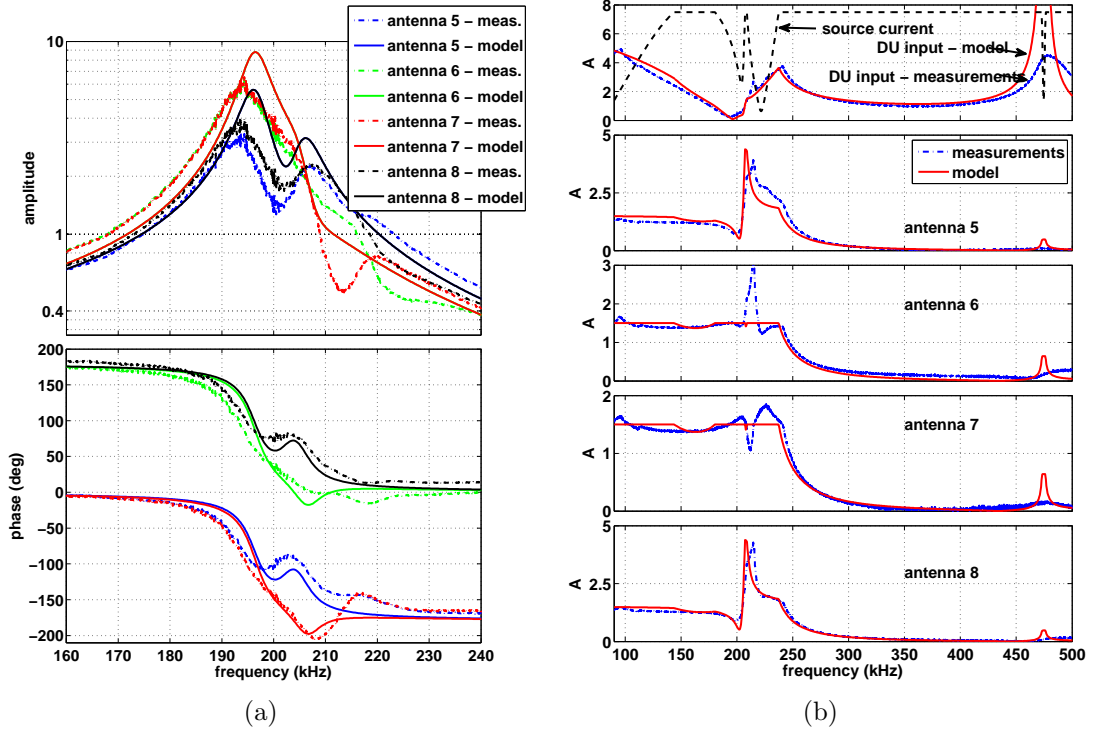


Figure 3.23: Exciter configuration: active antennas 5, 6, 7 and 8, phasing $+-+-$ and DU 1:4, the LB current of antenna 7 is controlled. Comparison between modeling and measurements. (a) Amplitude (top) and phase (bottom) of G_{lb} showing the effect of the antenna inductive coupling around 210 kHz. Notice the big differences between the antennas in both the amplitudes and the phases of the antenna currents. (b) DU input and LB currents obtained in the actual experimental conditions. The differences in the G_{lb} between the individual antennas lead to strong variations and peaks in the currents around 210 kHz. The difference between model and measurements at the resonance of 470 kHz, is due to the fact that the quality factor of the resonance is overestimated in the model (this is explained in the caption of figure 3.20).

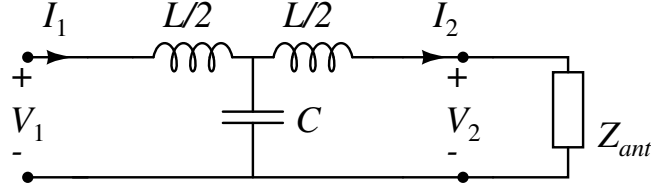


Figure 3.24: Reduced model of transmission line terminated by one antenna.

3.3.6 Discussion

The modeling described in the previous sections allowed a deeper understanding of the engineering limitations and the problems that occurred in the initial phase of operation. As a consequence, it led to first steps towards the optimization of the antenna currents.

3.3.6.1 Interpretation of the resonances of current gain G_{lb}

The electrical resonance at ~ 200 kHz leading to a local maximum in both transfer functions, current gain $G_{lb}(\omega)$ and impedance $Z(\omega)$ (figures 3.20 and 3.19), is created by the combined inductance of the antenna and of the transmission lines, and the total capacitance of the transmission lines. This can be illustrated with a simple calculation. Consider the circuit of the figure 3.24, a reduced representation of an individual antenna circuit. The transmission lines are represented by a single “T” model with two inductors in series and a capacitor in parallel. The total inductance and capacitance of the transmission lines are L and C , respectively. The antenna can be represented by an inductor and a resistor in series, i.e. $Z_{ant} = R_{ant} + i\omega L_{ant}$. The input impedance is

$$Z(\omega) = \frac{V_1}{I_1} = i\omega \frac{L}{2} + \frac{R_{ant} + i\omega L'}{1 - \omega^2 CL' + i\omega R_{ant}C} , \quad (3.14)$$

where $L' = L_{ant} + \frac{L}{2}$. The current gain is

$$G(\omega) = \frac{I_2}{I_1} = \frac{1}{1 - \omega^2 CL' + i\omega R_{ant}C} . \quad (3.15)$$

Thus, $Z(\omega)$ and $G(\omega)$ have the same parallel resonance at the frequency

$$\omega_1^2 = \frac{1}{L'C} = \frac{1}{(L_{ant} + \frac{L}{2})C} . \quad (3.16)$$

It is observed that the terminal “1” shown in the circuit model 3.24 can be moved along the transmission lines to represent either the DU output or the LB. Hence, for the LB, one has

$$\frac{I_{ant}}{I_{lb}} = \frac{1}{1 - \omega^2 C_1 (L_{ant} + \frac{L_1}{2}) + i\omega R_{ant} C_1} , \quad (3.17)$$

where L_1 and C_1 correspond to the series of the riser and in-vessel cables. For the DU, one has

$$\frac{I_{ant}}{I_{tot}} = \frac{1}{1 - \omega^2 C_2 (L_{ant} + \frac{L_2}{2}) + i\omega R_{ant} C_2} , \quad (3.18)$$

where L_2 and C_2 correspond to the series of the J1H-J1T, riser and in-vessel cables. Thus, the expression G_{lb} of equation (3.13) can be calculated

$$G_{lb} = \left(\frac{I_{ant}}{I_{lb}} \right)^{-1} \frac{I_{ant}}{I_{tot}} = \frac{1 - \omega^2 C_1 (L_{ant} + \frac{L_1}{2}) + i\omega R_{ant} C_1}{1 - \omega^2 C_2 (L_{ant} + \frac{L_2}{2}) + i\omega R_{ant} C_2} . \quad (3.19)$$

The analytic formula 3.19 shows the existence of a series resonance at

$$\omega_1^2 = \frac{1}{C(L_{ant} + L_1/2)} \quad (3.20)$$

and a parallel resonance at

$$\omega_2^2 = \frac{1}{C(L_{ant} + L_2/2)} . \quad (3.21)$$

Using the data provided in the previous sections, the frequency of the parallel resonance is estimated at 211 kHz while the frequency of the series resonance is estimated at 440 kHz. These frequencies are in good agreement with the measurements shown in figure 3.20. They depend on the inductive coupling between the neighboring antennas and can change as much as 10% when the antenna phasing changes.

3.3.6.2 Maximization of the antenna currents and limitations

Because of the series resonance in G_{lb} and the high antenna impedance at the amplifier output for frequencies higher than 300 kHz, the amplifier is pushed to deliver a high current on a high impedance load. This causes power reflections on the amplifier and it hampers its operation. A way to avoid this problem is

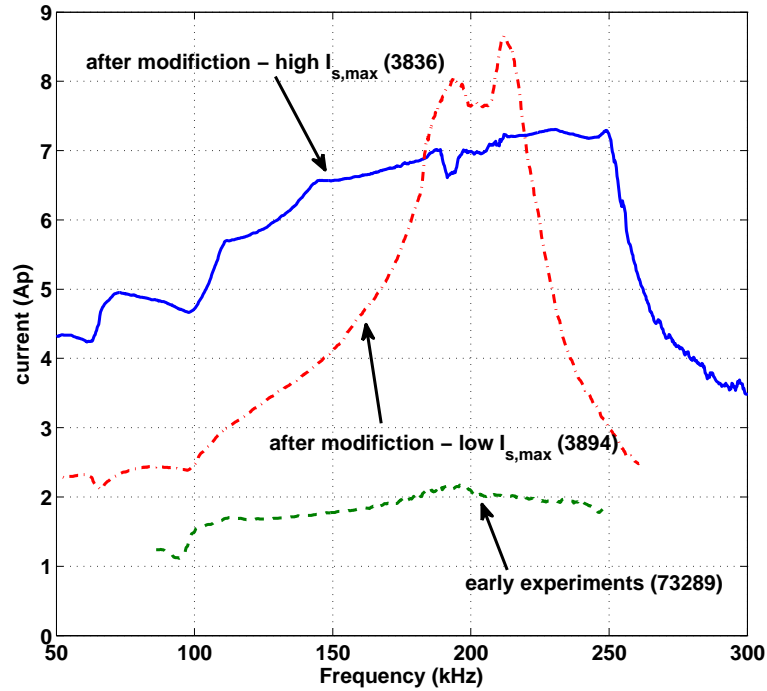


Figure 3.25: Antenna current before and after the modification of the attenuation stage at the amplifier input. For the latter, the two responses that are shown correspond to high/low zero-load current of the amplifier $I_{s,max}$.

to increase the attenuation at the amplifier input enough, so that the amplifier can tolerate the power reflections even at maximum AGC gain. This was the configuration used in the early experiments, of which an example is shown in the figure 3.23b. However, this limits too much the amplifier output even when the amplifier can deliver more current and thus, the full potential amplifier output is not utilized.

A second possibility is to decrease the attenuation at the amplifier input and operate in frequencies below ~ 300 kHz at high AGC reference, benefiting from the full output capacity of the amplifier and thus maximizing the antenna currents. With this modification, the antenna currents are almost quadrupled, as seen in figure 3.25. When it is required to operate in frequencies higher than 300 kHz, the AGC reference should be set at a very low level or the AGC should be disabled. With this configuration, relatively high antenna currents are available in the TAE frequency range, between 100 and 250 kHz. On the other hand, for excitation of EAEs (twice the TAE gap frequency) and NAEs (three times the TAE gap

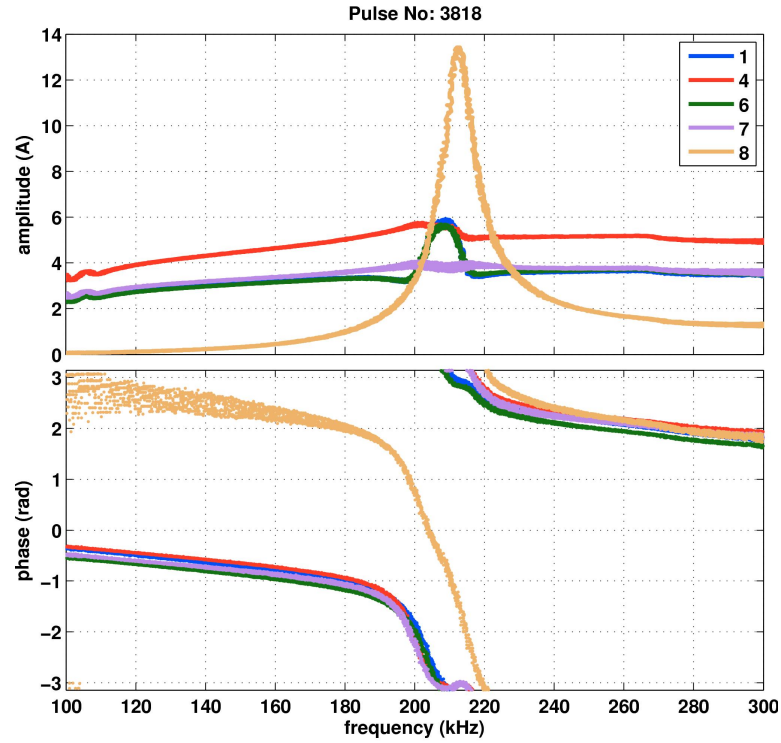


Figure 3.26: Antenna currents. The active antennas are the 1, 4, 6, 7 while the antenna 8 is passive. The currents on antennas 2, 3 and 5 cannot be measured because the LB connections are open. Notice the important amplitude of the current on antenna 8.

frequency), situated usually above 250 kHz, relatively low currents are available because of the low current gain and the high impedance at the amplifier output.

3.3.6.3 Minimization of the antenna inductive coupling effects

In the section 3.3.5, it has been shown how the antenna coupling can lead to strong variations and peaking of the antenna currents around the 200 kHz resonance, as well as to modifications of the antenna phasing.

The effect of the inductive coupling is strong because the individual antenna circuits, namely the part DU-antenna, are tuned at approximately the same frequency and have similar quality factors. Resonant circuits with such characteristics exhibit strong perturbation of the system transfer functions around the resonant frequency ([77], p. 63).

Operating with active antennas that are far from each other, e.g. only with the

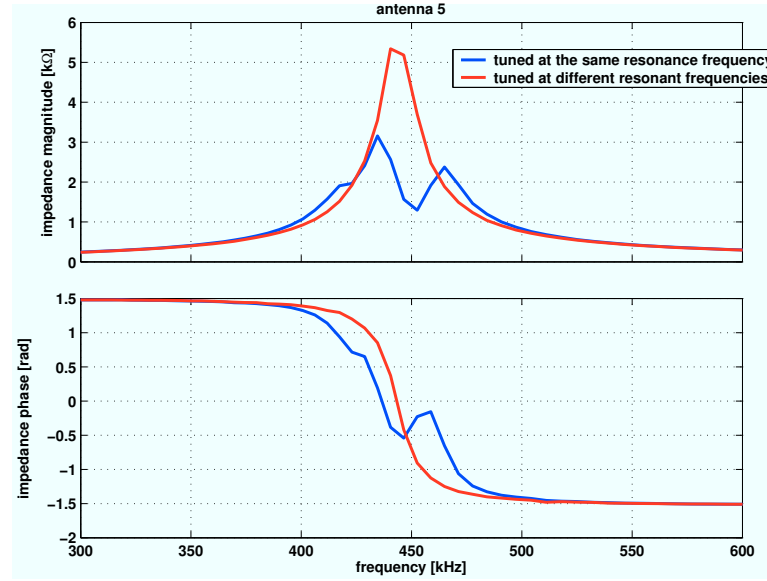


Figure 3.27: Antenna impedance measured at the LB. The double humps that appear are due to the inductive coupling. By changing the resonant frequency of the neighboring antenna (antenna 6) the coupling effect on the impedance is removed. This is also referred to as ‘detuning’.

outer antennas in the same frame, is not sufficient for reducing the coupling effect because important currents are induced on the neighboring passive antennas, as shown in figure 3.26. The current on the passive antennas flows through the shunt capacitance of the transmission lines. What is further needed, is to detune the individual antenna circuits. This is achieved by opening the LB connections of the neighboring passive antennas which moves the resonant frequency from ~ 200 kHz to ~ 450 kHz. The method of circuit detuning is also confirmed by the measurement of the antenna impedance at the LB, shown in figure 3.27. In this case, the detuning is achieved by short-circuiting the neighboring antennas at the LBs.

3.4 Matching

The second step towards the optimization of the antenna currents was the design and the use of matching units. The MUs are circuits that implement an impedance transformation resulting in a plateau of maximum antenna currents

in a specified frequency range. The circuits are virtually lossless, composed by inductors and capacitors. Broadband solutions are sought in order to avoid confusion with the weakly damped plasma modes.

This section is divided in two parts: the first part (subsection 3.4.1) describes the design aspects and the simulation results and the second part (subsection 3.4.1.2) analyzes the experimental results.

It should be noted that the nominal BONN amplifier specifications are used for the design, with the amplifier output impedance being $50\ \Omega$. This is a standard specification for MU designs because of the extensive use of $50\ \Omega$ transmission lines. Indeed, the transmission line AMP-MU has a characteristic impedance of $50\ \Omega$. The design takes into account the long-term utility of the diagnostic: the envisaged upgrade of the system will include the replacement of the current power amplifier with 8 independent amplifiers configured for optimal power transfer at a $50\ \Omega$ nominal impedance.

Because of the later change of the amplifier output characteristics that was described in the subsection 3.3.4, experimental testing of the matching units could not be performed with the same amplifier output characteristics as the ones assumed for the design. However, despite the difference of the amplifier output characteristics between the design and the particular experimental conditions, the experimental results that are presented in the subsection 3.4.1.2 show that the matching circuits do implement the impedance transformation which they are designed to achieve.

3.4.1 Matching unit design

The design is basically an optimization problem. In the first part of this subsection, we describe the model and the optimization aspects. With a fixed model, numerous optimization runs were made to study several circuit topologies. In the second part of this subsection, the results of the simulations are presented for a selection of matching circuits. The tradeoff between bandwidth and gain is shown and it is found that circuits with series capacitors can, in general, achieve higher current gains.

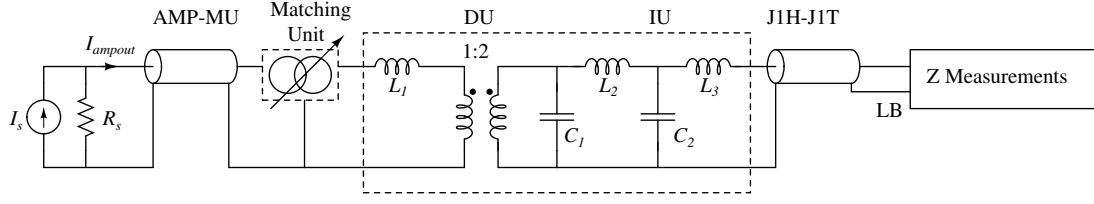


Figure 3.28: Reduced model for a configuration with 4 active antennas.

3.4.1.1 Equivalent model and optimization aspects

The RF software APLAC[®] has been used for the design of the matching circuits. APLAC offers the possibility of prescribing an arbitrary number of optimization goals, constraints and variables. The main limitation was that only the student version of the software was made available, which does not allow the simulation of a big circuit model as it imposes an upper limit on the memory needed to run a simulation. Thus, an equivalent model of 4 active antennas with a reduced number of elements was constructed and is shown in figure 3.28.

This model assumes that the individual antenna circuits from the DU to the antennas are the same. The inductive coupling between the antennas is neglected. The part LB-antennas is modeled as a black box using impedance measurements, so only the LB currents could be entered in the optimization goals. As shown in Section 3.3, the LB currents are a good approximation to the antenna currents for frequencies up to 300 kHz.

The 1:4 DU module was considered since it used to be part of the standard four active antenna configuration in the 2007 experiments. The conversion from the 1:4 DU to a 1:1 equivalent needs to be done carefully. The secondary side of each individual 10:40 DU transformer remains unchanged. The primary sides of the 4 transformers are connected in series, hence their impedances are added. This leads to $L_1 = 4L_p$, where L_p is the leakage inductance of the 10:40 primary coil. The winding ratio needs to be changed so that the impedance seen at the primary side of the reduced model is equal to the original one. For the case of the 1:4 DU configuration, the equivalent winding ratio is 1:2. The relevant calculation is provided in the appendix A.1. With the above modifications, a good agreement is obtained between model and measurements for the impedance at the DU input, as shown in figure 3.29.

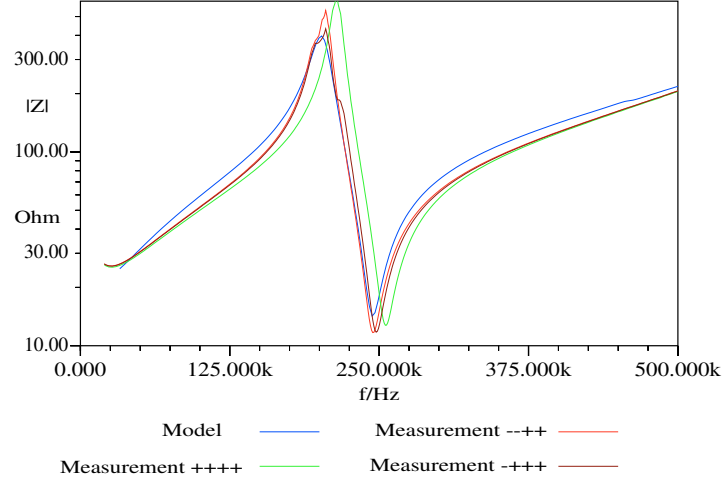


Figure 3.29: Impedance comparison between measurements at the DU input and the model of figure 3.28.

The nominal specifications of the amplifier are used (subsection 3.3.4). The amplifier is modeled as a current source with an output resistive impedance Z_s of 50Ω . The maximum source current is 25 A and the maximum voltage is 700 V (peak values).

The optimization algorithm is trying to maximize the total current gain

$$G_{tot} = \frac{I_{ant}}{I_s}(\omega) = G_{ampout}(\omega) \frac{Z_s}{Z_s + Z_{ant}(\omega)} \quad (3.22)$$

in a specified range of frequencies by varying the matching circuit parameters which enter in the transfer functions G_{ampout} and Z_{ant} . Here,

$$G_{ampout} = \frac{I_{ant}}{I_{ampout}} \quad (3.23)$$

is the transfer function of the ratio of the antenna current over the amplifier output current and Z_{ant} is the antenna impedance that is measured at the amplifier output when the amplifier is not connected (see also figure 3.28). The expression (3.22) shows that the solution to the optimization problem involves minimizing $|Z_{ant}|$ and maximizing $|G_{ampout}|$. These two partial goals are in conflict with each other because, as shown in the appendix A, $G_{ampout} = 1/D$ and $Z_{ant} = N/D$, so increasing G_{ampout} (by decreasing D) by a certain amount makes increase also Z_{amp} by the same amount.

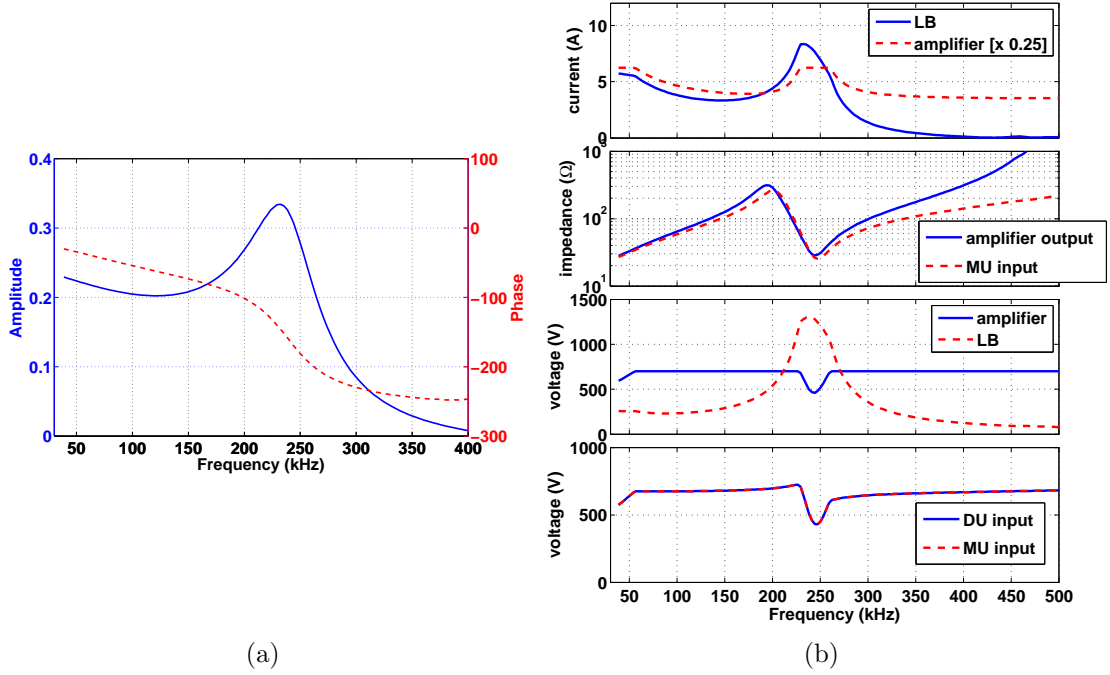


Figure 3.30: Exciter without matching unit. (a) Total current gain with HWHM = 11%. (b) Exciter engineering signals in a simulated operation with AGC and impedance at the MU input.

In order to obtain a significant current gain G_{tot} , the aforementioned matching criteria lead typically to the presence of one or multiple resonances in the frequency range of interest. In order to characterize the width of the resonance, we use the half width at half maximum (HWHM) of the power frequency response, i.e. the square of G_{tot} , normalized to the resonance frequency. The HWHM of such a resonance should be large enough (low quality factor Q) so that there is no risk to confuse it with plasma resonance, which has high quality factor Q . Therefore, the matching units have been designed with an estimated $\text{HWHM} \gtrsim 15\%$, which is quite higher than the relatively low damped modes that one wants to measure, which have typically $\text{HWHM} < 6\%$. It should be noted here additionally that the aforementioned risk is practically negligible because the construction of the plasma transfer function involves normalization to the measured antenna currents.

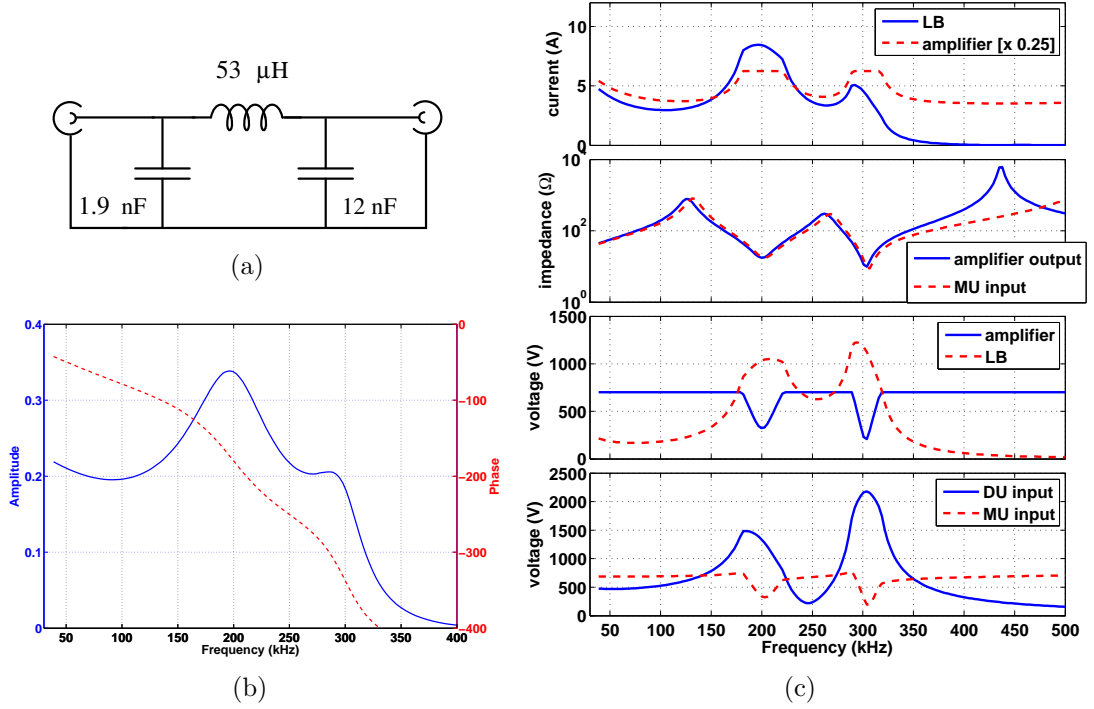


Figure 3.31: Matching at 196.6 kHz. (a) Matching circuit with Π topology. (b) Total current gain with HWHM= 21%. (c) Simulation (from top to bottom): current at the LB and at the amplifier, impedance at the amplifier output and at the MU input, voltage at the amplifier and at the LB, voltage at the DU and MU inputs.

3.4.1.2 Results

According to the assumed modeling, for a 4-antenna configuration without a matching unit, the current gain G_{tot} has a maximum at 230 kHz (figure 3.30a). Indeed, the LB currents show also a maximum around the same frequency in an antenna-current-controlled frequency sweep shown in figure 3.30b.

Various matching circuit topologies were investigated. The matching units with the most interesting properties are shown in the figures 3.31, 3.32 and 3.33. The circuits are accompanied by the plots of G_{tot} (e.g. figure 3.31b), the antenna impedance at the amplifier output and the MU input and various engineering signals in a simulated operation with the AGC (e.g. figure 3.31c). Two additional matching units centered at different frequencies are shown in the appendix A.2: they have similar characteristics to the MUs shown in figures 3.31 and 3.33

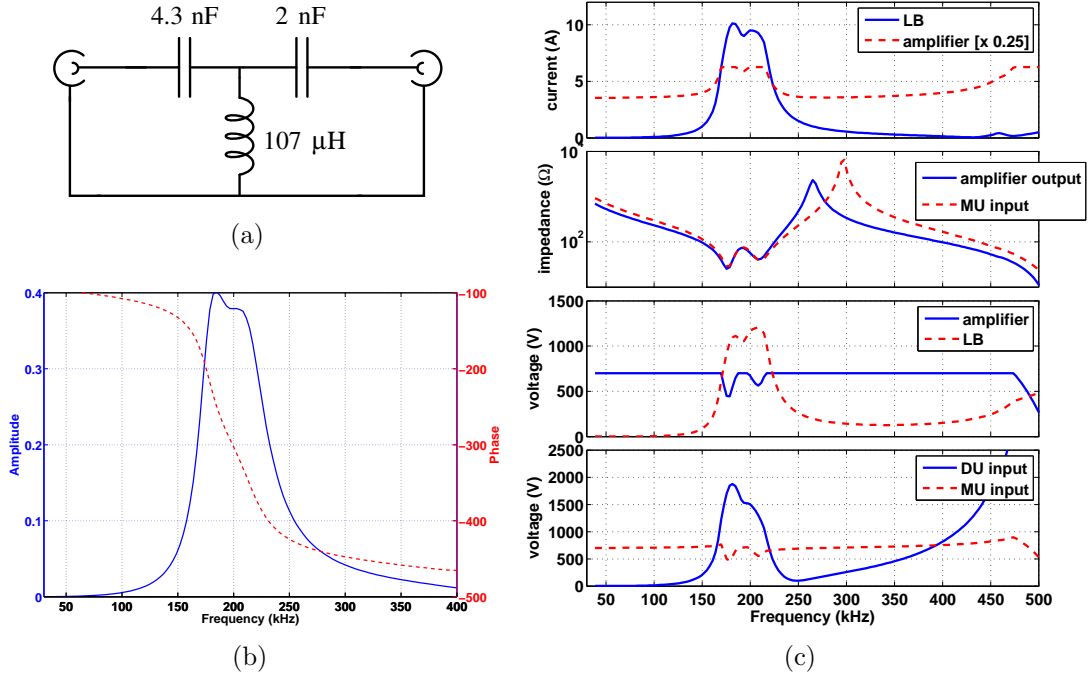


Figure 3.32: Matching at 196.5 kHz. (a) Matching circuit with T topology. (b) Total current gain. HWHM= 14.4%. (c) Simulation (from top to bottom): current at the LB and at the amplifier, impedance at the amplifier output and at the MU input, voltage at the amplifier and at the LB, voltage at the DU and MU inputs.

respectively.

The current gain maxima G_{max} that are obtained are between 0.35 and 0.43 (figures 3.31b, 3.32b and 3.33b). A tradeoff is observed between maximizing matching bandwidth and G_{max} . The more peaked is the current gain inside the matching frequency range, the lower it is outside. This can be seen by comparing the figures 3.31b and 3.32b. the Π MUs (figures 3.31 and A.1) have relatively low G_{max} and broad bandwidth. Conversely, the MUs that include series capacitors (figures 3.32, 3.33 and A.2) have higher G_{max} and narrower bandwidth. In general, it has been observed, that relatively high current gains can be obtained for circuits that include series capacitors.

To understand the interplay between the system transfer functions, the amplifier characteristics and the current control (AGC), we consider the figures 3.31c, 3.32c and 3.33c. It is observed that the amplifier, though being pushed to

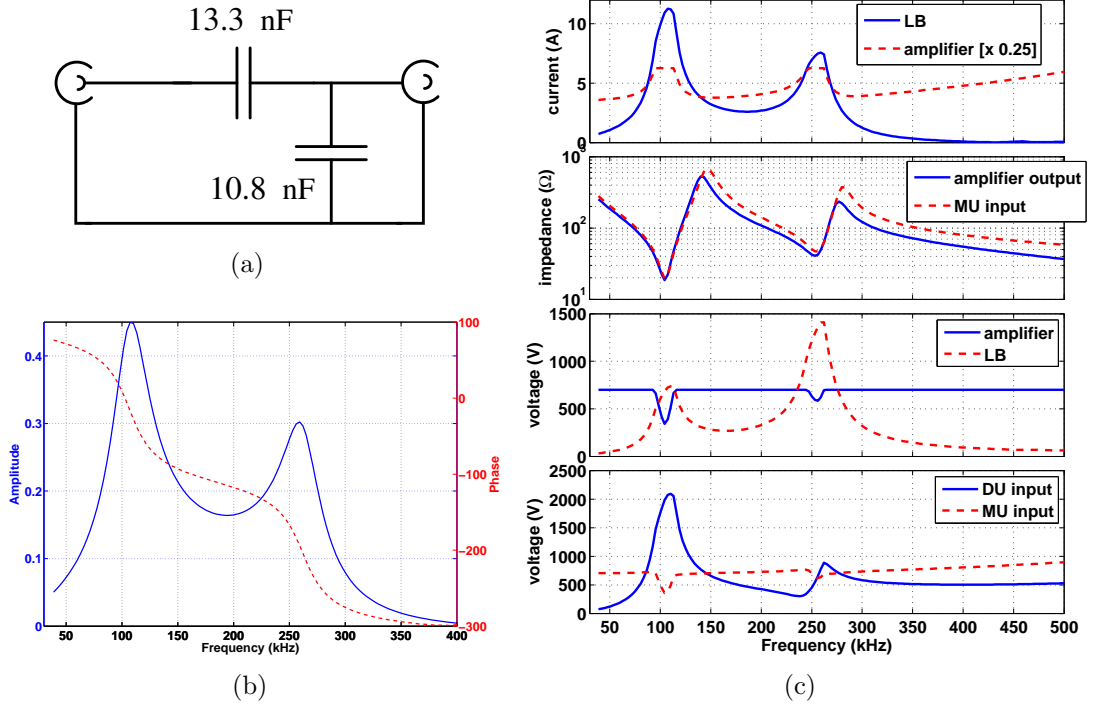


Figure 3.33: Matching at 107.3 kHz. (a) Matching circuit with Γ topology. (b) Total current gain. HWHM= 16%. (c) Simulation (from top to bottom): current at the LB and at the amplifier, impedance at the amplifier output and at the MU input, voltage at the amplifier and at the LB, voltage at the DU and MU inputs.

deliver maximum current, is limited in most of the frequency range from the voltage limit at the output and thus delivers less current. In the matching frequency range of all MUs, the conditions become favorable with sufficiently small antenna impedance and sufficiently high current gain, allowing thus for a maximization of the LB-antenna and amplifier currents. Furthermore, favorable conditions are created in secondary frequency ranges, such as the one at 300 kHz for the MU shown in 3.31 and at 250 kHz for the MU shown in 3.33. The estimated voltage at the MU input and output is shown in the bottom plots of the figures 3.31c, 3.32c and 3.33c. It is estimated that the voltage drop across any capacitor does not exceed 3 kV, which is much less than their breakdown voltage, typically being at 15 or 20 kV.

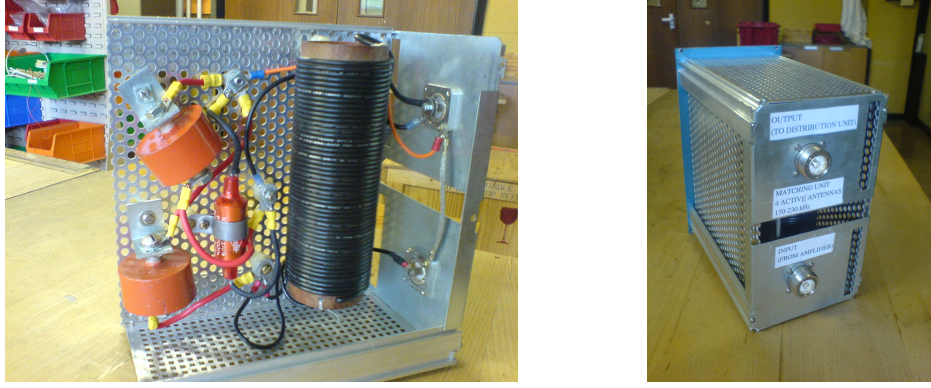


Figure 3.34: Internal (left) and external (right) view of the MU of figure 3.31. One can observe the high-voltage capacitors and the air core coil (left), as well as the metallic box and the coaxial connectors (right).

3.4.2 Experimental results

The MUs that are shown in figures 3.31, 3.33, A.1 and A.2 were built (an example is shown in figure 3.34), tested in vacuum conditions and used in plasma pulses without any problem. A tolerance of the order of $\sim 5\%$ applies for the capacitors and the inductors. In the following, we analyze in detail the experimental results obtained with the 2 MUs that are shown in figures 3.31 and 3.33 by means of a direct comparison between simulation and current measurements.

Figure 3.35a shows the currents measured at the DU input and at the LBs as function of frequency and the simulation results when the MU of figure 3.31 is used. Figure 3.35b shows a set of the measured transfer functions of the exciter that *do not* depend on the amplifier (current gain I_{lb}/I_{tot}) and the ones predicted by the model. A very good agreement (between model and measurements) is obtained both for the transfer functions (figure 3.35b) and the simulation (figure 3.35a). This shows that the MU indeed transforms the load impedance according to the design.

Moreover, one can notice the effect of the amplifier output impedance Z_s on the antenna currents. As seen in figure 3.35a where $Z_s = 200 \Omega$, the maximum antenna currents are obtained around 160 kHz, in contrast to the case when $Z_s = 50 \Omega$ shown in figure 3.31, where the maximum currents are obtained around 200 kHz. This follows from the influence of Z_s on the total current gain G_{tot} through the term $\frac{Z_s}{Z_s + Z_{ant}(\omega)}$ in the equation (3.22): the maximum of G_{tot}

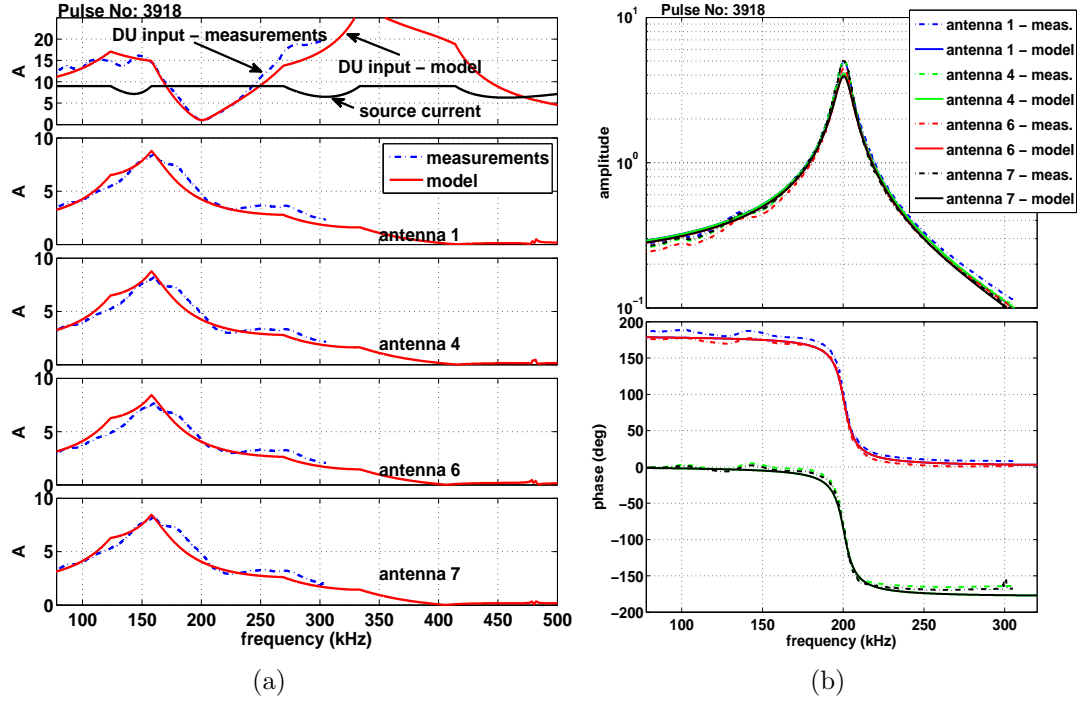


Figure 3.35: Exciter configuration: active antennas 1, 4, 6 and 7, phasing $+-+-$ DU 1:2 and use of MU shown in figure 3.31. Comparison between modeling and measurements. (a) Exciter currents (measurements at the DU input and at the LBs) . (b) Ratio I_{lb}/I_{tot} for the four active antennas.

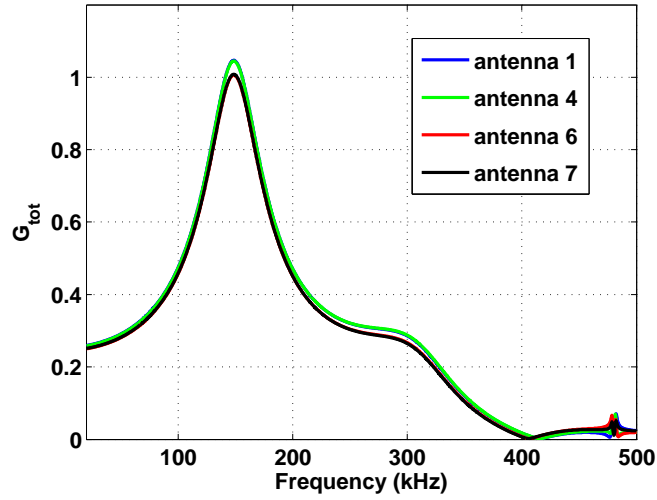


Figure 3.36: Same exciter configuration as shown in figure 3.35. Total current gain G_{tot} predicted by the model with $Z_s = 200 \Omega$.

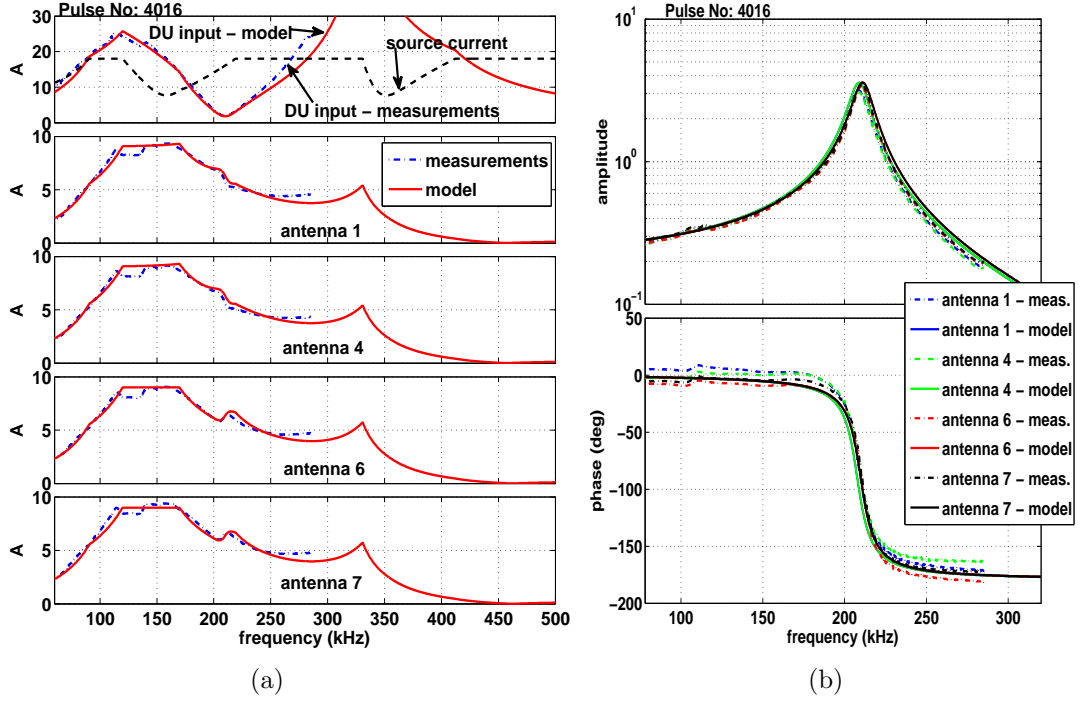


Figure 3.37: Exciter configuration: active antennas 1, 4, 6 and 7, phasing $+-+-$ DU 1:2 and use of MU shown in figure 3.33. Comparison between modeling and measurements. (a) Exciter currents (measurements at the DU input and at the LBs) (b) Ratio I_{lb}/I_{tot} for the four active antennas.

with $Z_s = 200 \, \Omega$ (figure 3.36) is at 150 kHz and has a value of 1.0, whereas G_{tot} with $Z_s = 50 \, \Omega$ (figure 3.31b) has a maximum of 0.35 at 200 kHz.

The analysis that has been just described for the pulse 3918 and that is shown in figure 3.35 is repeated for a configuration where the Π -topology MU of figure 3.33 is installed: the results are shown in figure 3.37. Similarly to the previous case, we find that the agreement between model and measurements allows for a validation of the designed impedance transformation from the specific MU. This configuration results in an extended maximum-current plateau in the frequency range 110-170 kHz. Note that the antenna load has not changed and this is reflected on the transfer functions shown in 3.37b. The small frequency shift of the maximum by 10 kHz, which is observed if one compares the figure 3.37b to the figure 3.35b is due to the change of antenna phasing and is successfully captured by the model.

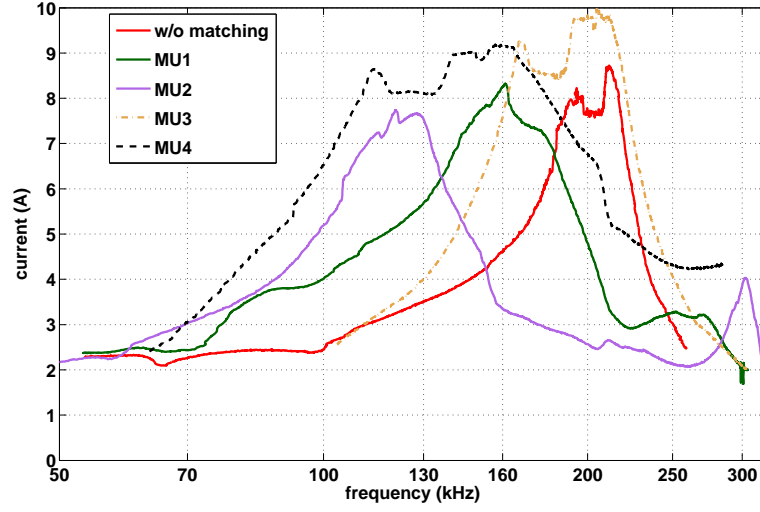


Figure 3.38: Overview of the maximum LB currents that were measured as a function of frequency with the use of MUs (MU1 corresponds to figure 3.31, MU2 to figure A.1, MU3 to figure A.2 and MU4 to figure 3.33).

An overview of the experimental results is shown in the figure 3.38. We observe that the MUs change the frequency response with respect to the no-MU configuration by shifting the maximum current frequency ranges. Using the MUs, relatively high currents of more than 6 A can be achieved in the range of 100-240 kHz, covering the usual TAE frequencies in JET plasmas. It has to be noted that the traces of the no-MU case, MU1 and MU2 correspond to the amplifier having $I_{s,max} = 9$ A. The traces of MU3 and MU4 correspond to the amplifier having $I_{s,max} = 18$ A. It was not possible to test all MUs with the same $I_{s,max}$ because $I_{s,max}$ is an intrinsic amplifier parameter that depends on the state of the vacuum tube stage, which, as seen in the paragraph 3.3.4, changed during the experimental campaigns.

3.5 Conclusions

The impedance characteristics of the AE exciter circuit, including the long transmission lines typical of large fusion devices, have required detailed modeling in order to understand the measured currents and voltages as function of frequency and to determine the feasible antenna currents. We have been able to predict

accurately the frequency response of the engineering signals in experimental conditions. It has been shown how the maximum antenna currents are determined by the total current gain of the circuit and the voltage/current limits of the power amplifier. The strong effect of the coupling between the neighboring antennas through their mutual inductances was identified, characterized and minimized.

The electrical model was used for the design of impedance matching circuits. Several matching units were built and tested. The experimental results showed discrepancies from the initial predictions of the matching unit design. The cause of these discrepancies has been identified as due to the fact that the properties of the power amplifier were not the nominal ones at the time of the experiments. Despite these discrepancies, the matching circuits have allowed us to achieve relatively high antenna currents, in the range of 6 to 10 A, in different frequency ranges.

Chapter 4

The n -spectrum of the antenna excitation and of the plasma response

4.1 Introduction

The Alfvén eigenmodes are characterized by the toroidal mode number n . The accurate estimation of the n -spectrum of the plasma response to the antenna excitation is a central issue in this work. We are thus interested in understanding the n -spectra that can be driven by the antennas and their correlation with the n -spectrum of the plasma response. Once an accurate estimation of the n -spectrum of the plasma response is obtained, it is important to have a reliable algorithm which can extract the damping rates for individual- n modes automatically.

This chapter deals with these aspects. In Section 4.2, we calculate the field produced by the antennas in vacuum and the resulting n -spectrum. We examine its spatial dependence and its dependence on the antenna currents. In Section 4.3, we make a relative calibration of the magnetic pick-up coils with a method that is based on their direct coupling with the AE antennas in vacuum. Section 4.4, discusses the tests that are carried out in order to verify the correct estimation of the n -spectrum of the plasma response. Section 4.5 reports on the upgrade of the real-time system of the Alfvén Eigenmode Active Diagnostic (AEAD) to track individual ns and on the benchmark against post-pulse analysis. Finally, section 4.6 reviews and analyzes the data processing algorithm that is used to

obtain the damping rate measurements.

4.2 The magnetic field of the AE antennas in vacuum

In this section, we calculate the magnetic field of the antennas in vacuum in the so-called antenna *near-zone*, in which the distance from the antenna is very small compared to the wavelength. The antennas are coils of 18 distinct thin rectangular turns, parallel to each other. The field is calculated using the actual tokamak coordinates of the antennas. Figure 4.1 (top) shows a view of a 4-antenna assembly as installed on the tokamak low-field-side (LFS) wall. A second identical assembly is installed at a toroidally opposite angle.

The effect of the conductive wall (vacuum vessel) is not included, but the significance of the effect of the wall is evaluated by considering its distance from the antennas. Thus, an approximate estimate is obtained for the range of validity of the subsequent calculations that do not include the effect of the wall.

It is considered that the wall surface is parallel to the planes defined by the antenna turns. It should be noted though, that the geometry of the wall behind the antennas is uneven and relatively complex because the 2 antenna assemblies are located under the NBI ducts and near the vacuum vessel bellows, as shown in the figure 4.1. The minimum distance between the wall and the nearest-to-the-wall antenna turn is approximately 41 cm. Because the conductivity σ of the wall (manufactured from Inconel 600 with a resistivity of $1.05 \cdot 10^{-6} \mu\Omega \cdot m$ at 205°C) is high enough so that $\sigma \gg \omega\epsilon$ in the frequency range of interest, the wall can be considered as a perfect conductor (the skin depth at 100 kHz is 1.15 mm). Thus, an image antenna with respect to the wall surface carrying a current $-I$ can be used in order to satisfy the boundary condition that the tangent electric field is null at the wall surface. Consider now a point along the antenna axis located at a distance R_1 from a given antenna turn and $R_2 = R_1 + 2d$ from the image turn. Because the magnetic field has an inverse dependence with the distance (as it will be shown later on), the ratio of the total field to the field produced only from the antenna without the effect of the wall can be approximated by

$$r_w = \frac{B_1 - B_2}{B_1} \sim 1 - \frac{R_1}{R_2} = 1 - \frac{1}{1 + \frac{2d}{R_1}} . \quad (4.1)$$

4.2 The magnetic field of the AE antennas in vacuum

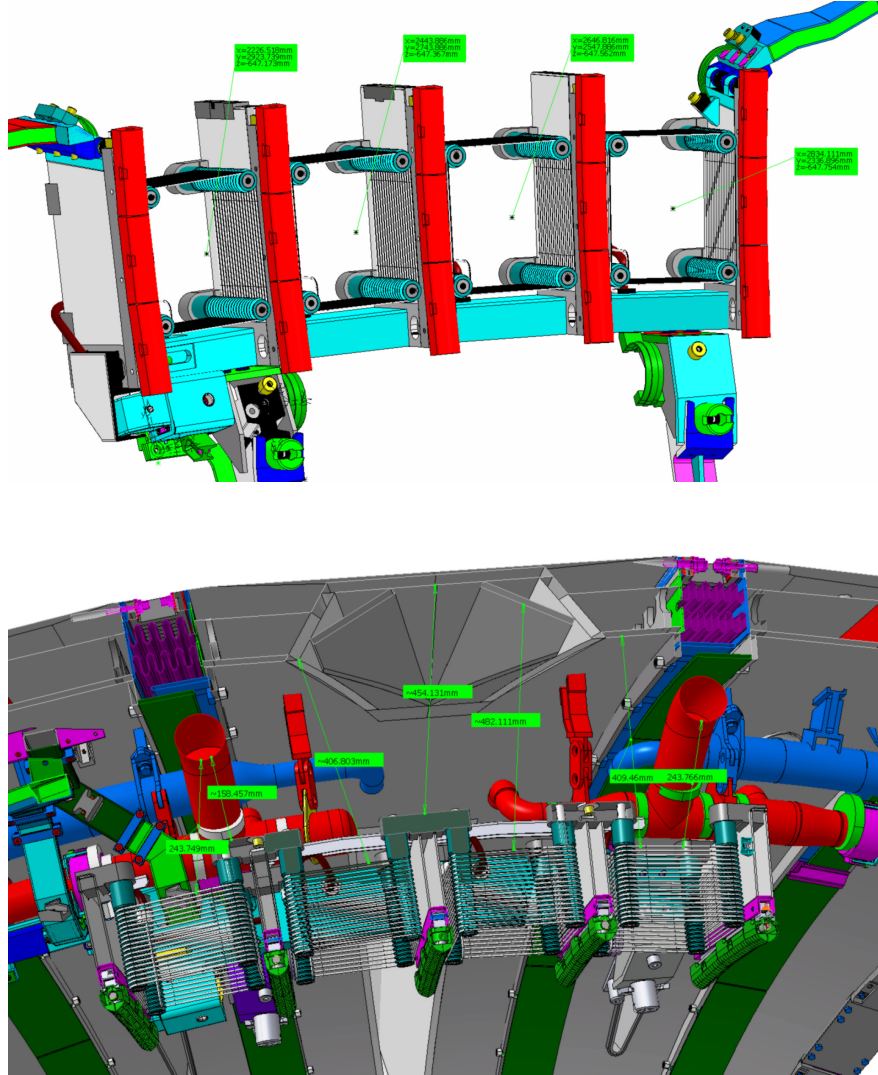


Figure 4.1: On top, view of a 4-antenna assembly as installed on the tokamak low-field-side wall. In the bottom, view of the wall structure and other installations between the antenna assembly and the wall (JET drawing office).

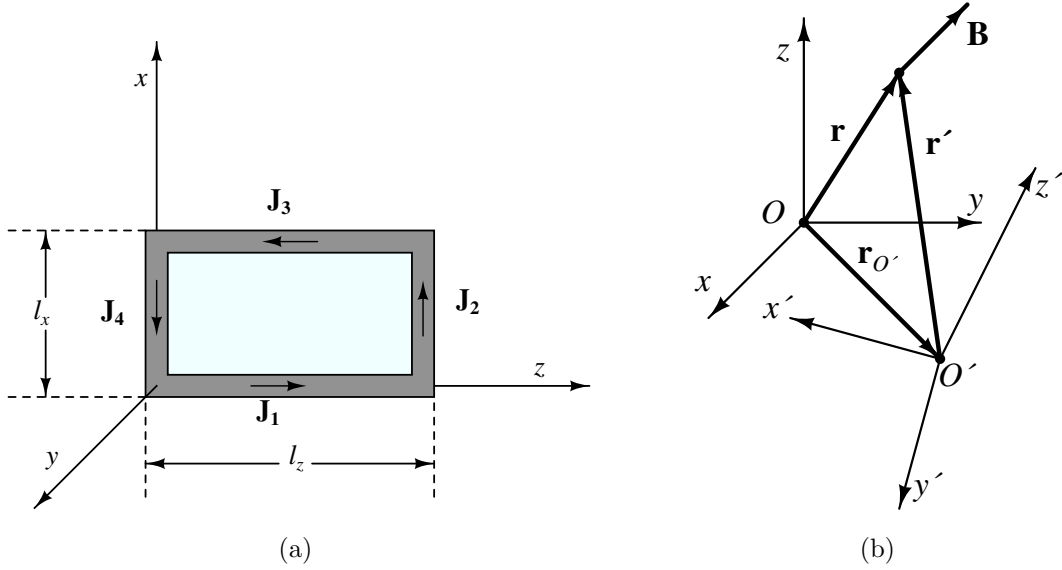


Figure 4.2: (a) Geometry of a rectangular loop used for the modeling of an antenna turn. (b) Change of coordinates from a local to a global coordinate system.

Thus, at $R_1 = 2d$ cm, approximately half of the field is canceled by the wall. The distance between the nearest-to-the-plasma antenna turn and the position of the last closed flux surface (LCFS) varies from ~ 4 cm for limiter plasmas to ~ 10 cm for diverted plasmas. The formula (4.1) can be used to evaluate the effect of the wall at these distances. If one considers a turn in the middle of the antenna solenoid (and bearing in mind that the length of the antenna solenoid is 13.6 cm), it is $d = 41 + 13.6/2 = 47.8$ cm and this results in $r_w = 0.9$ and $r_w = 0.85$ for a limiter and a diverted LCFS respectively. Thus, the effect of the wall on the antenna field is from 10 to 15% at these distances. At larger distances, i.e. beyond of the position of the LCFS, the antenna field is shielded by the plasma: because of the high frequency and the high plasma conductivity, the skin depth is of the order of a centimeter and the antenna field can only penetrate the plasma at distances of the order of such a skin depth.

We now consider a rectangular turn in the $y = 0$ plane with the lengths of its sides being ℓ_x and ℓ_z , carrying a current $Ie^{i\omega t}$, as shown in figure 4.2a. I is the

4.2 The magnetic field of the AE antennas in vacuum

current in A. The current density distribution can be described as

$$\mathbf{J} = \sum_{i=1}^4 \mathbf{J}_i, \quad (4.2)$$

where

$$\mathbf{J}_1(x, y, z) = \hat{\mathbf{z}} I \delta(x) \delta(y), \quad 0 \leq z \leq \ell_z \quad (4.3)$$

$$\mathbf{J}_2(x, y, z) = \hat{\mathbf{x}} I \delta(z - \ell_z) \delta(y), \quad 0 \leq x \leq \ell_x \quad (4.4)$$

$$\mathbf{J}_3(x, y, z) = -\hat{\mathbf{z}} I \delta(x - \ell_x) \delta(y), \quad 0 \leq z \leq \ell_z \quad (4.5)$$

$$\mathbf{J}_4(x, y, z) = -\hat{\mathbf{x}} I \delta(z) \delta(y), \quad 0 \leq x \leq \ell_x. \quad (4.6)$$

The vector potential at a point \mathbf{r} in space produced by the above current distribution in the Lorenz gauge [52, 78] is

$$\mathbf{A}(\mathbf{r}) = \frac{\mu_0}{4\pi} \int \mathbf{J}(\mathbf{r}') \frac{e^{ikR}}{R} d^3r', \quad (4.7)$$

where $R = |\mathbf{r} - \mathbf{r}'|$ and the wave number is $k = \frac{2\pi}{\lambda}$. In our frequency range of interest, the wavelength is much bigger than the possible distances R at which we would like to calculate the field. Thus, the inequality $|kR| \ll 1$ holds and the exponential in (4.7) can be replaced by unity. In this spatial region, the antenna field depends in detail on the properties of the source, it is oscillating harmonically as $e^{i\omega t}$ but otherwise it is static in character [52, Ch. 9].

The term \mathbf{J}_1 in 4.2 consists in calculating the following integral

$$\mathbf{A}_1(x, y, z) = \hat{\mathbf{z}} \frac{\mu_0 I}{4\pi} \int_0^{\ell_z} \frac{dz'}{x^2 + y^2 + (z - z')^2}. \quad (4.8)$$

This integral has an exact analytical solution. The points where $x = y = 0$ need to be integrated separately. The entire solution is

$$\mathbf{A}_1(x, y, z) = \begin{cases} \hat{\mathbf{z}} \frac{\mu_0 I}{4\pi} \ln \frac{\ell_z - z + \sqrt{x^2 + y^2 + (z - \ell_z)^2}}{-z + \sqrt{x^2 + y^2 + z^2}} & \text{if } x^2 + y^2 \neq 0 \\ \hat{\mathbf{z}} \frac{\mu_0 I}{4\pi} \ln \frac{z - \ell_z}{z} & \text{if } x = y = 0 \text{ and } (z < 0 \text{ or } z > \ell_z) \\ \infty & \text{if } x = y = 0 \text{ and } 0 < z < \ell_z \end{cases} \quad (4.9)$$

The rest of the terms of (4.2) yield the same type of integral and can be calculated in a similar fashion. Thus, the total vector potential has non-zero x and z components, $A_x(x, y, z)$ and $A_z(x, y, z)$, and the component A_y is zero. The

4.2 The magnetic field of the AE antennas in vacuum

analytical formulas are available in the appendix B. The magnetic field is then calculated with $\mathbf{B} = \nabla \times \mathbf{A}$ and its components as a function of \mathbf{A} are given by

$$\begin{aligned} B_x &= \partial_y A_z \\ B_y &= -\partial_x A_z + \partial_z A_x \\ B_z &= -\partial_y A_x . \end{aligned}$$

In the Lorenz gauge, the electrical field can be evaluated from the vector potential with [78]

$$\mathbf{E} = -i\omega\mathbf{A} - i\frac{1}{\omega\mu\epsilon}\nabla(\nabla \cdot \mathbf{A}) \quad (4.10)$$

Because there is no free charge and the sole source of the electric field is the time-varying \mathbf{B} , the scalar potential can be set to zero. As a result $\mathbf{E} = -i\omega\mathbf{A}$ and by virtue of the law of Gauss, both \mathbf{A} and \mathbf{E} are solenoidal, i.e. $\nabla \cdot \mathbf{A} = 0$. Indeed, this is what comes out from the above calculations and this is a way to verify their validity. We also note that all the components of \mathbf{B} are in phase, whereas \mathbf{E} lags 90 degrees behind \mathbf{B} .

In order to calculate the antenna field in the relevant toroidal coordinates, we use successive coordinate transformations of the field calculated previously by one rectangular turn and add up all the contributions. This is the problem of the change of the coordinates of a vector field: given a direct calculation of the field in convenient local coordinates \mathbf{r}' , find the field in a global coordinate system as a function of the global coordinate position vector \mathbf{r} . The global coordinates are related to the local coordinates by the translation vector $\mathbf{r}_{O'}$ that connects the 2 origins of the coordinate systems and by the rotation matrix \mathbf{Q} that defines the orientation of the local coordinate system with respect to the global coordinate system (figure 4.2b). To correctly represent the position of the AE antennas in the tokamak, a general representation of the rotation matrix \mathbf{Q} is needed. Thus, \mathbf{Q} is defined in terms of the commonly used Euler angles, following the convention in reference [79]. The algorithm for calculating the global field \mathbf{B} at \mathbf{r} can be summarized:

1. Calculate the local coordinates

$$\mathbf{r}' = \mathbf{Q}(\mathbf{r} - \mathbf{r}_{O'}) . \quad (4.11)$$

4.2 The magnetic field of the AE antennas in vacuum

2. Using the known function f , calculate the field as a function of \mathbf{r}' and possibly a set of external parameters p_1, p_2, \dots

$$\mathbf{B}' = f(\mathbf{r}', p_1, p_2, \dots) . \quad (4.12)$$

3. Finally, project the field onto the global coordinate system,

$$\mathbf{B} = \mathbf{Q}^{-1} \mathbf{B}' . \quad (4.13)$$

Notice that one can benefit from the property $\mathbf{Q}^{-1} = \mathbf{Q}^T$.

Using the above algorithm, a single antenna is produced by adding the displaced individual turns along the z axis. Then, every antenna is displaced and rotated in order to occupy its real position in tokamak coordinates. A three-dimensional view of the resulting field for two antenna configurations with different antenna current phasing is shown in figure 4.3.

Having calculated the antenna field in real space, it is interesting to examine the dependence of its n -spectrum as function of R and Z . Because of the symmetry of the antenna geometry and the linearity of the fields with respect to the antenna currents, the frequency dependence of an individual n -components is decoupled from their (R, Z) dependence.

The field of a single antenna is directly proportional to its current I and the factor B_I which depends only on the spatial coordinates. In addition, the antennas are essentially identical with the respect to the R and Z coordinates. Thus, any given component of the total field can be written as a linear combination of the currents as follows

$$B(R, Z, \phi, \omega) = \sum_{j=1}^8 I_j(\omega) B_{Ij}(R, Z, \phi) = \sum_{j=1}^8 I_j(\omega) B_I(R, Z, \phi - \alpha_j) , \quad (4.14)$$

where α_j are the toroidal angles of the 8 antennas. If B_I is developed into a Fourier series along the variable ϕ as

$$B_I(R, \phi, Z) = \sum_{n=-\infty}^{\infty} \tilde{B}_I(R, Z, n) e^{in\phi} \quad (4.15)$$

where

$$\tilde{B}_I(R, Z, n) = \frac{1}{2\pi} \int_0^{2\pi} d\phi B_I(R, Z, \phi) e^{-in\phi} , \quad (4.16)$$

4.2 The magnetic field of the AE antennas in vacuum

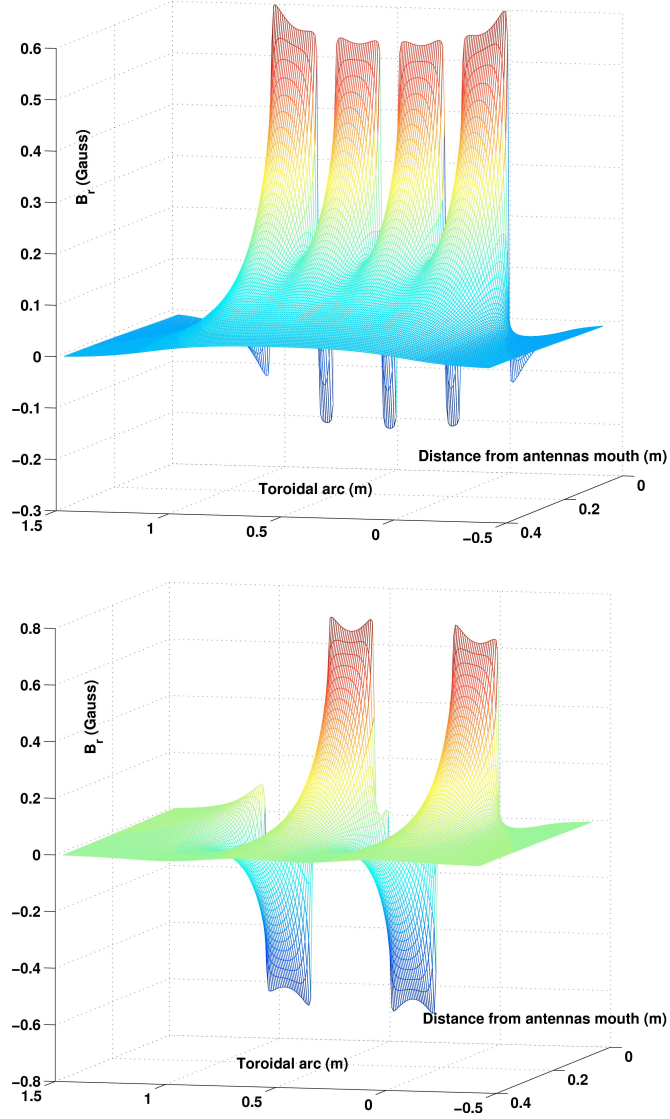


Figure 4.3: Radial component of the antenna magnetic field produced by an array of 4 antennas carrying 1 A current. 2 phasings are shown: + + + + (top) and + - + - (bottom). Close to the antennas mouth, the field has a value of about 0.6 G. It decays with the inverse of the distance from the antennas and it has less than 0.01 G at 0.4 m away from the antennas. In limiter plasmas, the value of the field at the last closed flux surface (LCFS), which is at ~ 0.04 m away from the antennas, is 0.45 G. In diverted plasmas, where the LCFS can be as far as 0.1 m away from the antennas, the field at the LCFS is 0.2 G. Very close to the antennas mouth, the field structure exhibits features that pertain to the details of the antenna geometry: its form is more rectangular-like and there is small local maxima at the points that are closer to the turns. These features smooth out quickly as one moves away from the antennas.

4.2 The magnetic field of the AE antennas in vacuum

then the Fourier components of the ϕ -shifted terms $B_I(R, Z, \phi - \alpha_j)$ in (4.14) are $\tilde{B}_I(R, Z, n) e^{-in\alpha_j}$. Thus, the Fourier series of (4.14) is

$$B(R, Z, \phi, \omega) = \sum_{n=-\infty}^{\infty} e^{in\phi} \left[\tilde{B}_I(R, Z, n) \sum_{j=1}^8 e^{-in\alpha_j} I_j(\omega) \right], \quad (4.17)$$

where the brackets contain the n -components of the antenna-driven spectrum in vacuum. It is observed that the frequency dependence of an individual n does not depend on the position $[R, Z]$ in the poloidal cross-section.

In practice, the position of the antenna assembly on octant 8 is at a major radius that is approximately 1 cm lower than that of the antennas sitting in the toroidally opposite octant 4. This introduces a small asymmetry in the magnitude of the field at a certain position $[R, Z]$. To include this asymmetry in the calculation, the expression (4.14) is modified so that it depends on the 2 toroidally-opposite reference antennas 1 and 5, i.e.

$$B(R, Z, \phi, \omega) = \sum_{j=1}^8 I_j(\omega) B_{Ij}(R, Z, \phi - \alpha_j) \quad (4.18)$$

where $B_{Ij} = B_{I1}$, $\alpha_j = \phi_j - \phi_1$ for $j = 1, \dots, 4$ and $B_{Ij} = B_{I5}$, $\alpha_j = \phi_j - \phi_5$ for $j = 5, \dots, 8$. Analogously to the derivation of (4.17), the Fourier components of this modified expression are

$$\tilde{B}_{I1}(R, Z, n) \sum_{j=1}^4 I_j(\omega) e^{-in\alpha_j} + \tilde{B}_{I5}(R, Z, n) \sum_{j=5}^8 I_j(\omega) e^{-in\alpha_j}. \quad (4.19)$$

The expression (4.19) is convenient in order to make a fast calculation of the driven spectrum and it is used in the normalization of the plasma response for the damping rate calculations (see Section 4.6). Figure 4.4 shows the radial component of the antenna field and its n -spectrum as function of the 3 sets of active antennas and the distance from the antennas (see figure 4.7 for a view of the antenna arrangement along the toroidal angle and the antenna numbering).

Figure 4.5 compares the n -spectra between a low- n and a high- n antenna current phasing. The phasing has an even symmetry, giving rise to predominantly even- n components. The low- n spectrum peaks at $n = 0$ with a half-width-at-half-maximum (HWHM) of $|n| \sim 11$. The high- n spectrum, peaks at $|n| = 14$ with the same HWHM. It is important to observe that, in the range $|n| = 0 -$

4.2 The magnetic field of the AE antennas in vacuum

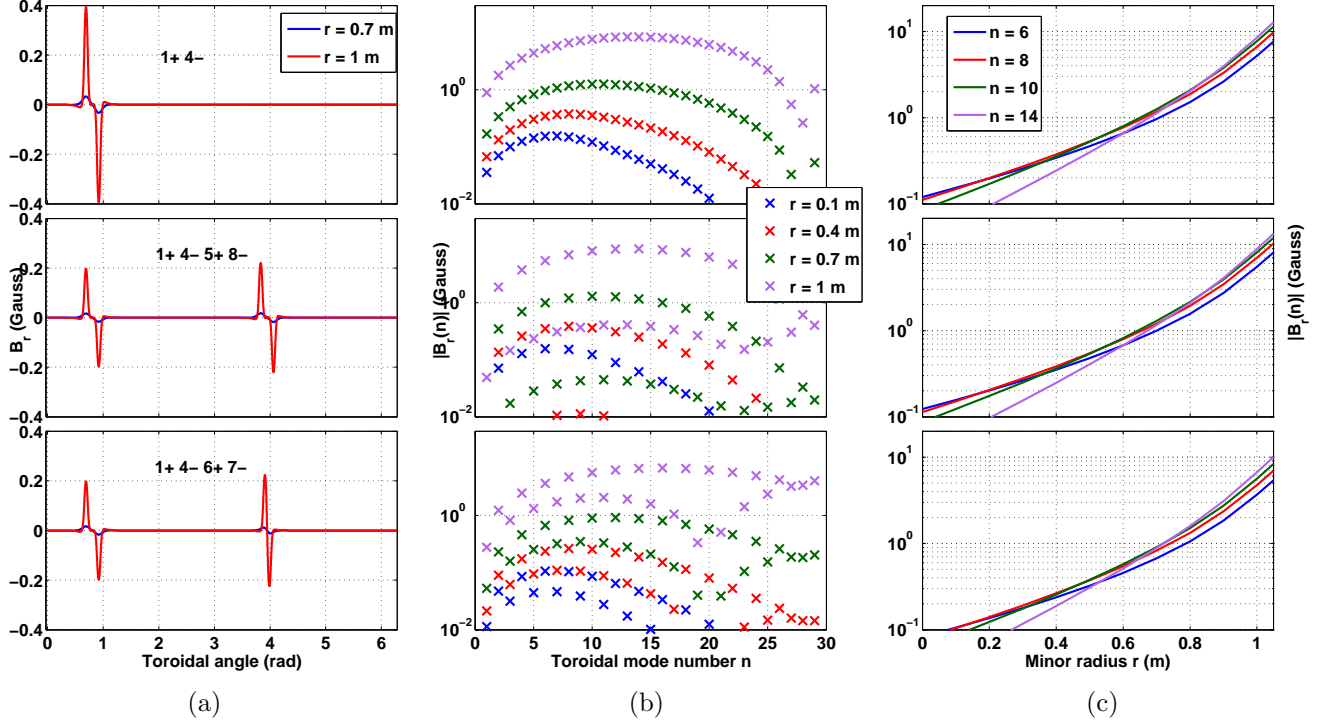


Figure 4.4: Antenna field as function of different sets of active antennas (top, middle and bottom rows), n number and the distance r (see figure 4.7 for a view of the antenna arrangement along the toroidal angle and the antenna numbering). Here, r is approximately the distance between the antenna mouth and the geometrical center of the torus. Figure (a) shows the radial field as a function of the toroidal angle. The top and middle plot in figure (b) shows the effect of adding active antennas at toroidally-opposite positions: the spectrum becomes purer as the odd components almost vanish because of the phasing even symmetry. The remaining part of the odd components is due the asymmetry in R between octant 4 and octant 8 and it is negligible (2 orders of magnitude less than the dominant even components). In practice, the bottom phasing was used during the experiments because of the unavailability of antennas 5 and 8. This makes the spectrum become less pure and the odd components are now about 2-5 times less than the dominant even ones. Figure (c) shows that the higher n -components decay faster as function of r than the their low- n counterparts. This behavior is especially stronger for $n \geq 10$ and it does not change qualitatively with the antenna phasing.

4.2 The magnetic field of the AE antennas in vacuum

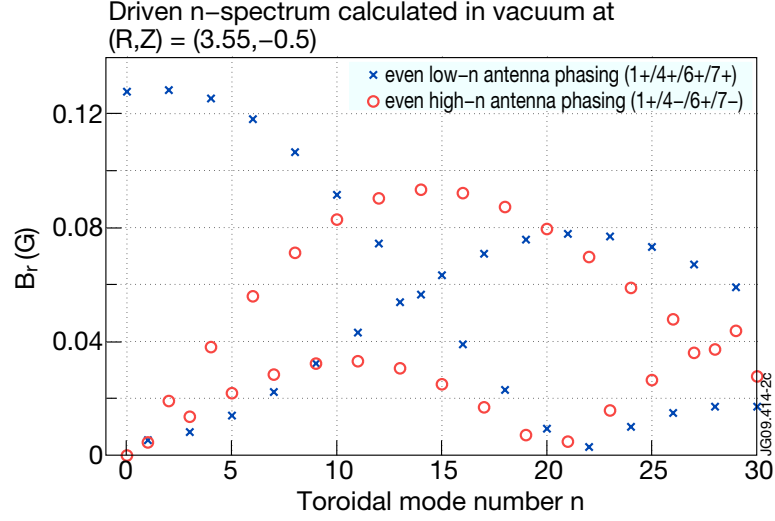


Figure 4.5: The n -spectrum of the antenna radial magnetic field in vacuum using the exact antenna geometry for even-symmetry low- and high- n antenna phasings. Only the right side-band of the spectrum is shown, as the driven n -spectrum is symmetric, i.e. the antenna excitation is stationary, comprising of toroidally counter-rotating waves of equal amplitude. The field is calculated at a position close to the last closed flux surface for antenna currents of 1 A. The active antennas are the 1, 4, 6 and 7.

10, the low- n phasing provides a stronger drive than the high- n phasing. The results for an odd-symmetry phasing are completely analogous, with the odd- n components being dominant. In this case, the low- n spectrum peaks at $n = 1$ and the high- n spectrum at $n = 15$.

A specific example of the driven n -spectrum that is calculated from actual current measurements is shown in figure 4.6. This is the case of a pulse where a strong coupling effect between the antennas 6, 7 and 8 occurs (figure 3.26). The n -spectrum is significantly distorted in the frequency range where the coupling is strong. This example implies that it is also possible to change the n -spectrum so that it is more peaked in narrower n -ranges by changing the relative phase and amplitude of the antenna currents. This is a very interesting possibility as it would enhance the antenna-plasma coupling for a much smaller set of n s and would greatly facilitate the n -decomposition of the plasma response and the interpretation of the data. As a result, there are already plans for an upgrade of the system that will include the installation of 8 independent amplifiers with the

4.2 The magnetic field of the AE antennas in vacuum

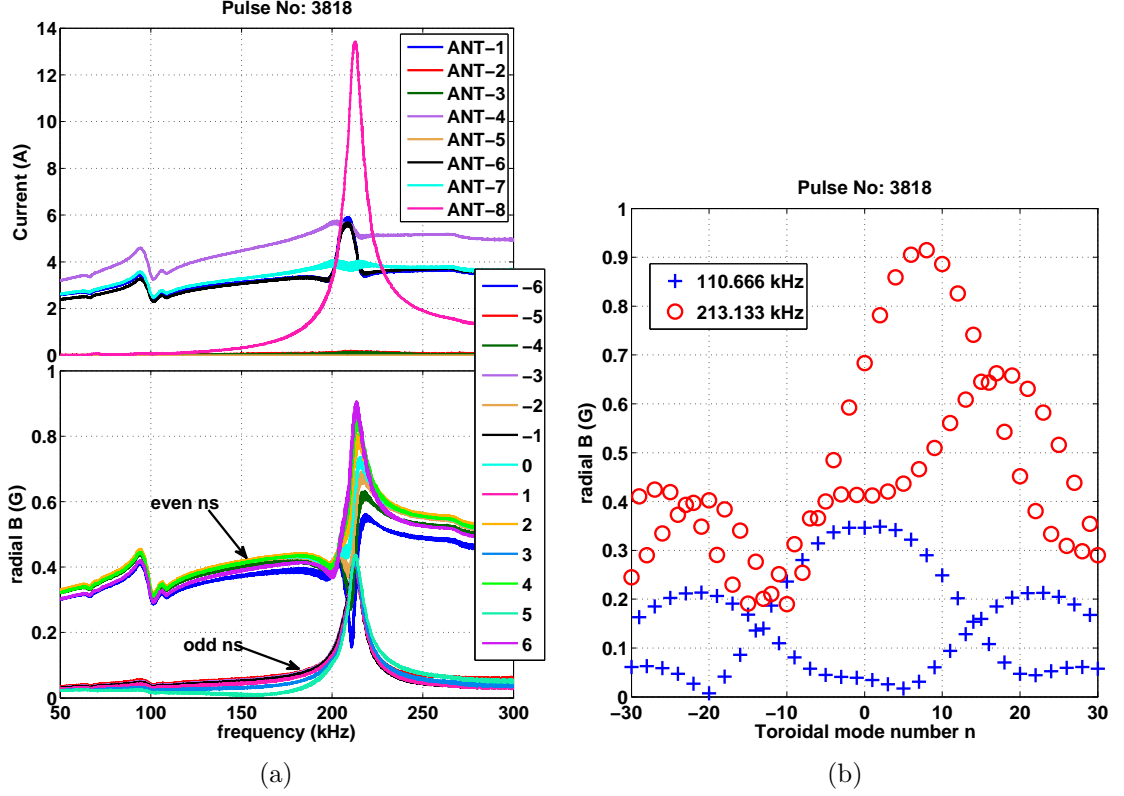


Figure 4.6: (a) Antenna currents (top) and the individual n -components (bottom) from $n = -6$ to $n = 6$ as function of frequency. Around 210 kHz, a large current flows on the passive antenna 8 because of the inductive coupling between neighboring antennas (top). As a result, the odd part of the spectrum around 210 kHz becomes comparable to the even components (bottom) and an asymmetry is developed between the positive and the negative part of the even n -spectrum ($n = -6$ decreases while $n = 6$ increases). (b) Complete n -spectrum at 2 different frequencies. At 110 kHz, there is no coupling and the n -spectrum is symmetric with respect to positive and negative ns and dominated by the even components (for $|n| < 12$). At 213 kHz, the whole spectrum becomes asymmetric with the positive ns having higher amplitude than the negative ns .

4.3 Calibration of the magnetic pick-up coils using their direct coupling to the AE antennas in vacuum

possibility to set arbitrary phases and amplitudes between them [80].

To summarize, the calculation of the magnetic field produced by the antennas in vacuum shows that the component of the radial magnetic field is the dominant component and that is 0.2-0.4 G/A at the plasma edge, depending on the plasma configuration. The antenna-driven n -spectrum that is derived from the field calculation confirms that the antenna currents determine the n -spectrum, while the exact geometry of the antenna coils or the asymmetry of the antenna position in R , which characterizes the two sets of coils, has a very small effect. The antenna excitation can be configured optimally to produce predominantly even or odd n -spectra using antennas from toroidally opposite positions. Such antenna configurations produce either a low- n spectrum, peaking at $n = 0 - 1$ with a half-width-at-half-maximum (HWHM) of $|n| \sim 11$ or a high- n spectrum, peaking at $n = 14 - 15$ with the same HWHM.

4.3 Calibration of the magnetic pick-up coils using their direct coupling to the AE antennas in vacuum

This Section describes the method that is used to calibrate the magnetic pick-up coils using their direct coupling to the AE antennas in vacuum. Figure 4.7 shows a view of the toroidal cross-section in JET, where the locations of the magnetic coils and the AE antennas are shown. The method benefits from the fact that several coils are at a sufficiently small distance from the antennas that a signal with relatively good signal-to-noise ratio (SNR) can be induced on them by the AE antennas. The coils that are calibrated using this method, as well as their toroidal angle coordinates, are shown in table 4.1. This set of coils is also used in this work for the damping rate calculations (see Section 4.6).

4.3.1 Direct coupling: background and formulation

According to Faraday's law of induction, the induced emf \mathcal{E}_k on a magnetic pick-up coil (called probe or sensor in the following) k due to a time-varying total flux

4.3 Calibration of the magnetic pick-up coils using their direct coupling to the AE antennas in vacuum

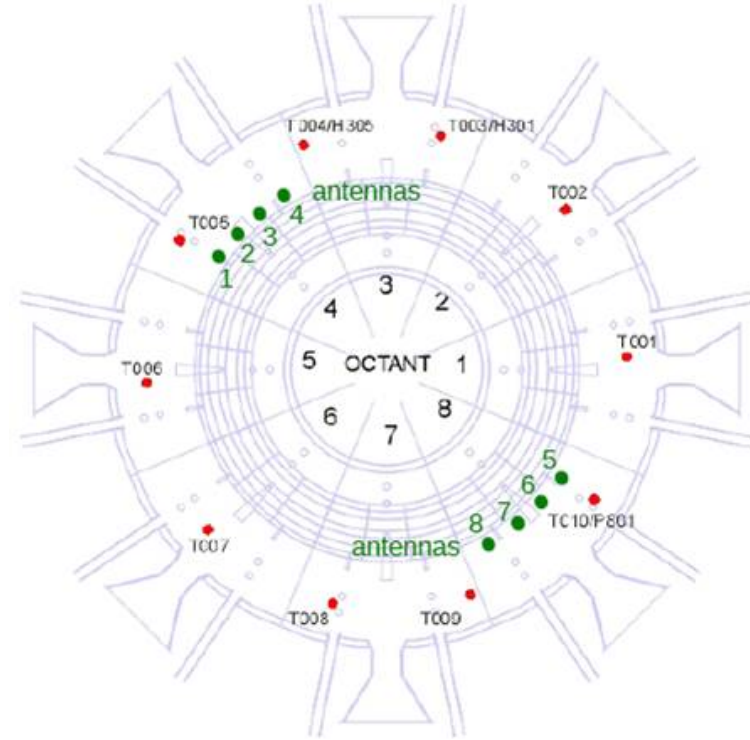


Figure 4.7: View of the toroidal cross-section in JET where the locations of the magnetic probes and AE antennas are shown. The coils H302-4 which are not shown are situated in octant 3 between T003 and T004.

Name	ϕ [$^\circ$]	Status 2008-2009
T001	2.97	OK
H302	92.94	OK
H303	103.11	OK
H304	108.74	OK
T004	110.38	OK
T006	182.94	OK ^a
T009	290.37	OK

^aIntermittently available.

Table 4.1: Summary of the toroidal array of the magnetic pick-up coils used in this work, all located at $[R, Z] \simeq [3.88, 1.01]$ m with a poloidal orientation 108.9° .

4.3 Calibration of the magnetic pick-up coils using their direct coupling to the AE antennas in vacuum

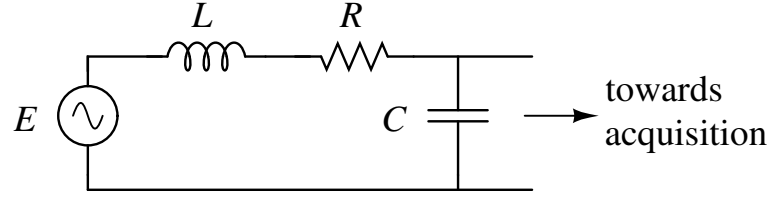


Figure 4.8: Circuit model of a magnetic coil.

λ_k^t crossing its effective area is:

$$\mathcal{E}_k^t = -\frac{d\lambda_k^t}{dt} \quad (4.20)$$

For the rest of the present Section, we consider time-varying quantities $A(t)$ that vary at a given frequency ω with amplitude and phase that are only a function of ω as follows

$$A(t) = A(\omega) \cos(\omega t + \theta(\omega)) = \Re\{\hat{A}(\omega)e^{i\omega t}\}, \quad (4.21)$$

where the complex quantity \hat{A} contains the information of the amplitude and the phase of A and it is called the phasor of A . From now on, only the phasors will be used and the hat notation will be omitted. Hence, the phasor representation of equation (4.20) is

$$\mathcal{E}_k^t(\omega) = -i\omega\lambda_k^t(\omega) \quad (4.22)$$

The flux is linked to the various currents present in the environment of the sensor through the inductance matrix

$$\lambda_k^t = \sum_n M_{kn} I_n \quad (4.23)$$

where $L_k = M_{kk}$ is the self-inductance of the sensor. Here, the effect of the wall is considered by modeling it as a perfect conductor and using the image method. This is valid approximation, as described in the section 4.2. Then, for any primary loop (be it an antenna or a coil), a identical secondary loop which carries an opposite current is situated symmetrically on the other side of the wall surface. Linearity allows to separate the emfs due to the various currents. In addition, by considering a proper electrical model of coil (shown in figure 4.8), we isolate the emfs \mathcal{E}_k and fluxes λ_k that are due to the presence of external

4.3 Calibration of the magnetic pick-up coils using their direct coupling to the AE antennas in vacuum

magnetic fields and are not self-induced by the current flowing in the coil. Hence, the total flux can be written as

$$\lambda_k^t(\omega) = (L_k - M_k^w) I_k(\omega) + \lambda_k(\omega) , \quad (4.24)$$

where

$$\lambda_k(\omega) = \sum_{n \neq k} (M_{kn} - M_{kn}^w) I_n(\omega) . \quad (4.25)$$

In the expression (4.25) M_k^w is the mutual inductance between the coil k and its image, M_{kn} are the mutual inductances between the coil k and the antenna n and M_{kn}^w are the mutual inductance between the coil k and the image of antenna n . These inductances are purely geometrical quantities that depend on the size, shape and relative positions of the coupled coils and the wall. Because the coils are located relatively far from the antennas, it is expected that M_{kn}^w are comparable to M_{kn} and cannot be neglected. Thus the equation (4.25) can be rewritten as

$$\lambda_k(\omega) = \sum_{n \neq k} M'_{kn} I_n(\omega) , \quad (4.26)$$

where $M'_{kn} = M_{kn} - M_{kn}^w$.

For every signal S , we define the calibration factor H_S that determines the relation between the raw value recorded on the acquisition side and the actual value of the physical quantity:

$$S^r = H_S S \quad (4.27)$$

Applying this equation to $\mathcal{E}_k(\omega) = -i\omega\lambda_k(\omega)$, one obtains:

$$\mathcal{E}_k^r(\omega) = -i\omega H_{\mathcal{E}_k}(\omega) \sum_{n \neq k} M'_{kn} \frac{I_n^r(\omega)}{H_{I_n}(\omega)} \quad (4.28)$$

From now on we will drop the $n \neq k$ index in the summation, as it is now clear that the sensor currents are not included. We may rewrite the relation as follows:

$$\mathcal{E}_k^r(\omega) = - \sum_n C_{kn}(\omega) I_n^r(\omega) \quad (4.29)$$

where $\mathcal{E}_k^r(\omega) = \frac{\mathcal{E}_k^r(\omega)}{i\omega}$, and the system coupling functions

$$C_{kn}(\omega) = M'_{kn} \frac{H_{\mathcal{E}_k}(\omega)}{H_{I_n}(\omega)} \quad (4.30)$$

4.3 Calibration of the magnetic pick-up coils using their direct coupling to the AE antennas in vacuum

depend on the transfer functions $H_{\mathcal{E}_k}(\omega)$, $H_{I_n}(\omega)$ and on the mutual inductances M'_{kn} .

Knowing the functions C_{kn} solves the direct coupling problem in vacuum. The functions C_{kn} can be calculated from their constituent components or measured. The estimation of the functions $C_{kn}(\omega)$ from their components is difficult, because the calculation of the parameters M'_{kn} needs to include a realistic wall geometry. The measurement of $\arg[H_{I_n}(\omega)]$ also presents technical difficulties. On the other hand, the functions C_{kn} can be evaluated from appropriate measurements that make use of the linearity of (4.29), giving

$$C_{kn}(\omega) = \frac{\mathcal{E}_k^r(\omega)}{I_n^r(\omega)} \Big|_{I_{n'}^r=0, \forall n' \neq n} . \quad (4.31)$$

The above expression means that C_{kn} can be determined by driving current into a single antenna n and measuring the response on the coil k . It should be noted here that the requirement that only 1 antenna carries current cannot be satisfied in the usual AE exciter configurations because of the intrinsic coupling between the neighboring antennas, which becomes non-negligible for certain frequencies. Nevertheless, it will be shown that the effect of a secondary current can be taken into account during calculations.

The measurements that have just been described can be used in order to derive information about $H_{\mathcal{E}_k}$ and M'_{kn} if an amplitude calibration of the antenna currents is available, i.e. if the functions $|H_{I_n}|$ are known, and if the functions $\arg H_{I_n}$ are very similar for all antennas. If we consider a current I_{n_1} that contributes to the signal of the coils k and is non-zero for all frequencies, the relation (4.28) can be rewritten as follows:

$$M_{kn_1} H_{\mathcal{E}_k}(\omega) \exp(-i \arg[H_{I_{n_1}}(\omega)]) = -\frac{\mathcal{E}_k^r(\omega)}{R_{kn_1}(\omega)} \frac{|H_{I_{n_1}}(\omega)|}{I_{n_1}^r(\omega)} , \quad (4.32)$$

where

$$R_{kn_1}(\omega) = 1 + \sum_{n \neq n_1} \frac{M_{kn}}{M_{kn_1}} \frac{I_n(\omega)}{I_{n_1}(\omega)} . \quad (4.33)$$

In the equation (4.32), the RHS can be readily calculated when any secondary currents in the vicinity of the coil k that are induced from the antenna n are zero or negligible, i.e., when $R_{kn_1} = 1$. When this condition cannot be satisfied and there are other currents in the vicinity of the coil k , the method described in the next paragraph needs to be used.

4.3 Calibration of the magnetic pick-up coils using their direct coupling to the AE antennas in vacuum

This method is based on the observation that, driving a current into different antennas that are directly coupled to the same coil k should lead to the same transfer function $H_{\mathcal{E}_k}$ for the coil k . Thus, one should be able to find a unique set of ratios $\frac{M_{kn}}{M_{kn_1}}$ and differences between the functions $\arg H_{I_n}$ that set the difference between the measurement of $|H_{\mathcal{E}_k}|$ for different coupled active antennas to zero. If a solution to this problem cannot be found, it might mean that the modeling is incorrect or some current has not been taken into account. Conversely, if a solution can be found for all frequencies, this is an additional indication that the modeling is correct and all the currents have been properly included in the calculation.

In practice, the unique set of $\frac{M_{kn}}{M_{kn_1}}$ ratios and the differences between the functions $\arg H_{I_n}$ can be found by means of an optimization method. In order to illustrate the method, we use equation (4.32) for 2 different active antennas n_1 and n_2 (which correspond to 2 different sets of measurements, a and b) and form the difference of their amplitudes, which serves as a cost function:

$$\min_{\mu} \left\| \frac{\mathcal{E}_k^{r,a}(\omega) H_{I_{n_1}}(\omega)}{I_{n_1}^{r,a}(\omega)} \frac{1}{1 + \frac{1}{\mu} \frac{I_{n_2}^a(\omega)}{I_{n_1}^a(\omega)}} - \frac{\mathcal{E}_k^{r,b}(\omega) H_{I_{n_2}}(\omega)}{I_{n_2}^{r,b}(\omega)} \frac{\mu}{1 + \mu \frac{I_{n_1}^b(\omega)}{I_{n_2}^b(\omega)}} \right\|. \quad (4.34)$$

Here $\mu = \frac{M_{kn_1}}{M_{kn_2}}$ is the unknown parameter and the difference between the phase calibration of the 2 antennas is assumed to be zero for simplicity. Assuming that the above cost function can be minimized to zero, the following final equation is obtained:

$$A(\omega)|1 + \mu C(\omega)| = |\mu + B(\omega)|, \quad (4.35)$$

from which the parameter μ can be specified, given the measured functions of frequency $A(\omega)$ (real), $B(\omega)$ (complex) and $C(\omega)$ (complex). Hence, with the above method, the LHS of (4.32) can be entirely specified for all the probes for which an antenna-induced signal has sufficient signal-to-noise ratio, even when the probe signal is induced by more than 1 antenna.

Consider now the equation (4.30) for two sensor-antenna pairs: (k, n_1) and (k', n_2) . By dividing the respective sides of the two equations, one obtains

$$\frac{M_{kn_1}}{M_{k'n_2}} \frac{H_{\mathcal{E}_k}}{H_{\mathcal{E}_{k'}}}(\omega) e^{-i \arg(H_{I_{n_1}} - H_{I_{n_2}})(\omega)} = - \frac{\mathcal{E}_k^{r'}(\omega)}{\mathcal{E}_{k'}^{r'}(\omega)} \frac{R_{k'n_2}(\omega)}{R_{kn_1}(\omega)} \left| \frac{H_{I_{n_1}}(\omega)}{H_{I_{n_2}}(\omega)} \right| \frac{I_{n_2}^r(\omega)}{I_{n_1}^r(\omega)} \quad (4.36)$$

4.3 Calibration of the magnetic pick-up coils using their direct coupling to the AE antennas in vacuum

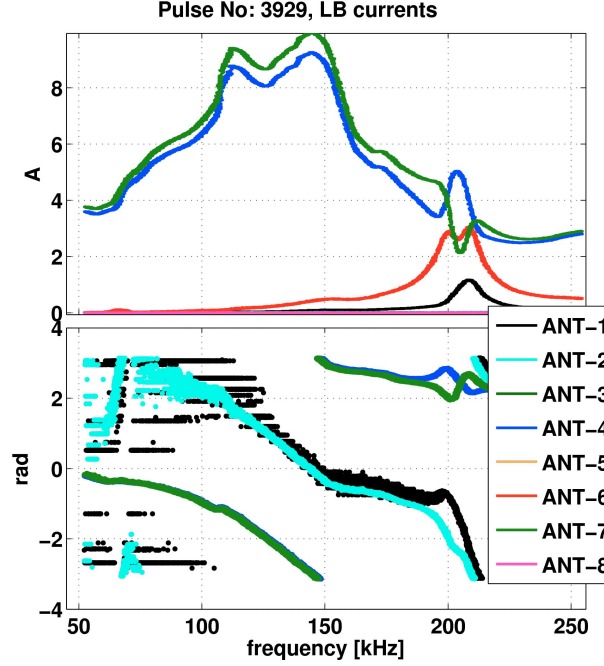


Figure 4.9: Antenna current measurements used for the calibration of the magnetic pick-up coils. Notice the currents on the passive antennas 1 and 6, because of the coupling between neighboring antennas. Less current is induced on antenna 1 by the active antenna 4, as compared to the current induced on antenna 6 by antenna 7, because the distances between antennas 1 and 4 is larger than that between antennas 6 and 7. AE exciter configuration: active antennas 4 and 7, phasing ++, DU 1:2 and AGC control of the I_{lb} of antenna 7.

From expression (4.36), the difference between the phases of the transfer functions of the probes k and k' can be obtained, when $H_{I_{n_1}} = H_{I_{n_2}}$ or when $n_1 = n_2$. In particular, when $n_1 = n_2$ and when there is no passive antenna contribution, *all* terms related to antenna currents cancel out and the phase difference estimation depends exclusively on the raw pick-up coil signals with virtually no approximation.

4.3.2 Measurements and results

The method that has been presented in the previous section was applied on the measurements made with the AEAD from a set of dedicated pulses (3897-3900, 3925-3929, 4000). The experimental setup was the following:

4.3 Calibration of the magnetic pick-up coils using their direct coupling to the AE antennas in vacuum

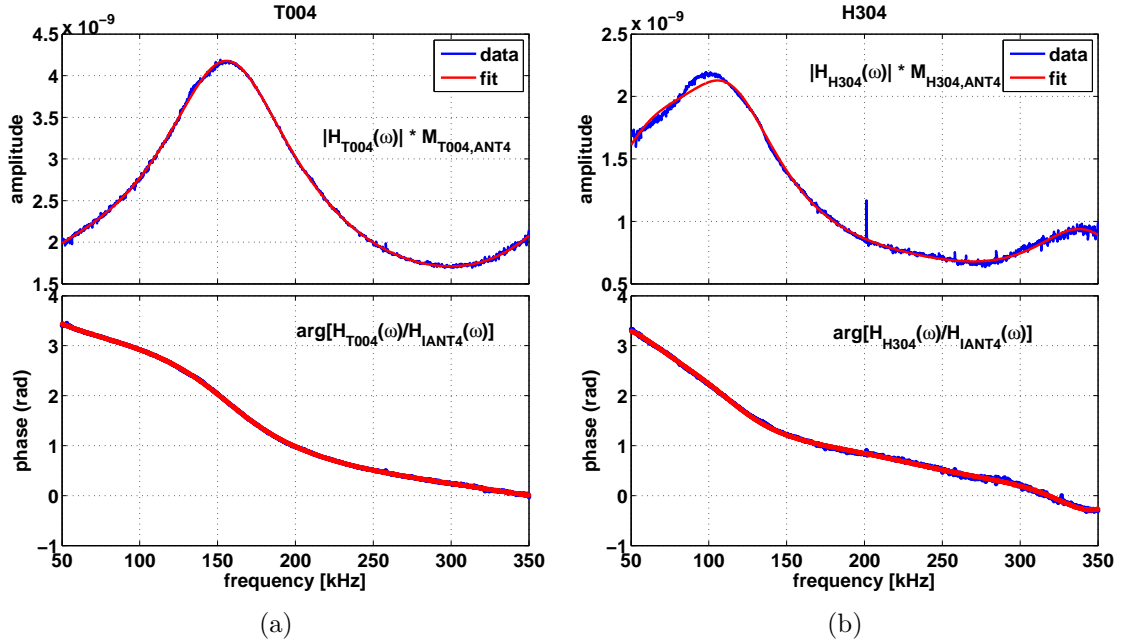


Figure 4.10: Amplitude (top) and phase (bottom) of the LHS term of equation (4.32) for the coils T004 (a) and H304 (b). The data that come from both coils are normalized to the current on antenna 4. The polynomial fit in frequency is also shown. Because of the proximity of the coils to the antenna 4, the data are of a very good quality with a high signal-to-noise ratio.

- Only 1 antenna was active in every octant.
- One high-current ($I_{\text{ant}} = 3 - 9\text{A}$) pulse was run for frequencies up to 250 kHz.
- Keeping the same configuration, a lower-current ($I_{\text{ant}} = 2 - 4\text{A}$) pulse was run for frequencies up to 500 kHz.

The data from all the pulses that were examined resulted always in the measurement of the same transfer functions, even if the antenna current responses were different from pulse to pulse (due to the different settings). This gives confidence in the validity of the results. The antenna currents measured on one particular pulse are shown in figure 4.9. Note that the 2 currents of antenna 6 and 7 contribute simultaneously to the signal of the coils that are coupled to, T001 and T009 as shown in figure 4.7, for frequencies around 210 kHz. It should be noted

4.3 Calibration of the magnetic pick-up coils using their direct coupling to the AE antennas in vacuum

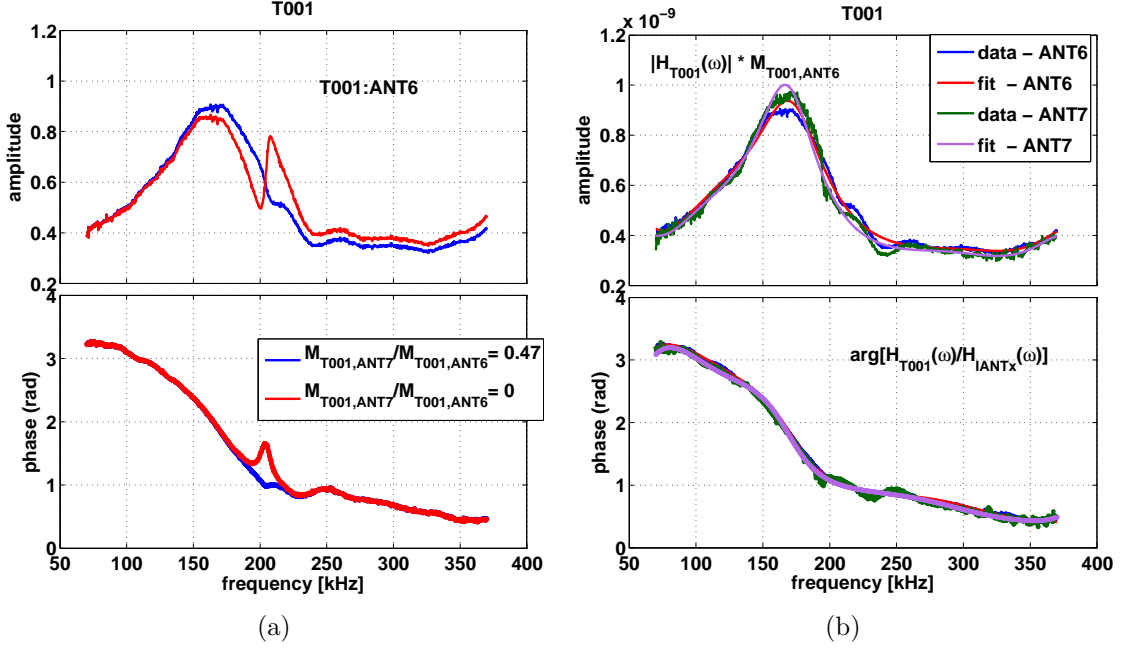


Figure 4.11: Amplitude and phase of the LHS term of equation (4.32) for the coil T001. In the following, the parameter μ is $\mu = M_{T001,ANT7}/M_{T001,ANT6}$. Figure (a) shows the 2 results that are obtained from the normalization the coil signal to the current of antenna 6 assuming zero, i.e. $\mu = 0$, and non-zero, i.e. $\mu \neq 0$ secondary coupling from antenna 7. With the assumption of zero coupling to the antenna 7, a fast variation of the transfer function occurs exactly in the frequency range where the antenna 7 current is high. The value of μ was determined by satisfying the requirement that the 2 normalizations with either the current of antenna 6 or the current of antenna 7 yield the same transfer function in amplitude, as shown in figure (b). The small difference that remains after compensating for the secondary coupling is attributed to the fact the phase difference between H_{IANT6} and H_{IANT7} has a frequency dependence which has not been accounted for in the optimization calculation with the equation (4.34).

4.3 Calibration of the magnetic pick-up coils using their direct coupling to the AE antennas in vacuum

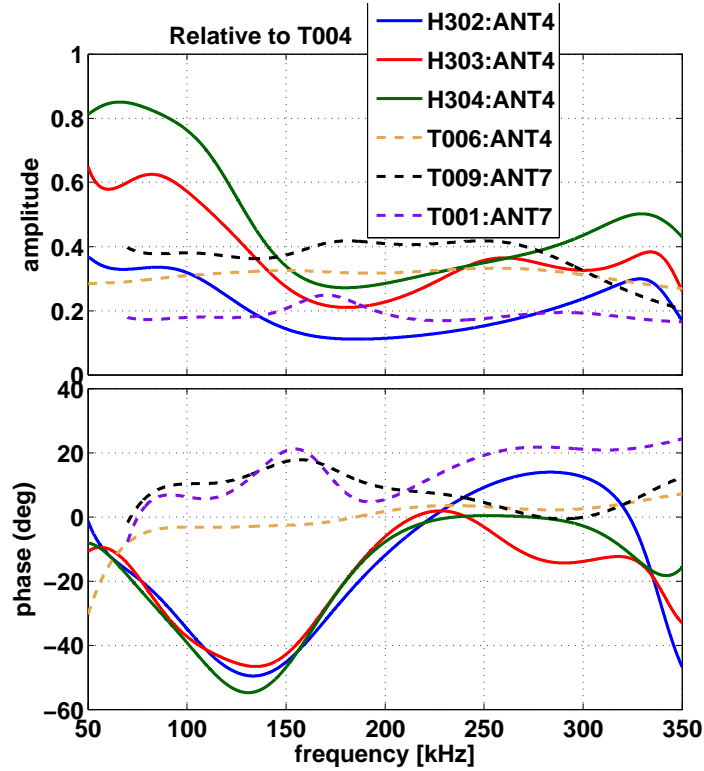


Figure 4.12: Relative amplitude and phase (following the LHS term of equation (4.36)) for the coils that have non-zero coupling to the antennas 4 and 7. The T004 coil is taken as reference.

that the upper frequency limit for the validity of the calibration is 350 kHz, above which, the antenna currents start to deviate from the currents measured at the LBs.

Figures 4.10a and 4.10b show the data and the fits obtained for coils T004 and H304. Because of the proximity of the two coils to antenna 4, the SNR is remarkably high. Here, there is practically no effect from the secondary current on antenna 1 because of the large distance. On the other hand, the effect of the secondary current when driving current into either antenna 6 or antenna 7 is strong. In this case we use the optimization method described in the previous section (equation (4.34)). Figures 4.11a and 4.11b show the data and the result of the method for the coil T001. Note that one obtains the same transfer function by normalizing the T001 signal either to antenna 6 or antenna 7 when the ratio $\mu = M_{T001,ANT7}/M_{T001,ANT6}$ is finite. If $\mu = 0$, a strong effect is observed around

4.3 Calibration of the magnetic pick-up coils using their direct coupling to the AE antennas in vacuum

~ 210 kHz, affecting both amplitude and phase.

We now apply equation (4.36) to the collected data. The results that were obtained for these probes are shown in figure 4.12. We first consider the group of coils H30x, T004 and T006 that have non-zero coupling to antenna 4. As underlined in the previous section, the data from these coils are normalized to the same antenna current, thus do not suffer any built-in uncertainty in their phase difference from T004. The data suggest that coils T004 and T006 have similar transfer functions: indeed, the ratio of the transfer functions amplitudes is fairly flat with respect to frequency and in addition, the phase difference is very small (less than 4 degrees) in most of the frequency range. The same observation can be made for coils H302, H303 and H304. The transfer functions of these coils follow the same pattern as a function of frequency and their phases differ by no more than 10 degrees up to 250 kHz. In figure 4.12, the amplitudes contain the ratios $\frac{M_{H30x,ANT4}}{M_{T004,ANT4}}$ and their scaling is consistent with the increasing distance between the coils and antenna 4.

A notable difference is observed between the transfer functions of the 2 groups of coils: in phase, an important difference (more than 20 degrees) characterizes the whole frequency range from 70 to 170 kHz, with a maximum of 55 degrees at 140 kHz. In amplitude, it is observed that the amplitude of the coil H304 drops from 0.8 at 50 kHz to a level of 0.3 at 200 kHz. This comparison between T004 and H304 is justified by the fact that they are located at almost equal distance from antenna 4 (2.10 and 2.18 m, respectively) and thus, the mutual inductances to the antenna 4 should be very similar.

We now consider coils T001 and T009, whose signals are normalized to the current of antenna 7. Again, the difference between their phases is small up to 200 kHz, while at higher frequencies they deviate up to 20 degrees. Their difference in phase with respect to T004 varies with frequency, with the maximum difference being at 20 degrees. Their relative amplitudes are reasonably flat with respect to frequency.

These results are consistent with the fact that the two groups of coils H30x and T00x were installed at different times and the characteristics of their connection to the acquisition system differ. These results are also similar to those obtained for the calibration of the KC1F fast magnetics system that was using the same coils [81, 82].

4.3 Calibration of the magnetic pick-up coils using their direct coupling to the AE antennas in vacuum

The main uncertainties in the preceding analysis are the following:

- the difference $\phi(\omega)$ between H_{I4} and H_{I7} . In principle, these 2 measurements are identical: the whole circuit between the measurement at the link boxes (LBs) and the digitizer (ADCs) are made with the same specifications. Indeed, the difference between the measured phases in various shots (e.g. figure 4.9) is no more than 5 degrees. Since the phases of the antenna currents should also be almost the same (due to the same antenna lines of the AE exciter), one can reasonably assume that the $\phi(\omega)$ should be in the range 5–10 degrees.
- the mutual inductances M'_{kn} . These can be calculated using a realistic geometry of the antennas, the coils and the wall.

Based on the above analysis, we can recommend a specific way in order to calibrate of the AEAD pick-up coil data:

- phase: use the T004 as reference and adjust the phases of the other coils.
- amplitude: treat the T00x and the H30x coils as 2 groups of coils different amplitude calibrations. Adjust one with respect to the other according to the ratio between H304 and T004.

This method is used to calibrate the data for the damping rate calculations (see Section 4.6).

4.3.3 Comparison with the calibration from impedance measurements

In this section we make a comparison between the results that were presented in the previous section and the absolute calibration curves that were extracted from impedance measurements [83], following the method presented in [81]. Another proof of the fundamental theorem that is used in this method (section D in [81]) is provided in the appendix A.3. This proof extends the class of circuits for which the method applies to all those circuits that can be represented with a network parameter matrix ABCD (also called transmission matrix, [76]).

The motivation for this comparison is that, if the normalized amplitude of the transfer functions derived with the 2 methods matches exactly in terms of their

4.3 Calibration of the magnetic pick-up coils using their direct coupling to the AE antennas in vacuum

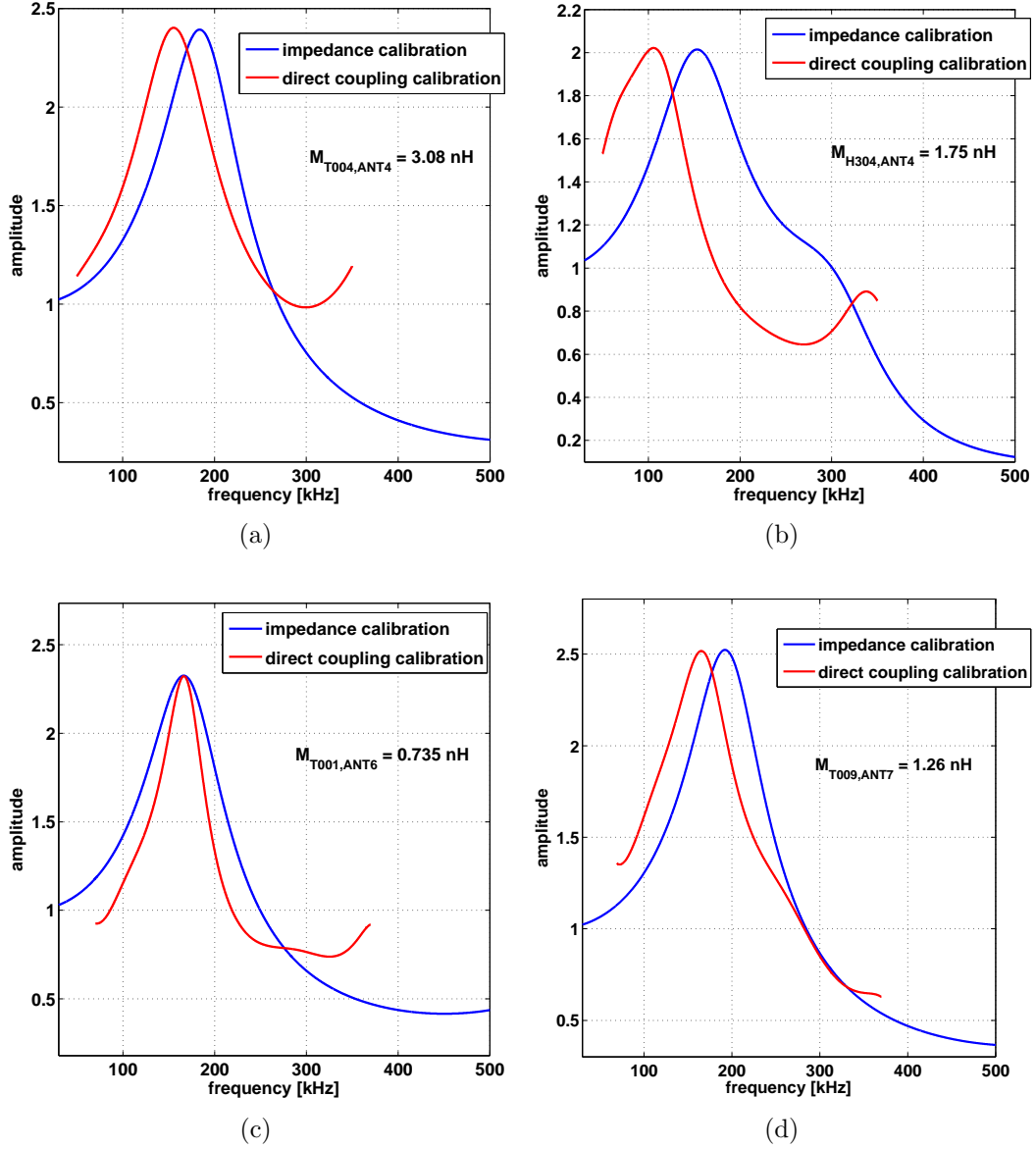


Figure 4.13: Comparison between the transfer function amplitudes that were measured with direct-coupling measurements and the calibration using the impedance measurements. The values of the mutual inductances M_{kn} that were used to make this comparison (so that the curves have the same maximum) are also shown. Since the 2 curves in comparison do not match in terms of frequency dependence, the comparison cannot lead to the determination of M_{kn} .

frequency dependence, then this would be very good evidence for the validity of the 2 calibrations and also, provide an estimate for M_{kn} . The comparisons for 4 coils are shown in the 4.13. It is observed that from both methods a resonance is detected between 100 and 200 kHz. However, with the exception of T001 (figure 4.13c), the calibration using the impedance method predicts a resonant frequency that is different from the direct-coupling measurements by 20 to 50 kHz. Thus, it is not possible to specify M_{kn} from this comparison and further work is needed to identify the reason of this discrepancy.

4.4 The n -spectrum of the plasma response

At any given time point, the plasma response to the antenna excitation can be a superposition of several modes with different n . In order to decompose this mixture into its individual n -components, the SparSpec algorithm [84] is used. SparSpec¹ is the implementation of a new method of fitting sinusoids to irregularly sampled data, based on a sparse spectrum representation of signals. Its performance has been shown to be superior to the other methods of mode number estimation for the post-pulse data analysis [85]. The implementation of the SparSpec algorithm that is used for the analysis of the AEAD data minimizes the following expression, similarly to the least-square criterion

$$J(\mathbf{x}) = \frac{1}{2} \|\mathbf{y} - \mathbf{W}\mathbf{x}\|^2 + \lambda_N \max |\mathbf{W}^* \cdot \mathbf{y}| \sum_{k=-K}^K |x_k|, \quad (4.37)$$

Here, $\mathbf{y} = [y_1 \dots y_P]^T$ is the vector of the complex data taken at toroidal angles ϕ_p , $\mathbf{x} = [x_{-K} \dots x_K]^T$ is the vector of the unknown complex spectral amplitudes associated with mode number n_k , $k = -K \dots K$ and \mathbf{W} is a matrix with elements $W_{pk} = \exp(i2\pi\phi_p n_k)$. The parameter λ_N can be set to values from 0 to 1 and is an input to the minimization algorithm. Higher values of λ_N make the algorithm converge to solutions with fewer non-zero spectral components. With SparSpec, the amplitude-phase information from all magnetic probes is transformed into amplitude-phase spectral information for individual n -components.

In order to ascertain the SparSpec estimations of the n number against errors due to hidden periodicities in the toroidal array of the coils or too much noise

¹available at <http://www.ast.obs-mip.fr/Softwares>

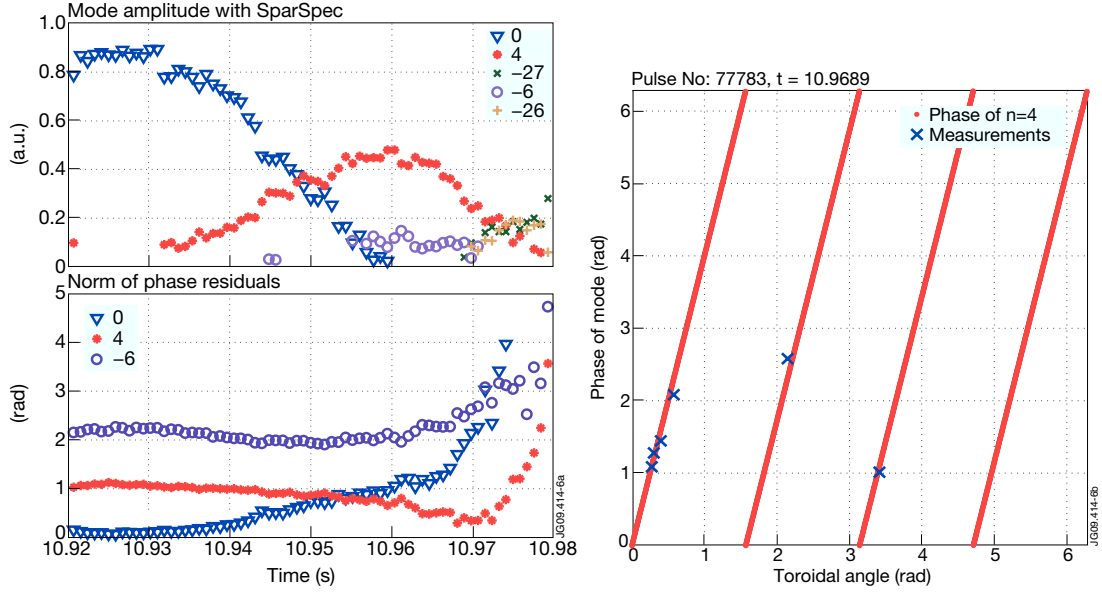


Figure 4.14: (Left) An example taken from JET pulse #77783 shows modes $n = 0$ and 4 overlapping with each other. SparSpec estimation (top) is in very good agreement with the norm of the residuals of the phase fits (bottom). (Right) Phases of the magnetic probes at $t = 10.9689$ s align very well with the phase of a $n = 4$ mode.

of the data, the penalization parameter λ was varied over a big range of values. It was verified that for small values of λ , i.e. when a big number of modes is tolerated, the dominant modes remain the same. Furthermore, SparSpec results have been shown to be in very good agreement with phase fitting calculations, as illustrated example for a typical example shown in figure 4.14.

The experimental data show a very good correlation between the observed- n spectrum and the driven- n spectrum. For example, it is predicted from the calculations of the driven- n spectrum in section 4.2 that, using active antenna at toroidally opposite angles, predominantly even or odd n 's are driven. Indeed, the measured plasma response is dominated by the same parity characterizing the driven spectrum, as shown in figure 4.15 for an odd- n excitation. Figure 4.16b shows an example for an even- n excitation. The experiments also show that when the antenna phasing changes from low- n to high- n , then the drive of the modes in the range $|n| = 0 - 8$ is reduced by an order of magnitude. This is also in agreement with the calculation of the driven spectrum.

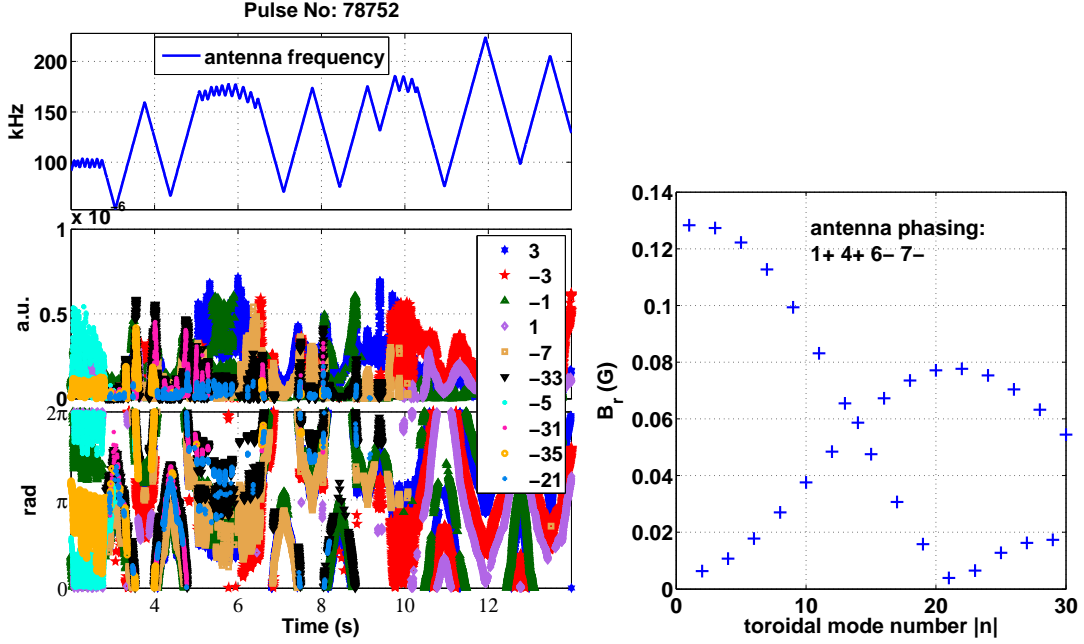


Figure 4.15: (Left) Example of the estimation of the n -spectrum of the plasma response with SparSpec. The antenna frequency is plotted on the top, the amplitudes and the phases of the n -components are shown in the middle and bottom plot, respectively. (Right) Driven n -spectrum calculated with the antenna phasing used in the specific discharge (#78752). Note that the n -spectrum of the plasma response is dominated by odd n , $|n| = 1, 3, 5, 7$, in very good agreement with the parity of the driven n -spectrum. The components of very high- n , $|n| > 20$ are numerical artifacts. The SparSpec calculation parameters in this case are $\lambda_N = 0.35$ and $K = 35$.

4.5 Integration of SparSpec in the real-time mode-tracking system

The AE antenna diagnostic is operated via the Alfvén Eigenmode Local Manager (AELM). The AELM includes an implementation of a real-time mode tracking algorithm, which was installed and used already for the saddle-coil experiments [57]. In the AELM, the plasma transfer function $H(\omega) = \frac{N(\omega)}{D(\omega)}$ is constructed from the input data, as described in [55]. The input data are synchronously detected signals. Any antenna current can be used for the denominator $D(\omega)$ and the signal from one magnetic probe or the sum of several of them can be used for

4.5 Integration of SparSpec in the real-time mode-tracking system

the numerator $N(\omega)$. For example, by subtracting the signals coming from two probes located at toroidally opposite position, $N(\omega) \propto 1 - e^{in\pi}$ and the even- n components of the spectrum are filtered out.

This method, although straightforward and robust, offers limited possibilities with respect to filtering specific n numbers. This can be done by integrating SparSpec into the AELM. The computational efficiency of SparSpec, which enables its real-time application, is due to the choice of the ℓ^1 -norm for the penalization function (the second term in equation (4.37)) and the use of an iterative coordinate descent procedure for the minimization of $J(\mathbf{x})$ [84]. When the AELM is set to use the SparSpec mode of operation, the numerator of the plasma transfer function is specific to an individual mode n , i.e. $N(\omega) \propto \delta \dot{B}_\theta(n, \omega)$.

In the following, we show how the successful integration of SparSpec in the AELM helps studying the medium and high- n AEs and we present a benchmark against the post-pulse analysis of the data. More information on the AELM upgrade is contained in reference [86].

The direct benefits from a real-time estimation of the n -spectrum are that tracking on low- n modes can be avoided and that tracking on individual- n modes is ensured. Moreover, the detection of simultaneously excited n 's by the antennas is in principle possible. These capabilities are illustrated in figure 4.16. In the top figure 4.16a, the real-time signals are shown, while in the bottom figure 4.16b, the post-pulse analysis of the data is shown. The user of the diagnostic can choose a set of mode numbers for which tracking is desirable. In this case, the range $|n| \in [4, 8]$ has been enabled. The program estimates the n -spectrum, then seeks to identify a mode resonance from that range. In this example, the candidate mode numbers, i.e. the modes found in the plasma response and belonging to the specified range, are $n = 4, -4, 8$ and -7 . For these modes, when AELM recognizes a candidate mode resonance, the tracking flag is raised and the twist, i.e. the variation of phase of the plasma transfer function, is computed. If the twist exceeds a given threshold and the mode amplitude falls below a given threshold, a full mode resonance has been covered and the frequency scan changes direction. In this case, the algorithm locks onto a $n = 4$ resonance at 9.5 s. As shown in the post-pulse n -spectrum, the resonances with $n = 0$ and $n = 2$ are avoided. Without the use of SparSpec, i.e. using directly the magnetic probe signals, the

4.5 Integration of SparSpec in the real-time mode-tracking system

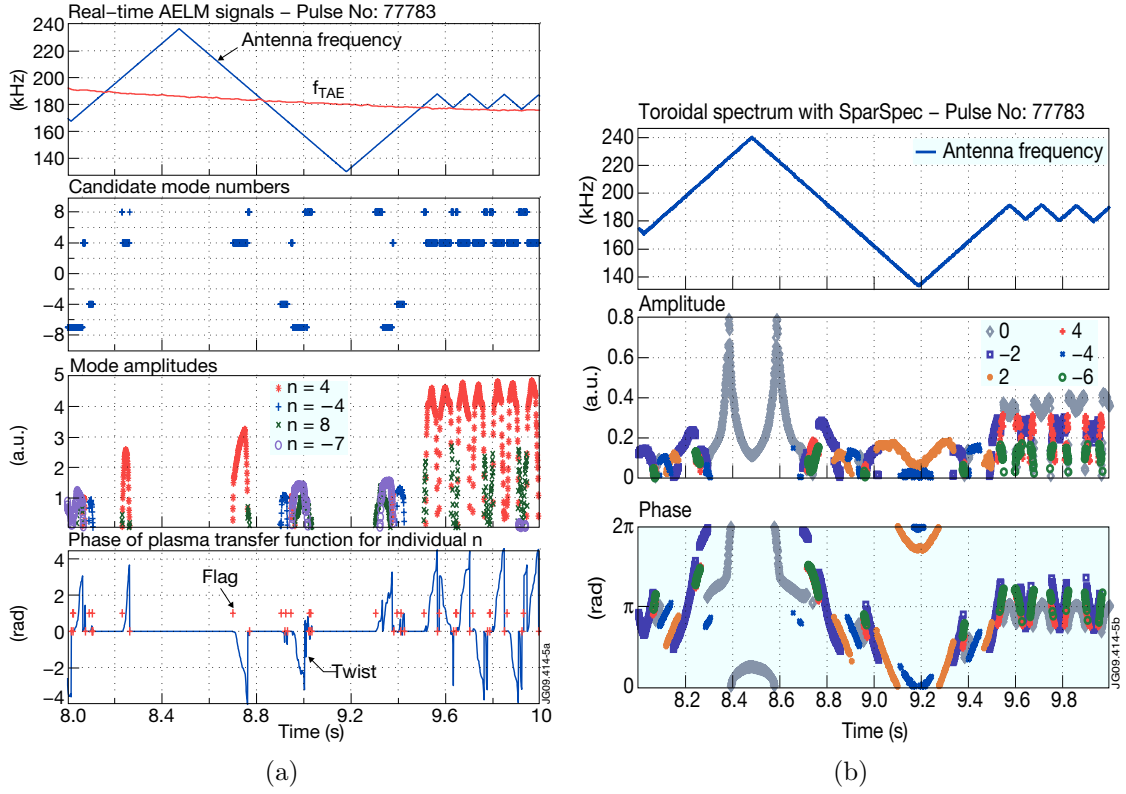


Figure 4.16: Illustration of the n -number filtering achieved in real-time. The system follows an $n = 4$ mode, while several other n s, namely $n = 0$, -2 and -6 , are excited inside the narrow frequency scans. (a) Real-time signals of the mode tracking system. The frequency $f_{TAE} = \frac{v_A}{4\pi qR}$ is evaluated in real-time assuming $q = 1.5$ and using a line-integrated interferometry measurement of the plasma core density for calculating the Alfvén speed v_A . R is torus major radius. (b) Post-pulse estimation of the n -spectrum with SparSpec.

tracking algorithm would lock onto the strong $n = 0$ mode and the resonances of higher n appearing in a different frequency band would have not been detected.

The differences between the real-time n -spectrum and the post-pulse n -spectrum are that modes with $n = 8$ and -7 appear in real-time whereas they are not detected in the post-pulse analysis. Instead, a mode with $n = -6$ is present in the post-pulse results. The other modes, namely with $n = 0$, 2 and -2 , have not been selected in real-time, hence they do not appear as candidate modes. The differences are due to three main reasons. First, the real-time calculation uses a fixed-frequency calibration which is not as accurate as the frequency-dependent

calibration used in the post-pulse analysis. Second, a digital filter is applied to the raw data in real-time, whereas the post-pulse analysis treats the raw data without filtering. Third, because of the limited processing power in real-time, the size of the mode number grid was set to $K = 15$, whereas the post-pulse analysis uses a grid of $K = 30$, better satisfying the model requirement for a sparse (i.e., a few non-zero components in the x vector) representation of the n -spectrum. Hence, the post-pulse result is a more accurate estimation of the spectral content of the plasma response. This conclusion is in agreement with the imposed antenna phasing (all antennas have the same phase), the symmetry of which leads to a predominant drive of even n 's. Despite the previously described differences, the real-time estimation is quite robust, as it finds successfully the same dominant n 's that are calculated in the post-pulse analysis.

Recently, a more powerful processor for the real-time calculation was installed and the software was modified to allow for an increase in the size of the mode number grid. Further improvements of the real-time system will include the possibility of using frequency-dependent calibration and having more options for the filtering of the data.

4.6 Estimation of the damping rates from the raw data

4.6.1 Data processing algorithm

In the reference [55], the original method for the estimation of the damping rate of AEs from the magnetic pick-up (or Mirnov) coil data is described. This method is modified and extended in order to resolve the problem of the existence of several degenerate modes. The steps that are used in this work are shown in figure 4.17 and they are described in the following paragraphs.

First, the raw data are calibrated. The antenna current data are calibrated using a frequency-dependent amplitude calibration. The Mirnov coil data are calibrated using the calibration derived from the direct-coupling measurements that was described in the Section 4.3.

In the original method, a mode resonance is identified and fitted for every pick-up coil and the residues of the resonances for all the coils are then used in

4.6 Estimation of the damping rates from the raw data

order to determine the n of the resonance. This technique is perfectly adequate as long as a single n is present. However, when several n s are excited at a single frequency, this method is no longer suitable, because the signal at a single coil is a superposition of different n s with different amplitudes and phases. Thus, the overlap of such multiple- n resonances creates a complicated response as a function of frequency, which is not characterized by well-defined resonances of individual n . In order to deal with this situation, the plasma response is decomposed in n with SparSpec and the result of this operation is used as a numerator N for the construction of the plasma transfer function (figure 4.17).

Another source of complication arises when the excitation n -spectrum varies as a function of frequency because of the relative variation of the antenna currents with respect to each other, as shown in figure 4.6. In such a case, using the current of one antenna as a denominator for the construction of the plasma transfer function is not a good approximation for describing the excitation, because the combined perturbation produced from all the antennas is no longer proportional to the frequency-evolution of one antenna current. Therefore, the antenna-driven n -spectrum is calculated from the expression 4.19 using the measured antenna currents and then used as denominator D for the construction of the plasma transfer function (figure 4.17).

The transfer function H is now available in terms of individual n -components, that are function of the antenna frequency. The following procedure is applied then separately to every monotonous frequency scan. For every n , the candidate resonances are selected according to a set of criteria. These criteria follow from the typical frequency response of a damped harmonic oscillator (or, equivalently, the response of a resonant cavity) for both amplitude and phase,

1. A local maximum in the amplitude should exist that exceeds a given threshold.
2. The 2 local maxima of the rate of change of the amplitude, i.e. the so-called “speed”, should exceed given thresholds before and after the resonance.
3. The rate of change of the phase should be negative during the resonance and should have a maximum (in absolute value) at the resonance peak.

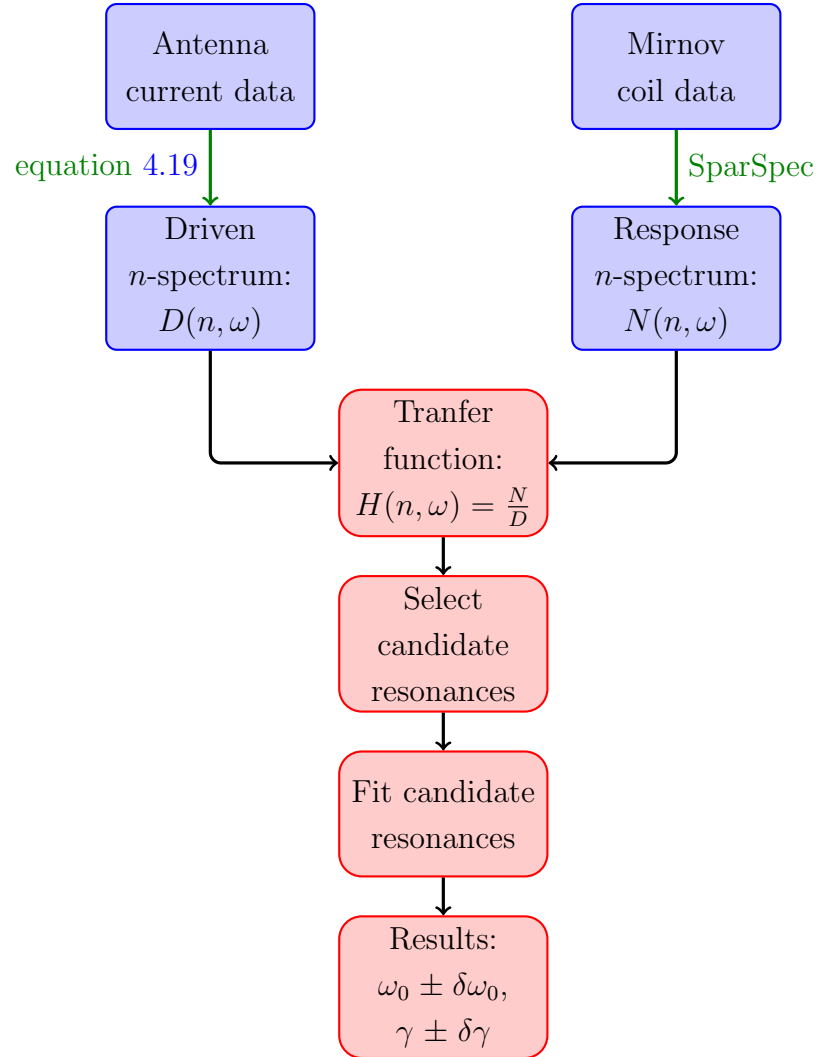


Figure 4.17: The steps that are followed for the estimation of the n , the frequency ω_0 and the damping rate γ of a plasma resonance from the magnetic pick-up coil data.

4.6 Estimation of the damping rates from the raw data

4. The twist, i.e. the integral of the change of the phase with respect to frequency during the resonance, should exceed a given threshold. The lower and upper bounds of the integration, f_{low} and f_{up} respectively, are determined as follows: initially, they are set to the values that they have at the 2 speed maxima. Then, they are extended to lower f_{low} and higher f_{up} until one of the following conditions becomes true:

- The amplitude is too small (e.g. less than 10% of the resonance peak).
- An amplitude local minimum (“valley”) is encountered.
- The phase is increasing.
- The twist exceeds π radians.

The selection procedure provides the lower and the upper bounds for the frequency scan data to be used for the resonance fitting. The fitting process consists in determining the zeros and the poles of a rational function of 2 polynomials that approximates the measured complex transfer function sufficiently precisely. The order of the denominator polynomial in $s = i\omega$, i.e. the Fourier space, is set to 2 to account for a single resonance. Two complex conjugate poles are estimated in the form $-(\gamma \pm \delta\gamma) \pm i(\omega_0 \pm \delta\omega_0)$, where γ is the damping rate, ω is the mode frequency and the uncertainties $\delta\gamma$ and $\delta\omega_0$ are estimated from the covariance matrix of the model. The order of the numerator polynomial is linked to the direct coupling dependence upon s which is not known precisely, therefore, values from 2 to 6 are used. The fitting algorithm that is used is described in the reference [54].

4.6.2 Automatic processing of the raw data

A MATLAB library has been built in order to automatically implement the data processing algorithm that was described in the previous section. The main routine finds and calculates all the measured damping rates for an entire pulse. The results of the automatic estimation of the damping rates are compared to a particular case where several resonances had been manually processed prior to writing the automatic estimation routines, as shown in figure 4.18. A reasonable agreement is found. The mean value of the differences between the manually-processed

4.6 Estimation of the damping rates from the raw data

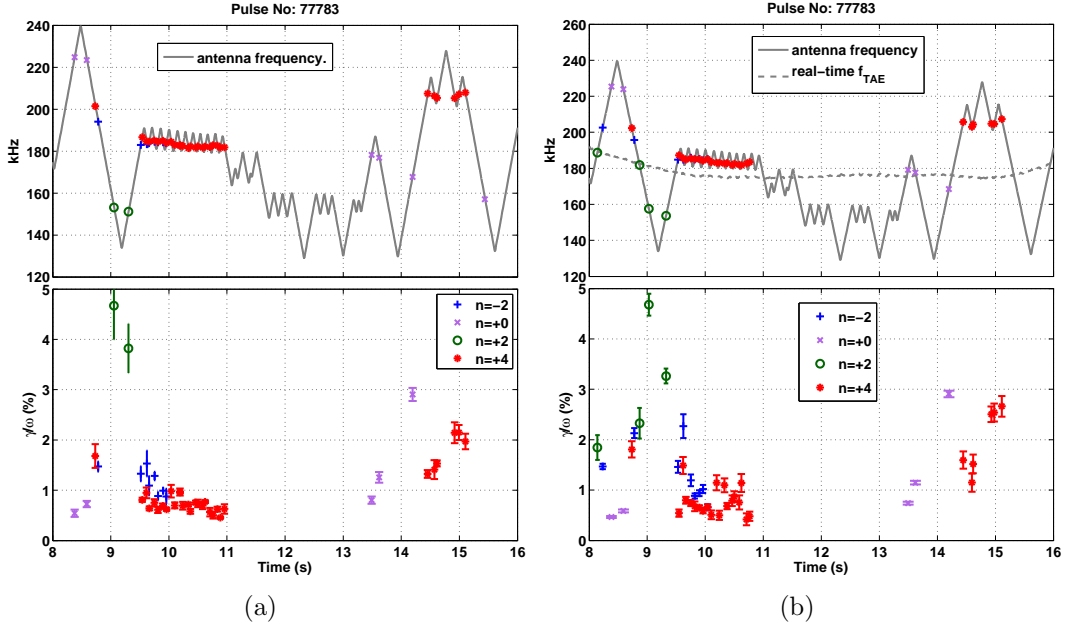


Figure 4.18: Comparison between manual (a) and automatic (b) processing of the data, used to extract the damping rate measurements. A reasonable agreement is found, given the sensitivity of the damping rate, which is proportional to the resonance width, to the exact frequency width that is selected to fit a candidate resonance (explained in figure 4.19).

$n = 4$ damping rates and the automatically-processed data is 0.092% with a standard deviation of 0.2562%. In the case of $n = 0$ modes, the corresponding values are 0.0774% and 0.0536% respectively. The differences are due to the sensitivity of the resonance fits to the selection of the candidate resonance data. Figure 4.19 shows an example of how much the selection of the candidate resonance data can affect the damping rate estimation. This sensitivity is increased when the number of the data points used to fit a candidate resonance is small and when the degree of the numerator is high. This accounts for a somewhat increased scattering when the damping rates are small ($\gamma/\omega \lesssim 1\%$) and thus more sensitive to the exact number of data points.

In order to find the best possible solution from the resonance-fitting stage, the automatic calculation routine can vary the degree of the numerator and check the goodness of the fit with the reduced χ_r^2 fit test, which consists in evaluating the

4.6 Estimation of the damping rates from the raw data

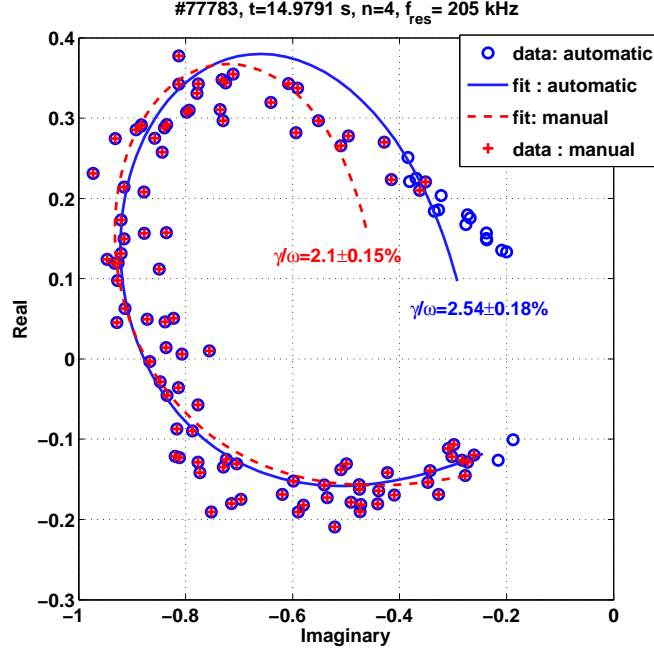


Figure 4.19: Comparison between the fits of the same resonance for 2 possible selections of the initial raw data (complex plane representation). The set used in the automatic processing contains slightly more (7.7%) data points of low amplitude than the set used for the manual processing. This makes the resonance circle slightly more elongated and finally results in the estimation of a higher damping rate (by 18%). Exactly the same settings are used for both fits: the degree of the numerator is 5, the degree of the denominator is 2 and the iterative algorithm converges with less than 30 iterations to a solution within the specified tolerance (10^{-10}).

quantity

$$\chi_r^2 = \frac{1}{N - \nu} \sum_{k=1}^N \frac{(y_k - f(x_k))^2}{\sigma_k^2}, \quad (4.38)$$

where N is the number of the data points, ν is the degrees of freedom, y_k is the raw data, $f(x_k)$ is the result of the resonance fit (model) and σ_k represent the variances of the data points. A uniform variance in the range $\sigma \approx 0.01 - 0.15$ is used, leading to χ_r^2 that is of the order or 1, which indicates good resonance fits ([87, p. 655], [88]). The degree of the numerator can vary because the data at the output of the SparSpec calculation still contain the possible contribution from the direct coupling, and this effect can be different depending on the n number. The

resonance fits that yield the least χ_r^2 are considered to give the best estimation of the damping rates. To avoid problems of over-fitting, i.e. when the algorithm tries to fit the noise or unphysical jumps or discontinuities of the signal, fits with too small χ_r^2 are rejected.

4.7 Summary and conclusions

The calculation of the magnetic field produced by the antennas in vacuum shows that the component of the radial magnetic field (dominant component) at the plasma edge is 0.2-0.4 G/A, depending on the plasma configuration. The antenna-driven n -spectrum that is derived from the field calculation confirms that the antenna current phasing that determines the n -spectrum, while the details of the antenna coil geometry or the asymmetry of the antenna position in R have a very small effect. The antenna excitation can be configured optimally to produce predominantly even or odd n -spectra using antennas from toroidally opposite positions. Such antenna configurations produce either a low- n spectrum, peaking at $n = 0 - 1$ with a half-width-at-half-maximum (HWHM) of $|n| \sim 11$ or a high- n spectrum, peaking at $n = 14 - 15$ with the same HWHM.

The calibration of the magnetic pick-up coils is essential for the estimation of the measured of the n -number. An *in situ* method was developed and applied for the calibration of the coils using the direct coupling to the AE antennas. The method is very accurate, especially in terms of phase, and takes into account of all the effects that intervene in the signal path from the coils up to the final data storage point.

The n -spectrum of the plasma response is calculated using a sparse spectrum representation method, implemented in the code SparSpec. The resulting n -spectrum is in very good agreement with phase-fitting calculations and with the parity of the driven n -spectrum. The SparSpec code has been integrated in the real-time resonance tracking system of the diagnostic. It has thus been possible to filter the n -spectrum of the plasma response and follow the variation of the damping rate of high- n modes in real-time in a plasma discharge.

Finally, an algorithm, as well as the associated software, are developed in order to automatically estimate the measured damping rates from the raw experimental data for post-pulse analysis. The algorithm incorporates the calculation of the

antenna field from the measured antenna currents, the calibration of the magnetic pick-up coils and the use of the SparSpec code. A sub-algorithm is developed in order to recognize the candidate plasma resonances, similar to the one employed by the real-time system. The post-pulse analysis agrees very well with the real-time system in terms of identification of the candidate mode resonances. Typical input settings for the post-pulse analysis code result in very good resonance fits for the recognized plasma resonances.

Chapter 5

Experimental measurements and comparisons with plasma models

5.1 Introduction

The comparison of the measured damping rates with the predictions of various plasma models helps one to identify the damping mechanisms that come into play. Such comparisons have been made for $|n| = 1 - 2$ antenna-driven AEs [63, 65, 67, 71, 89, 90]. They helped to explain qualitatively and quantitatively the damping of these modes and gain confidence in our understanding of the fundamentals of the TAE-plasma interaction. Here, we adopt the same approach for the more ITER and reactor-relevant intermediate- n modes.

Specifically, the damping of the experimentally measured $n = 3, 4$ and $n = -7$ TAEs is investigated using the codes LEMan and CASTOR. These codes incorporate different approaches for the plasma description. LEMan [91, 92] solves the Maxwell equations where the plasma enters the calculation through a warm model for the dielectric tensor. CASTOR [93] solves the resistive MHD equations using a normal-mode approach. The modeling studies are time-expensive and thus, a representative sample of specific measurement cases is considered for the application of the above models.

This chapter is organized as follows. Sections 5.2 and 5.3 describe briefly the most important aspects of the codes LEMan and CASTOR, which are relevant for the modeling of the Alfvén waves. The $n = 3$ TAE damping measurements that are used for the comparison with the plasma models are introduced in Section

5.4. The description of the measurements is followed by the analysis of the results of the simulations. The same procedure is followed in Sections 5.5 and 5.6 for the $n = 4$ and $n = -7$ TAEs. The results are summarized discussed in section 5.7.

5.2 LEMan

The LEMan code is a full-wave direct solver of the Maxwell's equations. Those are written in terms of potentials in order to avoid the so-called numerical pollution and under the assumption that the Coulomb Gauge is satisfied. The plasma model is implemented through a “warm” dielectric tensor, which is obtained by linearizing the Vlasov equation and retaining only terms of the zeroth order in the Finite Larmor Radius (FLR) expansion [92]. In the Alfvén frequencies domain, the convolution method used in LEMan computes the solution of this problem by considering the exact expression of the parallel wave vector. A precise evaluation of this term is crucial as it affects strongly the wave propagation and the damping. The plasma model that is included in LEMan allows one to calculate the Landau damping and the conversion to the kinetic Alfvén wave (KAW) and the surface quasi-electrostatic wave (SQEW). The non-ideal effects of finite electron inertia and parallel electric field are modeled, but the effects of FLR and finite particle orbits are not taken into account.

From a numerical point of view, the solution is discretized as a Fourier series for the poloidal and toroidal angles and as Hermite cubic finite elements in the radial direction. The numerical scheme corresponds to a weak Galerkin form. LEMan uses three-dimensional equilibria computed from VMEC [94] that are mapped into the Boozer coordinate by the TERPSICHORE [95] code. The latter retains presently the up-down symmetry and does not allow LEMan to take into account such asymmetry that appears, for example, in the presence of an X-point. In the case of an elongated up-down asymmetric equilibrium, the profiles of q and shear are retained and the input equilibrium to LEMan is elongated but up-down symmetric.

The modes are excited by an antenna in the form of an external electric current. The latter is a superposition of all poloidal Fourier components retained for the resolution of the wavefield. All the harmonics are driven equally with the same amplitude. The modes are excited by a virtual antenna in the form

of poloidal Fourier components at the edge of the plasma. For the simulations presented in this work, the antenna occupies the radial region, $\phi_N = 0.91 - 0.98$, where ϕ_N is the normalized toroidal flux. This corresponds to $\sqrt{\psi_N} \sim 0.98 - 1$, where ψ_N is the normalized poloidal flux, depending on the edge q values of each case. LEMan solves the system of the wave equations onto the ϕ_N grid.

5.3 CASTOR

CASTOR (Complex Alfvén Spectrum of TORoidal plasmas) solves the single-fluid, resistive MHD equations by means of a normal-mode analysis [93]. It considers small perturbations and linearizes the MHD equations around axisymmetric toroidal equilibria, i.e. solutions of the Grad-Shafranov equation. The time dependence is expressed by the eigenvalue λ in the form

$$\xi(\mathbf{r}, t) = e^{\lambda t}(\mathbf{r}) . \quad (5.1)$$

The imaginary part of λ describes oscillatory behavior with frequency $\omega = \Im(\lambda)$, while the real part, $\gamma = \Re(\lambda)$, corresponds to the exponentially growing ($\gamma > 0$) or damped ($\gamma < 0$) motion. The inclusion of plasma resistivity η in the Ohm's law,

$$\mathbf{E} + \mathbf{v} \times \mathbf{B} = \eta \mathbf{J} \quad (5.2)$$

allows a finite electric field parallel to the magnetic field and is used to resolve the singularities of the eigenmodes crossing the Alfvén continua. While a complex resistivity can be used to take into account non-ideal effects, such as finite Larmor radius (FLR) [33, 90, 93], the resistivity used in this work is real and makes it possible to estimate of the continuum damping and the electron collisional damping.

There are two versions of CASTOR: one is the eigenvalue code and the other is the antenna version of the code [96]. While the antenna version is more suited for the study of problems of external antenna excitation [96], only the eigenvalue code could be made available for this work. The eigenvalue solver uses an inverse vector iteration scheme, which is used to calculate single eigenvalues.

5.4 Damping of $n = 3$ TAEs

5.4.1 Damping rate measurements

The $n = 3$ TAE measurements of the JET pulse #77788 shown in figure 5.1 were chosen for a comparison with the theory. In this experiment, the antenna-plasma distance was minimized and the plasma configuration was optimized in order to achieve a good antenna-plasma coupling. In addition, a good diagnostic coverage was available, with MSE measurements that allow a relatively accurate measurement of the q profile and charge-exchange measurements for the ion temperature profile and the toroidal rotation. The exciter configuration was also optimized with the use of a matching unit in order to achieve maximum antenna currents. Thus, the plasma response had a very good signal-to-noise ratio and this allowed to obtain good damping measurements.

These measurements became also the base reference for a broad theory-versus-experiment comparison and a benchmark between various codes, undertaken as part of the International Tokamak Physics Activities (ITPA) activities in the fast particles group [97].

In the discharge #77788, the plasma configuration was designed for a slow edge elongation increase from $t = 9$ s to $t = 16$ s, while the other background plasma parameters are relatively constant. The evolution of the q profile throughout the discharge is shown in figure 5.3. Several $n = 3$ TAEs are successfully identified, both in real-time and with the post-pulse analysis throughout the discharge.

We focus on the observation of two effects. The first is related to the q profile relaxation in the initial phase of the discharge, i.e. in the time interval $t = 4.5 - 9$ s. In this phase, the damping increases from 0.3% to $\sim 2\%$. The second effect is the variation of the damping with increasing edge elongation and edge shear. It is noted that the edge q is also increasing during the elongation scan. At the beginning of the elongation scan ($t = 9$ s), the damping rate is at $\sim 2\%$ and it increases by $\sim 2.3\%$ at the end of the elongation scan, up to 4.3%. It is noted that the last measurement at $t = 15.8$ s is obtained after the X-point formation, when the plasma is in diverted configuration. Examples of the fits of $n = 3$ TAE resonances are shown in figure 5.2.

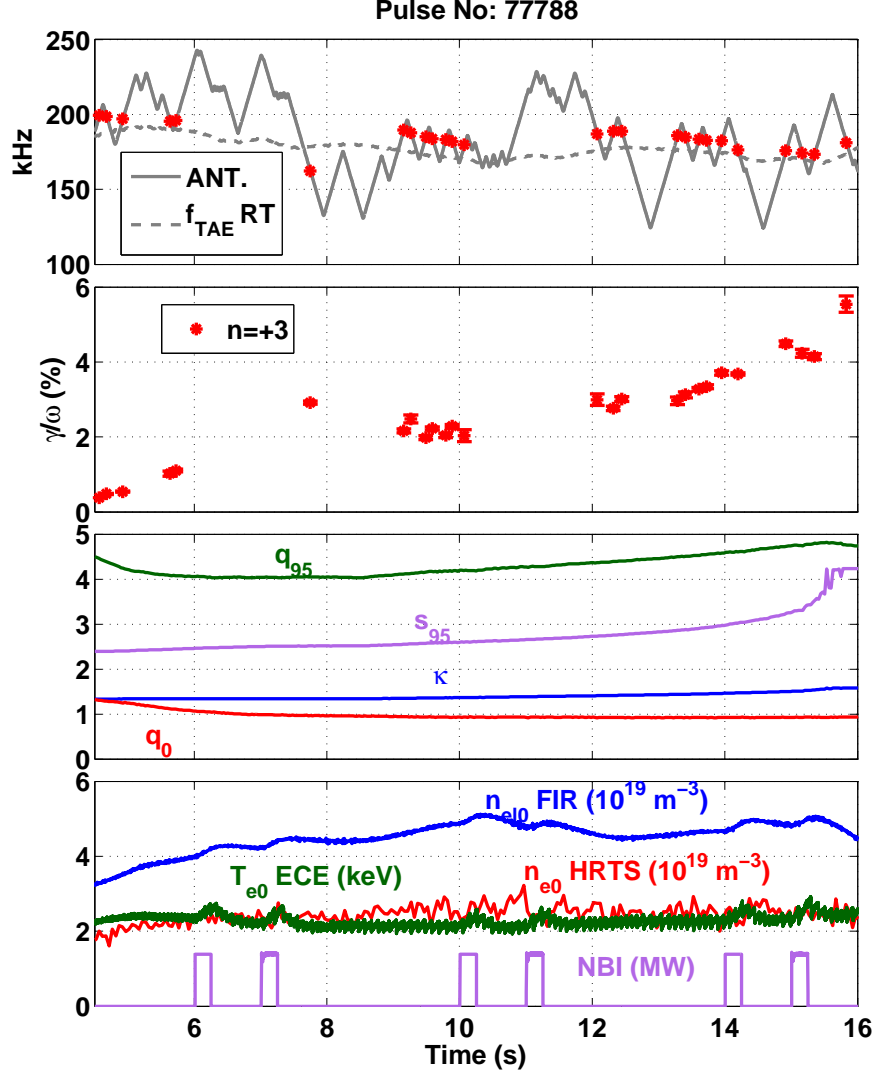


Figure 5.1: Damping rate measurements of $n = 3$ TAEs and time evolution of plasma parameters. The label ‘ANT.’ denotes the antenna frequency and ‘ f_{TAE} RT’ is a real-time estimate of the TAE frequency and it is used as a reference for the frequency scan. The plasma elongation is denoted by κ , s is the magnetic shear, q is the safety factor, n_e is the electron density and T_e is the electron temperature, with the suffixes ‘0’ and ‘95’ indicating values at 0 at 95% of the normalized poloidal flux respectively. The values of q , κ and s come from standard EFIT equilibrium reconstruction. The label ‘FIR’ refers to line-integrated measurements using FIR interferometry, ‘HRTS’ refers to measurements using high-resolution Thomson scattering and ‘ECE’ refers to measurements from electron cyclotron emission. The low-power neutral beam blips (NBI) are used to obtain MSE measurements. Antenna configuration: 1 + 4 + 6 – 7–.

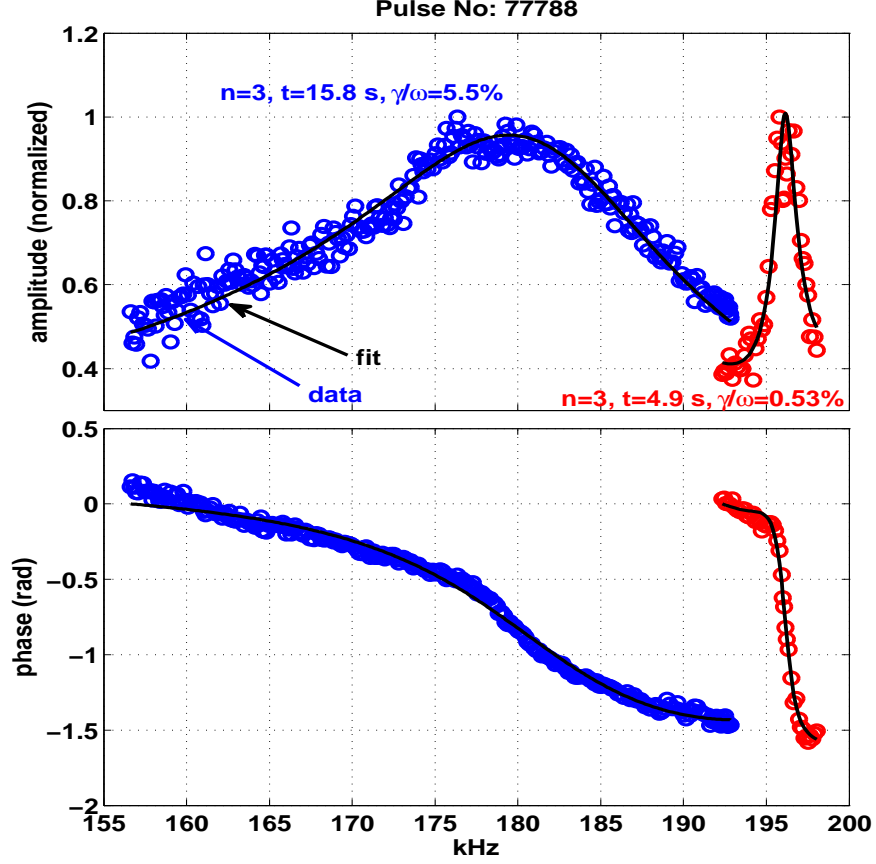


Figure 5.2: Examples of the resonance fits of the $n = 3$ TAEs of the discharge #77788 (5.1): a low damping rate measured in the early phase of the plasma discharge (right) and a high damping rate measured in the X-point configuration (left).

As it will be shown in the Chapter 6, the dependencies of the $n = 3$ damping on the edge shear and the central q profile are consistently observed in the JET plasma discharges. They are, therefore, general effects, which can robustly be anticipated for other tokamak scenarios.

5.4.2 Input data for the simulations

Five time slices were selected for the reconstruction of the equilibrium and the density and temperature profiles: $t_0 = 4.985$ s, $t_1 = 6.144$ s, $t_2 = 10.157$ s, $t_3 = 14.139$ s and $t_4 = 15.835$ s. These times span the entire range of the damping measurements, from the initial phase of the discharge when the measured damping

is low ($\gamma/\omega \sim 0.5\%$) to the X-point phase, when damping is large ($\gamma/\omega \sim 5.5\%$). The evolution of the profiles of the safety factor q , density and temperature are shown in figures 5.3 and 5.4. An example of the error bars on the density profile is shown in figure 5.5. The equilibrium was reconstructed with the EFIT code [98]. Faraday rotation measurements were used to constrain the reconstruction at t_0 and t_4 and MSE measurements for times t_1 , t_2 and t_3 . The electron density and temperature profiles were provided by the high resolution Thomson scattering diagnostic. Charge exchange measurements show that the ion temperature is equal to the electron temperature within error bars, so $T_e = T_i$ was set. The charge exchange measurements show also that the Ohmic plasma has a toroidal rotation frequency f_{tor} of about 0.5 kHz. The corresponding Doppler shift nf_{tor} is small compared to the frequency separation of the modes and also compared to the error on the mode frequency that can arise from the uncertainty in the q and density profiles.

5.4.3 Results from LEMan

5.4.3.1 Comparison with experiment

Figure 5.6 shows a direct comparison between the results from the LEMan simulations and the experimental measurements, in terms of frequency and damping rate of $n = 3$ TAEs. The theoretical modes that match best the experimental frequency are selected for the comparisons. No ambiguity has been found for the comparisons of all the time slices, as a unique mode could be found, much nearer than the others, to the experimental frequency. We observe that all the predicted frequencies fall within a range of less than 3% around the measured frequencies. The predicted damping rates are lower than the experiment by a factor of 1.5 – 2, with the exception of t_0 , where the predicted damping is higher by a factor of 2 (which, nevertheless, represents only a relatively small excess of 0.5% in absolute values).

5.4.3.2 Sensitivity to q and density profiles

Before analyzing the damping mechanisms that play a role in these measurements, it is useful to assess the sensitivity of the LEMan results to variations in the q

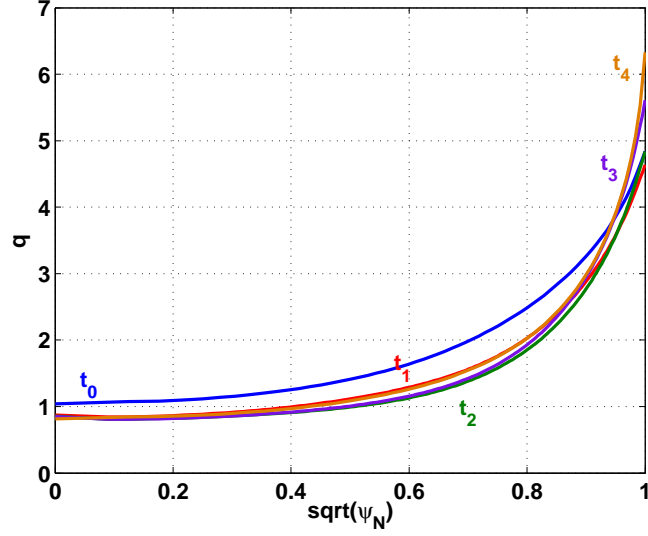


Figure 5.3: Profiles of the safety factor q used for LEMan simulation at the following times: $t_0 = 4.985$ s, $t_1 = 6.144$ s, $t_2 = 10.157$ s, $t_3 = 14.139$ s and $t_4 = 15.835$ s. The profiles are shown as function of $\rho_\psi = \sqrt{\psi_N}$, where ψ_N is the normalized poloidal flux. We note the following variations: from t_0 to t_1 the q profile is decreasing across the entire range of ρ_ψ , from t_1 to t_2 the part of the q profile that is in the range $\rho_\psi = 0.4 - 0.8$ further decreases and the edge shear slightly increases, from t_2 to t_3 the edge q and shear are increasing. At t_4 , the plasma is no longer in limiter configuration as it is bounded by a separatrix with an X-point at the plasma bottom.

and the density profiles. The modified profiles that are considered in this work have been proposed in the context of the ITPA benchmark.

First, the impact of slightly different q profiles is considered for the case t_2 . The basic q profile comes the EFIT reconstruction and the modified profile comes from the code HELENA. As shown figure 5.7, the difference between the two profiles is about 5%, which is within the typical experimental uncertainty in q . The frequency of the mode of interest changes very slightly, by about 0.5 kHz. The damping of the mode decreases by 0.15%. It is interesting to observe that the frequencies of the other modes found by LEMan in the TAE gap are more affected: for example, the mode at 196 kHz has its frequency shifted at 200 kHz. Furthermore, the plasma response that lies in the frequency range from 210 to 250 kHz is altered.

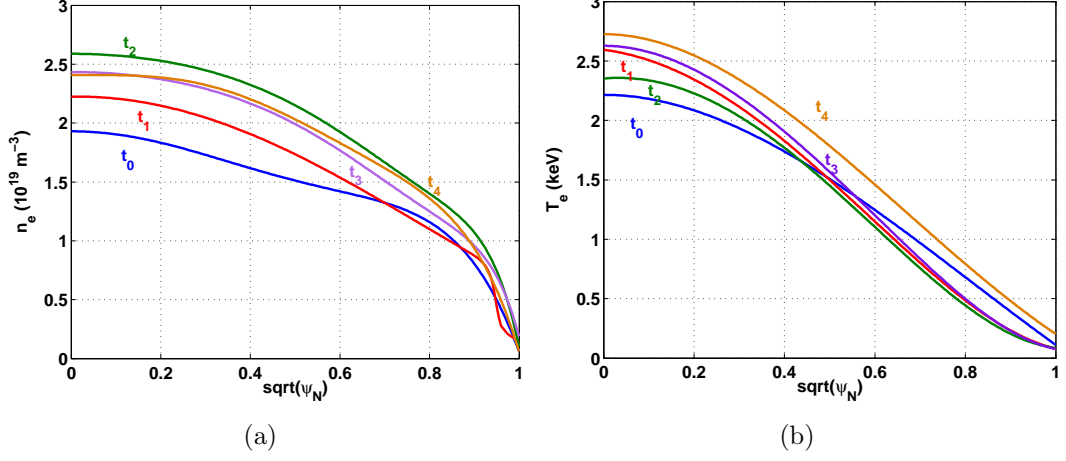


Figure 5.4: Profiles of density and temperature used for LEMan simulations. The indicated time slices t_i correspond to those described in figure 5.3. We note the increase in the density by $\sim 20\%$ in the time interval $t_0 - t_2$ and the fact that the temperature profile does not vary significantly.

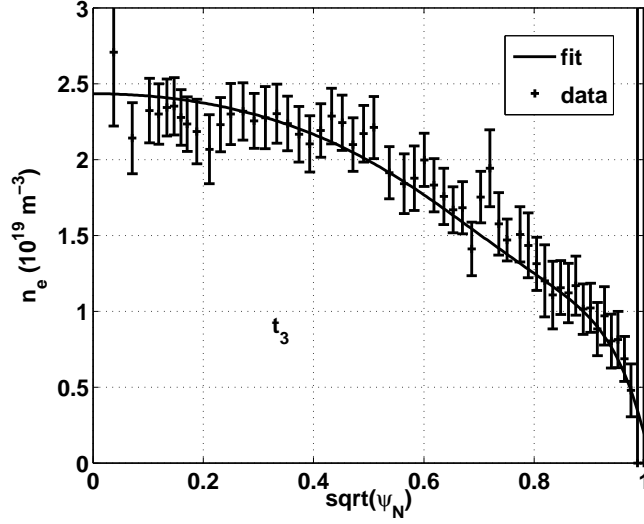


Figure 5.5: Error bars on the density profile for the time slice t_3 of the discharge #77788.

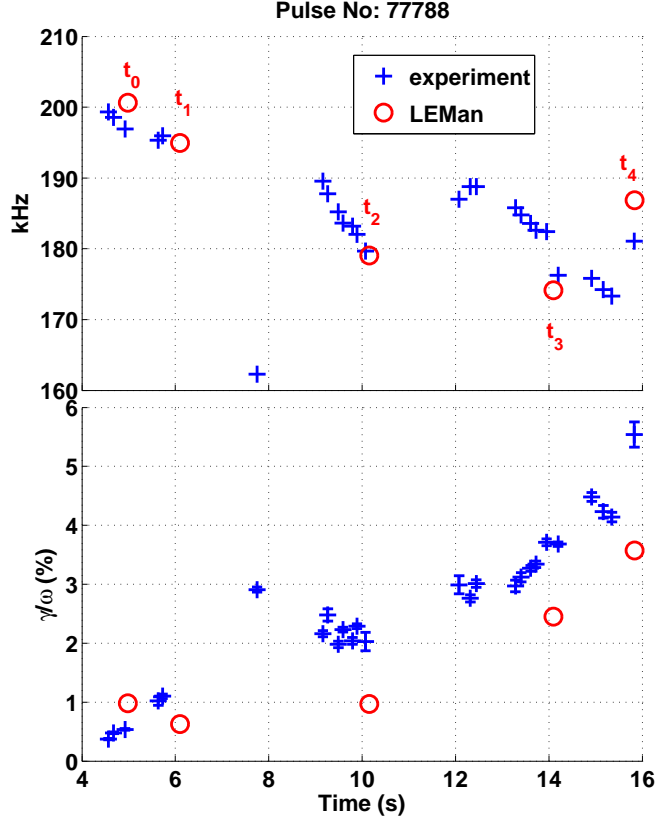


Figure 5.6: Comparison between LEMan and experiment in terms of $n = 3$ TAE frequencies (top) and damping (bottom). The predicted and experimental frequencies agree with each other within 3% of their value. The predicted dampings are in general a factor of 1.5-2 lower than the experiment and the increasing trend that is observed experimentally is well reproduced by the code.

A second case that shows the effect of slightly different edge density profiles is shown in figure 5.8. The error bars of the density profile of t_3 are shown in figure 5.5. Despite the relatively small modification of the profile, the edge details of the continuum change sufficiently so that the plasma response is modified significantly (figure 5.8b). In particular, the plasma response in the frequency range $f > 180$ kHz is affected strongly by the change in the edge continuum and the peaks that appear in this range are shifted in frequency by 15 kHz. The mode of interest, that is found around 176 kHz, is much less affected: the frequency changes by 4 kHz and the damping by 0.15%.

Thus, the impact is important in the frequency range in which the modes

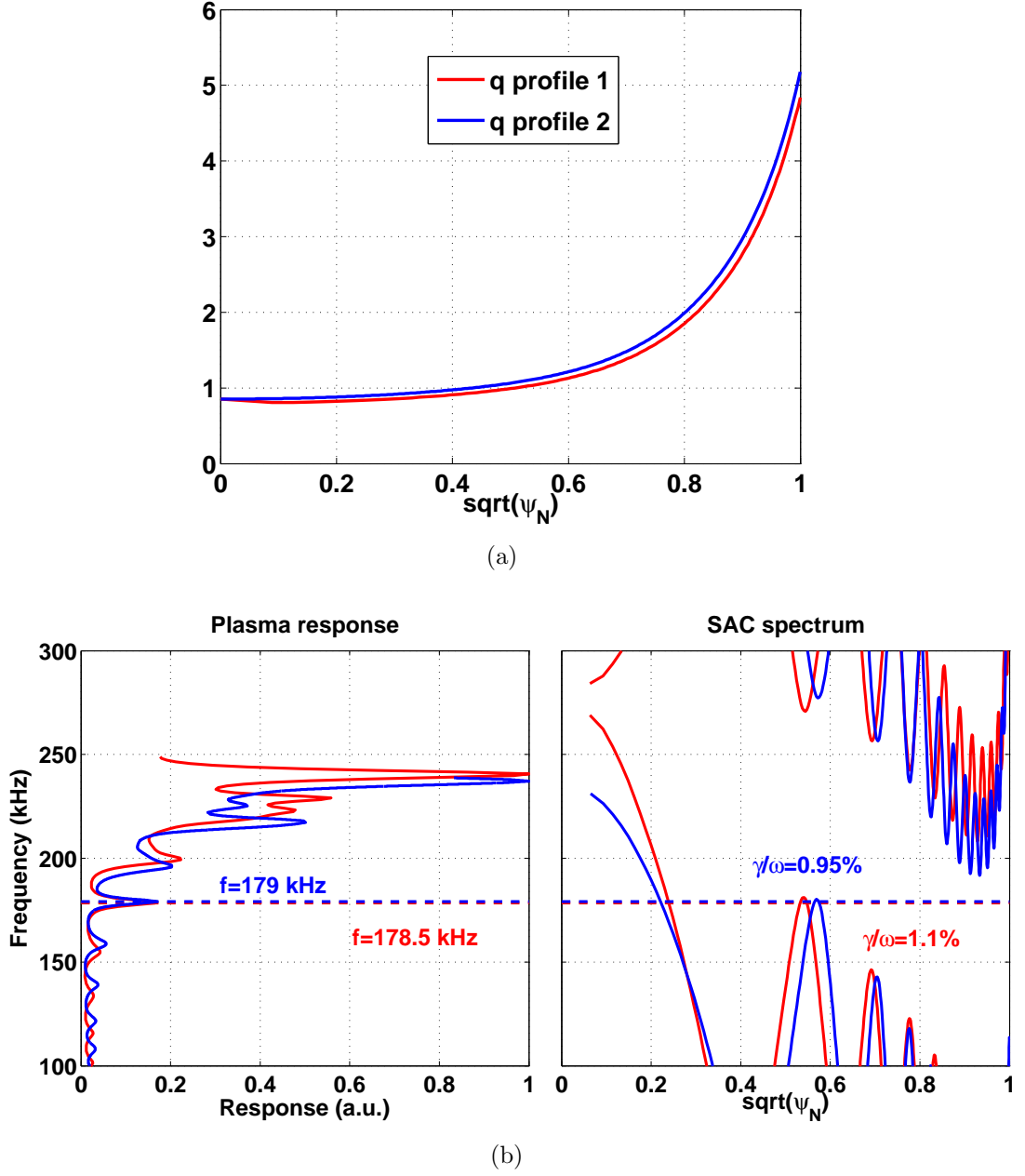


Figure 5.7: Sensitivity of LEMan calculation to slightly different q profiles, as shown in figure (a). The change in q modifies the shear Alfvén continuum (SAC) structure (figure (b), right). The frequency of the mode of interest changes very slightly (0.5 kHz). Its damping rate changes by a small amount, i.e. 0.15%. Notice however that the frequencies of the other eigenmodes are more affected: for example, the mode at 196 kHz had its frequency shifted at 200 kHz.

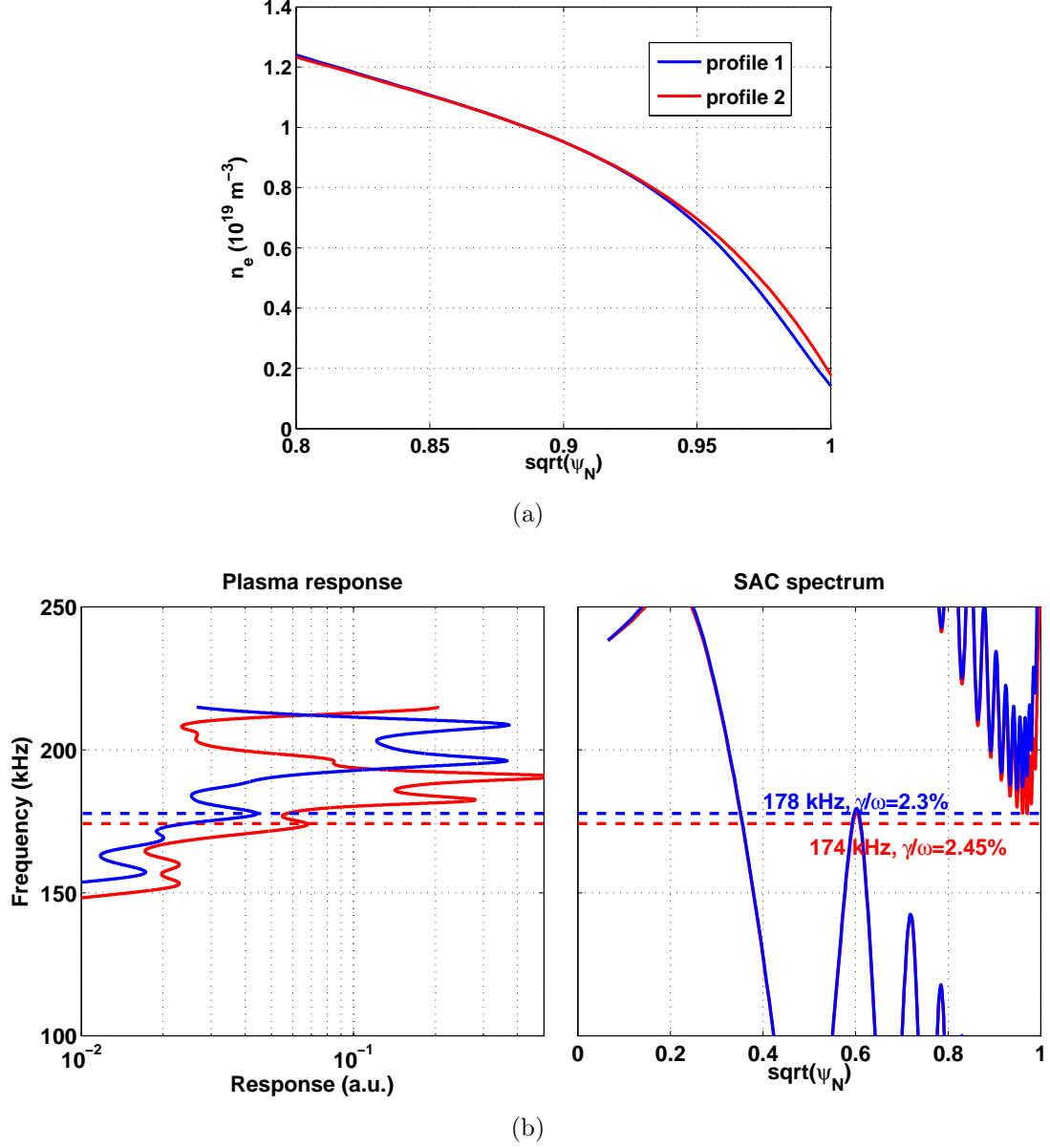


Figure 5.8: Sensitivity of LEMan calculation to slightly different edge n_e profiles, shown in figure (a) (time slice t_3). As seen in figure (b), the edge details of the continuum change and the plasma response is modified significantly. The mode of interest is affected but is not altered completely: the frequency changes by 4 kHz and the damping by 0.15%.

intersect the continuum at the edge, while the mode that is identified with the experimental measurement ($f_{exp} = 176$ kHz), which is just below the edge continuum, is less affected.

Having presented the above tests, it is now easy to see that the plasma response may change significantly if one considers even larger variations in the density profiles, within the experimental uncertainty. For example, if the density profile $n_e(t_3)$ is used at the place of the profile $n_e(t_4)$ (as shown in figure 5.9a, the two profiles are very similar with their difference being within the experimental error bars), the plasma response is completely altered and the modes found initially for $n_e(t_4)$ are not recovered at all for $n_e(t_3)$ (figure 5.9b). Instead, a very broad peak appears in the calculated plasma response centered at 170 kHz and with a HWHM of 11%.

In the case of t_0 , a sensitivity test was carried out, in which the density profile was modified in the range of the experimental error (figure 5.10a). This resulted in a reduction in the predicted damping of about 0.1% (figure 5.10b).

The sensitivity tests that have been presented in this section should be seen as an effort to determine the conditions under which the damping rates calculated with LEMan are sensitive to small variations of the density and q profiles within the experimental error bars. It is found that a small variation of the edge density in conditions of high edge shear alters significantly the overall plasma response (time slices t_4 and t_3). The modes that are identified as those that are excited by the antennas experimentally are more robust in terms of frequency and damping rate against the considered profile modifications, compared to the modes that are predicted by LEMan at different frequencies (tests for the time slices t_0 , t_2 and t_3). This may be the reason why the modes at high frequency are not seen experimentally, even though they correspond to a stronger plasma response according to LEMan.

Overall, the tests show that the comparison between data and experiment may be affected by the uncertainty in the profiles, and by an amount that depends on the specific plasma configuration and the interaction of the considered TAE mode with the Alfvén continuum.

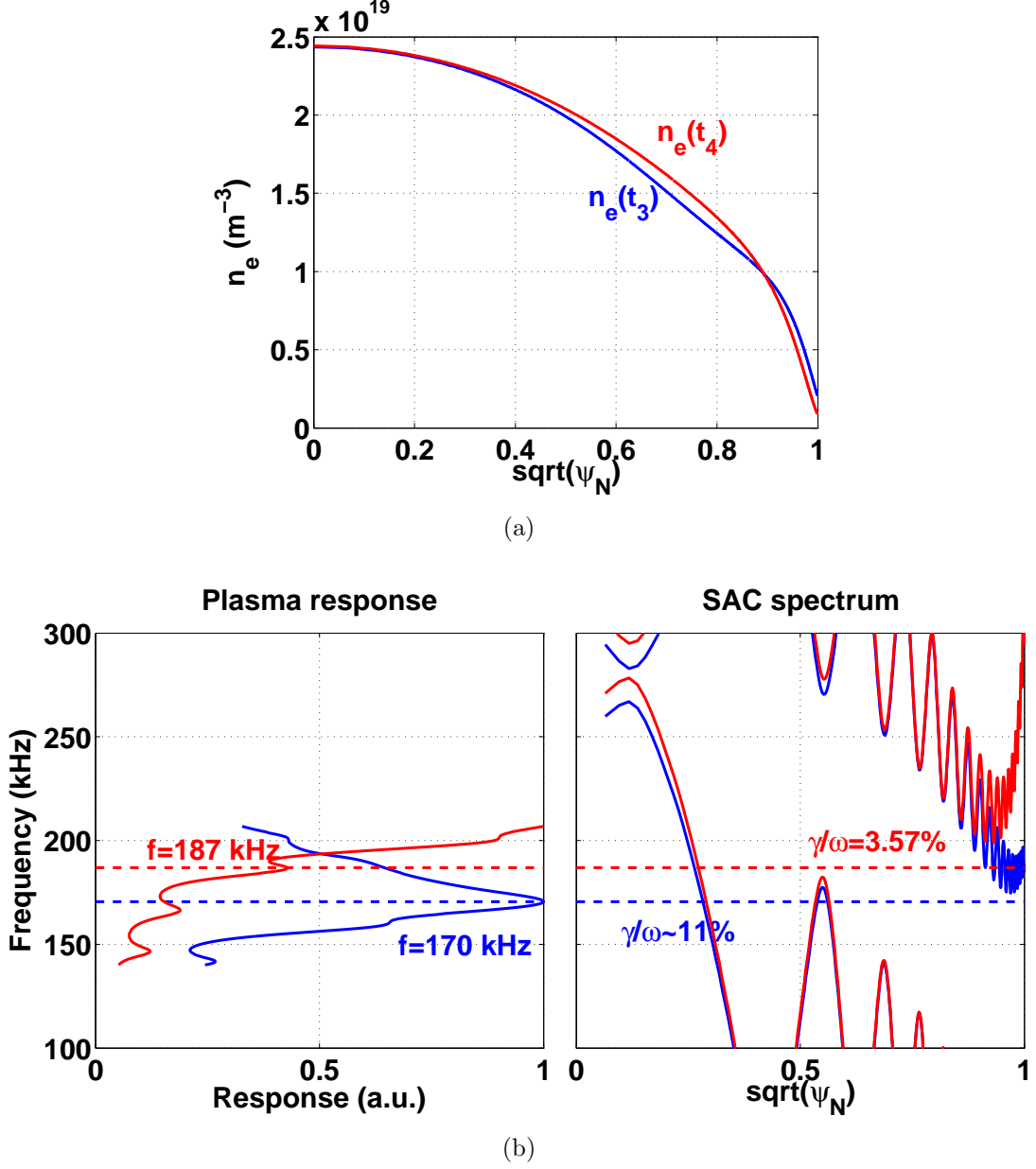


Figure 5.9: Sensitivity of LEMan calculation for the time slice t_4 to slightly different n_e profiles, shown in figure (a). As seen in figure (b), it is the edge details of the continuum that are mostly modified. This has a radical effect on the plasma response: a heavily damped with $\gamma/\omega \sim 11\%$ appears in the frequency range of interest.

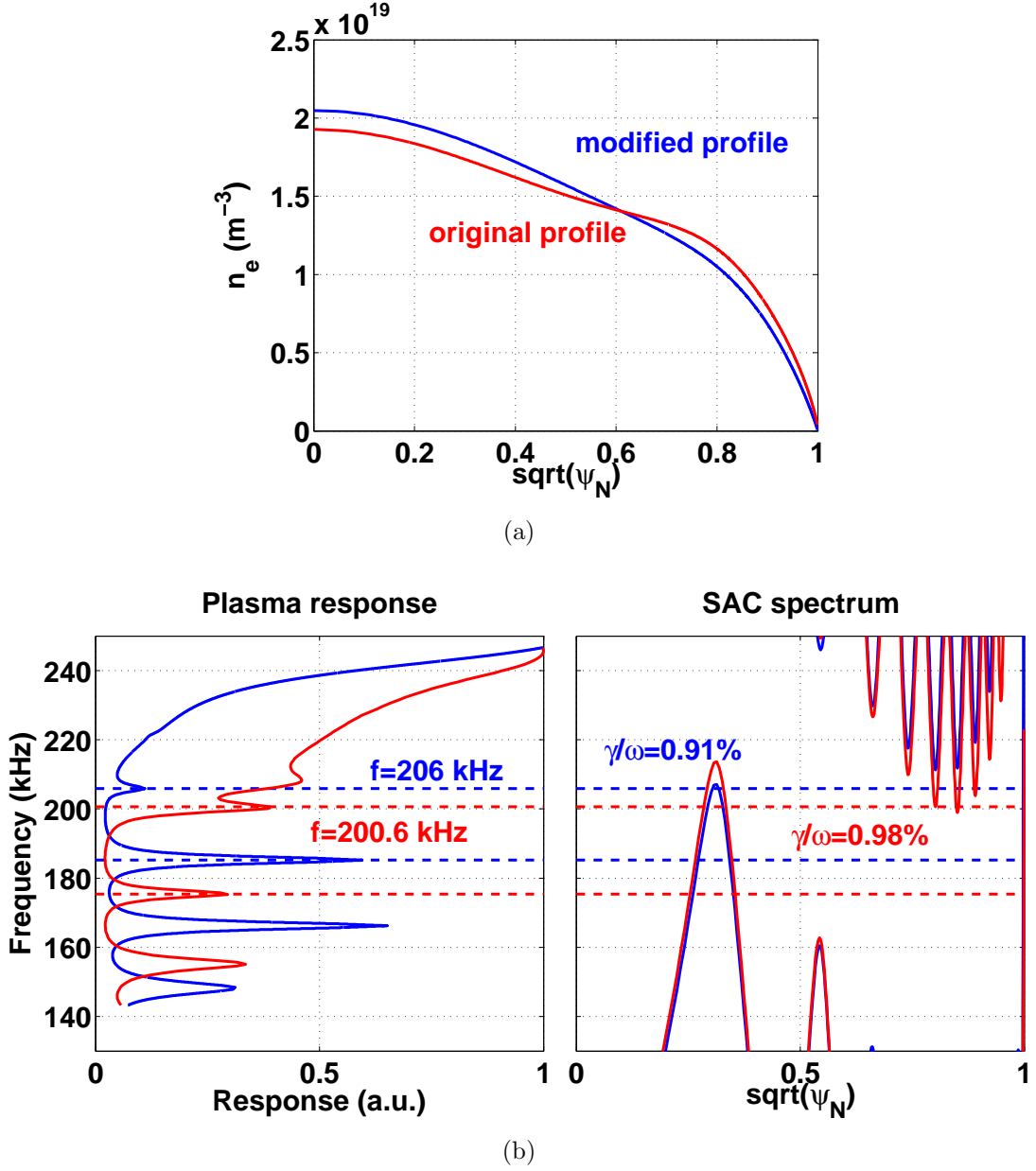


Figure 5.10: Sensitivity of LEMan calculation for the time slice t_0 to different n_e profiles, shown in figure (a). As seen in figure (b), the damping rate of the mode of interest decreases from 0.98% to 0.91% whereas its frequency increases from 200.6 to 206 kHz.

5.4.3.3 Mode structure and damping mechanisms

More insight into the damping mechanisms that act on the antenna-driven TAEs can be gained with an in-depth inspection into the results for specific time slices.

As a representative example in conditions of low damping, we consider the time slice $t_1 = 6.144$ s. Figure 5.11 shows an overview of the results, with the plasma response, the shear Alfvén continuum (SAC) spectrum, the radial mode structure, the radial profile of power absorption integral and the wavefield of parallel component of the electric field. Several peaks appear in the plasma response along the TAE frequency range, corresponding to different $n = 3$ TAEs. The horizontal lines at 215, 195 and 170 kHz mark the three eigenmodes that are the nearest to the experimentally measured frequency (at $t = 5.72$ s with $f_{exp} = 196$ kHz and $\gamma/\omega_{exp} = 1.1$, shown in figure 5.6). The experimental mode can be clearly identified with the mode predicted by LEMan at 195 kHz. This follows not only from the proximity in frequency, $\Delta f \sim 1$ kHz), but also by the fact that the distance to the other modes is much greater than Δf . The mode is extended radially from $\rho_\psi = 0.2$ to the edge of the plasma and comprises many coupled poloidal harmonics from $m = 3$ to $m = 15$ (figure 5.11b, top).

In order to estimate the contributions of the damping mechanisms, we consider the power absorption profile. As shown in figure 5.11b, the integrated power absorption exhibits an incremental character: a step of $\sim 0.05\%$ is observed at $\rho_\psi \sim 0.25$ at the intersection with the continuum, followed by a flat region, i.e. zero absorption, up to $\rho_\psi = 0.5$. At $\rho_\psi = 0.5 - 0.55$ strong absorption takes place accounting for half of the total absorption. At higher ρ_ψ , the absorption continues to increase in an incremental way and it always takes place at the centers of the local TAE gaps. Strong increase of the power absorption occurs at the radial points where the continuum approaches locally very close the mode eigenfrequency, i.e. at $\rho_\psi \sim 0.55$ and $\rho_\psi \sim 0.92$. The finite E_\parallel that is shown in figure 5.11c shows peaking, in the form of concentric circles, at the same radii where the incremental increases take place in the power absorption profile. Finally, the short wavelength features of the mode conversion to the kinetic Alfvén wave (KAW) are seen clearly in the imaginary part of the eigenfunctions of the vector potential A_\parallel and the scalar potential ϕ , shown in figure 5.12.

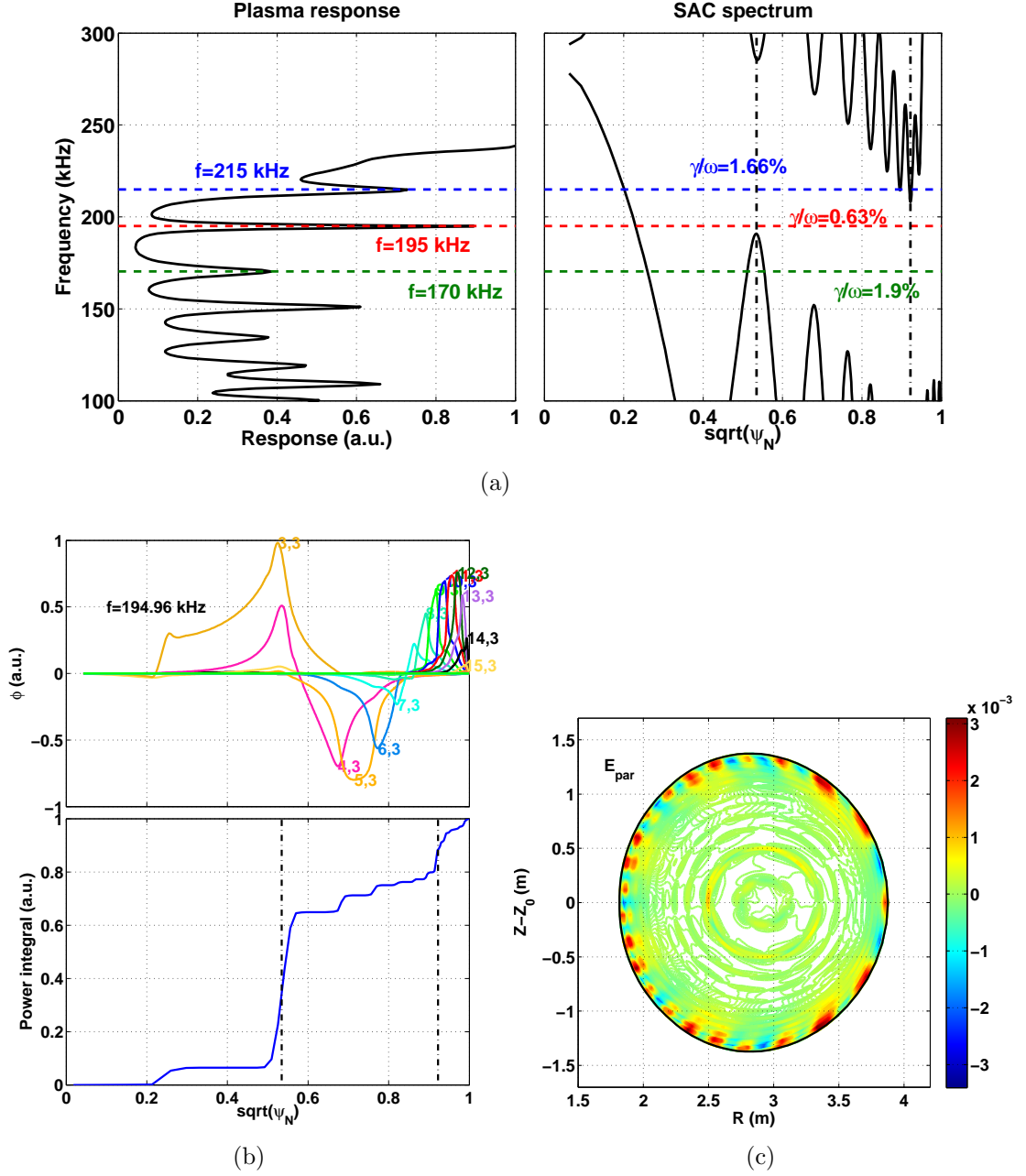


Figure 5.11: LEMan results for t_1 in the discharge 77788. (a) Plasma response (left) and $n = 3$ shear Alfvén continuum (SAC) spectrum (right, zoom in the TAE gap). (b) Radial structure of the scalar potential $\Re(\phi)$ (top) and power absorption integral (bottom). (c) Contour plot of the parallel electric field E_{\parallel} . In figure (a), the horizontal lines mark the three eigenmodes that are the nearest to the experimentally measured frequency at 196 kHz. The black dash-dotted vertical lines mark the radial position where strong absorption occurs, as seen in the power absorption profile.

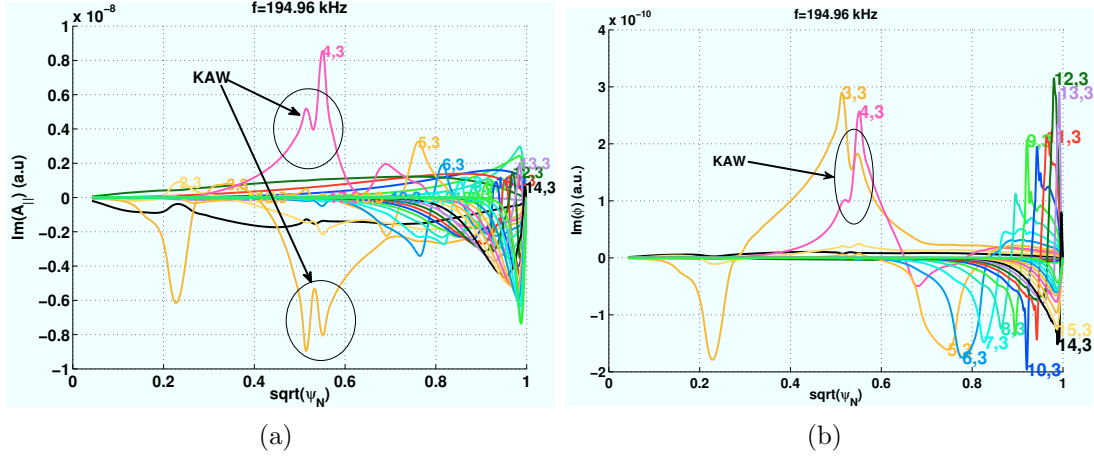


Figure 5.12: Imaginary part of the eigenfunctions of A_{\parallel} (a) and ϕ (b) for the time slice t_1 in the discharge #77788. The short wavelength features of the mode conversion to the kinetic Alfvén wave are seen at $\rho_{\psi} = \sqrt{\psi_N} \sim 0.5$.

The above observations suggest that the plasma absorbs energy from the TAE by direct Landau interaction of the electrons with the finite parallel electric field and by mode conversion to KAWs. The KAWs are subsequently damped by Landau damping.

As a representative example in conditions of high damping, we consider the time slice $t_4 = 15.8$ s. At t_4 s the plasma is bounded by a separatrix with an X-point at the bottom. In such a configuration, theoretically, q and shear tend to infinity as one approaches the separatrix. Nonetheless, for the simulation, the q and shear at the plasma boundary, q_a and s_a , take finite values, with $q_a = 6.3$ and $s_a = 22.6$. To have a measure of comparison, at $t = t_1$ we had $q_a = 4.6$ and $s_a = 2.5$. In these conditions of very high edge shear, all the modes found in the TAE gap close to the experimentally measured frequency (181 kHz) with eigenfrequencies that do not intersect the continuum at the edge, are subject to strong damping (figure 5.13a).

The mode that corresponds to the measurement is the one at 186.8 kHz, since its eigenfrequency is the nearest to the measured frequency. Moreover, this mode has a very similar radial structure to the modes identified for the previous time slices (for example, see figure 5.11b). This invariance of the mode structure implies that the TAEs that are found experimentally in the range from 175 to 200 kHz correspond to the same gap mode and in particular, to the mode that is

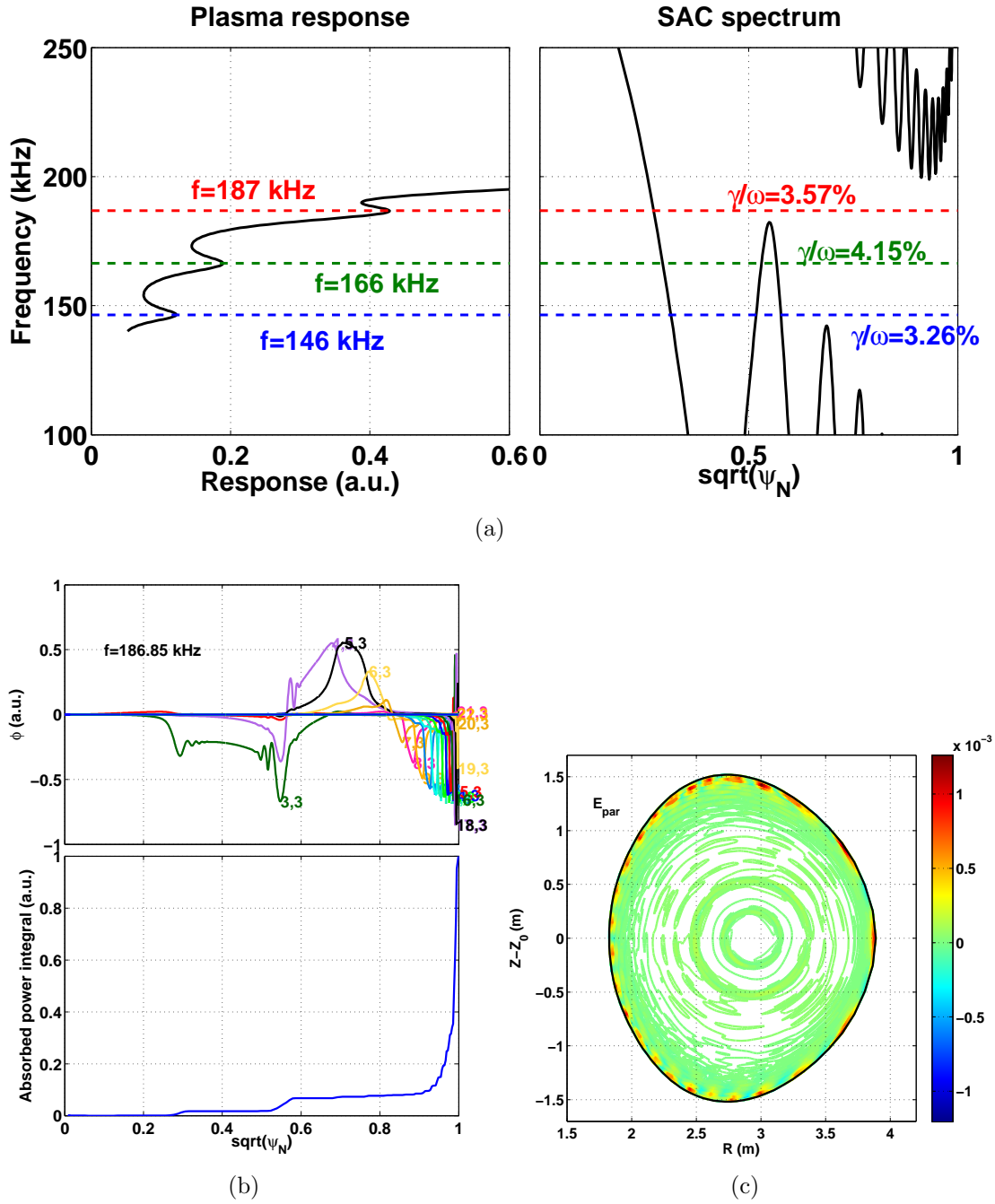


Figure 5.13: LEMAN results for t_4 in the discharge #77788. (a) Plasma response (left) and $n = 3$ SAC spectrum (right, zoom in the TAE gap). (b) Radial structure of the eigenmode scalar potential ϕ (top) and power absorption integral (bottom). (c) Contour plot of the parallel electric field E_{\parallel} .

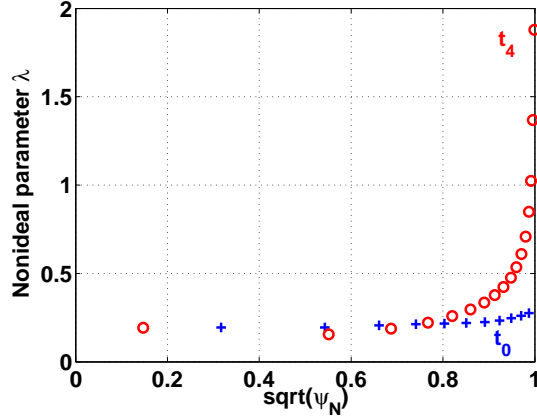


Figure 5.14: Non-ideal parameter λ in #77788 estimated at the positions of the TAE gaps. At t_4 , the high edge shear leads to a strong peaking of λ very close to the plasma boundary. Conversely, at t_0 when the edge shear is much lower, λ does not vary much, and at the edge, it remains low, a factor of 7 less than t_4 .

peaking at the $q = 7/6$ surface, produced locally by the coupling of the $m = 3, 4$ poloidal harmonics. This is in agreement with the very good correlation of the experimental frequency with the density evolution as function of time (figure 5.1). Note that, experimentally (figure 5.6), another $n = 3$ mode is identified at lower frequencies, namely at $t = 7.7$ s with $f = 162$ kHz, and with higher damping than the rest of the other $n = 3$ measurements. This mode may correspond to one of the $n = 3$ modes predicted by LEMan at lower frequencies, which have indeed higher damping, as shown in figure 5.7b.

The relatively large damping predicted for this mode, $\gamma/\omega = 3.57\%$, is a factor of 1.5 less than the measured damping (in the experiment $\gamma/\omega = 5.5\%$). Most of the mode energy, namely 90%, is dissipated at the edge of the plasma, $\rho_\psi > 0.9$, and 10% is dissipated in the plasma center and mid-radius. The power absorption peaks at a narrow radial region, $\rho_\psi = 0.96 - 0.98$, where the poloidal harmonics with $m = 16 - 18$ become dominant. The poloidal harmonics with non-zero amplitude extend up to $m = 24$. This is a consequence of the high q_a , s_a and the absence of intersection with the continuum at the edge. To have a measure of comparison, at t_1 , with lower q_a , s_a , the poloidal harmonics with the higher amplitude at the edge are $m = 12, 13$ and the harmonics with non-zero amplitude extend up to $m = 15$ (figure 5.11b).

The strong edge damping that is observed in the case of t_4 is due to the combination of electron Landau damping due to the finite E_{\parallel} and radiative damping (mode conversion to KAWs). This is in very good agreement with the high peaking that is observed at the edge in the kinetic parameter λ (figure 5.14), which is indicative of the radiative damping [24, 43]. The parameter λ is evaluated at the center of the local TAE gaps using the expression (2.19). Additionally, similarly to t_1 , a good spatial correlation is observed between the distribution of the finite parallel electric field (figure 5.13c) and the calculated power absorption (figure 5.11b).

In order to examine closer the effectiveness of the electron Landau damping, we calculate the local electron Landau damping using the expression (2.18), which is repeated here for convenience,

$$\frac{\gamma_L}{\omega} = \frac{\sqrt{\pi}}{2} (k_{\perp} \hat{\rho}_i)^2 \frac{v_A}{v_{Te}} \exp\left(-\frac{v_A^2}{v_{Te}^2}\right), \quad (5.3)$$

where k_{\perp} is the projection of the wave vector onto the plane perpendicular to \mathbf{B}_0 , $\hat{\rho}_i$ is the ion Larmor radius evaluated with the electron temperature and $v_{Te} = \sqrt{2k_B T_e / m_e}$. We have used the approximation that $k_{\perp} \sim O(1/\Delta r_s) \approx 2\pi/\Delta r_s$ with $\Delta r_s = 1/nq'$ being the distance between the neighboring mode-rational surfaces [39, 99]. Figure 5.15 shows γ_L/ω for conditions of small radial mode localization (t_0) and high localization (t_4). The maximum in the curves of γ_L/ω indicates the position where $v_A \approx v_{Te}$. It is observed that the damping γ_L/ω increases and shifts radially toward the edge because of the increase in the mode localization, expressed here through k_{\perp} . Thus, the concurrence of the condition $v_A \approx v_{Te}$ and the high shear enhance the effect of electron Landau damping.

In order to further demonstrate the importance of the electron temperature, the plasma response is calculated for various combinations of the electron and ion temperatures, as shown in figures 5.16. We observe that if the ion temperature is reduced by a factor of 10 to 0.27 keV from the original value of 2.7 keV, the change in the plasma response and in the damping is negligible. On the contrary, if the electron temperature is reduced by a factor of 10, the change in the plasma response and in the damping is radical: the strongly-damped modes that interact with the continuum at high temperature are replaced by multiple and less damped modes, which may be modes of the surface quasi-electrostatic wave (SQEW) or ‘cold plasma surface wave’. The SQEW is recovered in the cold plasma limit

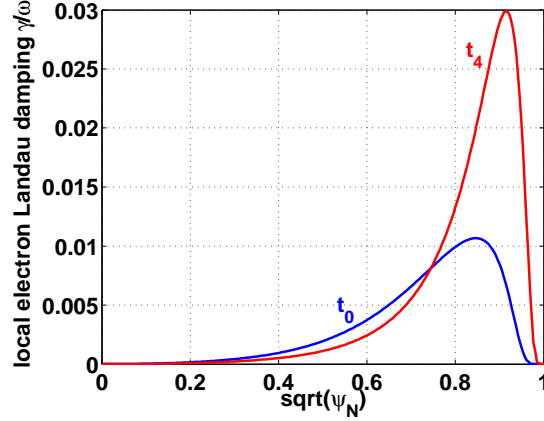


Figure 5.15: Local electron Landau damping in the discharge #77788, evaluated using expression (2.18) at t_0 and t_4 . The damping increases and shifts toward the edge, as the shear increases and the mode becomes more localized towards the edge.

where $v_A > v_{Te}$ and comes from the finite m_e modification of the dispersion relation of the Alfvén wave [15]. In addition, an intermediate situation is shown, when the temperature is decreased by a factor of 3 (0.9 keV): the damping of the mode at 187 kHz is reduced from 3.6% to 2.1% and the modes of the SQEW start to emerge in the Alfvén continuum frequency range ($f > 180$ kHz).

An overview of the evolution of the power absorption profiles figure 5.17. The curves are scaled so that the integral of the power absorption corresponds to the predicted γ/ω . It is observed that from t_0 to t_2 , the increase of the damping is due mainly to increasing contributions from the central and mid-radius regions. This is due to the evolution of the central q and density profiles, which lead to more interaction of the mode with the continuum, either via continuum damping (intersection with the continuum) or via radiative damping (wave tunneling to the continuum). From t_2 to t_4 , the increase in the damping is due to an increasing contribution from the edge region. This is the result of the increase of the edge shear and q , which leads again to stronger interaction with the continuum via tunneling.

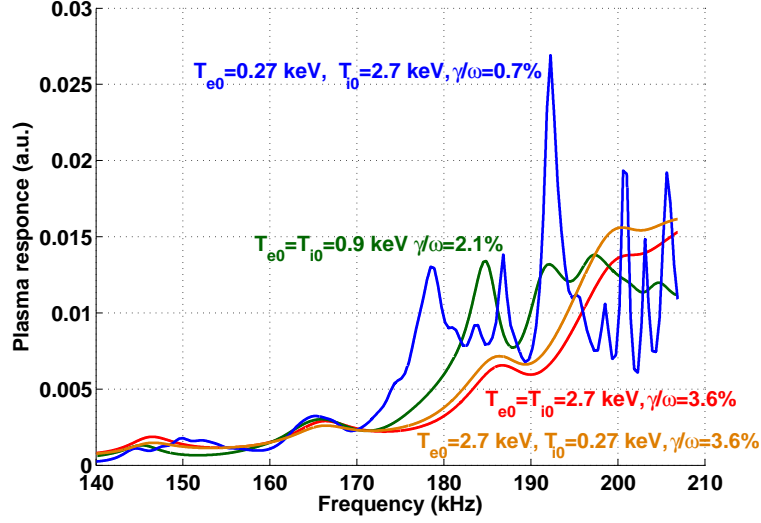


Figure 5.16: Temperature scan for the plasma response at t_4 in #77788. The dampings correspond to the peaks appearing at 187 kHz ($T_{e0} = 2.7$ keV), at 185 kHz ($T_{e0} = T_{i0} = 0.9$ keV) and 192 kHz ($T_{e0} = 0.27$ keV, $T_{i0} = 2.7$ keV). Note that it is the electron temperature that determines the plasma response and the estimated damping. The plasma response is modified significantly as function of the temperature, for frequencies higher than 180 kHz, as the interaction with the Alfvén continuum is strongly influenced by kinetic effects. At low temperature, a multiple-peak structure makes its appearance at the frequencies that are close to or on the Alfvén continuum.

5.4.4 Results from CASTOR

5.4.4.1 Input data and parameters

Six time slices were selected for the preparation of the equilibrium and density data. For three of these times, namely for $t_1 = 6.144$ s, $t_2 = 10.157$ s and $t_3 = 14.139$ s, the density profiles are the same as those used previously for LEMan. CASTOR does not use directly the equilibrium information from EFIT but the code HELENA [100] is used as intermediary step for the preparation of the final input data. This results in slightly different q profiles (figure 5.18), which should be taken into account when comparing with the LEMan results. The density profiles were derived by mapping the HRTS density measurements onto the EFIT grid.

A spatial resolution of 601 radial grid points was used to make sure that the

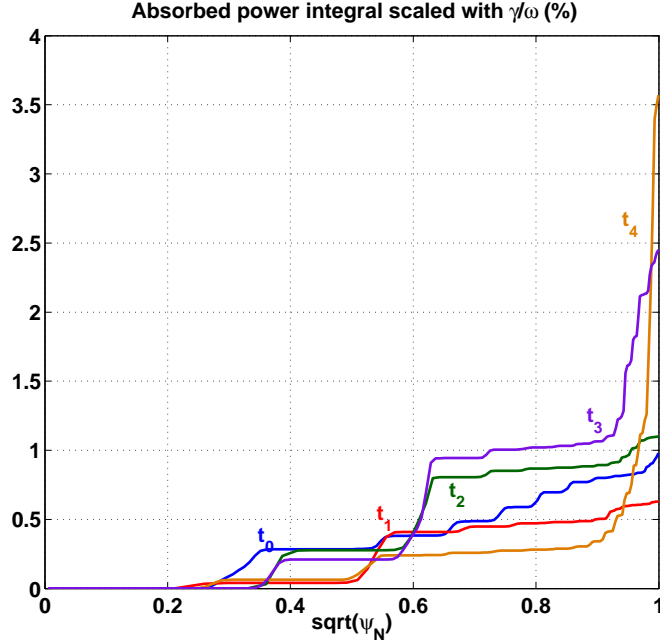


Figure 5.17: Overview of the power absorption profiles in #77788. It is observed that from t_0 to t_2 , the increase of the damping is due to increasing contributions from the central and mid-radius regions. This is due to the evolution of the central q and density profiles. From t_2 to t_4 , the increase in the damping is due to an increasing contribution from the edge region. This is the result of the increase of the edge shear and q .

nearly-singular layers are well resolved for low values of the plasma resistivity η . Scans of η were carried out where η was varied from 10^{-5} down to 10^{-8} : it was found the eigenvalue does not change with η for $\eta \lesssim 10^{-7}$, so the value $\eta = 10^{-7}$ was used. These values for the radial resolution and resistivity have been shown to be sufficient for the study of the damping of global Alfvén waves [101]. The value $\eta = 10^{-7}$ is a standard value and it has been used previously to study the antenna-driven modes at JET [61, 96]. Since the plasma has a low beta ($\beta_N \sim 0.4\%$, with $\beta_N = \beta_t/(I_p/aB_0)$), the effect of compressibility is negligible and the ratio of the specific heats was set to zero to suppress the ‘slow’ continuum (created by finite compressibility and the coupling to the sound wave) [96].

The maximum number of poloidal harmonics that could be used in these simulations was 11. Thus, the TAE gaps that are formed by the coupling of high- m harmonics and that correspond to high values of q can be artificially closed by

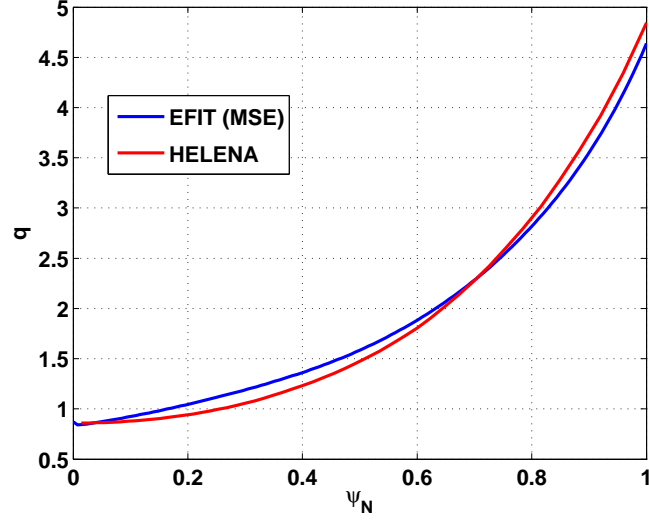


Figure 5.18: Comparison of the q profile between EFIT and HELENA for the time t_1 in the discharge #77788. The total value of the current has been adjusted to have the same q_0 , but a small difference remains between the q profiles.

the Alfvén continuum. This is the reason why for these simulations the boundary condition of the conducting wall was imposed at $\sqrt{\psi_N} = 0.95$, so as not to have an artificial intersection with the continuum.

5.4.4.2 Comparison with experiment

Figure 5.19 shows the direct comparison between the measurements and the CASTOR results. We observe that sometimes it is not possible to clearly identify the experimental measured mode using the proximity in frequency, e.g. in the case of $t = 6.1$ s where two eigenmodes are found at similar distances in frequency and with different damping rates. The agreement in the dampings varies too, from predictions that are very close to the measured damping, e.g. at $t = 4.5$ s and at $t = 7.8$ s, to predictions of 4 times lower than the measured value, e.g. at $t = 10.15$ s. This comparison suggests that the damping mechanisms that are incorporated in the CASTOR plasma model are not always sufficient to explain the measured damping rates.

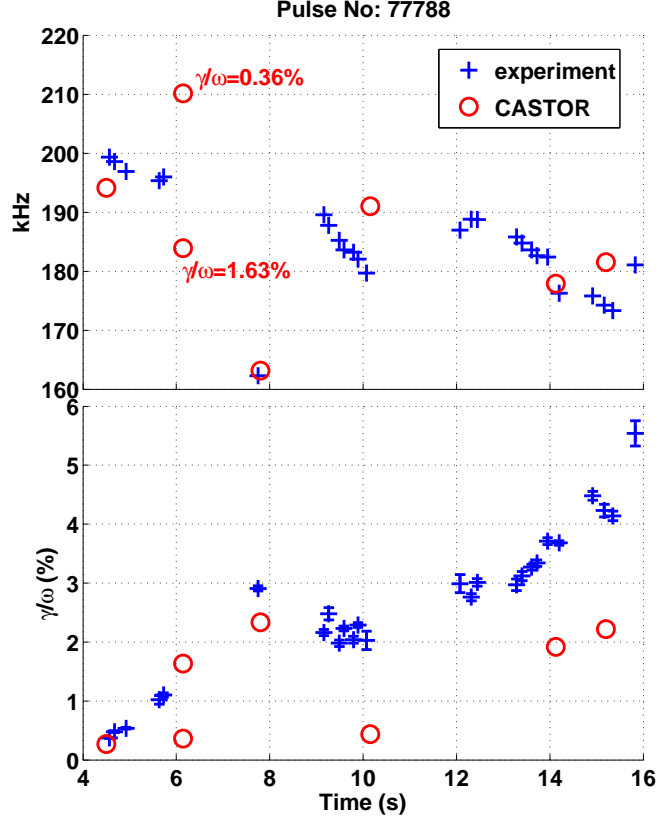


Figure 5.19: Comparison between CASTOR and experiment in terms of $n = 3$ TAE frequencies (top) and damping (bottom). We observe that the agreement in frequency varies and sometimes it is not possible to clearly identify the experimental measured mode using the proximity in frequency, e.g. in the case of $t = 6.1$ s where 2 eigenmodes are found at similar distances in frequency and with different damping. The agreement in the dampings varies, from predictions that are very close to the measured damping, e.g. at $t = 4.5$ s and at $t = 7.8$ s, to predictions that resulting in a damping of 4 times lower than the measured value, e.g. at $t = 10.15$ s.

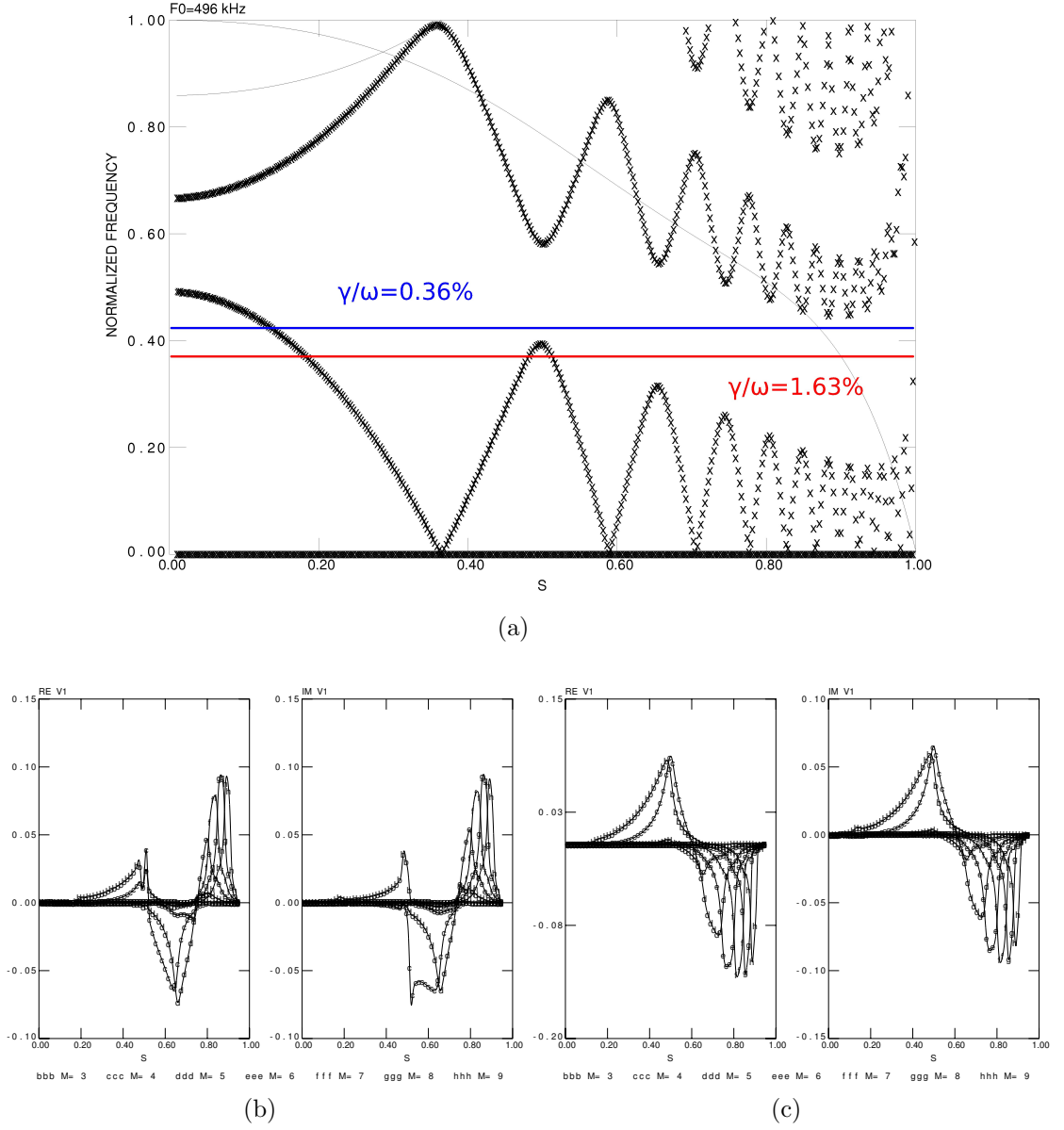


Figure 5.20: CASTOR results for $t = 6.1$ s in the discharge 77788. (a) The shear Alfvén continuum calculated by CSCAS. The frequency is normalized with the Alfvén frequency at the magnetic axis, i.e. v_{A0}/R_0 (shown in the top left corner of the plot). The radial coordinate is $s = \sqrt{\psi_N}$. The 2 horizontal lines mark the frequencies of the two eigenmodes that are found below (in red) and above (in blue) the experimentally measured mode. Below figure (a), the eigenfunctions of the lower-frequency mode (b), and the upper-frequency mode (c) are shown. Both real (left) and imaginary (right) parts of the normal velocity sv_{\perp} are shown.

5.4.4.3 Mode structure and damping mechanisms

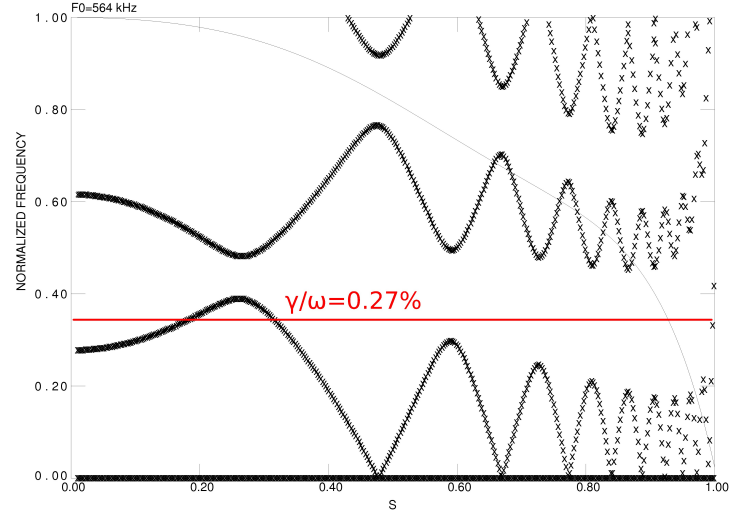
The main damping contribution in the CASTOR model comes from the continuum damping. Continuum damping takes place whenever the eigenfrequency intersects the shear Alfvén continuum. Thus, it is particularly important to consider the mode properties depending on its intersections with the continuum. In all the cases, the candidate theoretical modes are found below the minimum of the TAE upper continuum. Moreover, the edge properties of the q and density profiles are such that the TAE gap is open at the edge. Thus, the modes are not damped by continuum damping at the edge. Conversely, it is in the central region of the plasma that continuum damping takes place.

These properties can be best illustrated by considering the results for $t = 6.1$ s, shown in figure 5.20. In this case, the measured eigenfrequency is found to be at mid-distance between 2 candidate eigenmodes. The upper-frequency mode intersects the continuum in the core at $s \approx 0.15$ ($s = \sqrt{\psi_N}$), while the lower-frequency mode intersects the continuum at 3 radial positions, namely at $s \approx 0.19, 0.45, 0.55$. As a result, the upper-frequency mode is less damped than the lower-frequency mode, 0.36% as opposed to 1.63%, while the experimentally measured damping is 1.1% (figure 5.19). The damping rates at the other time slices can be either relatively low, as the upper-frequency mode, when the eigenfrequencies of the modes do not intersect the continuum at mid-radius ($t = 4.5, 10.15$ s), or higher, by $\sim 1.5\%$, when the eigenfrequencies of the modes do intersect the continuum at mid-radius ($t = 7.8, 14.1$ s).

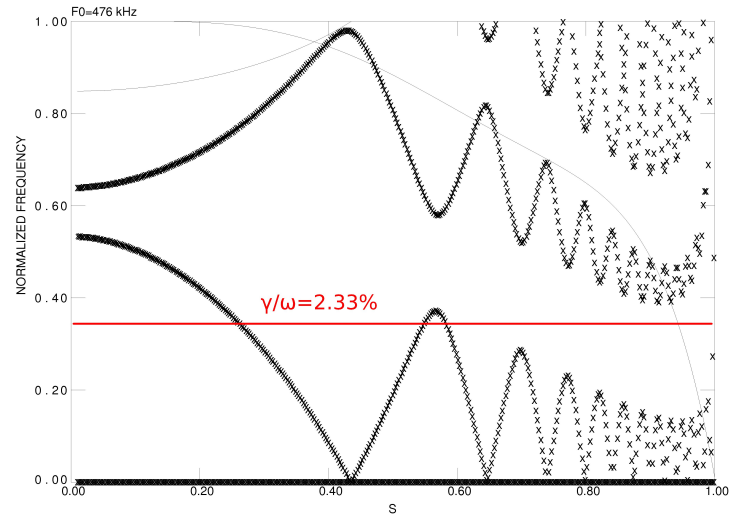
Thus, the CASTOR model suggests that the increase in the damping of the modes is due to a progressive misalignment of the TAE gaps, leading to more continuum damping in the central region of the plasma. Indeed, as shown in figure 5.21, this continuum damping model is confirmed by part of the measurements ($t = 4.5, 7.8$ s). However, the relatively big discrepancy with the other part of the measurements ($t = 6.1, 10.15$ s) suggests that the kinetic effects that are not included in the CASTOR model can be significant.

5.4.5 Comparison between CASTOR and LEMan

By comparing figures 5.6 and 5.19 and in particular the times $t = 6.1, 10.1$ and 14.1 s, it can be readily observed that, overall, LEMan has a better agreement with



(a)



(b)

Figure 5.21: The shear Alfvén continuum and the eigenfrequencies (marked with the horizontal line) that are close to the experimental measurements at $t = 4.5$ (a) and 7.8 s (b) (see also figure 5.20), for which a good agreement in both frequency and damping is obtained.

the experimental data than CASTOR. LEMan results suggest that the properties of the TAEs are modified due to kinetic effects, including the eigenfrequencies, when these are determined by the peaks in the plasma response. In the LEMan model, the dependence on the electron temperature is strong and the radiative damping is the dominant damping mechanism. As seen in Section 2, this is a kinetic effect and in the LEMan model, it comes from the finite electron inertia. The absence of these kinetic effects in the CASTOR model seems to account for the observed discrepancies, since, according to LEMan, the modes are strongly influenced by electron Landau and radiative damping. It should be noted that at $t = 14.1$ the agreement between the 2 codes is somewhat misleading, as the continuum damping in LEMan is 1%, with the total damping being 2.45%, whereas in CASTOR the continuum damping, which also makes up the total damping, is 2%.

While the difference in the q profile between EFIT and HELENA is small, this might account for some of the discrepancy. However, it is interesting to note that studies with the same input data (from HELENA) that have been carried out with the code CASTOR-K, the kinetic version of CASTOR, and they are presented in the reference [97], predict slightly different mode frequencies from the ones found here and closer to the experimental ones. This could be due to the way that CASTOR-K includes the kinetic effects for the description of the plasma.

Conversely, the good agreement between CASTOR and the measurements for modes that have either low damping due to well-aligned TAE gaps, namely at $t = 4.5$ s (figure 5.21a), or high damping due to multiple intersections with the continuum, namely at $t = 7.8$ s (figure 5.21b) suggests that the CASTOR model can predict reasonably well modes that have small interaction with the continuum via tunneling and are damped principally because of continuum damping.

5.5 Damping of $n = 4$ TAEs

5.5.1 Damping rate measurements

The $n = 4$ TAE measurements of the JET pulse #77783 shown in figure 5.22 were selected for a comparison with the LEMan model. The discharge #77783 comes from the same experimental session as #77788 (of which the $n = 3$ TAE

measurements have been analyzed in the previous section) and the plasma configuration is identical. In this experiment, several $n = 4$ TAE damping rates were measured in the starting phase of the elongation scan ($t = 8.7 - 11$ s) and also at the end of it ($t = 14 - 15$ s). This allows one to investigate the effect of the edge shear and elongation on the $n = 4$ damping.

As seen in figure 5.22, in the beginning of the elongation scan, the damping rate decreases from $\gamma/\omega = 1.8\%$ at $t = 8.7$ s to $\gamma/\omega = 0.5 - 1\%$ around $t = 10$ s, while s_{95} and κ_{95} start to increase already at $t = 9$ s. The damping rate of the $n = 4$ modes increases and reaches a value of $\gamma/\omega = 2.5\%$ before the X-point formation which takes place at $t = 15.8$ s. Notice that no mode is detected in the upward frequency scan during the time interval $t = 15.6 - 16.3$ s.

Compared to the $n = 3$ damping measurements shown in figure 5.1, it is observed the $n = 4$ modes are damped less by a factor of 2 approximately, both in the beginning and at the end of the elongation scan. Thus, the $n = 4$ damping shows an increasing trend as function of the elongation, similarly to the $n = 3$, though the maximum damping that is measured in these conditions is a factor of two smaller. Furthermore, in the X-point phase, the antenna-plasma coupling for the $n = 4$ is lost, in contrast to the $n = 3$ mode, for which a damping rate measurement is obtained after the X-point formation. The reason of the different behavior between $n = 4$ and $n = 3$ may lie in the fact that the $n = 4$ mode becomes more localized than the $n = 3$ mode, as a result of the increase in the edge shear.

5.5.2 Input data for the simulations

The plasma configuration of the JET discharge #77783 is very similar to #77788 as the 2 discharges were part of the same experimental session. Three time slices were selected for the comparison between the damping measurements and the LEMan predictions: $t_1 = 8.7$ s, $t_2 = 10.7$ s and $t_3 = 15.0$ s. These times are distributed along the edge elongation scan, which starts at $t = 8.5$ s and ends at 15.5 s with the formation of the separatrix. The equilibrium is reconstructed using the code EFIT. The electron density profiles enter as polynomial fits to high resolution Thomson scattering (HRTS) data, after being mapped to the EFIT flux grid. Electron cyclotron emission data have been used for the temperature profile. Figure 5.23a shows the evolution of the q profiles, where one can observe

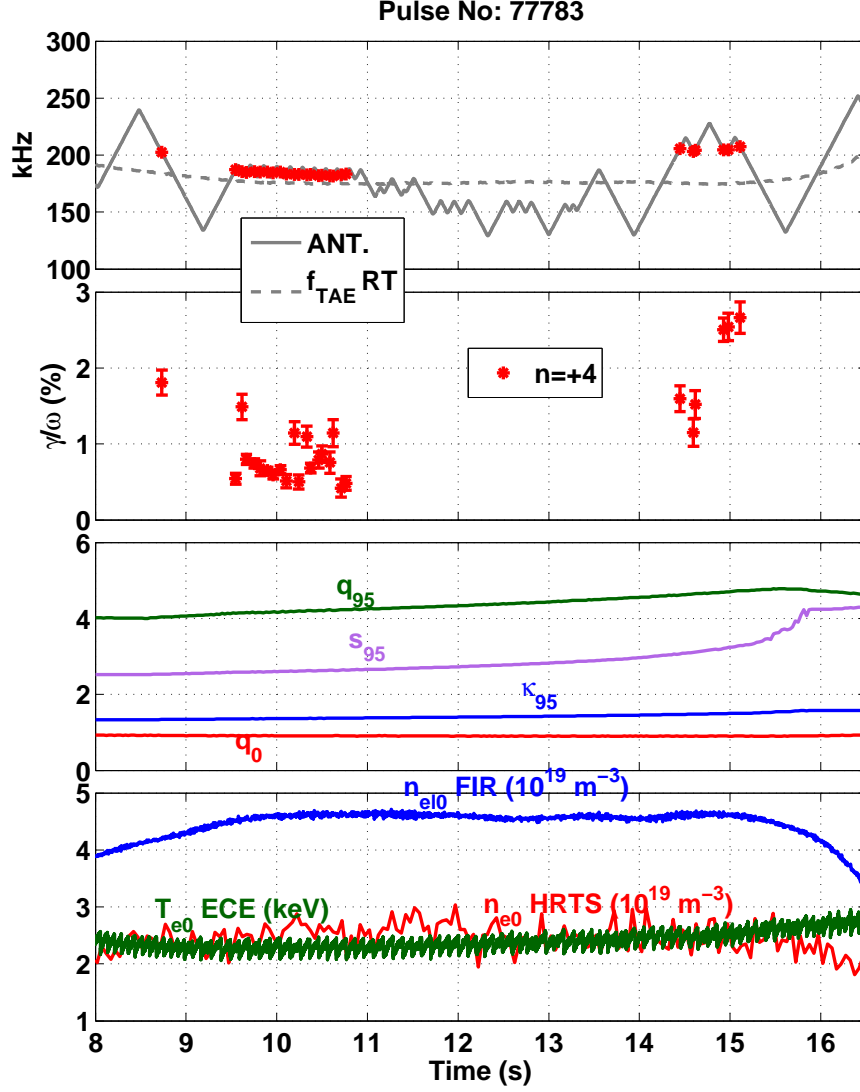


Figure 5.22: Damping rate measurements of $n = 4$ TAEs and time evolution of plasma parameters. In the beginning of the elongation scan in $t = 8.5 - 11$ s, the $n = 4$ damping decreases. At the end of the elongation scan in $t = 14 - 15$ s, with high s_{95} and q_{95} , the $n = 4$ damping increases up to $\sim 2.5\%$. Antenna configuration: 1+4+6+7+. (The reader can refer to figure 5.1 for the explanation of the labels and the symbols).

the increase in the edge values of q and shear. The q values in the center of the plasma are constant. Figure 5.23b shows the density profiles, where an increase of about 20% in the plasma center is observed between t_1 and t_2 . The edge density in the region $\rho_\psi > 0.9$ is basically constant during the considered time interval. In the absence of significant impurity concentrations in the plasma, the ion (deuterium) density is assumed to be equal to the electron density. Moreover, the ion temperature is assumed equal to the electron temperature, as in the discharge #77788.

5.5.3 Comparison between measurements and simulations

Figure 5.24 shows a direct comparison between the results from the LEMan simulations and the experimental measurements, in terms of frequency and damping rate of $n = 4$ TAEs. The agreement in frequency varies: at t_2 the agreement is very good, whereas at t_3 a relatively big discrepancy of 6.5% (the experimental measurement is at 207 kHz against 221 kHz found in the LEMan calculation) is found. For the case of t_3 , some further investigation has been carried out by modifying the density profile within the error bars. As shown in figure 5.25, no other mode is predicted at a closer frequency and in addition, neither the frequency nor the damping changes practically with the respect to the two different density profiles.

The predicted dampings are in good agreement with the measured dampings, especially for t_1 and t_2 . Furthermore, the two trends that are experimentally observed, namely, the first from t_1 to t_2 that shows the damping decreasing and the second from t_2 to t_3 that shows the damping increasing, are reproduced by the simulations.

5.5.4 Mode structure and damping mechanisms

Figure 5.26 shows the detailed LEMan results for $t_2 = 10.7$ s. From the plasma response, it can be seen that the predicted mode at 183 kHz can be clearly identified with the experimental mode that is excited at 182 kHz, as the other predicted modes are far away in terms of frequency. The mode is extended radially, from $\rho_\psi = 0.3$ to the plasma boundary, and comprises poloidal harmonics from $m = 4$ to $m = 22$ (figure 5.26c). The dominant m at the edge has $m = 18 - 19$. The

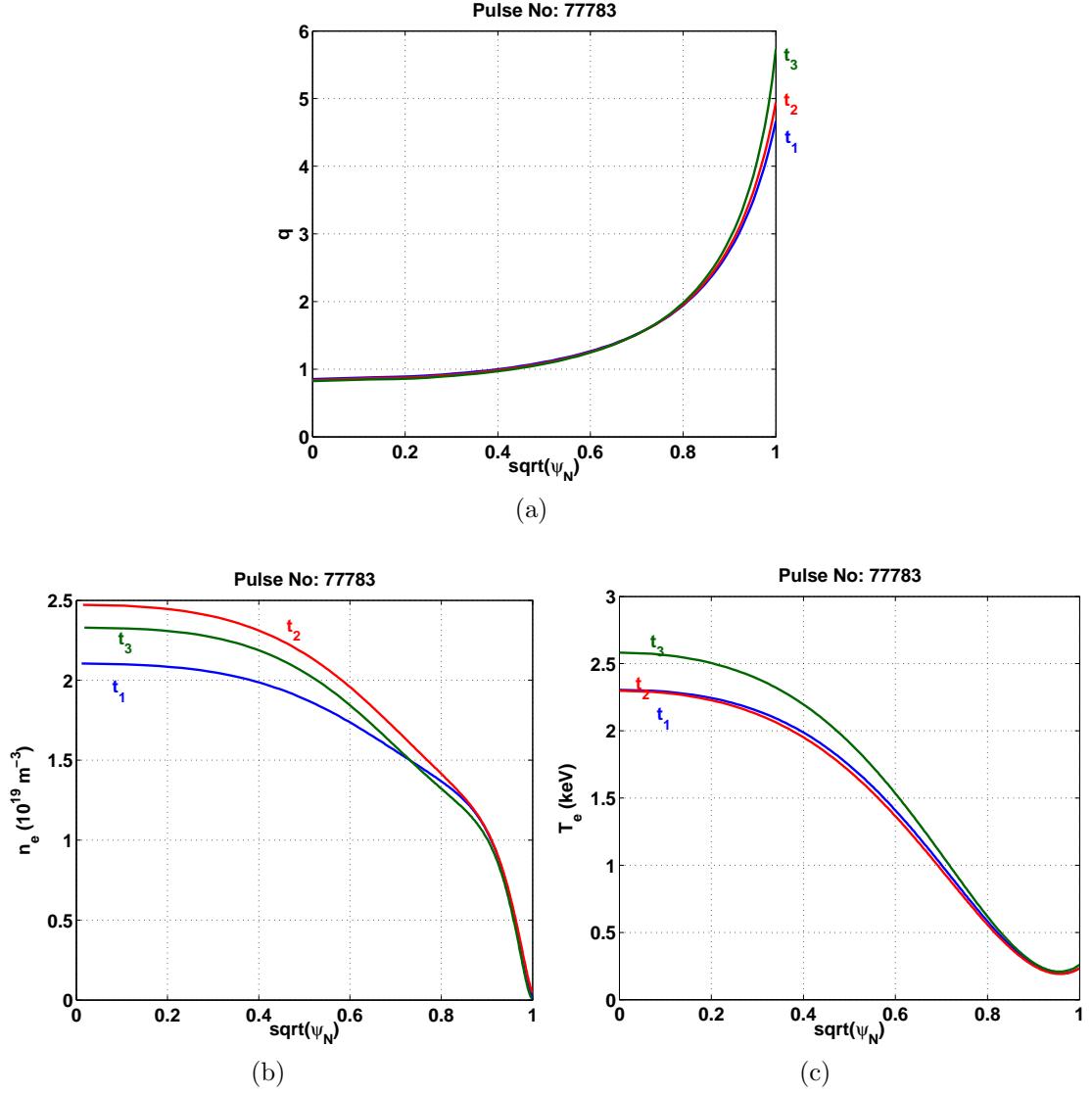


Figure 5.23: Profiles of q (a), density (b) and temperature (c) at $t_1 = 8.7$ s, $t_2 = 10.7$ s and $t_3 = 15$ s. Values of other basic plasma parameters at $t = 10$ s: $B_{t0} = 2.81$ T, $I_p = 1.95$ MA, $T_{e0} = 2.3$ keV, $\beta_N = 0.3688\%$.

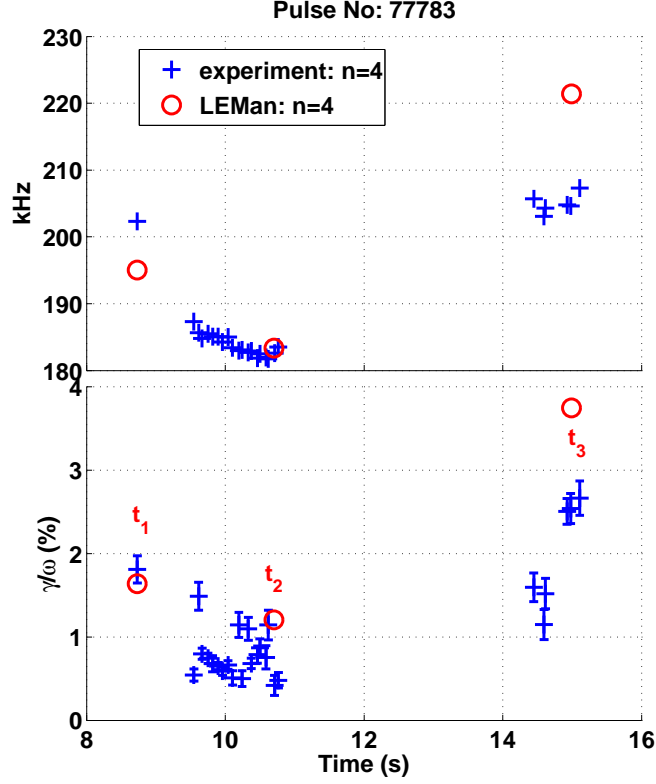


Figure 5.24: Comparison between LEMan and experiment in terms of frequencies (top) and dampings (bottom) of $n = 4$ TAEs. A good agreement is observed for the dampings and the evolution that is experimentally observed is also reproduced by the simulations.

power absorption profile has features in common with the $n = 3$ case shown in figure 5.11. Apart from the small contribution from continuum damping at $\rho_\psi = 0.3$, accounting for 5% of the total absorption, the rest is due to electron Landau damping from the finite parallel electric field E_\parallel (figure 5.26b) and mode conversion to KAWs. Again, radial correlation is observed between E_\parallel and the power absorption profile.

At $t_1 = 8.7$ s, the mode found at 195 kHz has a very similar radial structure to that of t_2 . The damping is found to be increased with the respect to t_2 , because the mode frequency intersects the continuum at $\rho_\psi = 0.5$ (figure 5.27).

At $t_3 = 15$ s, the mode found at 221 kHz has a different structure with respect to t_1 and t_2 . Contrary to the previous cases, the frequency of this mode is not just under the minimum of the upper continuum of the TAE gap but it intersects

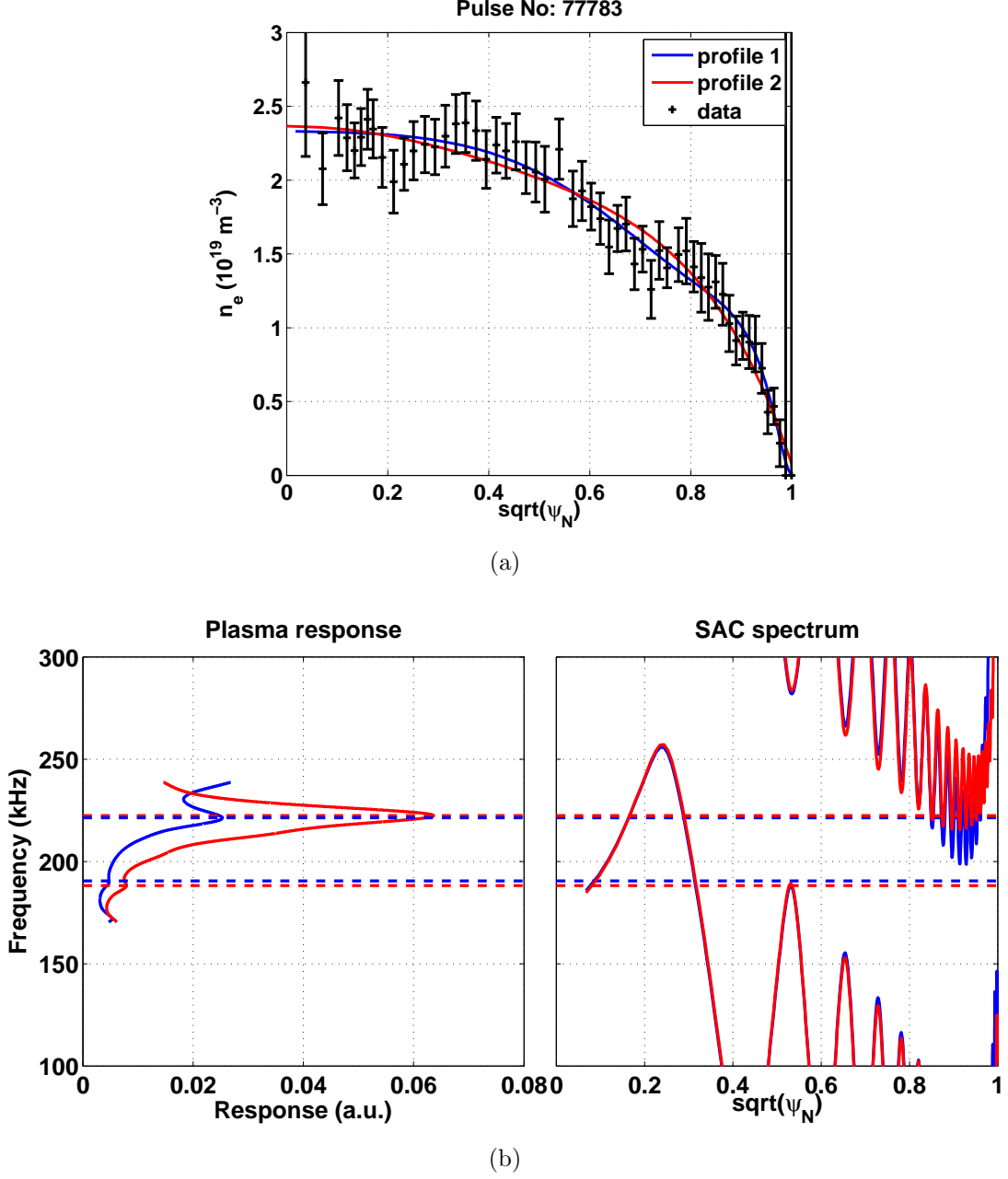


Figure 5.25: Sensitivity of LEMan calculation to slightly different n_e profiles, shown in figure (a) at $t_3 = 15$ s. As seen in figure (b), the plasma response remains basically the same, with the modes of interest at ~ 220 kHz having practically the same frequency and damping.

the continuum at the edge (figure 5.25b). This leads to continuum damping and all the power absorbed by the plasma takes place in the edge region, $\rho_\psi = 0.8 - 1$ (figure 5.28). It is noteworthy that the intersection with the continuum at $\rho_\psi = 0.3$ does not add any contribution to the total absorption.

To summarize, the LEMan results suggests that the main damping mechanisms of the $n = 4$ TAEs are mode conversion to KAWs coming from the interaction with the Alfvén continuum and direct electron Landau damping due to the finite E_\parallel . The $n = 4$ TAEs have a radially extended mode structure, similar to that of $n = 3$ TAEs. In conditions of high edge shear, the theoretical mode is found to intersect the Alfvén continuum at the edge and all the mode energy is dissipated in the edge region. The predicted damping is 3.7%, exceeding the experimental damping which is 2.5%.

5.6 Damping of $n = 7$ TAEs

5.6.1 Damping rate measurements

To address the damping of even more ITER-relevant mode numbers, we compare the measured damping of $n = -7$ TAEs to the LEMan model. It is interesting to investigate the high- n damping against lower- n , especially when such a comparison can be made for the same plasma conditions, in order to elucidate the relative weight of the different damping mechanisms for different kinds of modes. The discharge #78740 is well-suited for such an investigation, since $n = -7$ TAEs are clearly measured in parallel with $n = 3$ TAEs. The measurements show that the $n = -7$ modes are less damped than $|n| = 3$ modes by a factor of 1.5-2 for $t > 6$ s, as shown in figure 5.29. This experimental observation suggests that the difference in the measured damping could be due to the difference in the mode structure, since the two observed n are also very close in frequency. We consider the time slice at $t = 6.5$ s, where two very close damping measurements are available: an $n = -7$ mode with $\gamma/\omega = 1.78 \pm 0.22\%$ and 147 kHz at $t = 6.457$ s, and an $n = 3$ mode with $\gamma/\omega = 4.23 \pm 0.18\%$ and 152 kHz at $t = 6.418$ s. The resonance fits of these modes, as well as two more representative examples, are shown in figure 5.30.

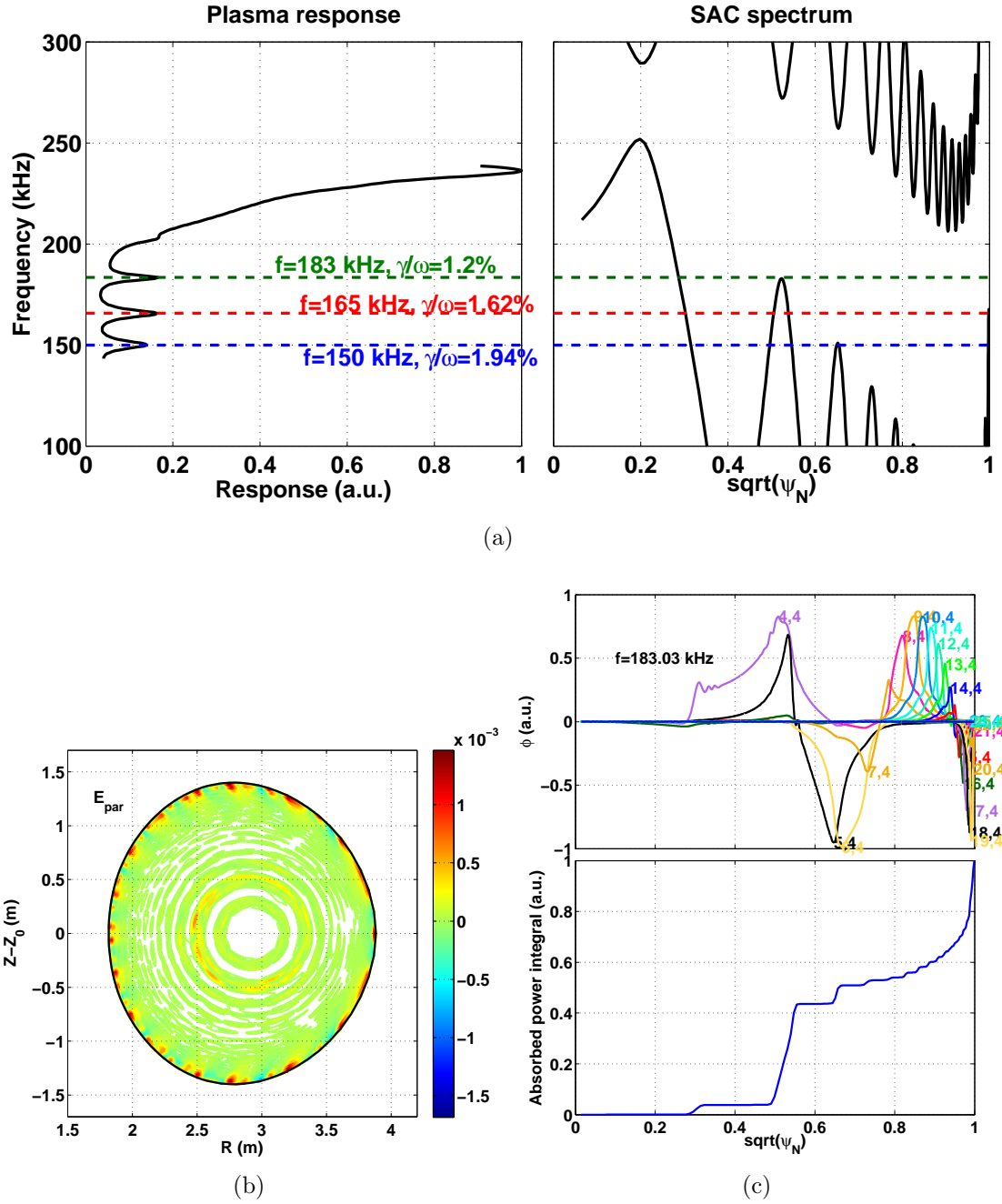


Figure 5.26: LEMan results for $t_2 = 10.7$ s in the discharge 77783. (a) Plasma response (left) and $n = 4$ SAC spectrum (right, zoom in the TAE gap). (b) Contour plot of E_{\parallel} . (c) Radial structure of the eigenmode scalar potential ϕ (top) and power absorption integral (bottom).

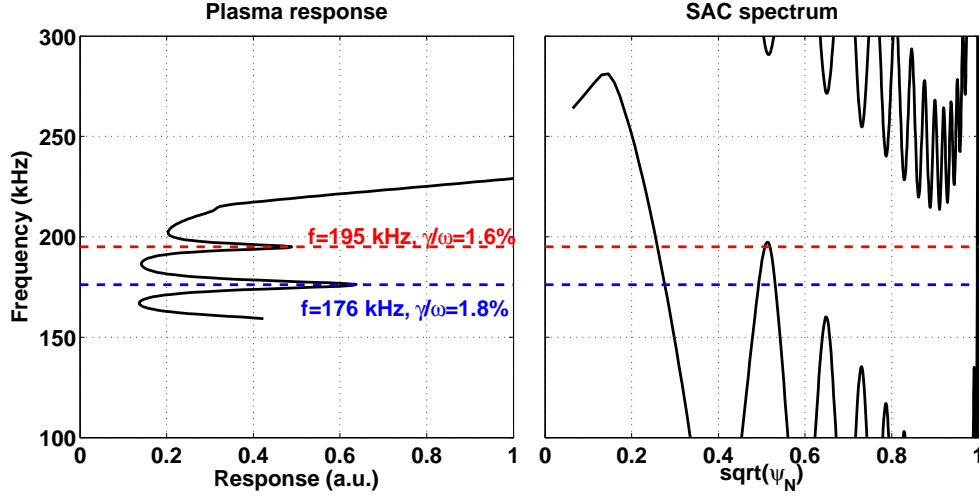


Figure 5.27: Plasma response (left) and Alfvén continuum (right) for $t = 8.7$ s in #77783, from LEMan calculation.

5.6.2 Input data for the simulations

The profiles of the safety factor q , electron density and temperature are shown in figure 5.31. The equilibrium is reconstructed using the code EFIT. The electron density and temperature profiles come from high resolution Thomson scattering (HRTS) data and are mapped to the EFIT flux grid. Because of the absence of charge-exchange measurements, there is no direct estimate of the toroidal rotation or the profiles of the ion temperature. However, as the plasma conditions are similar to those of the discharge #77788 where a complete diagnostic coverage was available (ohmic phase, similar density and temperature profiles), it is reasonable to assume that $T_e \approx T_i$ and $n_e \approx n_i$. In addition, the line average Z_{eff} measurement is very similar to that of the discharge #77788.

It has to be noted that this is the first time that such a high- n ($|n| = 7$) case is simulated with LEMan. There are numerical difficulties that are related to the high number of harmonics and the wave propagation. Initial simulations were carried out with a radial grid of 150 points. To ensure that the radial resolution is adequate, further simulations were carried with a radial grid of 300 points. The results of the LEMan simulations for $n = +7$ showed that the plasma response remains the same when the radial resolution increased. Furthermore, no numerical problems appeared and the condition that $\nabla \cdot \mathbf{A} = 0$ was well satisfied.

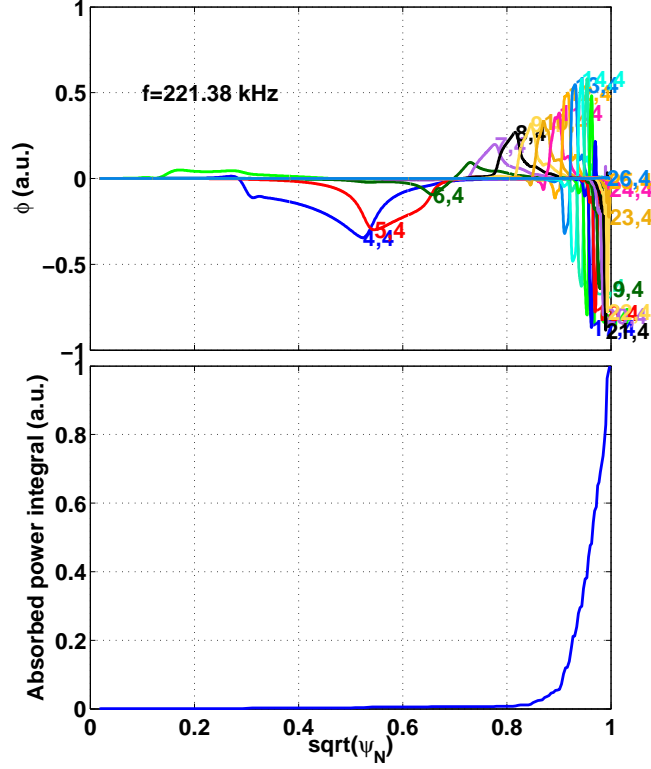


Figure 5.28: LEMan results for $t = 15$ s in the discharge #77783. Radial structure of the eigenmode scalar potential ϕ (top) and power absorption integral (bottom). The absorption takes place in the region $\rho_\psi = 0.8 - 1$, as a result of the intersection of the mode frequency with the Alfvén continuum (shown in figure 5.25).

While the LEMan model should produce in principle very similar results for $n = -7$ as for $n = +7$, some numerical problems were observed in the results of the simulations for $n = -7$. Hence, the LEMan results that are reported in this work come from the $n = +7$ simulations. The number of harmonics that was used for the frequency scans was from $m = 3$ to $m = 35$, covering by far all possible TAE gaps (the core gap is created by the coupling of $m = 5$ and $m = 6$ while the edge gap is created by $m = 27$ and $m = 28$).

5.6.3 Mode identification and interpretation

First, in the plasma response calculated by LEMan, we try to identify the modes that correspond to the experimental observation. The plasma response and the

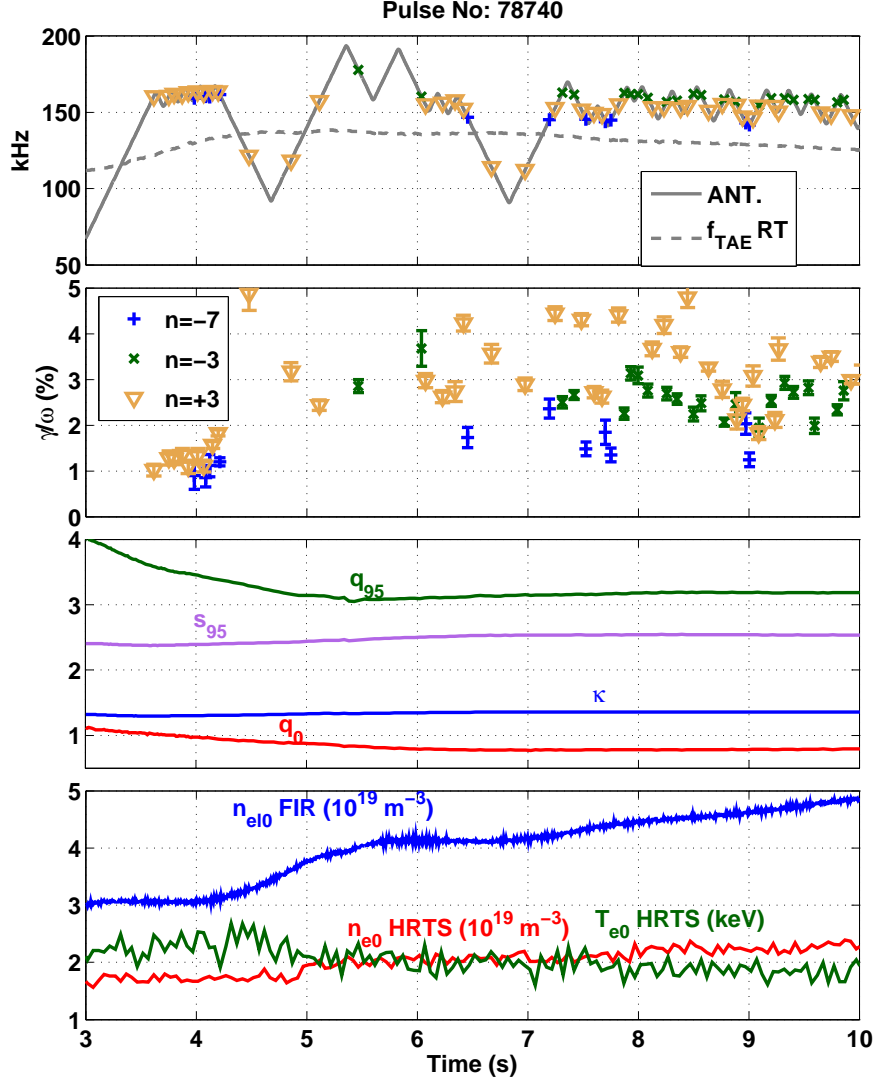


Figure 5.29: Damping rate measurements of $|n| = 3$ and $n = -7$ TAEs and time evolution of plasma parameters. Both n have a damping rate of $\sim 1\%$ at $t = 3.7$ s. The damping of $|n| = 3$ modes increases to levels of 2-5%, whereas the $n = -7$ modes are damped less than $|n| = 3$ by a factor of 2. Antenna configuration: $1 + 4 + 6 - 7 -$. (The reader can refer to figure 5.1 for the explanation of the labels and the symbols).

5.6 Damping of $n = 7$ TAEs

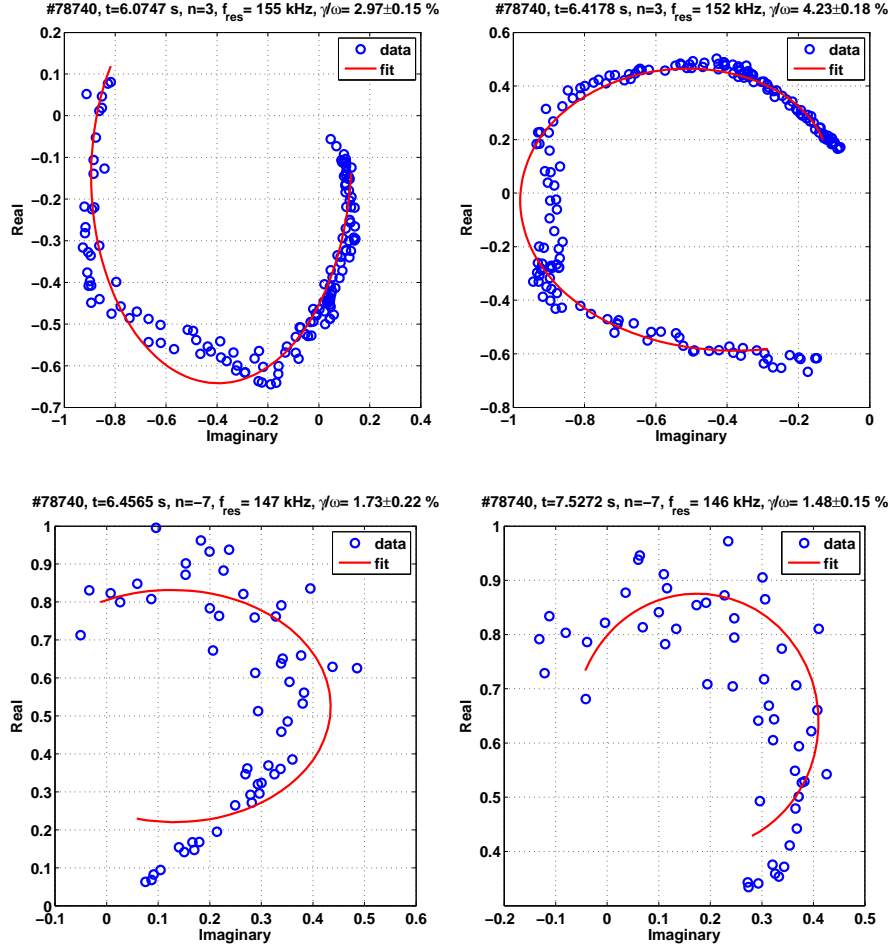


Figure 5.30: Representative resonance fits for $n = 3$ TAEs (top) and $n = -7$ TAEs (bottom). Compared to $n = 3$, we observe that the $n = -7$ have a lower signal-to-noise ratio (SNR), as seen in the increased scattering of the experimental points. Typically, high- n modes are observed to have relatively low amplitudes and high SNR.

shear Alfvén continuum for the $n = 3$ and $n = 7$ modes are shown in figure 5.32. For the $n = 3$ mode, two peaks, one at 163.5 kHz and the other at 136 kHz, appear near the experimental frequency of 152 kHz. This suggests that the experimental mode is more likely to be the one at 163.5 kHz. In the code, this has a damping rate of 1.94%. For the $n = 7$ mode, multiple peaks appear the frequency range of interest. The mode that is closest to the experimental frequency of 147 kHz is the one at 152 kHz with a damping rate of 3.9%. The comparison between the identified modes and the experimental measurements is summarized in table 5.1.

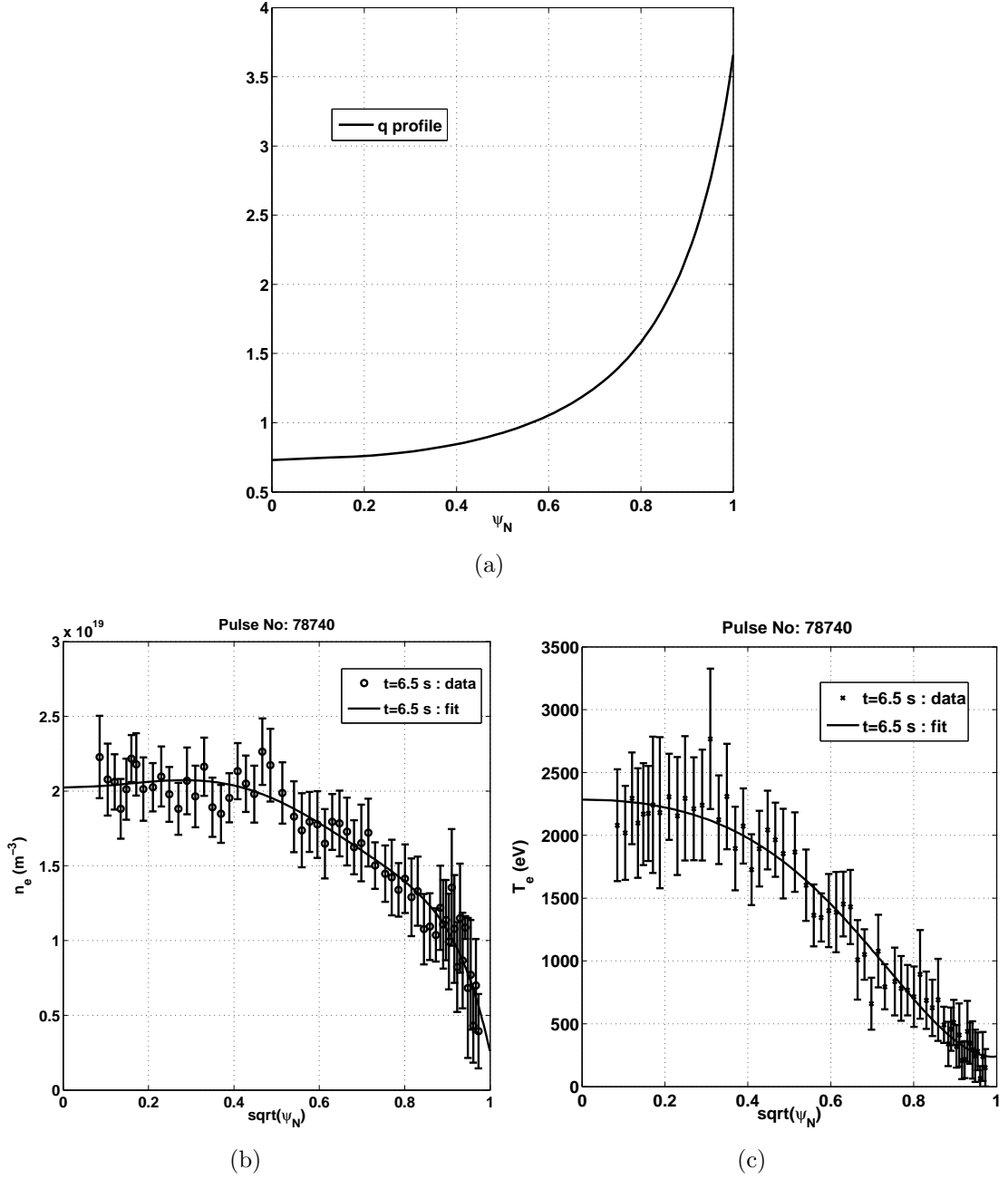


Figure 5.31: Profiles of q (a), density (b) and temperature (c) at $t = 6.5$ s. Values of other basic plasma parameters at $t = 6.5$ s: $B_{t0} = 2.144$ T, $I_p = 1.92$ MA, $\beta_N = 0.4571\%$.

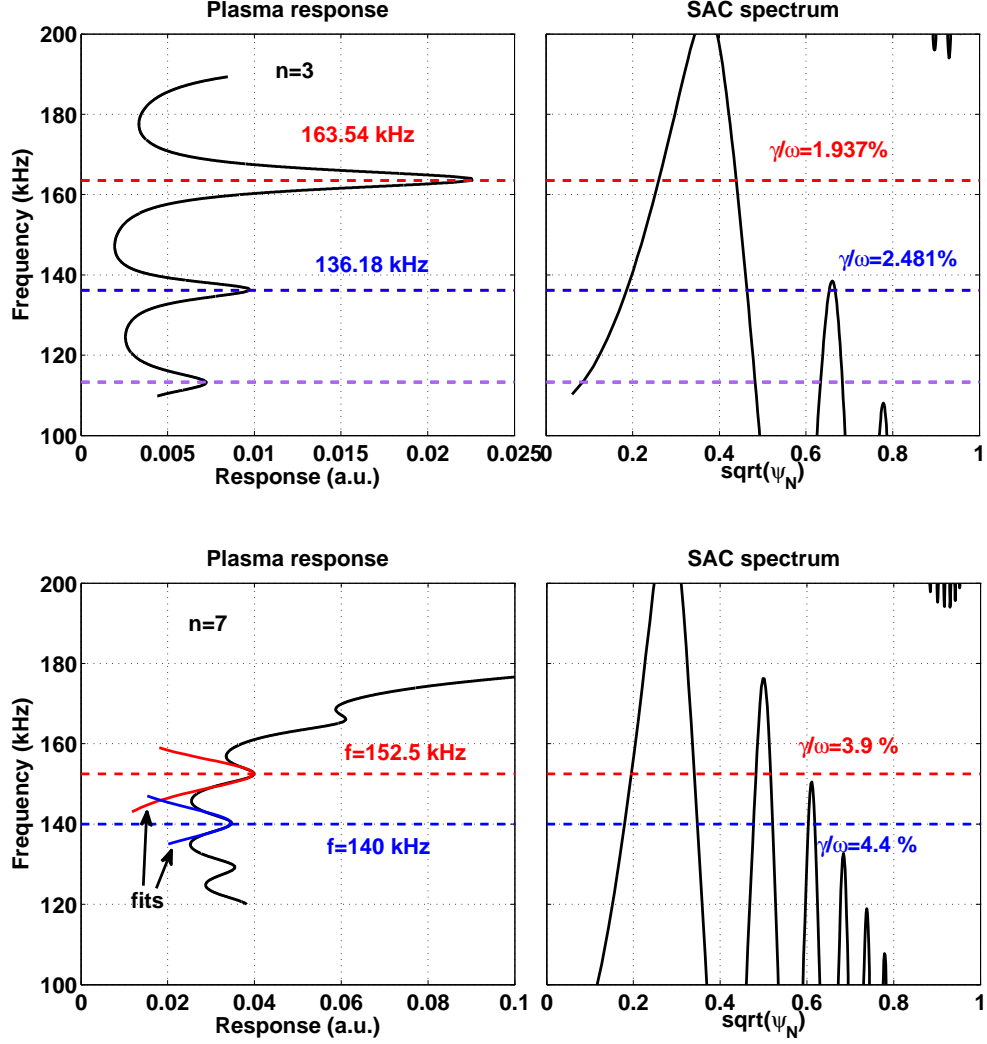


Figure 5.32: LEMan results for $n = 3$ (top) and $n = 7$ (bottom) modes: plasma response (left) and shear Alfvén continuum (right). The damping rates of the $n = 3$ resonances are estimated from the HWHM. The damping rates of the $n = 7$ resonances are estimated by fitting the plasma response of the mode frequency using the expression (2.21), since the half-maximum of the peaks cannot be recovered from the plasma response.

5.6 Damping of $n = 7$ TAEs

$ n $	experiment		theory	
	f (kHz)	γ/ω (%)	f (kHz)	γ/ω (%)
3	152	4.23 ± 0.18	163.5	1.94
7	147	1.73 ± 0.22	152	3.90

Table 5.1: LEMan results against the experiment measurements for the discharge #78740, $t = 6.5$ s.

The calculated mode structure, the power absorption integrals and the parallel electric field E_{\parallel} are shown in figure 5.33. It is observed that the $n = 3$ mode is more extended radially, from the edge to the plasma core ($\rho_{\psi} = 0.1$), while the $n = 7$ mode is more localized, i.e. from the edge to $\rho_{\psi} = 0.35$. For $n = 3$, 80% of the power absorption takes place at $\rho_{\psi} = 0.41 - 0.49$ and it is due to continuum damping (the intersection of the mode frequency with the continuum in the top of figure 5.32). For $n = 7$, the continuum damping around the position $\rho_{\psi} \approx 0.5$ contributes to only 7% of the total absorption (the intersection of the mode frequency with the continuum in the bottom of figure 5.32). The largest amount of the total absorption, about 60%, comes from the edge, specifically from $\rho_{\psi} > 0.95$, while the remaining absorption takes place at the centers of the TAE gaps in the region $\rho_{\psi} = 0.6 - 0.9$. The field E_{\parallel} has a clear spatial correlation with the centers of the TAE gaps both for $n = 3$ and for $n = 7$. Finally, it is interesting to notice the tunneling of the poloidal harmonics $(m, n) = (2, 3)$ and $(m, n) = (6, 7)$ through the continuum (figures 5.33 and 5.32).

Thus, the main damping mechanism for both n cases is the mode conversion to KAWs, with some possible contribution of direct electron Landau damping at the edge due to the finite E_{\parallel} . However, continuum damping around the plasma mid-radius is much more important for $n = 3$ than for $n = 7$; a consequence of the mode localization. Nonetheless, the predicted damping rate has the inverse dependence on n when compared to the experiment: in LEMan, the $n = 7$ damping is approximately twice the $n = 3$ damping, while in the experiment, the inverse is true, i.e. the $n = 7$ damping is approximately roughly half the $n = 3$ damping. In absolute values, the difference in the damping rates between experiment and LEMan is a factor of two.

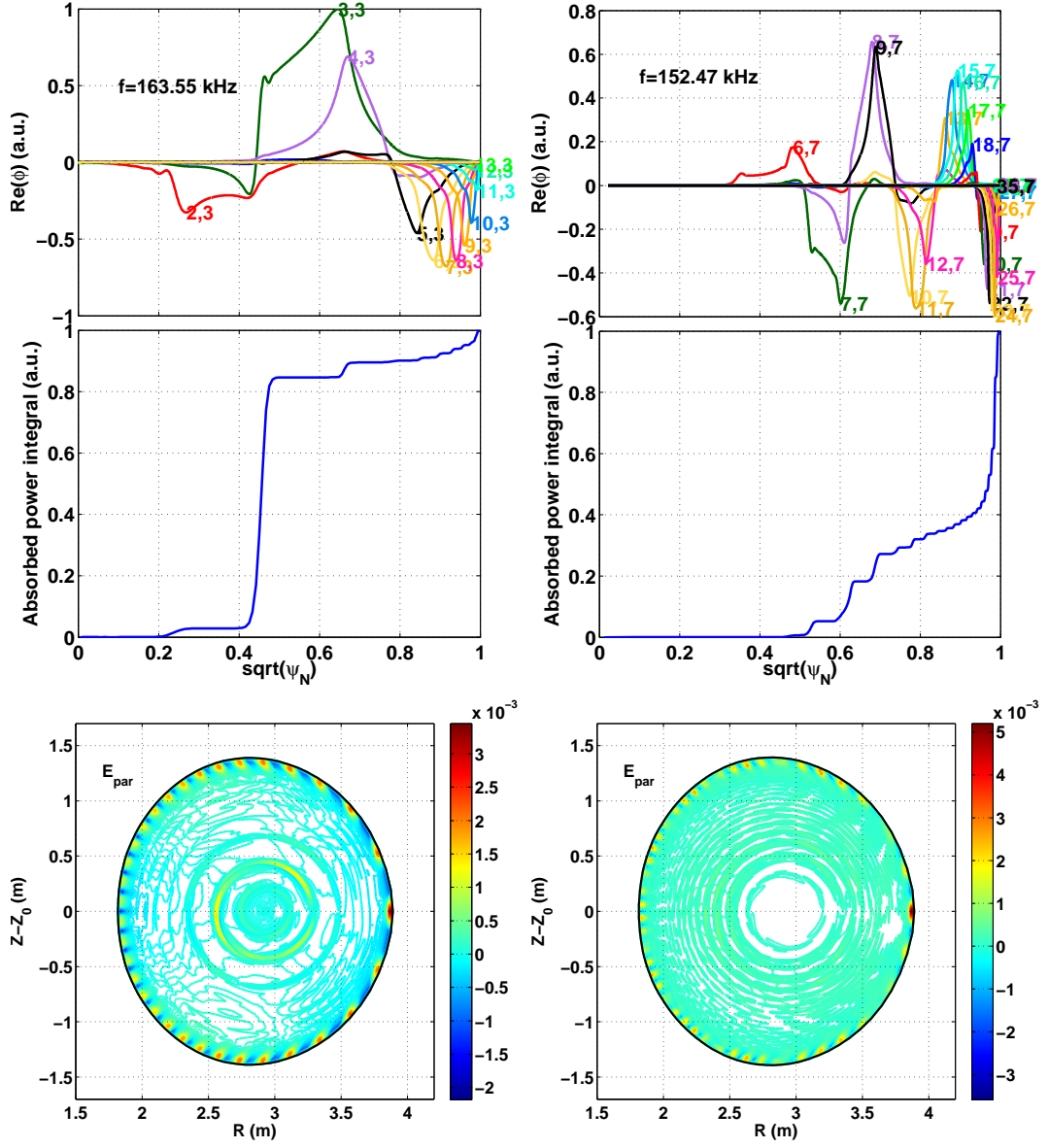


Figure 5.33: LEMan results for $n = 3$ (left) and $n = 7$ (right) modes: scalar potential (top), power absorption integral (middle) and contour plot of the parallel electric field (bottom).

The fact that LEMan gives a relatively large damping rate of the $n = 7$ mode, coming mostly from the edge, even though the mode frequency does not intersect, nor is it close to the edge continuum, is an issue that needs clarification.

5.7 Summary and discussion

The comparison of the experimental measurements of antenna-driven TAEs with the results of LEMan and CASTOR simulations leads to the following observations:

- The profiles of q and density lead to typical structures for the shear Alfvén continuum (SAC). In the early phase of the discharge when $q_0 > 1$, the TAE gaps are relatively well-aligned. As the q profile settles down, the gaps become more misaligned, as shown in figure 5.21. The upper TAE continuum has a minimum close to the edge in the region $\rho_\psi = 0.8 - 0.9$. The structure of the continuum is important because the TAEs interact strongly with it, especially at the edge.
- In most cases, it is straightforward to identify the mode found experimentally with a unique theoretical mode, the nearest in frequency. In addition, the difference between the experimental and theoretical frequencies is much smaller than the frequency separation between the frequencies of the other theoretical modes and the measured ones.
- The theoretical modes that have been identified as those that have been experimentally measured, are radially extended comprising many coupled poloidal harmonics. The $n = 3$ and $n = 4$ modes extend from $\rho_\psi \sim 0.2$ to the plasma boundary, while the $n = 7$ mode extends from $\rho_\psi \sim 0.4$ to the plasma boundary. In most cases, their frequency is found to be under the minimum of the upper TAE continuum. In one case ($n = 4$, #77783, $t = 15$ s), they are found to be just above this minimum, thus intersecting the continuum at the edge. They intersect the continuum also in the plasma center. All the identified modes satisfy the requirement that they have finite amplitude at the edge of the plasma, as suggested in [71]. These observations suggest that the antennas couple better to modes of which the frequency does not intersect the upper TAE Alfvén continuum. The antenna-plasma coupling seems also to be favored by low edge shear so that the modes can have sufficient radial extent.
- The sensitivity tests indicate that the effect of the profile uncertainty on the LEMan damping calculation depends on the specific plasma configuration.

For example, if the mode of interest is coupled to the continuum at the edge, it is likely to be sensitive to edge density profile. However, apart from a single case (t_4 , #77788), the modes that were identified with the experimental measurements are found to be robust against the considered profile changes.

- A good agreement is obtained between the $n = 3$ and $n = 4$ measurements and the LEMan plasma model, especially in the case of the $n = 4$ damping rates, where in the simulations of two time points the predicted damping rates agree with the experiment within the error bars. The experimental trends in the damping of $n = 3$ and $n = 4$ are reproduced to a reasonable degree. The overall level of agreement suggests that the main damping mechanisms that are accounted for in the LEMan plasma model can explain reasonably well the damping of these AEs. The most important mechanisms are mode conversion to KAWs via continuum damping and radiative damping and direct electron Landau damping due to the finite E_{\parallel} .
- Concerning the CASTOR plasma model, the agreement with the $n = 3$ TAE measurements is not as good as for LEMan. This result is reasonable because the continuum damping can be a small contribution to the total damping and other kinetic effects are not included in the model. Indeed, it is found that the discrepancy is bigger in cases where the kinetic effects of radiative and finite E_{\parallel} are important, and it is smaller where the latter effects are weak and the main contribution comes from continuum damping.
- These comparisons suggest specific ways of how the changes in the profiles of q , shear and density drive the evolution of the measured damping rate. In particular, the profiles of q and density determine the Alfvén continuum structure and the alignment of the gaps and thus affect directly the interaction with the continuum. The q and density profiles that are observed at the beginning of the discharge during the current ramp-up lead to relatively well-aligned gaps and small dampings. As q_0 settles down to lower values, the gaps become more misaligned. The high edge q leads to a increased number of high- m harmonics. This, combined with the radial localization due to the increased shear, leads to significant mode conversion to KAWs and direct electron Landau damping due to finite E_{\parallel} .

- Damping measurements of $n = -7$ and $n = 3$ TAEs obtained in the same plasma conditions and at very close frequencies have been compared to the LEMan model. The absolute values of the measured and predicted damping rates agree within a factor of two. Nonetheless, the dependence with respect to n is different: according to the experiment, the $|n| = 7$ mode is damped less than the $n = 3$ by a factor of ~ 2 , while LEMan suggests that the $|n| = 7$ mode is damped more than the $n = 3$ by a factor of ~ 2 . This occurs in spite of the fact that the $n = 7$ mode is subject to much less damping in the plasma core than the $n = 3$ mode because of its stronger radial localization. LEMan indicates that the dominant contribution of the $n = 7$ mode comes from the edge even though the mode frequency does not intersect nor is it close to the continuum.

Part of the modeling studies for the $n = 3$ TAEs of the discharge #77788 with LEMan is also reported in [97, 102]. In reference [102], it was conjectured that retaining the up-down asymmetry in the simulations is important for calculating a damping rate which is close to the experimentally measured value. More recent simulation results presented in this work for $t = 15.835$ s, when the plasma is even more elongated and up-down asymmetric, and the sensitivity study with respect to density (figure 5.8b), suggest that the up-down asymmetry may not be as essential as initially thought. Both results for $n = 3$ and $n = 4$ TAEs for plasmas with high elongation indicate that the high edge shear and q can lead to the level of damping that is observed experimentally.

The modeling studies for the $n = 3$ TAEs of the discharge #77788 have been undertaken by other codes in the framework of the ITPA benchmarking studies [97]. The results are generally in good agreement with the measurements and the LEMan results, in terms of frequency, radial structure and damping. The codes reproduce reasonably well the experimental scaling of the $n = 3$ damping rate. The differences that are observed between the codes are consistent with the different plasma models. For example, the linear gyrokinetic code LIGKA [103], which includes the effects of finite Larmor radius and finite orbit width, predicts slightly higher damping in the region $\rho_\psi = 0.5 - 1$ for the case of $t = 10.157$ s, leading to an increase of 0.25% in the total damping.

5.8 Conclusions

The experimental measurements of $n = 3$, $n = 4$ and $n = -7$ TAEs have been compared to the predictions of the codes LEMAN and CASTOR. The predicted damping rates by LEMan agree with the experiment better than a factor of 2 in all considered cases. They reproduce the measure damping evolution, increasing and/or decreasing, driven by the changes in the background plasma parameters for $n = 3$ and $n = 4$ modes. However, the LEMan results show that the $n = 7$ modes are damped more than $n = 3$ modes by a factor of two, contrary to the experiment where the $n = -7$ modes are less damped by a factor of two. According to the LEMan model, that main damping mechanisms are mode conversion to KAWs induced by intersections with, or proximity to, the Alfvén continuum and direct electron Landau damping due to finite parallel electric field. The comparisons with the CASTOR model for $n = 3$ TAEs does not reach the same level of agreement, due to an insufficient description of the kinetic effects that modify the TAEs. Conditions of high edge shear and q enhance the coupling of the modes to the Alfvén continuum, leading to increased dissipation of the mode energy in the plasma edge region. The effect of mode localization starts becoming quite effective for the $n = 4$ modes and can lead to small or negligible damping from intersections of the mode frequency with the continuum in the plasma core. LEMan confirms that the effect of mode localization is even stronger of the $n = 7$ modes.

Chapter 6

AE damping rate measurements

6.1 Introduction

This chapter presents the experimental results that were achieved with the optimized AEAD system. A large collection of AE damping rate measurements was obtained during the JET experimental campaigns of 2008/2009. The data have been collected in plasma discharges with ohmic heating and relatively small amounts of ion-cyclotron resonance heating (ICRH) and/or heating with neutral beam injection (NBI). The diagnostic was operated on more than 700 JET pulses, providing tens of damping measurements per pulse on average.

In order to simplify the analysis of this amount of data, a reduced number of ~ 66 discharges with a low- n phasing and active antennas on two octants were considered. Such a configuration produces a dominant drive in the range $|n| = 0 - 10$, as shown in figure 4.5. This range of n is sufficient for studying the most unstable modes in JET and in future reactors, such as ITER, for which the range 3–15 is predicted to be the most unstable. Moreover, the specific discharges were considered for the relatively high antenna currents that were achieved over a wide frequency range with the use of the designed matching units (Chapter 3). Thus, the AE fluctuation data that corresponds to the selected discharges have the highest possible signal-to-noise ratio in the considered n range. The damping rate database was assembled using the algorithm that is presented in the Section 4.6. The post-pulse treatment of the data was manually validated individually for several of these 70 discharges and this provides a further check of the quality of these measurements.

These 66 discharges contain approximately 3000 damping rate measurements of TAEs and $n = 0$ GAEs. To analyze this amount of data, three approaches were adopted:

1. perform a statistical treatment of the data and look for correlations with plasma parameters and relevant variables,
2. consider discharges where the damping variation is tracked by the real-time system and where the cause of this variation can be identified and,
3. compare discharges with different damping rates but similar overall plasma parameters and explore the reason for the difference.

The statistical analysis is presented first in order to give an general overview of the damping rate measurements. This is followed by observations and comparisons from individual discharges that allow a more in-depth investigation of the damping rates.

All discharges considered in the database are ohmically heated. Including discharges with ICRH or NBI heating complicates considerably the analysis. As the toroidal β is low in ohmic configurations, we examine the damping dependence on the plasma shape and, specifically, on the q profile, the magnetic shear and the plasma elongation. The effect of ICRH drive on the damping of the modes is investigated separately.

This chapter is organized as follows. Section 6.2 describes the range of plasma parameters and configurations that are covered in this work and presents a statistical analysis of the measurements. Section 6.3 analyzes the damping rate measurements from individual plasma discharges as a function of the edge elongation and edge shear. The role of the range of values of the q profile is highlighted. Section 6.4 studies more specifically the effect of the q profile on the damping rate measurements in the initial phase of the plasma discharges when the q profile is still “relaxing”. Section 6.5 analyzes damping measurements of different- n modes that are measured in the same plasma conditions. The effect of ICRH-driven fast ions on the $|n| = 3$ TAE damping is illustrated in Section 6.6, where the fast-ion drive is also estimated. The results are summarized and discussed in Section 6.7.

plasma parameter	min	max
I_p (MA)	0.93	2.57
B_0 (T)	1.87	3.37
κ_{95}	1.25	1.71
q_0	0.72	2.70
q_{95}	2.63	6.56
s_{95}	2.21	4.73
b_N %	0.15	0.54
R_0 (m)	2.85	3.03
n_{e0} (10^{19} m^{-3})	~ 1	~ 3
T_{e0} (keV)	~ 1	~ 4

Table 6.1: Range of ohmic plasma parameters. The equilibrium data come from EFIT. The density and temperature come from the HRTS and LIDAR measurements. Because of the big uncertainty of the LIDAR measurements, approximate values are given. I_p is the plasma current, B_0 is the toroidal magnetic field on the magnetic axis, κ is the elongation, q is the safety factor, b_N is the normalized beta, R_0 is the R coordinate of the magnetic axis, n_{e0} is the axial electron density and T_{e0} is the axial electron temperature. The suffix ‘95’ denotes that the quantity corresponds to the surface of 95% normalized poloidal flux.

6.2 AE database and statistics

The TAE damping rate measurements from the ohmic phase of 70 discharges are entered into a database, which includes a total number of 2889 measurements. Table 6.1 shows the range of basic plasma parameters that is covered. As shown in table 6.1, in the ohmic discharges the maximum temperature and density are relatively small. In addition, the toroidal β is low. Hence, the data can be effectively used for studying the dependence of the damping on the plasma shape, naturally associated with the the q profile (current profile) and the magnetic shear profile. The q profile is monotonic in these discharges.

Figure 6.1 shows the number of damping measurements as function of n . It is observed that most of the measurements have $|n| = 2$ and $|n| = 3$ (figure 6.1, left). A smaller number of measurements is for $n = 0$ and $|n| = 1$: this is due to the real-time n -filtering, which allowed to skip these n and track higher n modes.

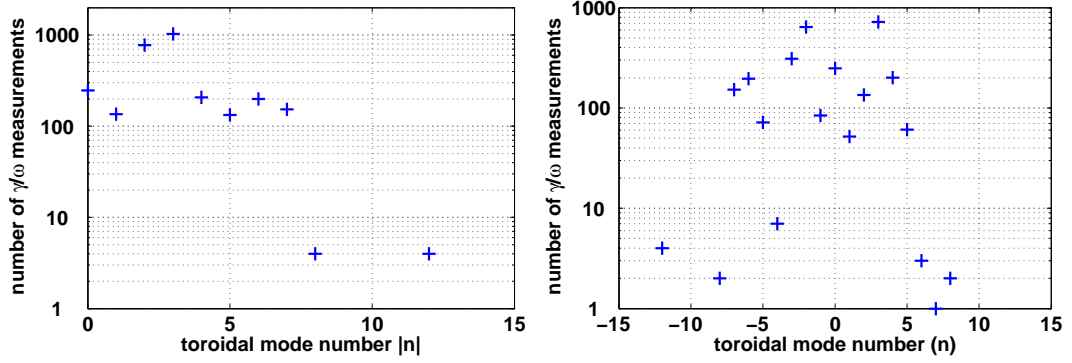


Figure 6.1: Number of damping rate measurements as function of $|n|$ (left) and n (right).

While the real-time system was typically set to look for $|n| > 2$, a relatively high number of $|n| = 2$ resonances are found. This is due to the very good low- n antenna-plasma coupling and to the fact that when the real-time tracking cannot find $|n| > 2$ resonances, the system executes large frequency scans during which several $|n| = 2$ modes are excited inside a TAE gap. In the range $|n| = 4 - 7$, a smaller number of data points are found: around 200 per n . For $|n| \geq 8$, very few damping rate measurements have been obtained. This dependence on n shows that the antenna-plasma coupling decreases strongly as function n . This decrease cannot be due to a decrease in the antenna drive since the antenna drive that is calculated in the vacuum decreases only by 30% up to $|n| \sim 10$ (figure 4.5). This indicates that high- n modes are strongly localized radially and thus more difficult to be coupled through the plasma and detected.

It is interesting to note the asymmetry with respect to the sign of $|n|$ (figure 6.1, right). For example, for $|n| = 6, 7$ modes, almost all the measurements have the minus sign. On the contrary, the $|n| = 4$ measurements have the plus sign. On the other hand, for $|n| = 5$ modes, an equal number of positive- n and negative- n is observed. As the antenna drive is equal for both n , this suggests a subtle mechanism that tips the scale of the antenna-plasma coupling in favor of a particular sign of n .

6.2.1 Damping rate dependence on plasma shape

We now focus on the damping rate dependence on the edge elongation κ_{95} , the edge shear s_{95} , the edge q , q_{95} , and the central q , q_0 . Figure 6.2 shows the damping rates for $|n| = 1 - 8$ plotted as function of κ_{95} . Several observations can be made. First, the maximum elongation $\kappa_{95,\max}$ for which damping rate measurements are achieved decreases with increasing $|n|$, $|n| = 1 - 5$. For $|n| = 1 - 2$, $\kappa_{95,\max} = 1.7$. For $|n| = 3$, $\kappa_{95,\max} = 1.6$. For $|n| = 4$, $\kappa_{95,\max} = 1.5$. For $|n| = 5$, $\kappa_{95,\max} = 1.35$. Surprisingly maybe, this trend slightly reverses when $|n|$ is increased from 5 to 7. Only a few measurements are obtained for $|n| = 8$ and $|n| = 12$ at low edge elongation. Second, the damping tend to increase with increasing κ_{95} for $|n| = 1 - 4$. This can be inferred from the absence of small damping rates at $\kappa_{95} > 1.5$. For $|n| = 5 - 7$, no clear trend with elongation is observed. Finally by looking in the range $\kappa_{95} = 1.3 - 1.4$ where most of the damping rate measurements are obtained, it can be seen that the maximum dampings measured for $|n| = 4 - 7$ are less than the dampings measured for $|n| = 2 - 3$.

Because the edge shear s_{95} increases with increasing κ_{95} , the previous observations on the damping as function of κ_{95} hold in a completely analogous manner for the dependence on s_{95} .

Figure 6.3 shows the damping rates as function of the q_0 . It is observed that for $|n| = 2 - 4$ the maximum damping rates decrease with increasing q_0 . The trend is more pronounced for $|n| = 4$. The $|n| = 5$ modes are excited only for high q_0 , $q_0 > 1.4$ (very few measurements are achieved for lower q_0). This observation does not continue to $|n| = 6 - 7$. For these n , no specific trend is clear. By comparing the magnitude of the damping rates for $q_0 = 0.8 - 1$ where most of the damping rates are measured, it can be seen that the maximum damping rates of the modes with $|n| = 4, 6 - 7$ are less than the damping rates of $|n| = 2 - 3$. Finally, the $|n| = 1$ modes exhibit a sharp increase in their damping for $q_0 < 0.8$.

Figure 6.4 shows the damping rates as function of the q_{95} . In this case, we cannot observe clear trends as function of q_{95} . However, two observations can be made: a), the damping rates of $|n| = 4$ are significantly weaker than those of $|n| = 1 - 3$ at the same q_{95} and b), $|n| = 5$ measurements are mostly achieved for high q_{95} , $q_{95} > 4.5$.

To summarize, the preceding analysis provides a useful overview of the damping rate measurements. It shows that the antenna-plasma coupling decreases as

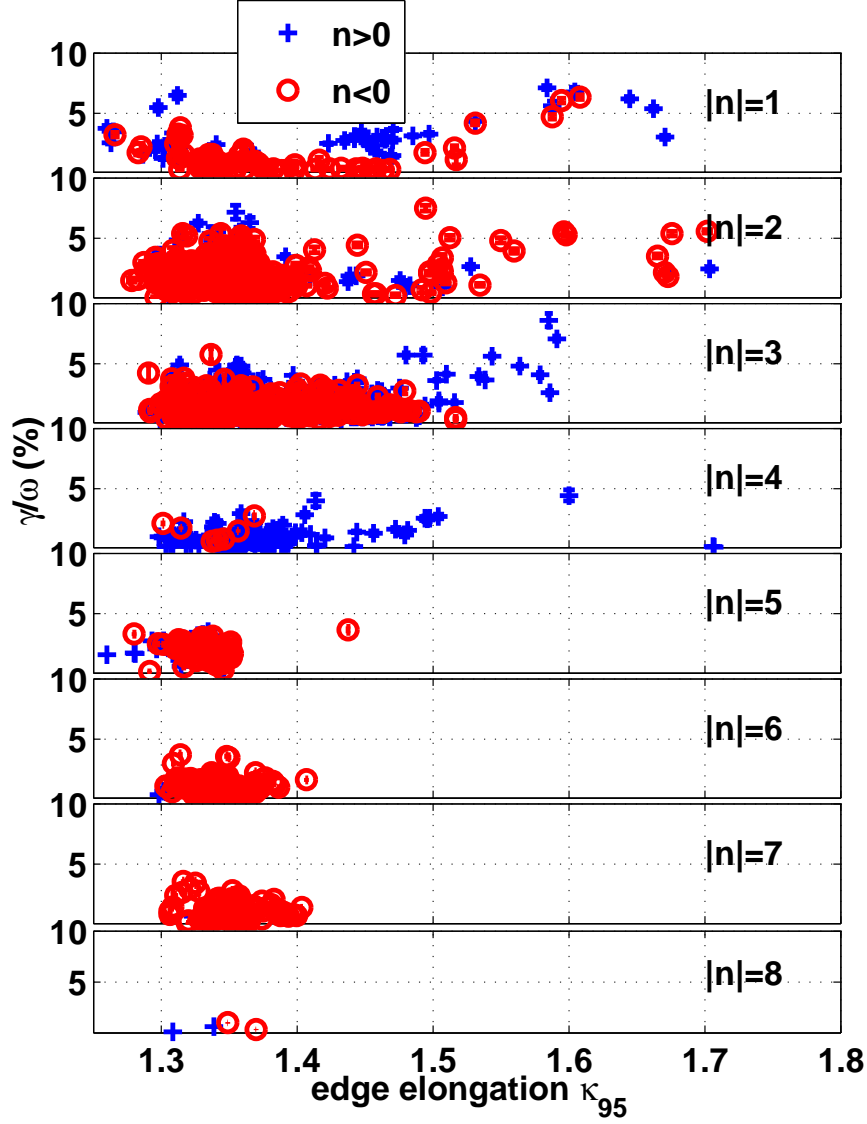


Figure 6.2: Database of damping rates as function of edge elongation

function of n and that this is controlled by the edge shear and elongation. An explanation for this observation is that the modes are becoming very localized at high shear and they cannot couple easily to an external excitation. The analysis also shows that the damping of modes with $|n| \leq 4$ increases with s_{95} and κ_{95} . Several observations could also be made for the dependence on the q profile parameters, q_0 and q_{95} .

Nevertheless, it is difficult to draw more specific conclusions on the role of the q profile and the difference between high- n and low- n . For example, the

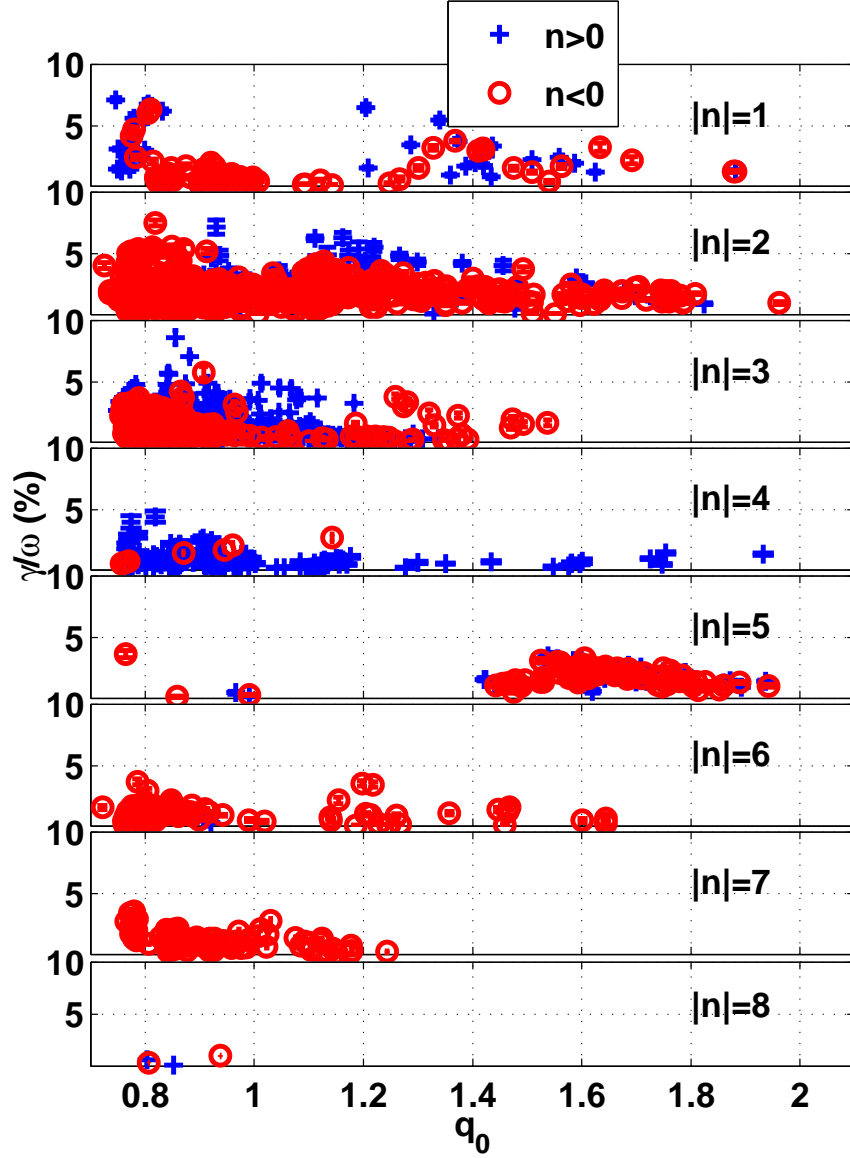
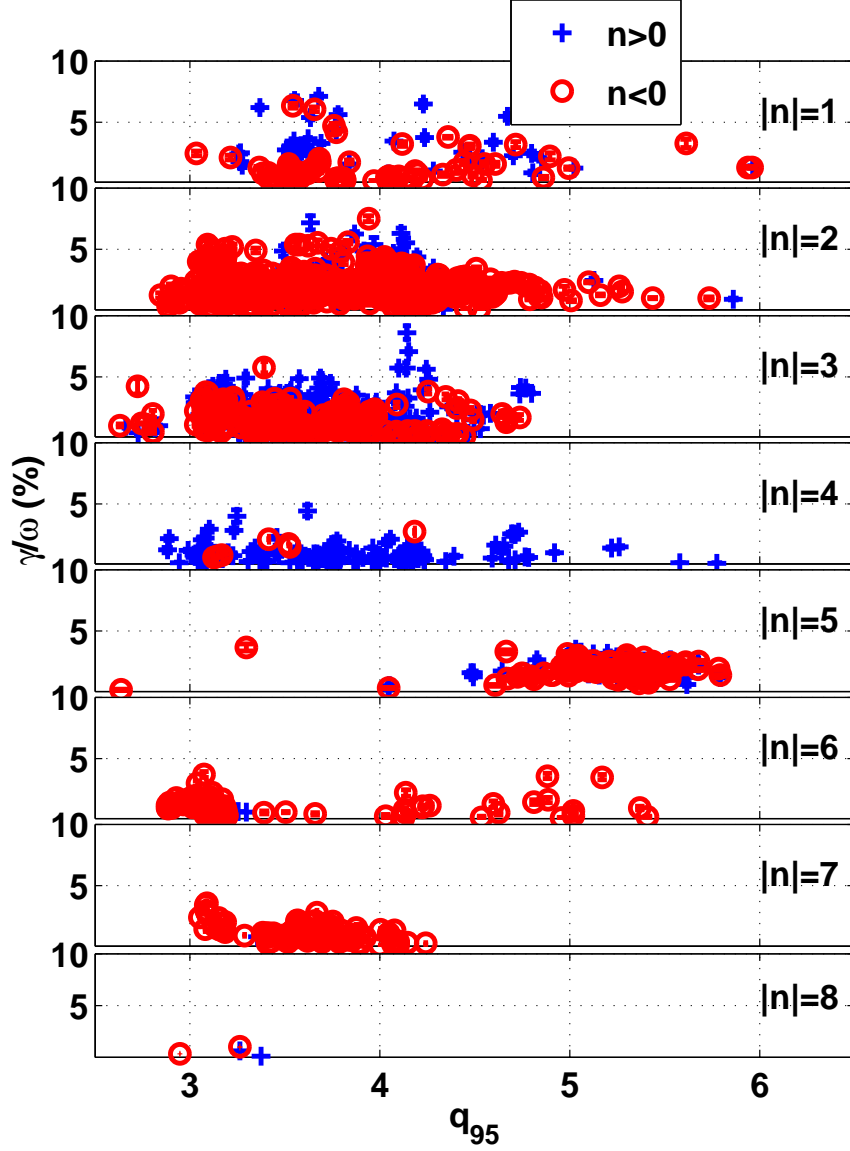


Figure 6.3: Database of damping rates as function of core safety factor q_0 .

bulk of the measurements for $|n| = 3$ as function of q_{95} does not reveal a clear dependency, nor the measurements of $|n| = 6$ as function of q_0 . For these reasons, an analysis that involves proper comparisons between similar plasma conditions is carried out in the following sections. Such an approach further confirms the general observations presented in this section.


 Figure 6.4: Database of damping rates as function of the edge safety factor q_{95} .

6.3 Effect of the edge shear/elongation and the role of the $q_{95} - q_0$

The typical scenario of the ohmic phase of the JET discharges that are studied here is the following: at the beginning of the discharge, the plasma current increases and penetrates into the plasma core, while the q profile is relaxing to lower values. This phase can be followed by a period of stationary q profile, after

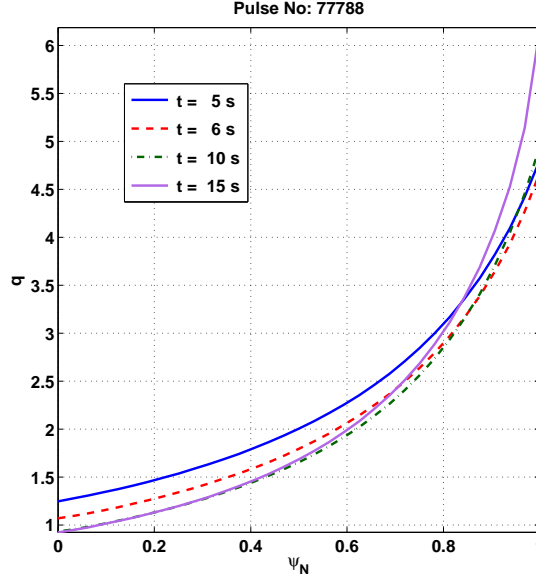


Figure 6.5: Evolution of the q profile (plotted as function of the normalized poloidal flux ψ_N) in the discharge 77788. During the initial phase of the discharge ($t = 5 - 9$ s), the central q is decreasing. Then, an elongation scan follows ($t = 9 - 15$ s) during which the edge shear increases, while q_0 remains constant. The q profile has been calculated using standard EFIT [98] equilibrium reconstruction.

which the plasma is typically led via an elongation scan to the formation of an X point at the plasma bottom. Figure 6.5 shows an example of such a scenario for a particular discharge.

6.3.1 $|n| = 3$ TAEs

In Section 5.4, the effect of the edge elongation and shear was analyzed in detail for the specific plasma configuration of the discharge #77788. It is interesting to check if the same scaling (increasing damping with increasing edge shear/elongation) is observed in different plasma conditions. To this end, we will proceed to comparisons of the damping measurements that are obtained during elongation scans between ohmic plasmas with very similar core density and core temperature but with different values of $q_{95} - q_0$.

In the discharge #77417, the evolution of $n = 3$ damping is followed during an elongation scan that starts at $t = 7$ s and ends at $t = 12$ s with an X-point formation (figure 6.6). Compared to #77788, the plasma of #77417 is very similar

in terms of density and temperature. The increasing trend of the damping as the plasma changes shape toward the X-point formation is again observed. However, the absolute magnitude of the damping is lower as γ/ω goes from 0.8% at $t = 6.8$ s to 1.7% at $t = 10.7$ s. Since q_0 are very similar in both discharges (~ 0.92 against ~ 0.89), the difference is related to q_{95} .

Let us now compare two damping rates at the same edge shear/elongation but at different q_{95} . Figure 6.8 shows a comparison between the q profiles that correspond to the same values of edge shear s_{95} and edge elongation κ . In the discharge #77788 (figure 5.1), at an elongation of $\kappa = 1.5$ at $t = 14.9$ s, γ/ω is measured at 4.48%. At the same time, the shear at the edge is $s_{95} = 2.86$ and the q at the edge is 4.73. In the pulse #77417, for the same elongation and edge shear (at $t = 10.67$ s, $\kappa = 1.5$ and $s_{95} = 2.86$), the edge q is 3.84 and the measured damping is $\gamma/\omega = 1.7\% \pm 0.11$. This shows a correlation of the damping with the q_{95} .

Indeed, q_{95} is higher in #77788 than in #77417 at all times. The overall variation of q_{95} during the elongation scan of #77788 is from 4.04 (at $t = 8.5$ s) up to 4.85, while in the pulse #77417 q_{95} varies from 3.7 ($t = 7$ s) to 3.9 ($t = 12$ s, just before the X-point formation).

Further measurements of the evolution of $n = 3$ TAE damping rates during elongation scans confirm both trends with κ_{95} and with q_{95} . For example, the measured damping in the pulse #77962 (figure 6.9) is very similar to the one of #77417 demonstrating the reproducibility of the results. In particular, figure 6.9 shows a case where q_{95} is at 3.8 at the beginning of the elongation scan (from $t = 7$ s to $t = 11$ s) and it is decreasing to 3.54 at the end of the scan. The scaling that the damping is increasing with increasing s_{95} is still observed, though lower γ/ω are measured compared to #77788, from $\sim 0.5\%$ to 1.8%.

In the previous examples, q_0 had a value around 0.9. When q_0 is lower, larger dampings are measured. Figure 6.10 shows such a case with q_{95} increasing from 3.8 to 4.2 and $q_0 \sim 0.83$. Two distinct $|n| = 3$ TAEs with eigenfrequencies at ~ 144 and ~ 182 kHz are tracked with the real-time system. Similarly to the measurements of #77788 with the high q_{95} (figure 5.1), the γ/ω of the upper TAE is at 2% at the beginning of the elongation scan and increases up to 4%, as both s_{95} and q_{95} increase toward the X-point formation. Notice also the damping

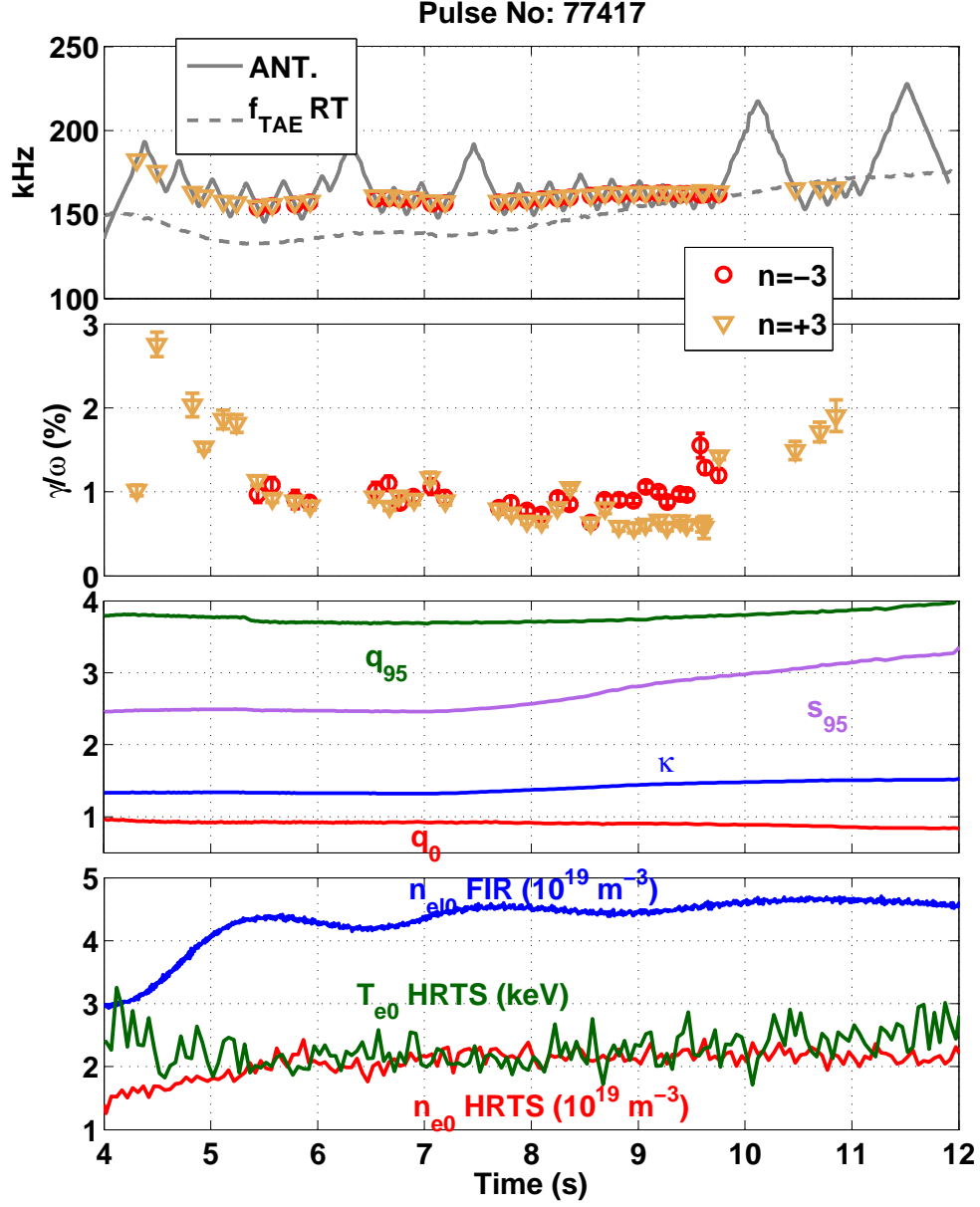


Figure 6.6: Damping rate measurements of $|n| = 3$ TAEs and time evolution of plasma parameters. During the elongation scan at $t = 7 - 12$ s, the measured dampings increase from $\sim 1\%$ to 2% at $q_{95} \sim 3.85$, almost constant. Examples of the resonance fits are shown in figure 6.7. Antenna configuration: 1 + 4 + 6 - 7 -.

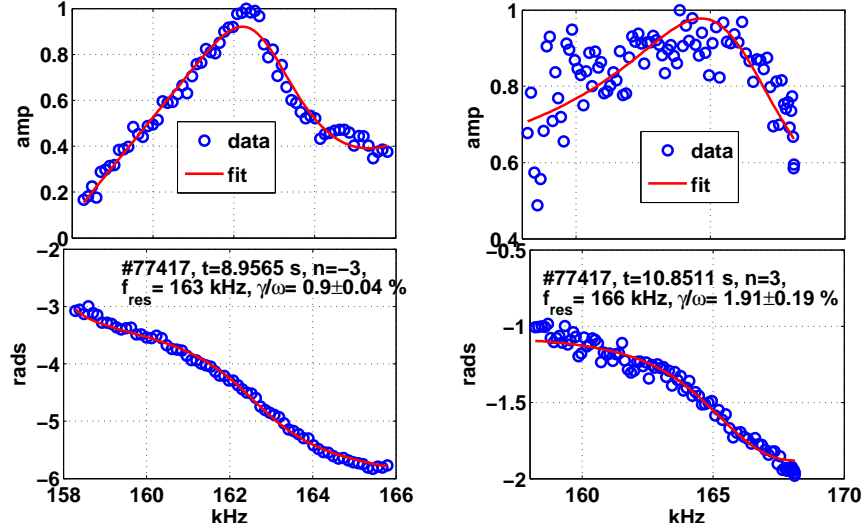


Figure 6.7: Examples of resonance fits for the $|n| = 3$ TAEs of the discharge #77417 (figure 6.6). Notice the small signal-to-noise ratio (SNR) for the data of the mode at $t = 10.85$ s at high s_{95} , in contrast to the very good SNR for $t = 8.957$ s at lower s_{95} .

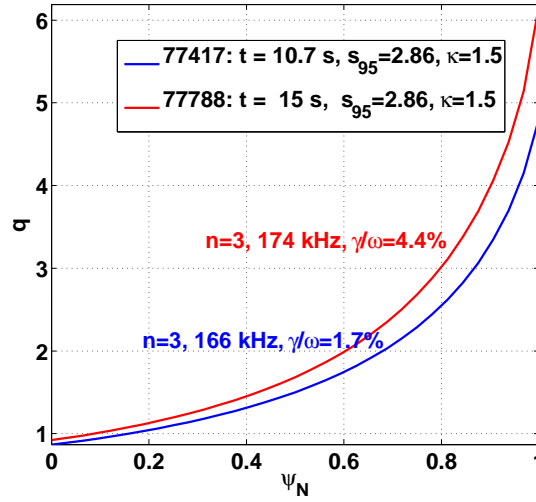


Figure 6.8: q profiles in the discharges #77417 and #77788 at the same edge shear and edge elongation: $s_{95} = 2.86$ and $\kappa = 1.5$. The measured dampings of $n = 3$ TAEs that correspond to each q profile are also shown. Note that higher $q_{95} - q_0$ leads to higher damping.

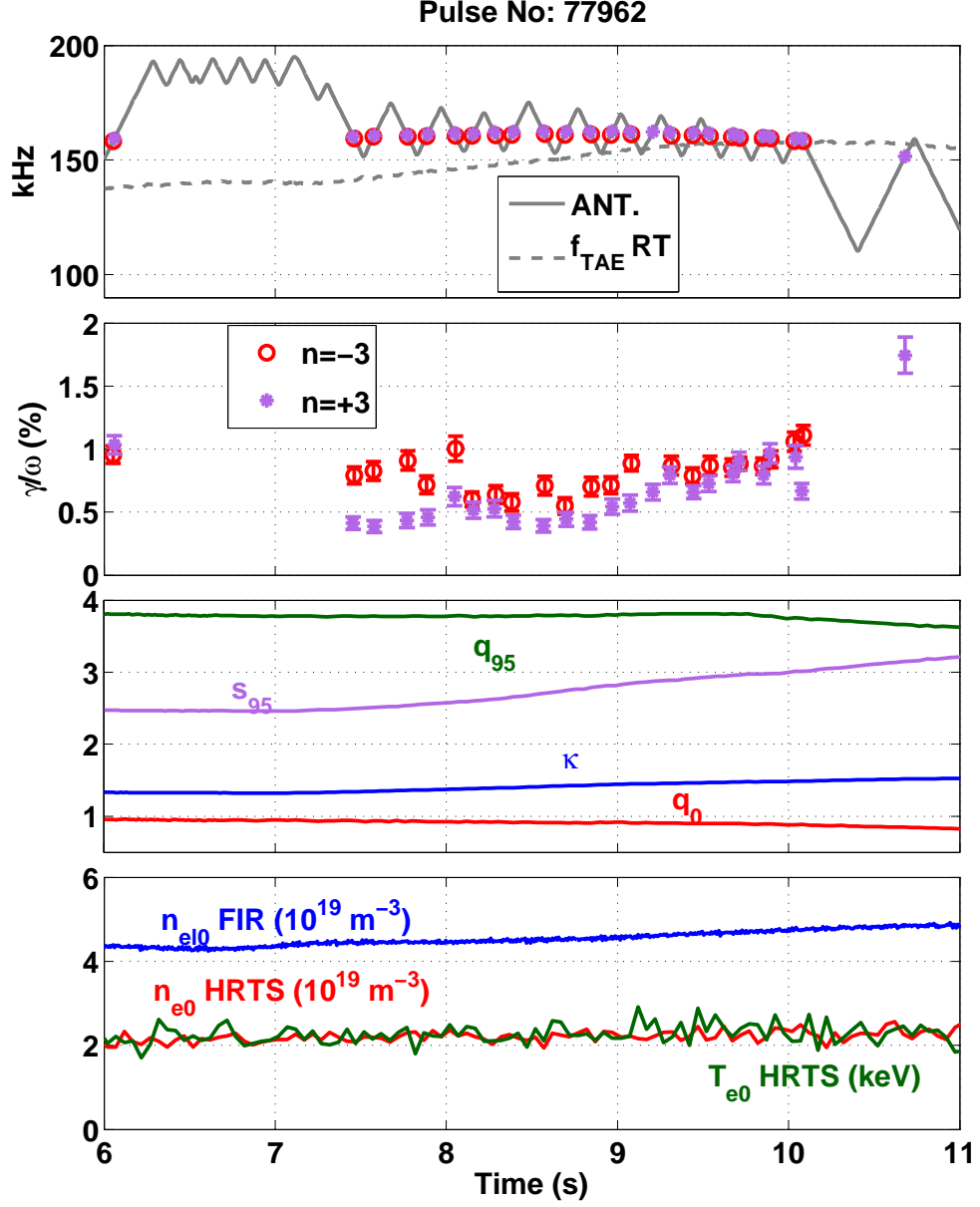


Figure 6.9: Damping rate measurements of $|n| = 3$ TAEs and time evolution of plasma parameters. During the elongation scan at $t = 7 - 11$ s, the measured dampings increase from $\sim 0.8\%$ to 2% at $q_{95} \leq 3.85$. The damping variation and magnitude is very similar to the discharge #77417 (figure 6.6). Antenna configuration: $1 + 4 + 6 - 7-$.

measurement at $t = 14.5$ s with $\gamma/\omega = 2.6\%$ when the plasma is already in X-point configuration. It is interesting to observe that this value is lower than the measurement at $t = 13.8$ s, with $\gamma/\omega = 4\%$ when both q_{95} and s_{95} take their maximum values.

To summarize, elongations scans in four different discharges have been examined. They all show an increase in the $|n| = 3$ damping as function of edge shear and elongation. Relatively low damping is measured when the q profile spans a relatively small range of values, (as in figure 6.9 at $\kappa = 1.49$, $q_0 = 0.884$, $q_{95} = 3.74$ and $\gamma/\omega = 0.67\% \pm 0.06$) whereas high damping occurs when the q profile spans a larger range of values (as in figure 6.10 at $\kappa = 1.48$, $q_0 = 0.834$, $q_{95} = 4.09$ and $\gamma/\omega = 2.93\% \pm 0.16$). Hence, the damping is controlled by the factor $\Delta q = q_{95} - q_0$ and increases when Δq increases.

6.3.2 $|n| = 6 - 7$ TAEs

In this section, examples from specific discharges show how the antenna-plasma coupling for $n = 6 - 7$ is lost when the edge shear/elongation exceeds a critical value. This is in line with the observations of the statistical analysis in Section 6.2.

Figure 6.12 shows measurements of $n = -6$ TAEs with real-time mode tracking that lasts several seconds (with a few breaks), from $t = 5.3$ s to $t = 10$ s. The tracking, as well as the post-pulse analysis, show the existence of this stable mode at ~ 190 kHz slowly decreasing in frequency because of the density increase. In the beginning of this phase, the damping of $n = -6$ is 1% and at $t = 6$ s it decreases rapidly to levels of $0.2-0.5\%$. The damping remains at levels well below 1% up to the point where s_{95} starts to increase at $t = 10$ s (at this time $s_{95} = 2.5$ and $\kappa_{95} = 1.36$) and the coupling to the mode is lost. Another mode $n = -6$ is excited at a significantly lower frequency than the tracked mode, with a $\gamma/\omega = 1.67\%$. During the subsequent scans at higher s_{95} and κ_{95} , no modes are detected.

Figure 6.13 shows another example with real-time tracking on $n = -7$ TAEs. Here, as the q profile is decreasing (both q_0 and q_{95} decrease while s_{95} remains constant), the $n = -7$ damping rate increases from 0.5% to 1.1% . The coupling to $n = -7$ is lost when the elongation scan starts (at $t = 10$ s). Note that it

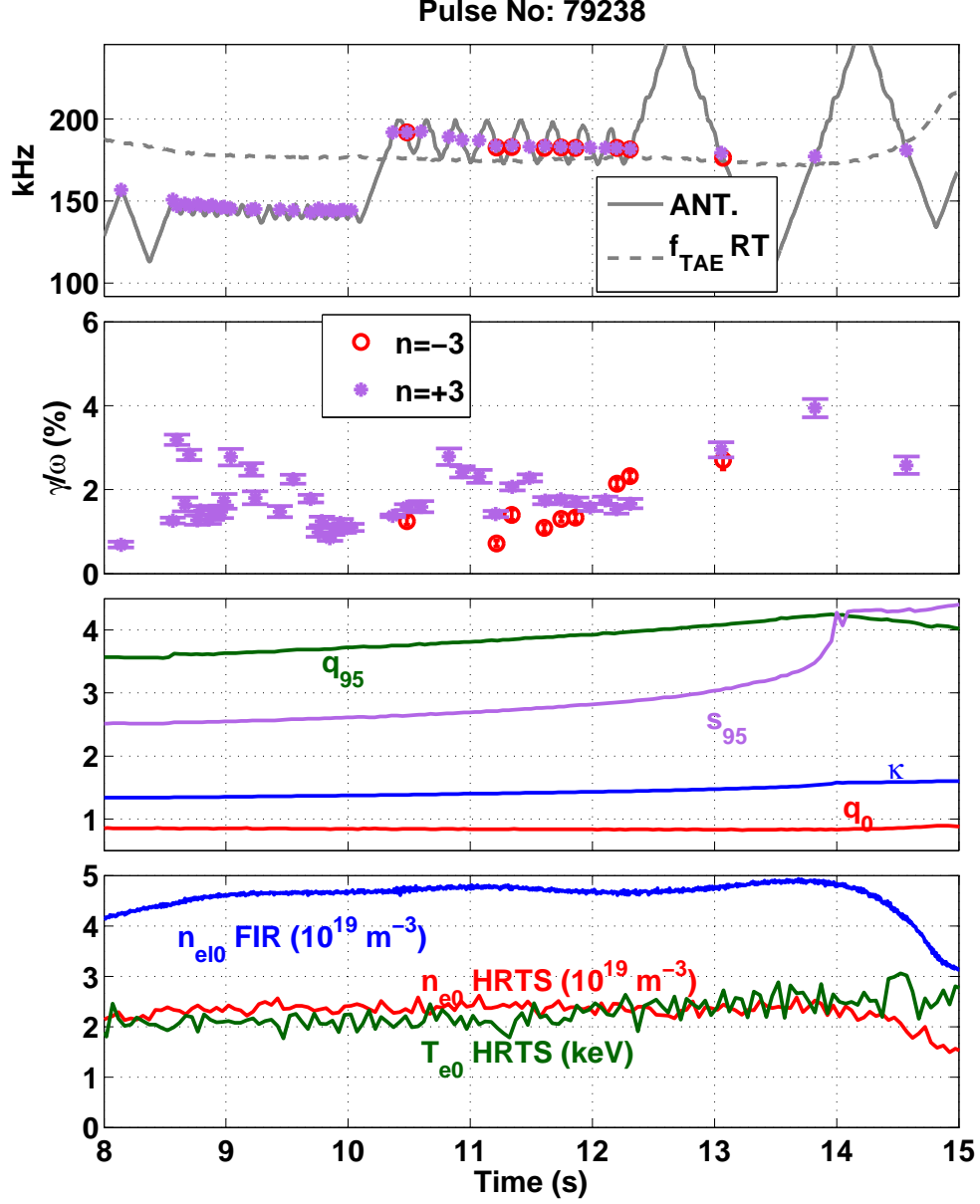


Figure 6.10: Damping rate measurements of $|n| = 3$ TAEs and time evolution of plasma parameters. During the elongation scan at $t = 10 - 14$ s, a increasing trend is observed, from $\gamma/\omega \sim 2\%$ to $\gamma/\omega \sim 4\%$, while q_{95} increases up to 4.24. Note the measurement at $t = 14.5$ s after the X-point formation (at $t = 14$ s) which yields a damping rate with $\gamma/\omega = 2.56\%$. Examples of the resonance fits are shown in figure 6.11. Antenna configuration: 1 + 4 + 6 - 7-.

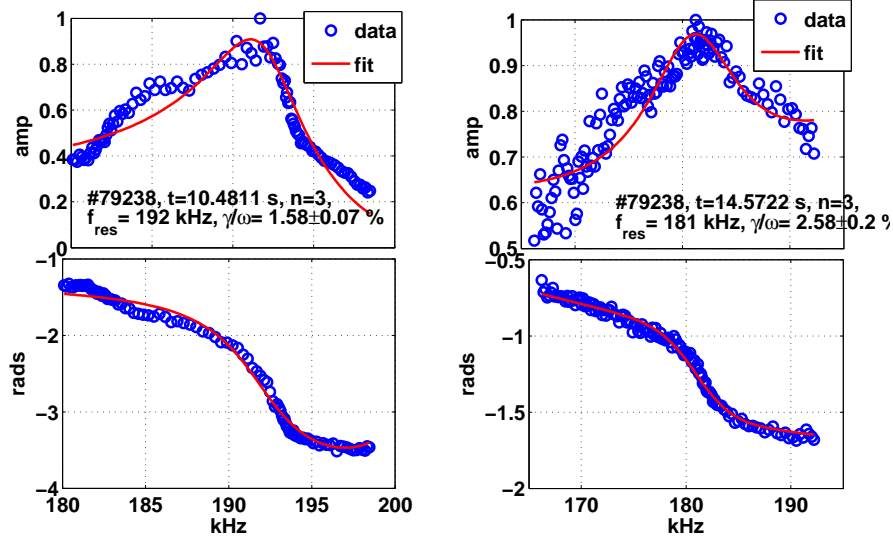


Figure 6.11: Examples of resonance fits for the $|n| = 3$ TAEs of the discharge #79238 (figure 6.10).

is difficult to identify with certainty one plasma parameter as the cause of the observed increase in the damping as both q profile and density are increasing.

It is noteworthy the coupling is lost at the same value of s_{95} and κ_{95} as for the $n = -6$ TAEs. The reproducibility of the observation suggests a common mechanism.

6.4 Effect of the q profile relaxation

We turn now our attention to the effect of the q profile relaxation at the beginning of the plasma discharges. It has already been observed for the discharge #77788 (figure 5.1) that the measured damping of $n = 3$ modes increases when q_0 decreases. The simulations showed that this is due to an increase in the misalignment of the gaps which results in a stronger damping through interaction with the continuum in the plasma core. In this section, further experimental evidence is provided in support of this mechanism for $|n| = 3$ modes. For higher- n modes, the experiment suggests that this mechanism is weaker or does not exist at all.

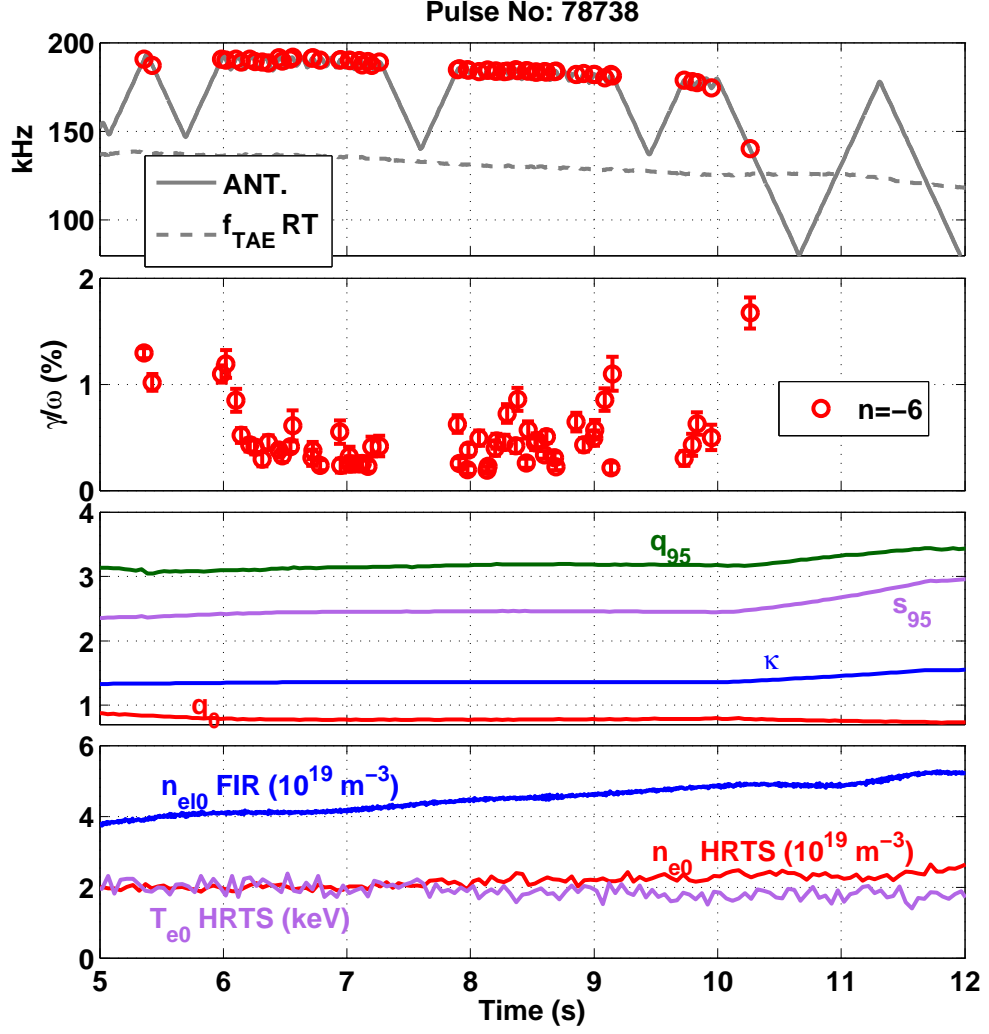


Figure 6.12: Damping rate measurements of $n = -6$ TAEs and time evolution of plasma parameters. Note the transition of the damping from $\gamma/\omega \sim 1\%$ to $\gamma/\omega \lesssim 0.5\%$ at $t = 6$ s. After $t \sim 6.5$ s, γ/ω remains around 0.5%. When s_{95} starts to increase at $t = 10$ s, the real-time tracking on $n = -6$ is lost. Examples of the resonance fits are shown in figure Antenna configuration: 1 + 4 + 6 - 7-.

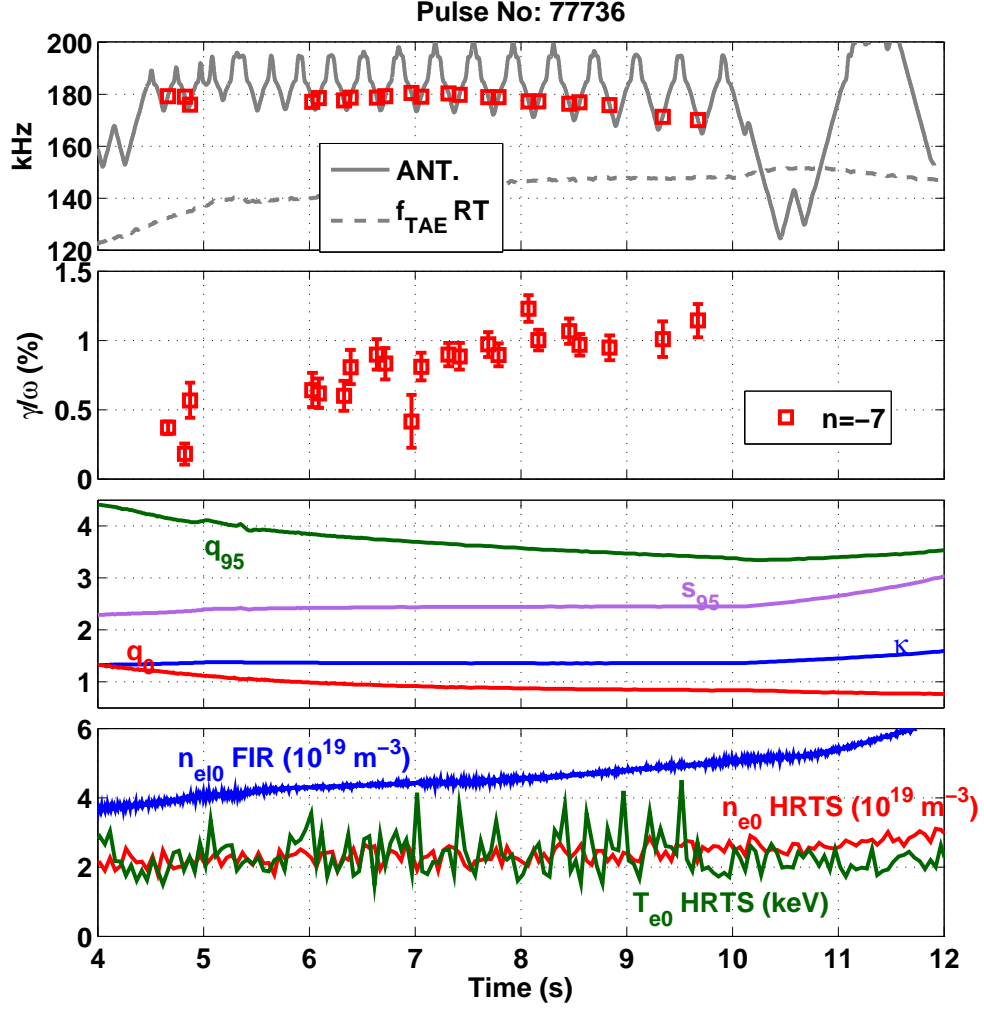


Figure 6.13: Damping rate measurements of $n = -7$ TAEs and time evolution of plasma parameters. The q_0 and q_{95} are decreasing, s_{95} and density are increasing. Note that the coupling to $n = -7$ is lost when the elongation scan starts (at $t = 10$ s). Antenna configuration: 1 + 4 + 6 - 7-. (see figure 5.1 for the explanation of the labels and the symbols).

6.4.1 $|n| = 3$ TAEs

Figure 6.14 shows a very clear increase of the damping while the eigenfrequency remains relatively constant (from 163 to 168 kHz). During this interval, q_0 varies from 1.25 to 0.91, q_{95} from 4.25 to 3.56 and the density changes slightly. An analogous behavior is observed in the discharge #78740 (figure 5.29), of which the $n = 3$ modes were modeled with the code LEMan in Chapter 5. In this plasma configuration, q_0 is relaxing to an even lower value at $q_0 = 0.78$. The dampings increases to even higher values: from 1% when $q_0 = 0.97$ to $\gamma/\omega \sim 3 - 5\%$ when the q profiles stabilizes. Figure 6.15 shows the evolution of the q profiles for 2 time slices in these discharges.

The characterization of the antenna-driven modes has showed that the $n = 3$ antenna-driven modes are excited with an open gap at the edge. Additionally, because of the high value of q_{95} , its variation does not weight as much as the variation of q_0 . Thus, it is more likely that the change in the observed damping is due to the decrease of of the central q profile.

The above observations point to the following damping scenario for the $|n| = 3$ modes: the decrease of central q increases the total damping in the central region of the plasma, via the mechanisms of continuum and radiative damping. In the discharges that have been considered, this evolution of the q profile builds up a basic damping contribution in the beginning of the discharge, onto which the later damping contributions from the edge are added. This possibility is consistent the modeling studies discussed in Chapter 5.

6.4.2 $|n| = 5$ TAEs

As observed in the section 6.2, the antenna-plasma coupling for $|n| = 5$ modes shows a strong correlation with the combination of high q_0 and q_{95} and low edge κ_{95} , $\kappa_{95} \lesssim 1.35$. In this paragraph, it is shown that this happens because these modes are consistently excited in the initial phase of the plasma discharge during the current ramp-up.

Two examples of such $|n| = 5$ measurements are given in figure 6.16. Typically, the modes are excited in the low and in the upper part of the TAE gap. The modes that are excited in the low part of the TAE gap are identified as TAEs because of their frequency correlates with the TAE gap frequency as shown in figure

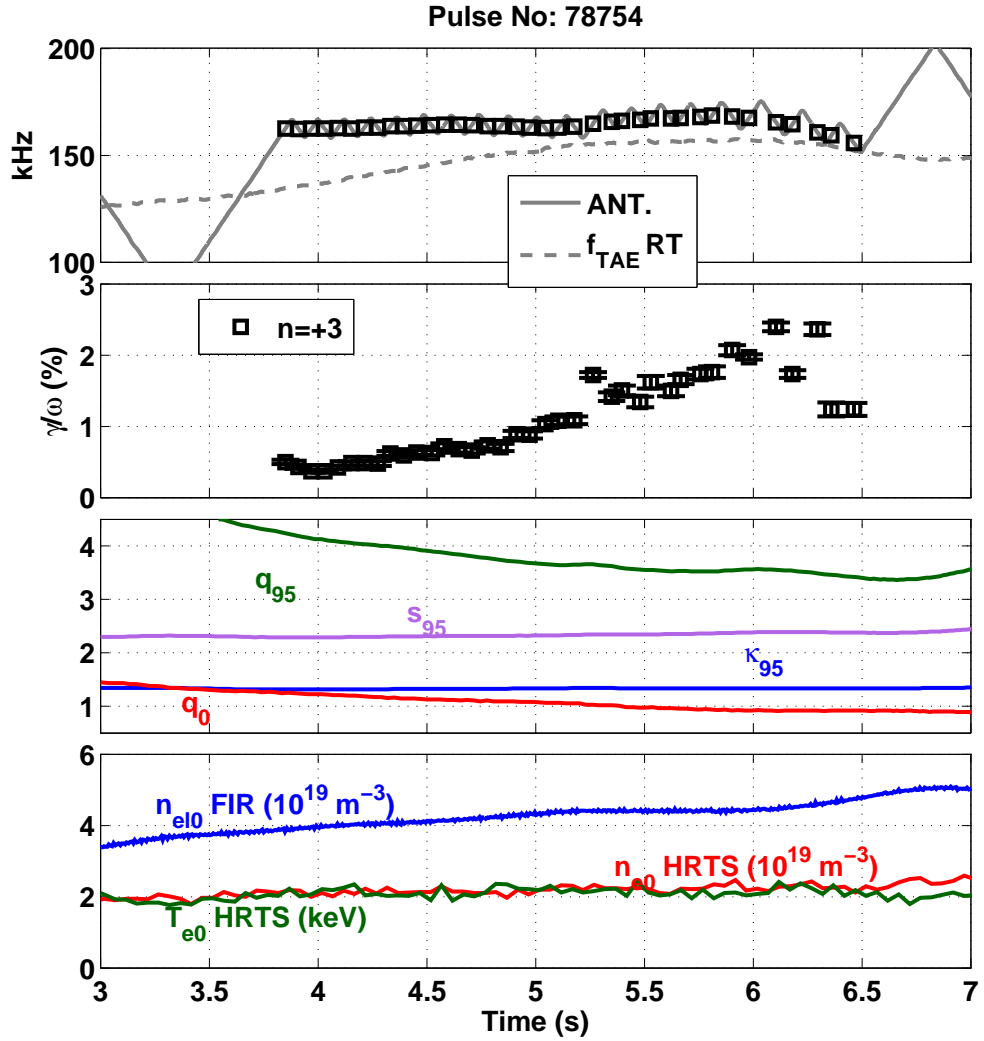


Figure 6.14: Damping rate measurements of $n = 3$ TAEs and time evolution of plasma parameters. While the q profile is relaxing, a strong increase is observed in the damping. Antenna configuration: 1 + 4 + 6 – 7–. (see figure 5.1 for the explanation of the labels and the symbols).

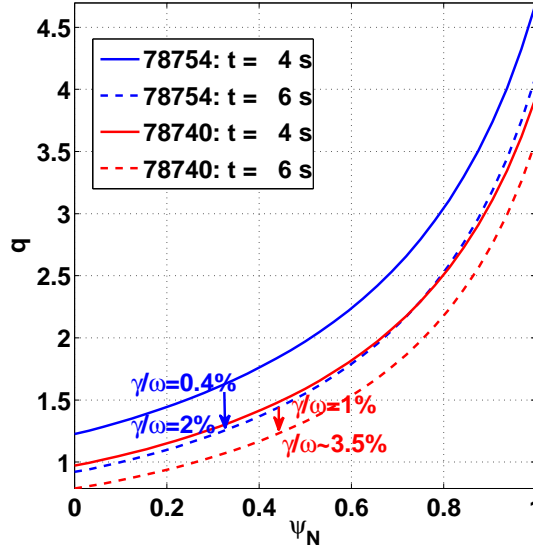


Figure 6.15: Evolution of the q profile in the discharges 78754 and 78740 from $t = 4$ s to $t = 6$ s. The dampings γ/ω that correspond to each q profile are also shown. It is systematically observed that the more relaxed is the q profile, higher damping is measured.

6.16b. The $|n| = 5$ damping rates that are measured in this phase are typically in the range 1-3%. During the current ramp-up, the profiles of q , density and temperature change substantially. This makes relatively difficult to understand the evolution of the $|n| = 5$ damping as function of the plasma parameters without the help of more detailed analysis, e.g. by employing plasma modeling. For example, the measurements in figure 6.16a show the $|n| = 5$ damping to increase, while those in figure 6.16b show it to increase and then decrease.

6.4.3 $|n| = 6 - 7$ TAEs

Figure 6.12 shows the damping of $n = -6$ TAEs to decrease rapidly at $t = 6$ s from about 1.2% to levels of $\sim 0.5\%$. This decrease is of importance because the central q profile is still decreasing during $t = 5 - 7$ s, as shown in figure 6.17. Such a decrease in the $n = -6$ damping at the particular phase of the discharge is consistently observed. Another example of $n = -6$ measurements in other discharges are provided in figure 6.18. It shows a decrease in the damping of the $n = -6$ modes, from about 2% to less than 0.5%. Figure 6.19 shows examples of

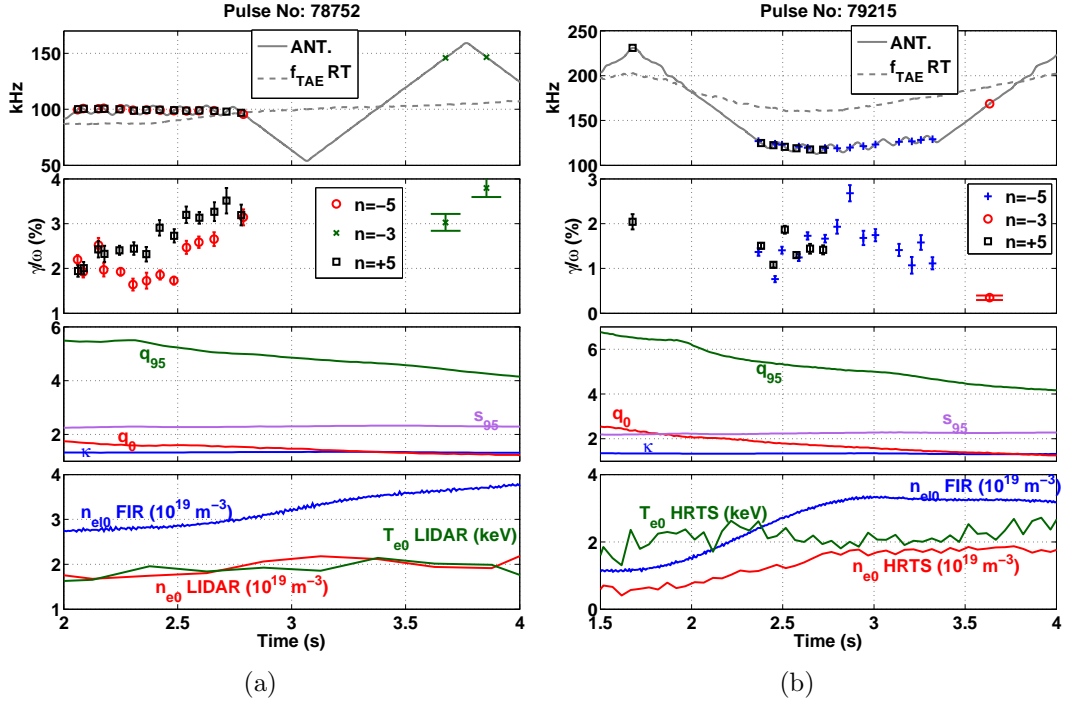


Figure 6.16: Damping rate measurements of odd- n TAEs and time evolution of plasma parameters. The focus here is on $|n| = 5$ modes. Both figures (a) and (b) show that $|n| = 5$ measurements are typically obtained during the current ramp-up phase. Because both q and density profiles are changing, it is difficult to identify the cause of the damping variation. Note in figure (a), that when the antenna scans upward in frequency in the time interval $t = 3.1 - 3.7$, no $|n| = 5$ is detected. This indicates an increased sensitivity of the antenna-plasma coupling to the particular plasma configuration in the current ramp-up phase. Antenna configuration: $1 + 4 + 6 - 7 -$. (see figure 5.1 for the explanation of the labels and the symbols).

the resonance fits in the complex plane.

The reproducibility of this behavior shows that the damping of these $n = -6$ modes is decreasing in spite of the decrease of the central q . The variation is concurrent with a small increase in the magnetic shear and/or with an increase in density. The observed behavior is in contrast to the observations of lower- n modes, $|n| = 2$ (figure 6.20) and $|n| = 3$ (figure 6.14) modes. This indicates a certain immunity of the damping of $n = -6$ mode with respect to changes in the central region of the q profile, and is consistent with the possibility that the mode

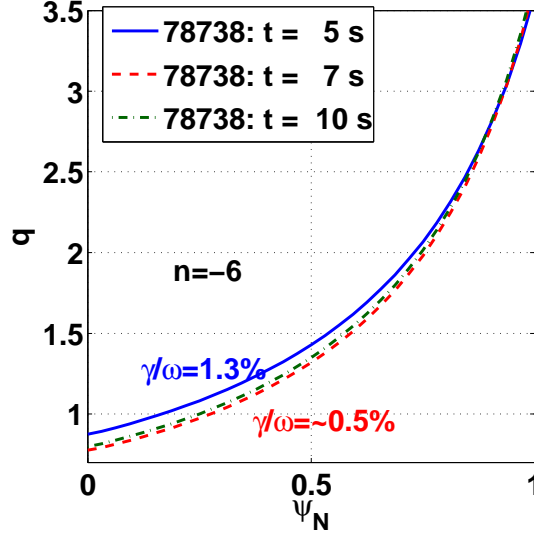


Figure 6.17: Evolution of the q profiles at various time slices during the $n = -6$ mode-tracking phase. The damping decreases in spite a decrease of central q , contrary to lower- n measurements.

is radially localized mostly in the outer region of the plasma. In addition, it is noteworthy that very subtle changes in the plasma parameters cause a significant variation in the damping of these $n = -6$ modes.

Observations of $n = -7$ modes are similar to those described previously for the $n = -6$ modes. Indeed, it has been possible to observe the different behavior between high- n against lower- n in the same discharge. As shown in figure 5.29, while both $|n| = 3$ and $n = -7$ modes start with $\gamma/\omega \sim 1\%$, they settle at different dampings when the q profile no longer changes. In particular, the $n = -7$ settles at $\gamma/\omega \sim 1.5\%$, while the $|n| = 3$ dampings is a factor of 2-3 higher. Bearing in mind the observations on the effect of q_0 on the damping of $|n| = 3$, it is seen that the $n = -7$ modes are less affected by the variation of q_0 , indicating a stronger radial localization compared to the $n = 3$ modes.

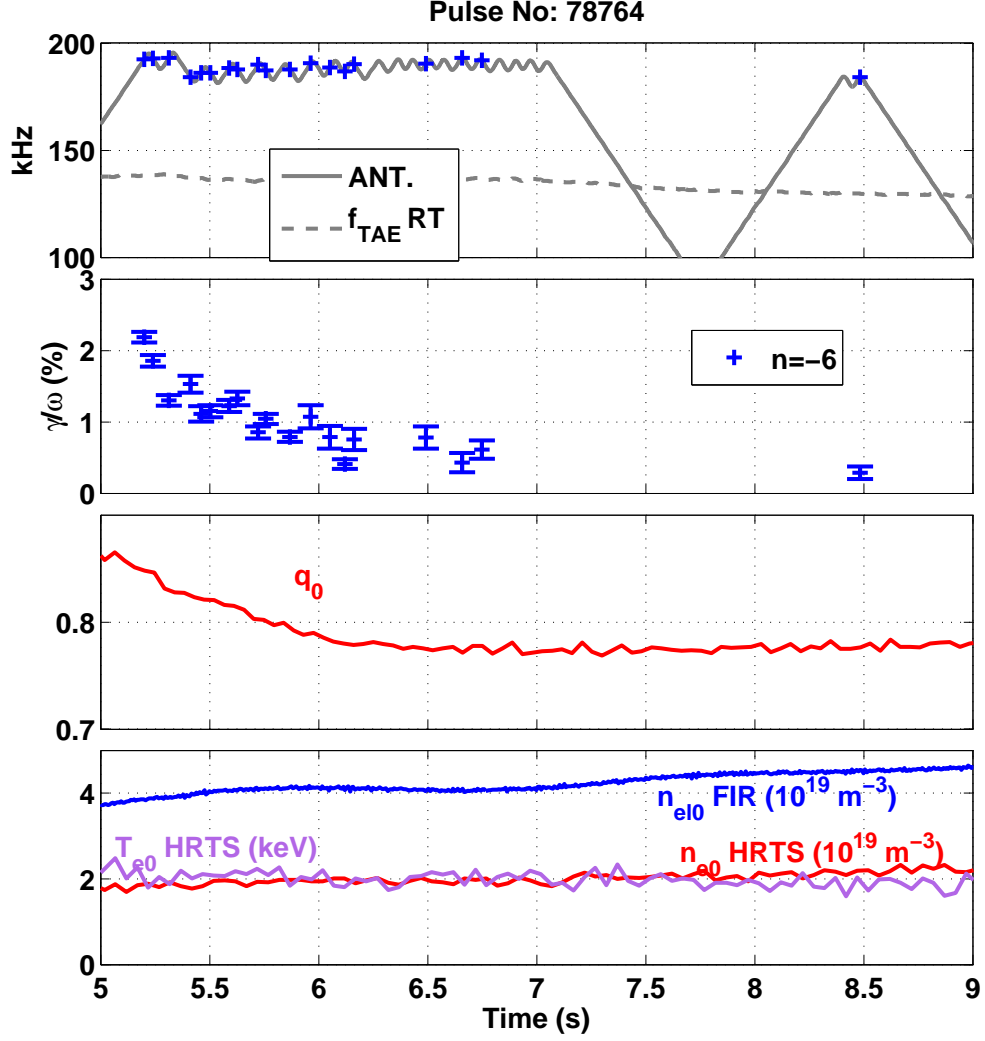


Figure 6.18: Damping rate measurements of $n = -6$ TAEs and time evolution of plasma parameters. While the central q profile is decreasing, a significant decrease is also observed in the damping. A small variation is observed in the other plasma shape parameters: $q_{95} = 3.1-3.2$, $s_{95} = 2.3-2.47$, $\kappa_{95} = 1.33-1.36$. Example of the resonance fits are shown in figure 6.19. Antenna configuration: $1 + 4 + 6 - 7 -$. (see figure 5.1 for the explanation of the labels and the symbols).

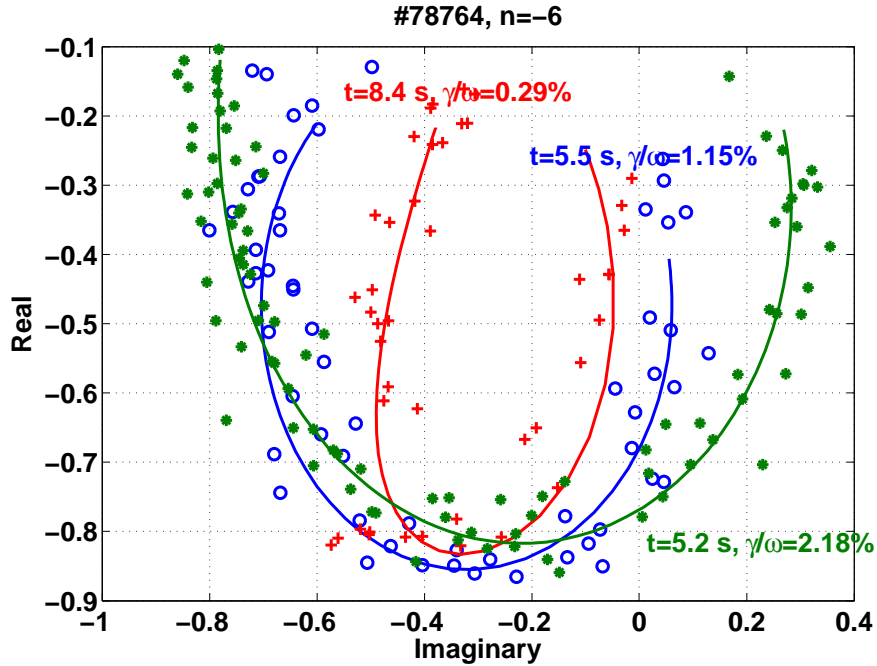


Figure 6.19: Resonance fits in the complex plane for the $n = -6$ TAEs of the discharge #78764 (figure 6.18).

6.5 Comparisons between modes of different n in the same plasma conditions

Very useful comparisons can be made for the cases of damping rate measurements corresponding to two modes of different n having approximately the same frequency. This is because the difference in the damping rate can be the direct consequence of the different mode structure. Such measurements provide good reference cases for testing the predictions of plasma models and contribute to identifying the effect of the damping mechanisms of function of n .

Measurements of $n = -7$ against $n = 3$ TAEs have been already described and modeled with the code LEMan in Section 5.6. These measurements show that the $n = -7$ modes are damped less than the $n = 3$ by a factor of two. In this section, further experimental observations are presented that highlight the difference between $n = 4$ and $n = -2$ TAEs. In this case too, the higher- n mode is less damped than the lower- n mode.

The two modes with $n = 4$ and $n = -2$ are excited very close to each other

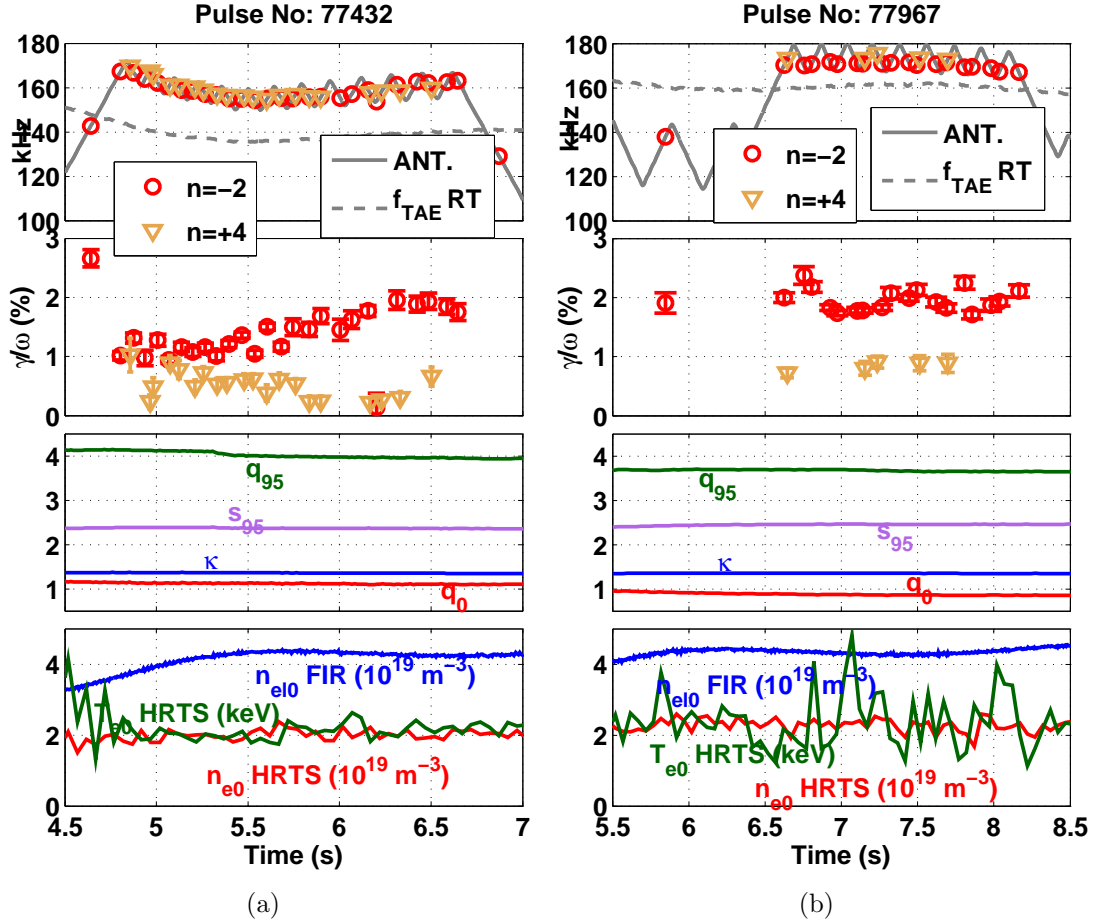


Figure 6.20: Damping rate measurements of even- n TAEs and time evolution of plasma parameters. In figure (a), the dampings the $n = 4$ and $n = -2$ modes depart from the same value, $\gamma/\omega \sim 1\%$, and diverge ($n = 4$ decreasing and $n = -2$ increasing) during a variation in the density profile. In the very similar plasma configuration that is shown in figure (b), the $n = 4$ and $n = -2$ are stabilized at 0.9% and 2% respectively. Notice that the q profile in (b) is lower than in (a) (figure 6.22). Examples of resonance fits are shown in figure 6.21. Antenna configuration: $1 + 4 + 6 + 7+$. (see figure 5.1 for the explanation of the labels and the symbols).

6.5 Comparisons between modes of different n in the same plasma conditions

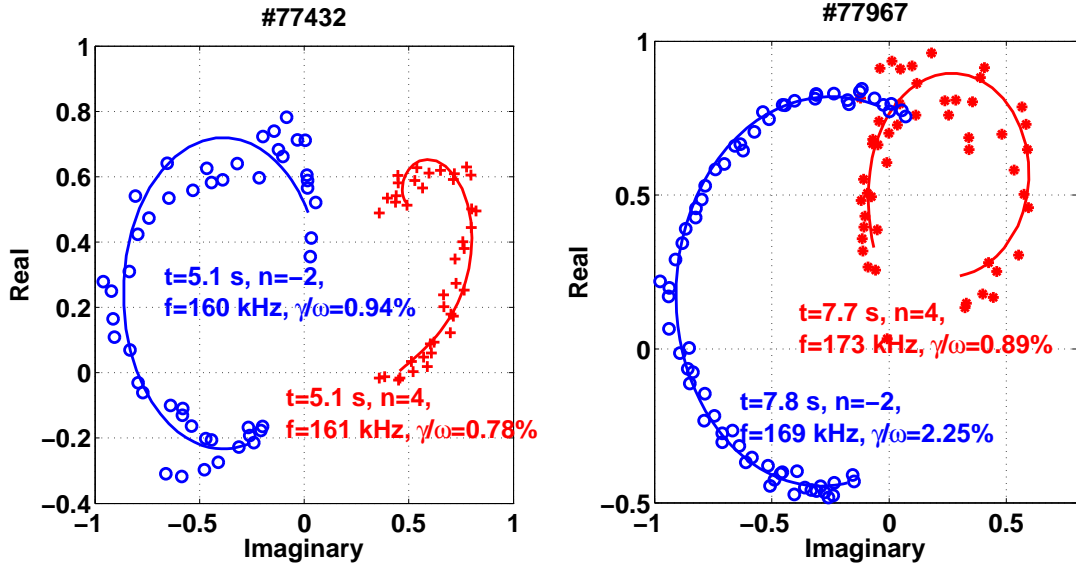


Figure 6.21: Resonance fits in the complex plane for the $n = -2$ and $n = 4$ TAEs of the discharges #77432 and #77967 (figure 6.20).

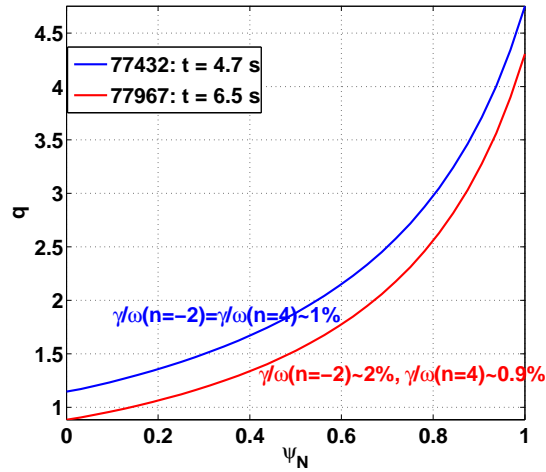


Figure 6.22: Comparison between the q profiles from 2 time slices in the discharges 77432 and 77967. The dampings γ/ω that correspond to each q profile are also shown.

in frequency and they are observed in two discharges (figure 6.20). As shown in figure 6.20a, their AE character is reflected in their frequency variation, which correlates very well with the variation in density. The very high degree of similarity between the two discharges in terms of plasma parameters and AE mode frequency suggests that the same TAEs are tracked.

Note, though, that the q profile is at a lower level in discharge #77967 (figure 6.20b) compared to #77432 (figure 6.20a): discharge #77967 has $q_0 = 0.86$ and $q_{95} = 3.65$ ($t = 7.5$ s), while discharge #77432 has $q_0 = 1.1$ and $q_{95} = 3.95$ (at $t = 6.5$ s). This is consistent with the measured mode frequencies, that are indeed higher in discharge #77967 than in discharge #77432. In figure 6.20a, it is observed that the damping rate of $n = -2$ mode increases from $\sim 1\%$ to about 2% , while the damping rate of $n = 4$ mode decreases from 1% to $\sim 0.5\%$ (possibly due to the change in the density) and then increases to 0.7% . In figure 6.20b, where the plasma conditions are stable, the damping rates of $n = -2$ and 4 are also constant at 2% and 0.9% respectively. Figure 6.22 shows a comparison of the q profiles between these two discharges and the corresponding measured dampings.

These measurements suggest that the $n = 4$ TAE is less affected by the decrease of the central q , compared to the $n = -2$ mode. This can be due to the smaller radial extent of the $n = 4$ mode, which would allow it to avoid part of the damping in the central region of the plasma. In the case considered, this difference in damping between an $|n| = 2$ and an $n = 4$ mode is approximately 1% .

6.6 Effect of the ICRF heating on $n = 3$ TAEs

Figure 6.23 shows $n = \pm 3$ measurements that were obtained in a plasma discharge with ICRF on-axis heating of hydrogen (minority species in a deuterium plasma at 42.5 MHz). The discharge belongs to the same experimental session as the discharge #77788 (figure 5.1). The plasma equilibrium is very similar between the two pulses, while the density and the temperature are naturally higher during the heating phase. An estimate of the drive the ICRH-accelerated ions on $n = 3$ TAEs can be made by comparing the damping measurements of the 2 discharges.

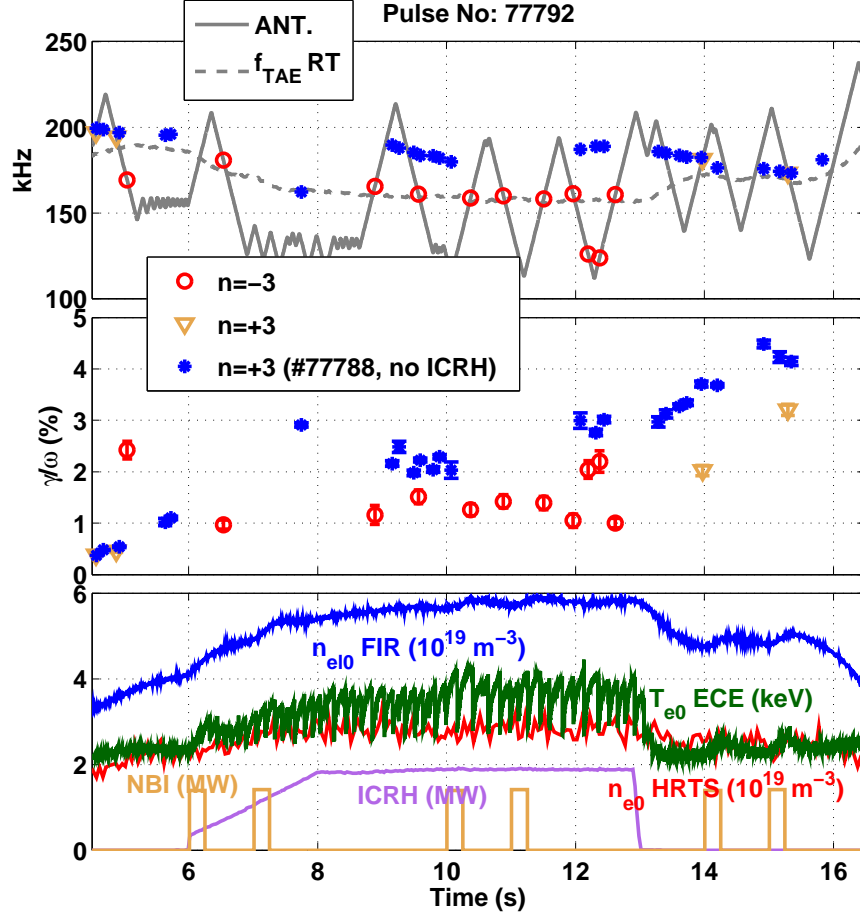


Figure 6.23: Damping rate measurements of $|n| = 3$ TAEs, time evolution of plasma parameters and total coupled ICRF heating power (the NBI blip are for MSE measurements). The $n = 3$ measurements of the similar discharge #77788 where no ICRH was applied are overlaid for comparison. Note the presence of $n = 3$ TAEs when ICRH is off and their notable absence during the heating phase. During the ICRH heating phase, damping rates of $n = -3$ TAEs are measured instead. Antenna configuration: 1 + 4 + 6 – 7 –. (see figure 5.1 for the explanation of the labels and the symbols).

In figure 6.23, the $n = 3$ measurements of the pulse #77788 are overlaid. One can readily observe the similarity of the damping measurements in terms of both frequency and damping rate before and after the heating phase. In particular, before the heating phase at $t \sim 4.9$ s, two $n = 3$ low-damped ($\gamma/\omega \sim 0.4\%$) modes are found at ~ 195 kHz, just as the $n = 3$ modes found at the same times in the pulse #77788. After the heating phase, the $n = 3$ modes are recovered at exactly the same frequencies (at 181 kHz and 173 kHz), just as the modes found in the same phase of the discharge #77788. During the heating phase, at the frequencies where one would expect to find the $n = 3$ modes of figure 5.1, one finds $n = -3$ modes. A difference should be noted regarding the magnitude of the damping rate of $n = 3$ for $t \geq 14$ s: the measured γ/ω is quite lower than those measured in the pulse #77788. It is not clear why there is such a difference since the plasma equilibrium is very similar: it is maybe due to a slight difference in the edge density profiles. Nonetheless, the increase of the damping as the edge elongation increases is still observed.

The above observations suggest that the fast ion population created by the ICRH reduces the damping of the positive $n = 3$ TAEs to such a small value that it cannot be detected by the synchronous detection system given its particular configuration. The reason is the relatively high frequency scan rate df/dt that had been set in this experiment, $df/dt = 150$ kHz/s, which amounts to an insufficient number of data points. Indeed, if we consider a damping rate of $\gamma/\omega = 0.2\%$ at $f_0 = 160$ kHz, the corresponding resonance frequency width is $\Delta f = \sqrt{2}f_0\gamma/\omega = 0.45$ kHz. This results to a small number of points N , specifically $N = \frac{\Delta f f_s}{df/dt} \approx 4$, where $f_s = 1.25$ kHz is the sampling rate of the AEAD acquisition. If this mode cannot be detected because of a very small γ/ω , the γ/ω of the $n = 3$ modes during the heating phase should be lower than 0.2% . With this information, one can then obtain information on the fast particle drive. The total measured damping rate γ_m of an antenna-driven mode comes from the balance between the background damping γ_b and the fast-ion drive γ_f

$$\gamma_m(n) = \gamma_b(n) - \gamma_f(n) , \quad (6.1)$$

where γ_f is negative if the fast ions damp the mode. By measuring the γ_m of opposite n modes and given that the background damping does not depend on

the sign of n , i.e. $\gamma_b(n) = \gamma_b(-n)$, one can estimate the difference between the drive on n and $-n$

$$\Delta\gamma_f(n) = \gamma_f(n) - \gamma_f(-n) = \Delta\gamma_m(n), \quad (6.2)$$

where $\Delta\gamma_m(n) = \gamma_m(-n) - \gamma_m(n)$. For example, for the measurement of $n = -3$ at $t = 9.56$ s, $\Delta\gamma_f/\omega = 1.5 \pm 0.23\%$.

From the measured γ/ω at $t = 14$ s and at $t = 12.6$ s, one can estimate the drive γ_f on $n = 3$ at $t = 12.6$ s, using the scaling of γ_b/ω with s_{95}/κ derived from the $n = 3$ measurements of the ohmic discharge #77788. Since the background damping γ_b/ω of $n = 3$ at $t = 14$ s ($s_{95} = 2.98$) is 2%, then at $t = 12.6$ s ($s_{95} = 2.76$), it should be approximately 1% less, i.e. $\gamma_b/\omega \approx 1\%$ (at $t = 14$ s, only background plasma damping is measured as the particle drive must have died out, since the typical slowing down time of ICRH-accelerated hydrogen in JET is 1 s [51]). Thus, from equation (6.1), a fast ion drive of $\gamma_f/\omega = \gamma_b/\omega - \gamma_m/\omega \approx 0.8\text{--}1\%$ is estimated for the $n = 3$ TAEs at $t = 12.6$ s, where $\gamma_m/\omega = 0\text{--}0.2\%$. This estimate leads, via equation (6.2), to a negligible fast-ion drive/damping on the $n = -3$ modes of $\sim 0\%$.

6.7 Discussion

Here, the main findings from the analysis in the preceding sections are summarized and discussed.

- The antenna-plasma coupling as function of n depends on the edge shear s_{95} and on the edge elongation κ_{95} . The maximum κ_{95} for which there is sufficient antenna-plasma coupling for damping rates to be measured decreases as function of n . TAEs with $|n| \geq 5$ are measured only for $\kappa_{95} \leq 1.4$. This behavior does not allow us to study modes with the $|n| \geq 5$ at high s_{95} and κ_{95} .
- Modes with positive (co-current) and negative (counter-current) n are excited. However, the excitation is not symmetric: depending on the n , positive (negative) modes are excited much more frequently than negative (positive) modes.

- The damping rate γ/ω of $|n| = 3$ and $|n| = 4$ TAEs is observed to increase with edge shear s_{95} and with edge elongation κ (figures 5.1, 5.22, 6.2, 6.6, 6.9, 6.10). This scaling is very robust for $|n| = 3$ modes and is not altered by the changes in the q profile. Damping measurements of $n = 3$ modes have been also achieved in X-point configuration: they show that the damping is large and specifically it is in the range of $2.5 - 5.5\%$ (5.1, 6.10).
- The damping of $|n| = 3$ TAEs has been found to be strongly affected by changes the values of the q profile. In particular, it increases with the difference $q_{95} - q_0$, i.e. it is higher when the q profile spans a big range of values (figures 6.6, 6.9, 6.10). Furthermore, a decrease in the central q increases the $|n| = 3$ damping (figures 6.14, 5.29, 5.1).
- Contrary to the $|n| = 3$ modes, the damping of $|n| = 4, 6$ and 7 (figures 6.20, 6.12, 6.18, 5.29) does not increase when q_0 decreases. The $n = -6$ damping consistently decreases to quite low levels ($\lesssim 0.5\%$) in spite of a decrease in q_0 and/or an increase in s_{95} (figures 6.12, figures 6.18). An intermediate situation is observed for $n = 4$ (figure 6.20). This suggests that the damping mechanism that acts in the center of the plasma for the low- n modes is weaker or not present for higher- n modes. This is consistent with the possibility that higher- n modes are more localized in the outer region of the plasma. It also agrees with theoretical mode structure of the $n = 7$ that were modeled with LEMan in Chapter 5 (figure 5.33).
- From the comparison between modes with higher and lower n at the same plasma conditions and very similar eigenfrequencies, clear differences in their dampings are observed. In particular, simultaneous damping measurements of $n = 4$ and $n = -2$ TAEs show that their damping rates diverge as the plasma parameters evolve, with the $n = 4$ damping rate settling at $\sim 0.9\%$ and the $n = -2$ damping at $\sim 2\%$ when the plasma conditions stabilize (figure 6.20). Similar behavior is observed for $n = -7$ modes that are measured in parallel to $|n| = 3$ modes (figure 5.29). These measurements demonstrate experimentally that higher- n modes can be less damped because of their more localized radial structure.

- An effect of fast-ion populations driven by ICRH of 2 MW in a limiter plasma has been observed on the damping rate of $|n| = 3$ TAEs. Specifically, the fast-ion drive on $n = 3$ TAEs reduces the total damping of $n = 3$ TAEs by approximately 0.8 – 1%. If the plasma conditions are reproduced, then an increase of less than 1 MW should be enough to destabilize these $n = 3$ TAEs.

The experimental results are consistent with the characterization of the antenna-driven modes via the modeling studies of Chapter 5. They highlight the role of the mode structure, which can be considered as the key factor to account for the difference between the damping of intermediate- n and low- n modes. For example, the dependence on the factor $\Delta q = q_{95} - q_0$ is indicative of the extended radial structure of the modes, as Δq is approximately proportional to the number of the coupled poloidal harmonics.

The measurements are very promising for further systematic comparisons with plasma models. The fact that the damping variation is measured dynamically as the background plasma parameters evolve is an important element because it can make such comparisons more stringent.

An important characteristic of the damping rate measurements is their reproducibility. As demonstrated by several comparisons (e.g. figures 6.23, 6.20), if two different discharges have the same plasma configuration, one measures the same n at the same frequencies with the same damping rates. This makes possible and validates the comparisons between discharges with similar plasma configuration.

6.8 Summary and conclusions

A database of approximately 3000 TAE damping rate measurements in ohmically heated discharges has been studied. The dependence of the damping of $|n| = 2 - 7$ TAEs on the edge magnetic shear, edge elongation and q profile has been investigated. It is found that the damping of $|n| = 3$ TAEs increases when the q profile in the central region of the plasma decreases and increases with increasing edge magnetic shear. Furthermore, it depends also on the factor $\Delta q = q_{95} - q_0$ and it increases with Δq . The damping of $n = 4$ TAEs increases also with the edge magnetic shear but its absolute magnitude can be a factor of two less than the $|n| = 3$ modes in high edge shear configuration. The effect from variations in

the central q on the $n = 4$ damping is weaker with respect to $|n| = 3$. Modes with $|n| = 5 - 7$ are excited in conditions of low edge shear and elongation, $\kappa_{95} \lesssim 1.4$. In these conditions, the damping of $|n| = 6$ TAEs decreases despite a decrease in q_0 and/or an increase in s_{95} , in contrary to lower- n modes. Comparisons between low- n and medium- n modes with close eigenfrequencies in the same plasmas conditions demonstrate that medium- n modes are less damped than low- n .

This analysis shows that the damping properties of TAEs with $|n| = 2 - 7$ change as the toroidal mode number n increases, possibly as a result of the change in the radial mode structure, which becomes more localized for higher ns . The turning point for the damping properties to change from low- n to medium- n behavior is found to be at the transition $|n| \approx 3 - 4$. This is consistent with the observations of unstable TAEs driven by fast ions on JET. The experimental results are also consistent with the results of modeling studies of Chapter 5.

Finally, it has been possible to estimate the ICRH fast-ion drive on $n = 3$ TAEs from the damping measurements: the drive has been estimated to be 0.8-1% for 2 MW of the ICRH power in the particular limiter plasma configuration.

Chapter 7

Conclusions and outlook

The need to measure the damping rate of Alfvén eigenmodes of intermediate toroidal mode number n on JET has required the optimization of the active MHD spectroscopy system, recently equipped with new compact in-vessel antennas suitable for high- n excitation. This optimization has allowed the full exploitation of the system and the collection of unique experimental data in terms of both quality and quantity. The analysis of a part of this data, both by detailed investigation of the experimental database as a function of plasma parameters and by comparisons with two different numerical plasma models, leads to several conclusions on AE stability and its implications for future burning plasma experiments. Furthermore, useful conclusions have been derived for the technical requirements of the diagnostic and its potential for studying AE stability and performing MHD spectroscopy.

7.1 Summary

Antenna currents and excitation

The impedance characteristics of the AE exciter circuit, including the long transmission lines typical of large fusion devices, have required detailed modeling in order to understand the measured currents and voltages as function of frequency and to determine the feasible antenna currents. It has been shown how the maximum antenna currents are determined by the total current gain of the circuit and the voltage/current limits of the power amplifier. The strong effect of the

coupling between the neighboring antennas through their mutual inductances was identified, characterized and minimized.

The electrical model was used for the design of impedance matching circuits. Several matching units were built and tested. The experimental results showed discrepancies from the initial predictions of the matching unit design. The cause of these discrepancies has been identified as due to the fact that the properties of the power amplifier were not the nominal ones at the time of the experiments. Despite these discrepancies, the matching circuits have allowed us to achieve relatively high antenna currents, in the range of 6 to 10 A, in different frequency ranges.

For given antenna currents, one is interested in knowing the characteristics of the magnetic field produced by the antennas. Such a calculation was carried out for the vacuum case. The perpendicular component of the magnetic perturbation (the dominant component) is $0.2 - 0.4$ G/A at the plasma edge (last closed flux surface), depending on the plasma configuration. The antenna-driven n -spectrum that is derived from the field calculation confirms that it is the antenna currents phasing that determine the n -spectrum, while the exact geometry of the antenna coils or the slight asymmetry of the antenna position in R , which characterizes the two sets of antennas in JET, have a very small effect.

Even when the antenna excitation is configured in an optimal way to produce as ‘pure’ an n -spectrum as possible, a broad range of different $|n|$ is driven, with approximately six dominant n of positive and negative sign. As the antenna can drive multiple- n modes of similar amplitude, the plasma response can be a mixture of all these modes. This prompts for the employment of a sophisticated method in order to n -decompose the plasma response.

Post-pulse analysis of the plasma response and upgrade of the real-time system

The n -decomposition of the plasma response requires an accurate relative calibration of the magnetic coils. An *in situ* method was developed and applied for the calibration of the coils using the direct coupling to the new AE antennas. The method is very accurate, especially in terms of phase, and takes into account all the effects that intervene in the signal path from the coils up to the final data storage point.

The n -spectrum of the plasma response is calculated using a sparse spectrum representation method, implemented in the SparSpec algorithm. The SparSpec algorithm was adapted to deal with complex data in tokamak plasmas. The resulting n -spectrum is in very good agreement both with the parity of the driven n -spectrum and with phase-fitting calculations.

The SparSpec algorithm has been integrated in the real-time resonance tracking system of the diagnostic. It has thus been possible to filter the n -spectrum of the plasma response and follow the variation of the damping rate of intermediate- n modes in real-time in a plasma discharge.

Finally, an algorithm, as well as the associated software, was optimized to automatically estimate the measured damping rates from the raw experimental data for the post-pulse data analysis. The algorithm incorporates the calculation of the antenna field from the measured antenna currents, the calibration of the magnetic pick-up coils and the use of the SparSpec code. A sub-algorithm was developed in order to recognize the candidate plasma resonances, similar to the one employed by the real-time system. The post-pulse analysis agrees very well with the real-time system in terms of identification of the candidate mode resonances. Typical input settings for the post-pulse analysis code result in very good resonance fits of the recognized plasma resonances.

Comparison between measured and calculated damping rates

The experimental measurements of $n = 3$, $n = 4$ and $n = -7$ TAEs have been compared to the predictions of the LEMan code. The damping rates predicted by LEMan agree with the experiment better than a factor of two in all considered cases. According to LEMan, the main damping mechanisms of the measured TAEs are mode conversion to KAWs induced by intersections with, or proximity to, the Alfvén continuum, and direct electron Landau damping due to finite parallel electric field. In the cases of $n = 3$ and $n = 4$ modes, these mechanisms reproduce the measured damping evolution, increasing and/or decreasing, driven by changes in the background plasma parameters. However, LEMan predicts that the $n = 7$ modes are damped more than $n = 3$ modes by a factor of two, contrary to the experiment where the $n = -7$ modes are less damped than the $n = 3$ modes by a factor of two.

The $n = 3$ TAE measurements were also compared with the CASTOR model. These comparisons do not reach the same level of agreement as with LEMan, due to an insufficient description of the kinetic effects that modify the TAEs. In some cases where continuum damping dominates, CASTOR results are in reasonable agreement with the experimental measurements.

Conditions of high edge magnetic shear and safety factor q enhance the coupling of the modes to the Alfvén continuum, leading to increased dissipation of the mode energy in the edge region of the plasma. The effect of mode localization starts to become quite effective for the $n = 4$ modes and can lead to small or negligible damping from intersections of the mode frequency with the continuum in the plasma core. LEMan confirms that the effect of mode localization is even stronger of the $n = 7$ modes.

Experimental study of the TAE database and estimate of the fast-ion drive

A database of approximately 3000 TAE damping rate measurements in ohmically heated discharges has been studied. The dependence of the damping rate measurements of $|n| = 2 - 7$ TAEs on the edge magnetic shear, the edge elongation and the q profile has been investigated experimentally. It is found that the damping of $|n| = 3$ TAEs increases when the q profile in the central region of the plasma decreases and increases with increasing edge magnetic shear. Furthermore, it depends also on the factor $\Delta q = q_{95} - q_0$ and it increases with Δq . This dependence demonstrates the importance of the number of the TAE gaps, which is proportional to Δq , for radially extended modes. The damping of $n = 4$ TAEs increases also with the edge magnetic shear but its absolute magnitude can be a factor of two less than the $|n| = 3$ modes in very similar plasma conditions. The effect from variations in the central q on the $n = 4$ damping is weaker with respect to the $|n| = 3$ case. Modes with $|n| = 5 - 7$ are driven in conditions of low edge shear and elongation. In these conditions, the damping of $|n| = 6$ TAEs decreases, despite a decrease in q_0 and an increase in s_{95} , contrary to lower- n modes. Comparisons between low- n and medium- n modes with close eigenfrequencies in the same plasma conditions demonstrate that medium- n modes are less damped than low- n by an amount that depends on the plasma conditions.

This analysis provides experimental evidence that the damping properties of TAEs with $|n| = 2 - 7$ change as the toroidal mode number n increases, as a result of the change in the radial mode structure, which, according to the models, becomes more localized for higher ns leading to less damping. The turning point for the damping properties to change from low- n to medium- n behavior is found to be at $|n| \approx 3 - 4$. This is consistent with the observations of unstable TAEs driven by fast ions on JET and other fusion devices. The experimental results are also consistent with the results of modeling studies of Chapter 5.

Finally, it has been possible to estimate the ICRH fast-ion drive γ_f/ω on $n = 3$ TAEs from the damping measurements: the drive has been estimated to be $\gamma_f/\omega = 0.8 - 1\%$ for 2 MW of ICRH power in the particular limiter plasma configuration.

7.2 Conclusions

The damping rate database that was assembled in JET and analyzed in this work is orders of magnitude richer (at least by a factor of 100) than any of the other machines worldwide that have attempted the same kind of experiments. We have found a strong consistency of the experimental measurements with the general theoretical prediction in that intermediate- n modes tend to have less damping because of a more localized radial structure. This gives a first element of confidence in our predicting capabilities for the stability of modes in burning plasmas. The experimental results justify *a posteriori* the effort that was put on the experimental side in order to optimize the antenna currents and to estimate correctly the n -spectrum of the plasma response. They also demonstrate the need to follow in real-time individual- n modes.

The comparisons of measured and calculated damping rates underline the importance of the kinetic effects in order to achieve a realistic estimation of the TAE damping. Given the insight gained from these comparisons, utilizing the damping rate measurements to test the plasma models that are embodied in the various numerical codes is a very promising method for ensuring the validity of AE stability predictions in future burning plasmas. The physics of damping seems generally understood, although quantitative details need to be refined. The JET

AE damping database is now available for general use, in particular to analyse ITER scenarios and prepare ITER exploitation.

7.3 Outlook

Several interesting perspectives have been opened by the experimental work. In the frame of a collaboration including MIT, CRPP and JET, an upgrade has been designed for the active MHD spectroscopy system on JET. The upgrade includes installing eight power amplifiers of 1 kW each for the separate and independent transmission of the antenna-driven power to the eight antenna coils. Imposing arbitrary phases between the antenna currents is foreseen, which can have multiple beneficial effects. It can peak the RF power in narrower n -ranges and impose the sign of n . This could allow to measure AE damping rates in plasma configurations in which the damping rates could not be measured so far due to insufficient drive. It would also simplify greatly the post-pulse analysis by reducing the number of the driven n .

One aspect that is missing so far from the present antenna-driven AE studies is a reliable measurement of the internal mode structure of the AEs. The possibility of measuring the antenna-driven radial eigenfunction using the X-mode reflectometry diagnostic on JET has been investigated but the results have not been conclusive, to date. It was found, confirming previous work, that cross-talk exists between channels of the fast data acquisition system on JET, which affects the cross-correlation analysis between the reflectometry and the magnetics. However, in some cases, evidence of antenna-driven modes was found in 3 of the 4 probing frequencies of the reflectometry system. More investigations are needed to explore further this possibility, e.g. by analyzing also correlation with signals of the electron cyclotron emission system.

In order to study the interaction of AEs with the fast ion populations, more experiments could be carried out to estimate the fast-ion drive as a function of n via the damping rate measurements. Finally, exploring the possibility of inducing a controlled fast-ion redistribution using the AE antennas could be envisaged. For this, it would be useful to have precise estimation of the AE amplitudes needed to induce a measurable redistribution effect, and if this is achievable with the upgraded 8 kW system.

Appendix A

Circuits

A.1 Single-line m-antenna model of the AE exciter

We describe here the way to construct a single-line equivalent model of the AE exciter. The goal is to merge the m outputs of the distribution unit into one.

Consider a circuit configuration with m ideal transformers of the same winding ratio $1:n$, whose primary sides are connected in series and their secondary sides are connect to m loads with impedance Z_L . A voltage V is applied on the primary side and a current I flows. The impedance that is measured at the primary side of this configuration is

$$Z_{in} = \frac{V}{I} = \frac{V_1 + V_2 + \dots + V_m}{I} = \frac{Z_{L1} + Z_{L2} + \dots + Z_{Lm}}{n^2} = \frac{m}{n^2} Z_L \quad (\text{A.1})$$

Now consider an equivalent circuit with 1 ideal transformer of winding ratio n_{eq} , terminated at the secondary side with a load of impedance Z_L . The impedance seen on the primary side is $Z'_{in} = \frac{1}{n_{eq}^2} Z_L$. By requiring that $Z_{in} = Z'_{in}$, we find that

$$n_{eq} = \frac{n}{\sqrt{m}} \quad (\text{A.2})$$

Furthermore, every voltage V'_s in the secondary side of the equivalent circuit is related to the voltage V_s in the secondary side of the original as follows

$$\frac{V'_s}{V_s} = \frac{nV/\sqrt{m}}{nV/m} = \sqrt{m} \quad (\text{A.3})$$

where V is the voltage at the primary side (same for the both models). Similarly, for the currents the following relation holds,

$$\frac{I'_s}{I_s} = \frac{I\sqrt{m}/n}{I/n} = \sqrt{m} \quad (\text{A.4})$$

A.2 Matching units

This section shows the results for two of the matching units that were designed. Figure A.1 shows a matching circuit with a Π topology and with central matching frequency at 143 kHz. Figure A.1 shows a matching circuit that consists of a series capacitor and has a central matching frequency at 175 kHz.

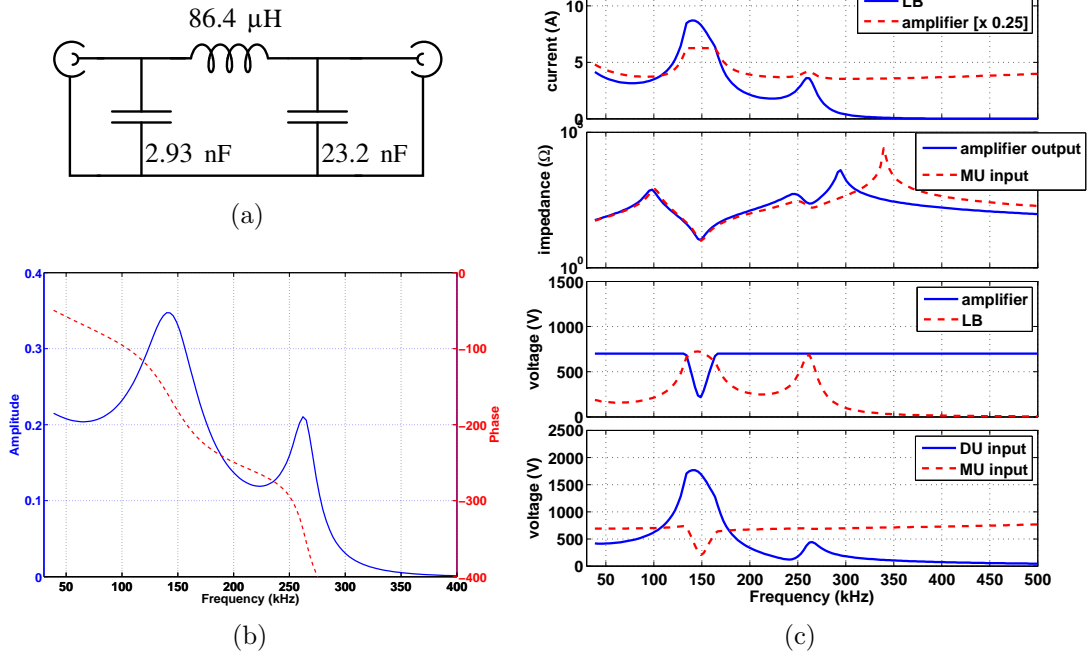


Figure A.1: Matching and central frequency at 143 kHz. (a) Circuit with Π topology. (b) Total current gain. HWHM=17%. (c) Exciter engineering signals in a simulated operation with AGC and impedance at the MU input.

A.3 Proof of the fundamental theorem for the remote calibration of the magnetic coils using impedance measurements

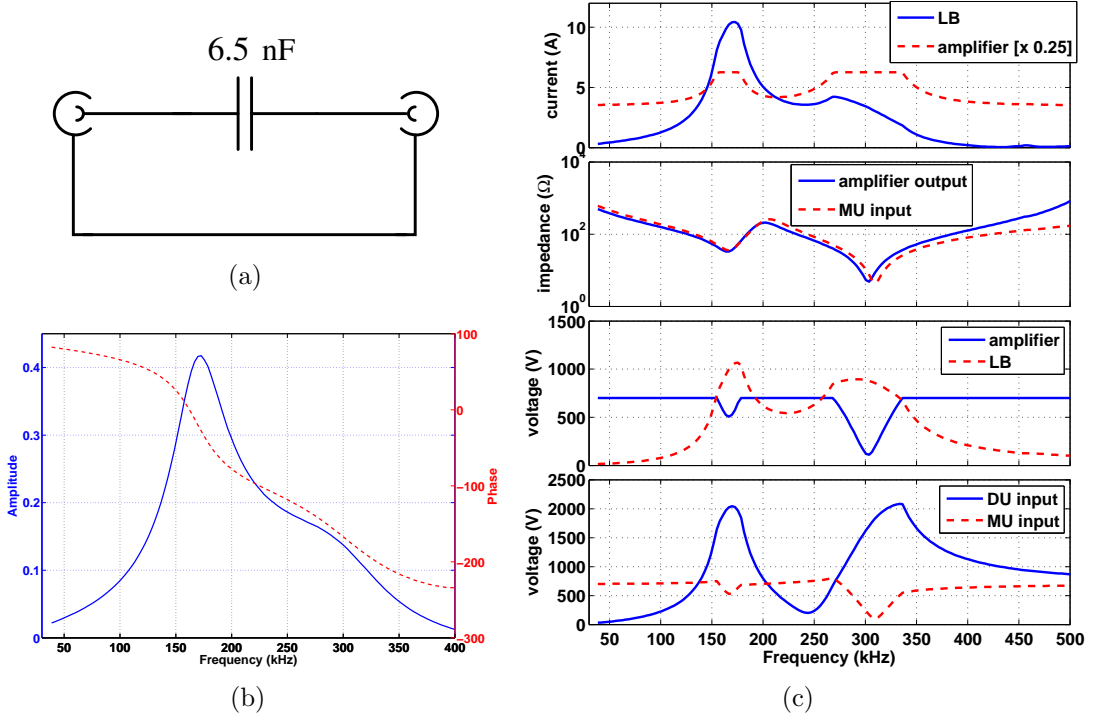


Figure A.2: Matching and central frequency at 175 kHz. (a) Circuit with one series capacitor. (b) Total current gain. HWHM=16%. (c) Exciter engineering signals in a simulated operation with AGC and impedance at the MU input.

A.3 Proof of the fundamental theorem for the remote calibration of the magnetic coils using impedance measurements

In reference [81], a procedure is developed and applied to calibrate remotely the magnetic pick-up coils on JET by measuring the impedance of the coils at the end of the transmission lines that connect them to the acquisition system. This method is based on the fundamental circuit theorem that is described in Section III.D of the reference [81] and it is proved therein using a lumped-element circuit representation in the appendix A. The lumped-element circuit approach is extended in reference [104] using transmission-line theory. Here, the same problem is considered and it is shown that the theorem holds for a wide class of circuits and measurement conditions.

A.3 Proof of the fundamental theorem for the remote calibration of the magnetic coils using impedance measurements

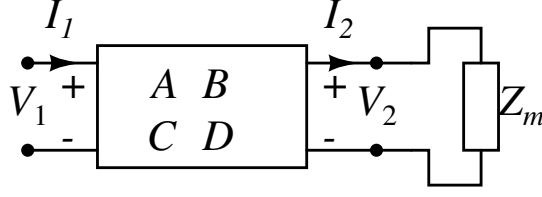


Figure A.3: The impedance is measured towards the torus at the port 1. The magnetic coil has an impedance Z_m .

We consider the circuit of figure A.3 that shows how the system is configured for the procedure of the impedance measurement. The magnetic coil has an impedance Z_m , with

$$Z_m = (R_m + i\omega L_m) \parallel (i\omega C_m)^{-1}, \quad (\text{A.5})$$

where R_m is the coil resistance in series with the coil inductance L_m and the shunt capacitance C_m is in parallel with the series combination of R_m and L_m . The operation between the impedance Z_1 and the impedance is Z_2 is defined as $Z_1 \parallel Z_2 \equiv Z_1 Z_2 / (Z_1 + Z_2)$. The coil impedance is not measured directly at the coil terminals, but at a measurement point that lies away from it, e.g. at the end of a transmission line. It is assumed that the circuit that connects the probe to the available measurement point can be described using a 2-port representation, and specifically via the transmission matrix $ABCD$

$$\begin{pmatrix} V_1 \\ I_1 \end{pmatrix} = \begin{pmatrix} A(\omega) & B(\omega) \\ C(\omega) & D(\omega) \end{pmatrix} \begin{pmatrix} V_2 \\ I_2 \end{pmatrix} \quad (\text{A.6})$$

This matrix provides the description of the network lying between the probe and the measurement point and is equivalent to the impedance matrix of the network [76]. Thus, the impedance is measured at the port 1 of the circuit shown in figure A.3. Then, the impedance measured is

$$Z_{meas} = \frac{V_1}{I_1} = \frac{AZ_m + B}{CZ_m + D}. \quad (\text{A.7})$$

For the normal operation of the diagnostic during plasma discharges, the circuit model that we have considered so far has to be modified to account for the emf that is not self-induced, \mathcal{E} (figure 4.8). Thus, the circuit is modified as shown in figure A.4, where the quantity \mathcal{E}' is related to \mathcal{E} as

$$\mathcal{E}' = \frac{\mathcal{E}}{1 + (R_m + i\omega L_m)i\omega C_m}. \quad (\text{A.8})$$

A.3 Proof of the fundamental theorem for the remote calibration of the magnetic coils using impedance measurements

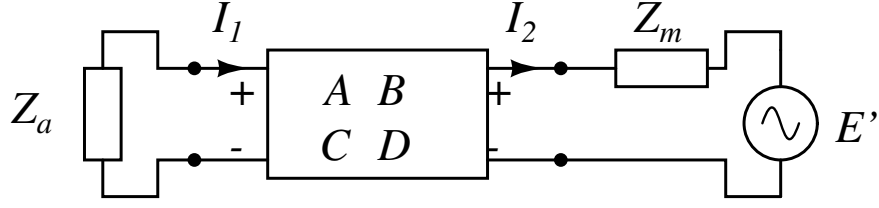


Figure A.4: Representation of the system during normal operation; Z_a is the input impedance of the analog-to-digital converters

In addition, at the point of the impedance measurement point, a circuit (e.g. the acquisition system) with input impedance Z_a is connected, as shown in figure A.4. For this configuration the description of the system is completed using the transmission equations (A.6) and the following termination equations

$$V_1 = -I_1 Z_a, \quad V_2 = I_2 Z_m + \mathcal{E}' \quad (\text{A.9})$$

The full linear system can be written as in a matrix form

$$\begin{pmatrix} 1 & Z_a & 0 & 0 \\ 0 & 0 & 1 & -Z_m \\ 1 & 0 & -A & -B \\ 0 & 1 & -C & -D \end{pmatrix} \begin{pmatrix} V_1 \\ I_1 \\ V_2 \\ I_2 \end{pmatrix} = \begin{pmatrix} 0 \\ \mathcal{E}' \\ 0 \\ 0 \end{pmatrix} \quad (\text{A.10})$$

from which one obtains, using (A.8),

$$\mathcal{H} = \frac{V_1}{\mathcal{E}} = \frac{AD - BC}{CZ_m + D + \frac{AZ_m + B}{Z_a}} \frac{1}{1 + (R_m + i\omega L_m)i\omega C_m} \quad (\text{A.11})$$

We consider now equations (A.7) and (A.11), and require that they take form $Z_{meas} = \mathcal{N}/\mathcal{D}$ and $\mathcal{H} = 1/\mathcal{D}$ (as needed for the impedance calibration method). The following conditions need to apply

$$AD - BC = 1 \quad (\text{A.12})$$

$$Z_a \gg Z_{meas} \quad (\text{A.13})$$

$$\omega \ll \frac{1}{\sqrt{L_m C_m}} \quad (\text{A.14})$$

The condition (A.12) means that the the circuit lying between the impedance measurement point and the coil has to satisfy the property of reciprocity. The condition (A.13) requires that the the magnitude of the measured impedance should not exceed the impedance Z_a . Finally, the condition (A.14) requires that

A.3 Proof of the fundamental theorem for the remote calibration of the magnetic coils using impedance measurements

the coil resonant frequency be much higher than the maximum frequency of interest (having made the reasonable assumption about the sensor resonant model, that the damping rate is much lower than the resonant frequency, i.e. $a \ll \omega_0$, where $a = \frac{R}{2L}$ and $\omega_0^2 = \frac{1}{LC}$).

Appendix B

Field formulas

In the following, we provide the analytical expressions of the vector potential \mathbf{A} and the resulting magnetic field in the near-field zone of the rectangular thin loop that is defined in chapter 4.

The y component of \mathbf{A} is zero. The z and x components are

$$A_z = \begin{cases} \frac{\mu_0 I}{4\pi} \ln \left[\frac{\ell_z - z + \sqrt{x^2 + y^2 + (z - \ell_z)^2}}{-z + \sqrt{x^2 + y^2 + z^2}} \frac{-\ell_z + z + \sqrt{(x - \ell_x)^2 + y^2 + (z - \ell_z)^2}}{z + \sqrt{(x - \ell_x)^2 + y^2 + z^2}} \right] \\ \quad \text{if } x^2 + y^2 \neq 0 \text{ and } (x - \ell_x)^2 + y^2 \neq 0, \\ \frac{\mu_0 I}{4\pi} \ln \left[\frac{z - \ell_z}{z} \frac{-\ell_z + z + \sqrt{\ell_x^2 + (z - \ell_z)^2}}{z + \sqrt{\ell_x^2 + z^2}} \right] \\ \quad \text{if } x = y = 0 \text{ and } (z < 0 \text{ or } z > \ell_z), \\ \frac{\mu_0 I}{4\pi} \ln \left[\frac{\ell_z - z + \sqrt{\ell_x^2 + (z - \ell_z)^2}}{-z + \sqrt{\ell_x^2 + z^2}} \frac{z}{z - \ell_z} \right] \\ \quad \text{if } (x = \ell_x \text{ and } y = 0) \text{ and } (z < 0 \text{ or } z > \ell_z), \\ \infty \\ \quad \text{if } (x = \ell_x \text{ or } x = 0) \text{ and } y = 0 \text{ and } 0 < z < \ell_z. \end{cases} \quad (\text{B.1})$$

and

$$A_x = \begin{cases} \frac{\mu_0 I}{4\pi} \ln \left[\frac{\ell_x - x + \sqrt{(x - \ell_x)^2 + y^2 + (z - \ell_z)^2}}{-x + \sqrt{x^2 + y^2 + (z - \ell_z)^2}} \frac{-\ell_x + x + \sqrt{(x - \ell_x)^2 + y^2 + z^2}}{x + \sqrt{x^2 + y^2 + z^2}} \right] \\ \quad \text{if } z^2 + y^2 \neq 0 \text{ and } (z - \ell_z)^2 + y^2 \neq 0, \\ \frac{\mu_0 I}{4\pi} \ln \left[\frac{x - \ell_x}{x} \frac{-\ell_x + x + \sqrt{(x - \ell_x)^2 + \ell_z^2}}{x + \sqrt{x^2 + \ell_z^2}} \right] \\ \quad \text{if } z = \ell_z \text{ and } y = 0 \text{ and } (x < 0 \text{ and } x > \ell_x), \\ \frac{\mu_0 I}{4\pi} \ln \left[\frac{\ell_x - x + \sqrt{(x - \ell_x)^2 + \ell_z^2}}{-x + \sqrt{x^2 + \ell_z^2}} \frac{x}{x - \ell_x} \right] \\ \quad \text{if } z = y = 0 \text{ and } (x < 0 \text{ and } x > \ell_x), \\ \infty \\ \quad \text{if } (z = \ell_z \text{ or } z = 0) \text{ and } y = 0 \text{ and } 0 < x < \ell_x. \end{cases} \quad (\text{B.2})$$

The magnetic field is derived using $\mathbf{B} = \nabla \times \mathbf{A}$. The expression is valid for all space (near-zone) apart from those positions in the plane $y = 0$ that coincide with the loop. Notice that the tangent components B_x and B_z are zero in the plane defined by the loop, i.e. where $y = 0$.

$$\begin{aligned}
B_x = \left(\frac{\mu_0 I}{4\pi} \right) & \left[- \frac{y}{\sqrt{(\ell_x - x)^2 + y^2 + z^2}(z + \sqrt{(\ell_x - x)^2 + y^2 + z^2})} \right. \\
& - \frac{y}{\sqrt{x^2 + y^2 + z^2}(-z + \sqrt{x^2 + y^2 + z^2})} \\
& + \frac{y}{\sqrt{(\ell_x - x)^2 + y^2 + (-\ell_z + z)^2}(-\ell_z + z + \sqrt{(\ell_x - x)^2 + y^2 + (z - \ell_z)^2})} \\
& \left. + \frac{y}{\sqrt{x^2 + y^2 + (-\ell_z + z)^2}(\ell_z - z + \sqrt{x^2 + y^2 + (z - \ell_z)^2})} \right]
\end{aligned} \tag{B.3}$$

$$\begin{aligned}
B_z = \left(\frac{\mu_0 I}{4\pi} \right) & \left[\frac{y}{\sqrt{x^2 + y^2 + z^2}(x + \sqrt{x^2 + y^2 + z^2})} \right. \\
& - \frac{y}{\sqrt{(-\ell_x + x)^2 + y^2 + z^2}(-\ell_x + x + \sqrt{(-\ell_x + x)^2 + y^2 + z^2})} \\
& + \frac{y}{\sqrt{x^2 + y^2 + (-\ell_z + z)^2}(-x + \sqrt{x^2 + y^2 + (z - \ell_z)^2})} \\
& \left. - \frac{y}{\sqrt{(-\ell_x + x)^2 + y^2 + (-\ell_z + z)^2}(\ell_x - x + \sqrt{(-\ell_x + x)^2 + y^2 + (z - \ell_z)^2})} \right]
\end{aligned} \tag{B.4}$$

$$\begin{aligned}
B_y = \left(\frac{\mu_0 I}{4\pi} \right) \bigg[& - \frac{\ell_x - x}{\sqrt{(\ell_x - x)^2 + y^2 + z^2} (z + \sqrt{(\ell_x - x)^2 + y^2 + z^2})} \\
& - \frac{z}{\sqrt{x^2 + y^2 + z^2} (x + \sqrt{x^2 + y^2 + z^2})} \\
& + \frac{x}{\sqrt{x^2 + y^2 + z^2} (-z + \sqrt{x^2 + y^2 + z^2})} \\
& + \frac{z}{\sqrt{(-\ell_x + x)^2 + y^2 + z^2} (-\ell_x + x + \sqrt{(-\ell_x + x)^2 + y^2 + z^2})} \\
& + \frac{\ell_x - x}{\sqrt{(-\ell_x + x)^2 + y^2 + (-\ell_z + z)^2} (-\ell_z + z + \sqrt{(-\ell_x + x)^2 + y^2 + (-\ell_z + z)^2})} \\
& - \frac{-\ell_z + z}{\sqrt{x^2 + y^2 + (-\ell_z + z)^2} (-x + \sqrt{x^2 + y^2 + (-\ell_z + z)^2})} \\
& - \frac{x}{\sqrt{x^2 + y^2 + (-\ell_z + z)^2} (\ell_z - z + \sqrt{x^2 + y^2 + (-\ell_z + z)^2})} \\
& + \frac{-\ell_z + z}{\sqrt{(-\ell_x + x)^2 + y^2 + (-\ell_z + z)^2} (\ell_x - x + \sqrt{(-\ell_x + x)^2 + y^2 + (-\ell_z + z)^2})} \bigg] \\
& \text{(B.5)}
\end{aligned}$$

Appendix C

Relation between damping rate expressions

The amplitude response of the damped harmonic oscillator model can be written in the following form in terms of the Laplace variable s

$$H(s) = \frac{A}{(s - p)(s - p^*)} = \frac{A}{2i\omega_0} \left(\frac{1}{s - p} - \frac{1}{s - p^*} \right) , \quad (\text{C.1})$$

where $p = -\gamma + i\omega_0$ and $\gamma \ll \omega_0$ can be assumed for the modes in question. The convention for the minus sign is used here so that the damping rate γ is positive. So, $-\gamma$ is real part of the pole and ω_0 is the imaginary part.

Experimentally, the plasma transfer function is constructed by dividing a quantity proportional to the mode amplitude, i.e. $\propto \delta B_\theta$, over the radial driven field that is proportional to the antenna currents. So, experimentally, the complex amplitude response

$$H(s) = \frac{A}{s^2 + 2\gamma s + \omega_0^2} . \quad (\text{C.2})$$

is measured.

We will derive the relationship between the inverse of the quality factor $1/Q_a$ defined as

$$\frac{1}{Q_a} = \frac{\Delta\omega}{\omega_0} = \frac{\omega_{a+} - \omega_{a-}}{\omega_0} , \quad (\text{C.3})$$

where $\Delta\omega$ is the full width of the resonance at the $1/a$ of the peak of the **power** steady-state response $|H(i\omega)|^2$. Note that FWHM = $1/Q_{1/2}$. Specifically, we are looking for the frequencies ω_a that satisfy

$$|H(i\omega_a)|^2 = \frac{|H|_{max}^2}{a} , \quad (\text{C.4})$$

where $|H|_{max} = \frac{1}{2\gamma\omega_0}$. From the expression

$$\frac{1}{|-\omega_a^2 + 2\gamma i\omega_a + \omega_0^2|^2} = \frac{1}{|a| + 2\gamma i\omega_0|^2} \quad (\text{C.5})$$

one ends up with a quadratic algebraic equation in ω_a^2

$$\omega_a^4 + B\omega_a^2 + C = 0, \quad (\text{C.6})$$

where $B = 2\omega_0^2(2x^2 - 1)$, $C = \omega_0^4(1 - 4ax^2)$ and $x = \gamma/\omega_0 \ll 1$. The discriminant is

$$\Delta = 4\omega_0^4(2x^2 - 1)^2 - 4\omega_0^4(1 - 4ax^2) \quad (\text{C.7})$$

$$\Delta = 4\omega_0^4(4x^4 + 1 - 4x^2 - 1 + 4ax^2) \quad (\text{C.8})$$

$$\Delta \approx 16\omega_0^4x^2(a - 1) \quad (\text{C.9})$$

So we find

$$\omega_{a,\pm}^2 = \omega_0^2(1 - 2x^2) \pm 4\omega_0^2x\sqrt{a-1} \approx \omega_0^2(1 \pm 2x\sqrt{a-1}) \quad (\text{C.10})$$

and

$$\omega_{a,\pm} = \omega_0\sqrt{1 \pm 2x\sqrt{a-1}} \approx \omega_0(1 \pm x\sqrt{a-1}) \quad (\text{C.11})$$

Now, one can calculate $1/Q_a$ from expression (C.3)

$$\frac{1}{Q_a} = 2x\sqrt{a-1} = 2\frac{\gamma}{\omega_0}\sqrt{a-1} \quad (\text{C.12})$$

For $a = 2$, one obtains that the FWHM is $1/Q_{1/2} = 2\frac{\gamma}{\omega_0}$. Thus, γ/ω is equal to either the HWHM, i.e. the half width at half maximum of the power response or to the FWHM divided by 2.

Appendix D

Publications and scientific presentations

This appendix provides a list of the peer-reviewed publications, conference contributions and scientific meeting presentations that the author has contributed to.

Publications in peer-reviewed journals:

Panis T *et al.* (2010) “Optimization of the active MHD spectroscopy system on JET for the excitation of individual intermediate and high- n Alfvén eigenmodes” *Nuclear Fusion*, **50**, 084019,

Testa D, Mellet N, Panis T *et al.* (2010) “The dependence of the damping rate of medium- n Alfvén eigenmodes on the edge elongation in JET” *Nuclear Fusion*, **50**, 084010.

Fasoli A, Testa D, Panis T *et al.* (2010) “Active excitation and damping rate measurement of intermediate- n toroidal Alfvén eigenmodes in JET, C-Mod and MAST plasmas” *Plasma Physics and Controlled Fusion*, **52**, 075015.

Alves D, Coelho R, Klein A, Panis T, Murari A (2010) “A real-time synchronous detector for the TAE antenna diagnostic at JET” *IEEE Transactions on Nuclear Science*, **57**, 577 .

Conference contributions:

Panis T *et al.* “Identification of background plasma damping mechanisms of antenna-driven toroidal Alfvén eigenmodes of medium- n on JET” 52nd Annual Meeting of the APS Division of Plasma Physics, Chigago, USA, November 2010.

Testa D, Panis T *et al.* “Recent JET Experiments on Alfvén Eigenmodes with Intermediate Toroidal Mode Numbers: Measurements and Modelling” 23rd IAEA Fusion Energy Conference, Daejon, Rep. of Korea, October 2010.

Panis T *et al.* “Recent damping rate measurements of antenna-driven toroidal Alfvén eigenmodes of intermediate n on JET and comparison with plasma models” 9th School and Workshop on Fusion Physics and Technology, Volos, Greece, April 2010.

Panis T *et al.* “Optimization of the active MHD spectroscopy system on JET for the excitation of individual intermediate and high- n Alfvén eigenmodes” Proc. 11th IAEA technical meeting on energetic particles in magnetic confinement systems, Kyiv, Ukraine, September 2009.

Testa D, Panis T *et al.* “Measurement of the damping rate of high- n toroidal Alfvén eigenmodes in JET” Proc. 11th IAEA technical meeting on energetic particles in magnetic confinement systems, Kyiv, Ukraine, September 2009.

Testa D, Blanchard P, Fasoli A, Klein A, Panis T, Snipes J A “Measurement of the damping rate of high- n toroidal Alfvén eigenmodes in JET” 13th EU-US Transport Task Force Workshop on transport in fusion plasmas, Copenhagen, Denmark, September 2008.

Panis T *et al.* “Electrical model of the Alfvén eigenmode exciter on JET” Annual meeting of the Swiss Physical Society, Geneva, Switzerland, March 2008.

International Tokamak Physics Activity (ITPA) meetings (topical group on energetic particles (EP)):

Panis T *et al.* “TAE damping comparison: LEMan simulations” ITPA EP meeting, Seoul, Rep. of Korea, October 2010.

Panis T *et al.* “Damping rate comparison: $n = 3$ antenna-driven TAEs on JET and results of the LEMan code” ITPA EP meeting, Kyiv, Ukraine, September 2009.

Fasoli A *et al.* “Damping rate of intermediate toroidal mode number n Alfvén eigenmodes” ITPA EP meeting, Daejon, Rep. of Korea, April 2009.

Testa D *et al.* “Measurement of the damping rate of medium- n Alfvén eigenmodes in JET: ideas and possibilities for comparisons experiments vs. theory” ITPA EP meeting, Lausanne, Switzerland, October 2008.

Scientific meetings in JET:

Testa D, on behalf of the KC1T project team “KC1T Diagnostic: Data analysis steps” Data Coordination and Validation Meeting, 14 September 2010.

Testa D, Panis T *et al.* “M-1.2.1: TAE antenna (isotope scan)” Task Force MHD Meeting, 15 March 2010.

Panis T *et al.* “Antenna-driven TAE measurements for comparison with numerical simulations within the ITPA framework” Data Coordination and Validation Meeting, 10 February 2010.

Panis T *et al.* “TAE damping comparison: LEMan simulations” Task Force MHD Meeting, 6 October 2009.

Panis T *et al.* “Routine reconstruction of TAE radial structure with X-mode reflectometry (KG8b)” Task Force Diagnostics Workshop on Reflectometry, 15 September 2009.

Testa D, on behalf of the KC1T project team “Experimental results on the damping of medium- n Alfvén eigenmodes in JET” EFDA-JET Science Meeting, 7 September 2009.

Fasoli A, Testa D, Panis T “TAE Upgrade Proposal: Scientific Motivation and Collaboration Framework” TAE upgrade proposal meeting, 15 July 2009.

Testa D, Panis T *et al.* “M-3.3.2: determine stability of medium- n AEs”
Task Force MHD Meeting, 10 March 2009.

Bibliography

- [1] Wesson J “Tokamaks” (Clarendon Press - Oxford, 1997) 2nd edn.
- [2] ITER Physics Expert Group on Energetic Particles H, et al. (1999) “Chapter 5: Physics of energetic ions” *Nuclear Fusion* 39, 2471.
URL <http://stacks.iop.org/0029-5515/39/i=12/a=305>
- [3] Fasoli A et al. (2007) “Physics of energetic ions” *Nucl. Fusion* 47, S264.
- [4] Fasoli A et al. (1995) “Overview of Alfvén eigenmode experiments in JET” *Nucl. Fusion* 35, 1485.
- [5] Panis T, et al. (2010) “Optimization of the active MHD spectroscopy system on JET for the excitation of individual intermediate and high-n Alfvén eigenmodes” *Nuclear Fusion* 50, 084019.
URL <http://stacks.iop.org/0029-5515/50/i=8/a=084019>
- [6] Alfvén H (1942) “Existence of electromagnetic-hydrodynamic waves” *Nature* 150, 405.
- [7] Lundquist S (1949) “Experimental investigations of magneto-hydrodynamic waves” *Phys. Rev.* 76, 1805.
- [8] Lundquist S (1949) “Experimental demonstration of magneto-hydrodynamic waves” *Nature* 164, 145.
- [9] Freidberg J P “Ideal Magnetohydrodynamics” (Plenum Press, New York, 1987).
- [10] Boyd T J M and Sanderson J J “The Physics of Plasmas” (Cambridge University Press, 2003).

- [11] Krall N A and Trivelpiece A W “Principles of Plasma Physics” (McGraw-Hill, 1973).
- [12] Bernstein I B, et al. (1958) “Waves in a plasma in a magnetic field” *Proceedings of Royal Society, London* A244, 17.
- [13] Hasegawa A and Chen L (1975) “Kinetic process of plasma heating due to Alfvén wave excitation” *Phys. Rev. Lett.* 35, 370.
- [14] Hasegawa A and Chen L (1976) “Kinetic processes in plasma heating by resonant mode conversion of Alfvén wave” *Physics of Fluids* 19, 1924.
URL <http://link.aip.org/link/?PFL/19/1924/1>
- [15] Vaclavik J and Appert K (1991) “Theory of plasma-heating by low-frequency waves - magnetic pumping and Alfvén resonance heating” *Nucl. Fusion* 31, 1945.
- [16] Ross D W, et al. (1982) “Kinetic description of Alfvén wave heating” *Physics of Fluids* 25, 652.
URL <http://link.aip.org/link/?PFL/25/652/1>
- [17] Appert K, et al. (1982) “Excitation of global eigenmodes of the Alfvén wave in tokamaks” *Plasma Physics* 24, 1147.
URL <http://stacks.iop.org/0032-1028/24/i=9/a=010>
- [18] Kieras C E and Tataronis J A (1982) “The shear Alfvén continuous-spectrum of axisymmetric toroidal equilibria in the large aspect ratio limit” *Journal of Plasma Physics* 28, 395.
- [19] Cheng C Z, et al. (1985) “High-n ideal and resistive shear Alfvén waves in tokamaks” *Annals of Physics* 161, 21 .
URL <http://www.sciencedirect.com/science/article/B6WB1-4DF4W77-83/2/543a597be9ffe296d3adfaa63e6c426a>
- [20] Cheng C Z and Chance M S (1986) “Low-n shear Alfvén spectra in axisymmetric toroidal plasmas” *Physics of Fluids* 29, 3695.
URL <http://link.aip.org/link/?PFL/29/3695/1>

- [21] Pinches S D (1996) “Nonlinear interaction of fast particles with alfvén waves in tokamaks” Ph.D. thesis University of Nottingham.
- [22] Heidbrink W W (2008) “Basic physics of Alfvén instabilities driven by energetic particles toroidally confined plasmas” *Phys. Plasmas* 15, 055501.
- [23] Sharapov S E, et al. (2001) “MHD spectroscopy through detecting toroidal Alfvén eigenmodes and Alfvén wave cascades” *Physics Letters A* 289, 127 .
URL <http://www.sciencedirect.com/science/article/B6TVM-442RTHW-3/2/43ce6ee7d29c907d9cf30aa5c5eb0a62>
- [24] Mett R R and Mahajan S M (1992) “Kinetic theory of toroidicity-induced Alfvén eigenmodes” *Physics of Fluids B: Plasma Physics* 4, 2885.
URL <http://link.aip.org/link/?PFB/4/2885/1>
- [25] Fasoli A, et al. (1996) “Observation of multiple kinetic Alfvén eigenmodes” *Phys. Rev. Lett.* 76, 1067.
- [26] Rosenbluth M N and Rutherford P H (1975) “Excitation of Alfvén waves by high-energy ions in a tokamak” *Phys. Rev. Lett.* 34, 1428.
- [27] Wong K L (1999) “A review of Alfvén eigenmode observations in toroidal plasmas” *Plasma Phys. Control. Fusion* 41, R1.
- [28] Fu G Y and Cheng C Z (1992) “Excitation of high-n toroidicity-induced shear Alfvén eigenmodes by energetic particles and fusion alpha particles in tokamaks” *Physics of Fluids B: Plasma Physics* 4, 3722.
URL <http://link.aip.org/link/?PFB/4/3722/1>
- [29] Berk H L, et al. (1992) “Finite orbit energetic particle linear response to toroidal Alfvén eigenmodes” *Physics Letters A* 162, 475 .
URL <http://www.sciencedirect.com/science/article/B6TVM-46G89D2-M6/2/f8999f5525fbd54ad271d0ec9fb6017a>
- [30] Breizman B N and Sharapov S E (1995) “Energetic particle drive for toroidicity-induced Alfvén eigenmodes and kinetic toroidicity-induced Alfvén eigenmodes in a low-shear tokamak” *Plasma Physics and Controlled Fusion* 37, 1057.
URL <http://stacks.iop.org/0741-3335/37/i=10/a=001>

- [31] Heidbrink W W (2002) “Alpha particle physics in a tokamak burning plasma experiment” *Phys. Plasmas* 9, 2113.
- [32] Betti R and Freidberg J P (1992) “Stability of Alfvén gap modes in burning plasmas” *Phys. Fluids B* 4, 1465.
- [33] Connor J W et al. “Non-ideal effects on toroidal Alfvén eigenmode stability” in E P Society (Ed.) *Controlled Fusion and Plasma Physics (Proc. 21st Eur. Conf. Montpellier)* vol. 18B.II p. 616 (Geneva, 1994).
- [34] Gorelenkov N N et al. (2003) “Study of thermonuclear Alfvén instabilities in next step burning plasmas proposals” *Nucl. Fusion* 43, 594.
- [35] Fu G Y and Dam J W V (1989) “Excitation of the toroidicity-induced shear Alfvén eigenmode by fusion alpha particles in an ignited tokamak” *Physics of Fluids B: Plasma Physics* 1, 1949.
URL <http://link.aip.org/link/?PFB/1/1949/1>
- [36] Gorelenkov N N and Sharapov S E (1992) “On the collisional damping of TAE-modes on trapped electrons in tokamaks” *Physica Scripta* 45, 163.
URL <http://stacks.iop.org/1402-4896/45/i=2/a=016>
- [37] Villard L and Fu G (1992) “Geometrical and profile effects on toroidicity and ellipticity induced Alfvén eigenmodes” *Nuclear Fusion* 32, 1695.
URL <http://stacks.iop.org/0029-5515/32/i=10/a=I01>
- [38] Zonca F and Chen L (1992) “Resonant damping of toroidicity-induced shear-Alfvén eigenmodes in tokamaks” *Phys. Rev. Lett.* 68, 592.
- [39] Rosenbluth M N, et al. (1992) “Mode structure and continuum damping of high-n toroidal Alfvén eigenmodes” *Physics of Fluids B: Plasma Physics* 4, 2189.
URL <http://link.aip.org/link/?PFB/4/2189/1>
- [40] Zonca F and Chen L (1993) “Theory of continuum damping of toroidal Alfvén eigenmodes in finite-beta tokamaks” *Physics of Fluids B: Plasma Physics* 5, 3668.
URL <http://link.aip.org/link/?PFB/5/3668/1>

- [41] Berk H L, et al. (1993) “Arbitrary mode number boundary-layer theory for nonideal toroidal Alfvén modes” *Physics of Fluids B: Plasma Physics* 5, 3969.
URL <http://link.aip.org/link/?PFB/5/3969/1>
- [42] Fu G Y, et al. (1996) “Analysis of alpha particle-driven toroidal Alfvén eigenmodes in tokamak fusion test reactor deuterium–tritium experiments” *Physics of Plasmas* 3, 4036.
URL <http://link.aip.org/link/?PHP/3/4036/1>
- [43] Candy J and Rosenbluth M N (1994) “Nonideal theory of toroidal Alfvén eigenmodes” *Physics of Plasmas* 1, 356.
URL <http://link.aip.org/link/?PHP/1/356/1>
- [44] Sassenberg K, et al. (2009) “Stability of toroidicity induced shear Alfvén eigenmodes in asdex upgrade” *Plasma Physics and Controlled Fusion* 51, 065003.
URL <http://stacks.iop.org/0741-3335/51/i=6/a=065003>
- [45] Van Zeeland M A, et al. (2006) “Radial structure of Alfvén eigenmodes in the DIII–D tokamak through electron-cyclotron-emission measurements” *Phys. Rev. Lett.* 97, 135001.
- [46] da Graça S, et al. (2007) “Localization of MHD and fast particle modes using reflectometry in ASDEX upgrade” *Plasma Physics and Controlled Fusion* 49, 1849.
URL <http://stacks.iop.org/0741-3335/49/i=11/a=007>
- [47] Nazikian R, et al. (1997) “Alpha-particle-driven toroidal Alfvén eigenmodes in the tokamak fusion test reactor” *Phys. Rev. Lett.* 78, 2976.
- [48] Heidbrink W W W, et al. (1991) “An investigation of beam driven Alfvén instabilities in the DIII-D tokamak” *Nuclear Fusion* 31, 1635.
- [49] Pinches S, et al. (2006) “Observation and modelling of fast ion loss in JET and ASDEX upgrade” *Nuclear Fusion* 46, S904.
URL <http://stacks.iop.org/0029-5515/46/i=10/a=S06>

- [50] Heidbrink W W, et al. (2007) “Anomalous flattening of the fast-ion profile during Alfvén-eigenmode activity” *Phys. Rev. Lett.* 99, 245002.
- [51] Sharapov S E, et al. (2008) “Chapter 5 - Burning plasma studies at JET” *Fusion Science and Technology* 53, 989.
- [52] Jackson J D “Classical Electrodynamics” (John Wiley, 1999) 3rd edn.
- [53] Ljung L “System identification: theory for the user” (Prentice-Hall, 1987).
- [54] Moret J M (1994) “Fitting of Transfer Functions to Frequency Response Measurements” Tech. rep. CRPP-EPFL.
- [55] Fasoli A et al. (1995) “Direct Measurement of the Damping of Toroidicity-Induced Alfvén Eigenmodes” *Phys. Rev. Lett.* 75, 645.
- [56] Collins G A, et al. (1986) “The Alfvén wave spectrum as measured on a tokamak” *Physics of Fluids* 29, 2260.
URL <http://link.aip.org/link/?PFL/29/2260/1>
- [57] Fasoli A et al. (1997) “Alfvén eigenmode experiments in tokamaks and stellarators” *Plasma Phys. Control. Fusion* 39, B287.
- [58] Testa D et al. (2001) “The effect of plasma shape on the damping of low n Alfvén eigenmodes in jet tokamak plasmas” *Nuclear Fusion* 41, 809.
- [59] Testa D, et al. (2005) “Experimental study of the dependence of the damping rate of $n = 1$ TAEs on the on-axis safety factor and toroidal rotation shear” *Nuclear Fusion* 45, 907.
URL <http://stacks.iop.org/0029-5515/45/i=8/a=019>
- [60] Fasoli A, et al. (2010) “Active excitation and damping rate measurement of intermediate- n toroidal Alfvén eigenmodes in JET, C-Mod and MAST plasmas” *Plasma Physics and Controlled Fusion* 52, 075015.
URL <http://stacks.iop.org/0741-3335/52/i=7/a=075015>
- [61] Holties H A, et al. (1997) “Determination of local tokamak parameters by magnetohydrodynamic spectroscopy” *Physics of Plasmas* 4, 709.
URL <http://link.aip.org/link/?PHP/4/709/1>

- [62] Fasoli A, et al. (2002) “MHD spectroscopy” *Plasma Phys. Control. Fusion* 44, B159.
- [63] Jaun A, et al. (1998) “Prediction of Alfvén eigenmode dampings in the joint european torus” *Physics of Plasmas* 5, 2952.
URL <http://link.aip.org/link/?PHP/5/2952/1>
- [64] Fasoli A, et al. (2000) “Isotope mass scaling of ae damping rates in the jet tokamak plasmas” *Physics Letters A* 265, 288 .
URL <http://www.sciencedirect.com/science/article/B6TVM-3YHG80M-8/2/9077ff64df247b02809411b60e44b0fb>
- [65] Lauber P, et al. (2005) “Kinetic properties of shear alfvén eigenmodes in tokamak plasmas” *Physics of Plasmas* 12, 122501.
URL <http://link.aip.org/link/?PHP/12/122501/1>
- [66] Fu G Y, et al. (2005) “Kinetic damping of toroidal alfv[e-acute]n eigenmodes” *Physics of Plasmas* 12, 082505.
URL <http://link.aip.org/link/?PHP/12/082505/1>
- [67] Testa D, et al. (2003) “Experimental test of damping models for $n = 1$ toroidal alfvén eigenmodes in jet” *Nuclear Fusion* 43, 479.
URL <http://stacks.iop.org/0029-5515/43/i=6/a=310>
- [68] Testa D et al. “The new Alfvén wave excitation system at JET” in Proc. 23rd Symposium on Fusion Technology (SOFT) (Venice, Italy, 2004).
URL <http://soft2004.igi.cnr.it/>
- [69] Snipes J A, et al. (2004) “Initial active MHD spectroscopy experiments exciting stable Alfvén eigenmodes in Alcator C-Mod” *Plasma Physics and Controlled Fusion* 46, 611.
URL <http://stacks.iop.org/0741-3335/46/i=4/a=003>
- [70] Snipes J A, et al. (2005) “Active and fast particle driven alfv[e-acute]n eigenmodes in alcator c-mod” *Physics of Plasmas* 12, 056102.
URL <http://link.aip.org/link/?PHP/12/056102/1>

- [71] Snipes J, et al. (2006) “A comparison of measured and calculated toroidal Alfvén eigenmode damping rates in Alcator C-mod” *Nuclear Fusion* 46, 1036.
URL <http://stacks.iop.org/0029-5515/46/i=12/a=006>
- [72] Titus P H et al. (2005) “Structural analysis of the JET TAE antenna” *Fusion Science and Technology* 47, 931.
- [73] Terman F E “Radio Engineer’s Handbook” (McGraw-Hill, 1943).
- [74] The MathWorks, Inc. (2001) Curve Fitting Toolbox User’s Guide.
URL www.themathworks.com
- [75] Chubar O, et al. (1998) “A three-dimensional magnetostatics computer code for instertion devices” *J. Synchrotron Rad.* 5, 481.
- [76] Pozar D M “Microwave engineering” (John Wiley, 1998) 2nd edn.
- [77] Terman F E “Electronic and Radio Engineering” (McGraw-Hill, 1955) fourth edn.
- [78] Balanis C A “Antenna Theory” (John Wiley, 1982) 1st edn.
- [79] Goldstein H “Classical mechanics” (Reading, Masschusetts : Addison-Wesley, 1980) 2nd edn.
- [80] Woskov P et al. “Transmitter upgrade for JET Alfvén eigenmode fast particle interaction studies” *in* 51st Annual Meeting of the APS Division of Plasma Physics vol. 54 (2009).
- [81] Heeter R F, et al. (2000) “Fast magnetic fluctuation diagnostics for Alfvén eigenmode and magnetohydrodynamics studies at the Joint European Torus” *Review of Scientific Instruments* 71, 4092.
URL <http://link.aip.org/link/?RSI/71/4092/1>
- [82] Heeter R F (2000) “Calibration and data analysis for the KC2F fast magnetics system” Tech. rep. JET Joint Undertaking (unpublished).
- [83] Testa D (2008) “Final report on EFDA task EP-DIA-MAG: Impedance measurement and transfer function evaluation for the JET-EP1 high frequency coils” Tech. rep. JET-EP1.

- [84] Bourguignon S, et al. (2007) “SparSpec: a new method for fitting multiple sinusoids with irregularly sampled data” *Astronomy & Astrophysics* 462, 379.
- [85] Klein A et al. (2008) “A sparsity-based method for the analysis of magnetic fluctuations in unevenly-spaced mirnov coils” *Plasma Physics and Controlled Fusion* 50, 125005.
- [86] Testa D, et al. (2010) “The JET Alfvén Eigenmode Local Manager for the real-time detection and tracking of a frequency-degenerate spectrum of mhd instabilities” Submitted to Review of Scientific Instruments.
- [87] Press H W “Numerical recipes in Fortran 77: The art of scientific computing” (Cambridge University Press, 1992).
- [88] Bevington P R “Data reduction and error analysis for the physical sciences” (McGraw-Hill, 1969).
- [89] Heidbrink W W et al. (1997) “Stable ellipticity-induced Alfvén eigenmodes in the Joint European Torus” *Phys. Plasmas* 4, 3663.
- [90] Borba D, et al. (2002) “Modelling of Alfvén waves in JET plasmas with the CASTOR-K code” *Nuclear Fusion* 42, 1029.
URL <http://stacks.iop.org/0029-5515/42/i=8/a=311>
- [91] Popovich P et al. (2006) “A full-wave solver of the Maxwell’s equations in 3D cold plasmas” *Computer Physics Communications* 175, 250.
- [92] Mellet N (2009) “Propagation and absorption of low frequency waves in two and three dimensional warm plasmas” Ph.D. thesis EPFL.
- [93] Kerner W, et al. (1998) “CASTOR: Normal-mode analysis of resistive MHD plasmas” *Journal of Computational Physics* 142, 271 .
URL <http://www.sciencedirect.com/science/article/B6WHY-45J592V-5Y/2/1abcb7f606f3619789144061ec9d4d2d>
- [94] Hirshman S P and Whitson J C (1983) “Steepest-descent moment method for three-dimensional magnetohydrodynamic equilibria” *Physics of Fluids* 26, 3553.
URL <http://link.aip.org/link/?PFL/26/3553/1>

- [95] Anderson D, et al. (1991) “The TERPSICHORE code for the stability analysis of magnetically confined fusion plasmas” *Supercomputer* 8, 32.
- [96] Huysmans G T A, et al. (1995) “Modeling the excitation of global Alfvén modes by an external antenna in the Joint European Torus (JET)” *Physics of Plasmas* 2, 1605.
URL <http://link.aip.org/link/?PHP/2/1605/1>
- [97] ITPA, Group on Energetic Particles “The influence of plasma shaping on the damping of toroidal Alfvén eigenmodes” in 23rd IAEA Fusion Energy Conference (Daejeon, Republic of Korea, 2010).
- [98] Lao L, et al. (1985) “Reconstruction of current profile parameters and plasma shapes in tokamaks” *Nucl. Fusion* 25, 1611.
- [99] Chen L and Zonca F (1995) “Theory of shear Alfvén waves in toroidal plasmas” *Physica Scripta* T60, 81 International Workshop on Alfvén Waves, Rio Janeiro, Brazil, Nov 08-10, 1994.
- [100] Huysmans G T A, et al. (1993) “Free boundary resistive modes in tokamaks” *Physics of Fluids B: Plasma Physics* 5, 1545.
URL <http://link.aip.org/link/?PFB/5/1545/1>
- [101] Poedts S, et al. (1992) “Damping of global Alfvén waves in tokamaks due to resonant absorption” *Plasma Physics and Controlled Fusion* 34, 1397.
URL <http://stacks.iop.org/0741-3335/34/i=8/a=003>
- [102] Testa D, et al. (2010) “The dependence of the damping rate of medium- n toroidal Alfvén eigenmodes on the edge plasma elongation in JET” *Nuclear Fusion* 50, 084010.
URL <http://stacks.iop.org/0029-5515/50/i=8/a=084010>
- [103] Lauber P et al. (2007) “LIGKA: A linear gyrokinetic code for the description of background kinetic and fast particle effects on the MHD stability in tokamaks” *Journal of Computational Physics* 226, 447.
- [104] Appel L C and Hole M J (2005) “Calibration of the high-frequency magnetic fluctuation diagnostic in plasma devices” *Review of Scientific Instruments*

76, 093505.

URL <http://link.aip.org/link/?RSI/76/093505/1>

BIBLIOGRAPHY

Acknowledgements

This work could not have been achieved without the contribution of many persons. I gratefully acknowledge the help of my thesis directors A. Fasoli and D. Testa. I owe also thanks to my co-workers and collaborators: A. Klein, P. Blanchard, N. Mellet, C. Bower, A. Goodyear, H. Carfantan, P. Marmillod, P. Lavanchy, S. E. Sharapov, L. Villard, P. Lauber, S. Pinches, M. Tsalas.

Because this thesis “consumed” the biggest part of my last four years, the limited time that I could spend with friends outside work had to be well spent, so that I could be more efficient. Thus, I remember all the friends that I made in JET and in Oxford, whose company helped me to relax during those stressful days: Cynthia, Laura, Matteo, Alessandro, Athena, Maximos, Alex, Patrick. Furthermore, I could not omit my friends in Lausanne and the PhD students, part of them are now already “Dr”: Andreas (absolute skiing experience, “...ce jour à Grand Saint-Bernard...”), Loïc (absolute classical music expert, “...aah, ce Ludwig...”), Silvano (absolute animal-imitating expert “...et après on lui tire de fléchettes...”) (my office mates), Francesco, Federico, Christian T., Christian S., Joaquim, Jonathan, Thibault, Kees, Lucia, Dávid W., David L., Mattia, Janos, Xavier, Ben, James, Edén, Andy and Nevena and Konstantinos (my “collocataires”), Elena and Claudi and Isabelle and Yolanda (my dancing partners), Yannis, Aristeidis, Leonidas, Nikos, Maria. If I have forgotten anyone, it is because I am in a hurry: I need to submit the final version of this thesis very soon...

BIBLIOGRAPHY

Curriculum vitae

Theodoros Panis

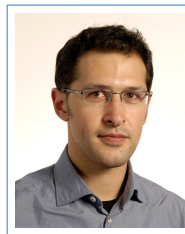
Avenue de la Harpe 45
CH-1007 Lausanne, SWITZERLAND

☎ +41 78 85 56 437

☎ +41 21 69 33 433

✉ theodoros.panis@epfl.ch

27 years. Single. Greek citizen.



Education

2006 – current **Ph.D. in Physics**, *Ecole Polytechnique Fédérale de Lausanne*, Switzerland.

Institute Centre de Recherches en Physique des Plasmas (CRPP), EPFL.

Title Direct measurements of the damping of Alfvén eigenmodes for an assessment of their stability limits in tokamak plasmas

Directors Prof. A. Fasoli and Dr. D. Testa.

2000 – 2005 **M.Sc. in Electrical and Computer Engineering**, *National Technical University of Athens (NTUA)*, Greece.

2005 **Diploma thesis**, *Université de Liège (ULg)*, Belgium.
(within student exchange program)

Institute Montefiore, Department of Electrical Engineering and Computer Science, ULg.

Title Steady-state Fitted Models for Composite Loads and Subtransmission Networks.

Directors Prof. T. Van Cutsem (ULg) and Prof. C. Vournas (NTUA).

Professional experience

2007-2010 Teaching support of lectures for undergraduate students.

2007-2010 Diagnostic coordinator for the experiments on the TCV tokamak (CRPP).

2007-2009 Operator of the TAE antenna system on the JET tokamak.

Computer skills

Computing MATLAB, Simulink, Mathematica

Operating system Unix, Linux, Mac OS X, Windows

Programming Basic skills in C, Fortran, Pascal

Electrical APLAC, PSpice, FEMM, ADS, SuperNEC

Typography, Graphics L^AT_EX, OpenOffice, Microsoft Office, iWork, XCircuit, Gimp

Languages

English Advanced level (C2, CPE)

French Advanced level (C2, DALF)

Spanish Intermediate level

Greek Native